amU
Aix Marseille Université

NNT : 2025AIXM0103

THÈSE DE DOCTORAT

Soutenue à Saint-Paul lez Durance - CEA Cadarache
le 15 Mai 2025 par

Matteo VERGANI

Advanced modelling of fission gas behaviour in the nuclear fuel at the grain scale

Discipline
Physique et Sciences de la Matière

Spécialité
Matière Condensée et Nanosciences

École doctorale
ED 352 : Physique et Sciences de la Matière

Laboratoire/Partenaires de recherche
PIIM, Aix-Marseille Université

CEA, IRESNE

Électricité de France (EDF)

Composition du jury

Thomas JOURDAN CEA Saclay	Rapporteur
Yves PIPON IP2I, CNRS	Rapporteur
Jonathan MOUGENOT LSPM, CNRS	Examinateur
Nathalie MONCOFFRE IP2I, CNRS	Présidente du jury
Yves FERRO PIIM, Aix-Marseille Université	Directeur de thèse
Laurence NOIROT CEA Cadarache	Co-directrice de thèse
Rodrigue LARGENTON EDF	Membre invité
François KREMER ASNR, Cadarache	Membre invité

cea iresne EDF PIIM

Affidavit

I, undersigned, Matteo Vergani, hereby declare that the work presented in this manuscript is my own work, carried out under the scientific supervision of [First Name Surname], in accordance with the principles of honesty, integrity and responsibility inherent to the research mission. The research work and the writing of this manuscript have been carried out in compliance with both the french national charter for Research Integrity and the Aix-Marseille University charter on the fight against plagiarism.

This work has not been submitted previously either in this country or in another country in the same or in a similar version to any other examination body.

Aix-en-Provence, 17/03/25

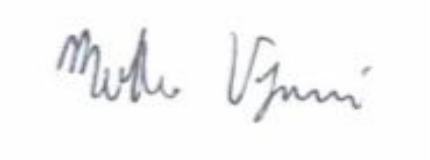

This work is licensed under Creative Commons Attribution-NonCommercial-NoDerivatives 4.0 International Public License

Liste de publications et participation aux conférences

Liste des publications et/ou brevets réalisées dans le cadre du projet de thèse :

1. M. Vergani, M.W.D. Cooper, L. Noirot. *A model for trapping and re-solution regarding intra-granular bubbles in UO_2, linked to atomic-scale simulations*. Journal of Nuclear Materials 605, 155562 (2025). [VERGANI et al. 2025]

Participation aux conférences et écoles d'été au cours de la période de thèse :

1. **NuFuel** - Marseille (France), November 2023. *Latest developments in the MARGARET fission gas and microstructure model, based on recent experimental findings and atomic scale modelling*. M. Vergani, L. Noirot - **Oral**
2. **TMS** - Orlando (Florida, USA), March 2024. *Results of MARGARET fission gas and microstructure model, following latest developments*. M. Vergani, L. Noirot - **Oral**
3. **NuMat** - Singapore, October 2024. *Improvements and validation of the new version of MARGARET fission gas and microstructure model, considering new experimental results and atomic scale simulations*. M. Vergani, L. Noirot - **Oral**

Résumé et mots clés

MARGARET est à la fois un code C++ de relâchement de gaz de fission (RGF) et un composant d'un code de comportement du combustible des réacteurs à eau légère, nommé ALCYONE. L'objectif de la thèse était d'améliorer MARGARET en tenant compte des dernières découvertes expérimentales et simulations à l'échelle atomique.
De nouvelles simulations de dynamique moléculaire classique (DM) pour étudier le phénomène de remise en solution dynamique des gaz de fission des bulles intra-granulaires dans la matrice du combustible sont disponibles. Nous avons développé un nouveau modèle de remise en solution qui peut être facilement adopté par les codes de comportement du combustible. Ce modèle est basé sur des simulations de MD publiées et sur les profils de remise en solution fournis par M.W.D. Cooper (Los Alamos NL), avec lequel nous avons publié un article inclus dans le manuscrit.
Les chercheurs du CEA ont obtenu des images expérimentales 3D de combustibles irradiés en base dont le RGF est non négligeable. Ces images semblent indiquer que les bulles inter-granulaires, dans ces conditions, ne forment pas un réseau interconnecté, contrairement à ce que l'on pensait précédemment. Nous avons donc inclus dans le modèle les phénomènes de remise and solution dynamique et thermique des bulles inter-granulaires vers les joints de grains, qui, en contrebalançant le piégeage peuvent a priori permettre le relâchement par diffusion à grande distance le long des joints de grains.
Une nouvelle restructuration du combustible, en centre pastille à haut taux de combustion, différente de la structure HBS, qui survient en périphérie, a été récemment découverte : elle est caractérisée par la formation de différents domaines à l'intérieur des grains initiaux, dont les orientations cristallines diffèrent légèrement. Ces domaines sont appelés "sous-domaines" et leur apparition coïncide avec la formation d'une deuxième population de bulles intra-granulaires plus grosses (appelées "bulles de précipitation") et à un RGF accru. Nous avons donc développé une modélisation de l'apparition et du comportement de ces sous-domaines, des joints de sous-domaines et des bulles de précipitation, en interaction avec les autres populations déjà présentes dans le code.
À haute température, les lacunes thermiques jouent un rôle clé dans le processus de gonflement du combustible. Avant le début de la thèse, MARGARET, pour les lacunes thermiques, manquait de cohérence entre les conditions d'irradiation de base et les conditions en rampe à haute température, ainsi qu'entre ce qui se passait aux joints de grains et à l'intérieur des grains pour les lacunes thermiques. Nous avons donc développé un nouveau modèle, appelé "Modèle de Speight généralisé", pour traiter cette question.
Enfin, nous avons proposé une description du comportement à haute température

des sous-domaines dans les conditions de rampe de puissance.
Ces nouveaux modèles ont été implémentés dans le code, vérifiés (vérification des bilans) et testés sur une série de vrais crayons irradiés dans des REP français, ainsi que sur quelques crayons rampés.
Le modèle dépend d'une série de paramètres physiques parmi lesquels plusieurs sont mal connus. À ce stade, un processus de calibration est donc nécessaire. Après un processus d'essais-erreurs, nous avons proposé un ensemble de paramètres qui donne de bons résultats pour l'irradiation de base. Cependant, nos résultats expliquent toujours le RGF par la connexion des bulles inter-granulaires. Un rôle particulier des joints triples (non modélisés pour le moment) pourrait être impliqué dans le RGF de l'irradiation de base et devrait être étudié plus en profondeur.
En conditions de rampe, nos premiers tests doivent être considérés comme exploratoires.

Mots clés : Relâchement des gaz de fission, RGF, Comportement des gaz de fission, Code de comportement du combustible, Sous domaines / Sous-domaines / Sous grains / Sous-grains, Remise en solution, UO_2, Combustible nucléaire.

Abstract and keywords

MARGARET is both a C++ fission gas release (FGR) code and a component of a wider Fuel Performance Code for Light Water Reactors named ALCYONE. The aim of the PhD was to improve MARGARET by taking into account the latest experimental discoveries and atomic scale simulations.
New classical Molecular Dynamics (MD) simulations that study the phenomenon of dynamic re-solution of fission gas from intra-granular bubbles back into the fuel matrix are available. We have built a new re-solution model that can be adopted easily by fuel performance codes, based on re-solution profiles provided by M.W.D. Cooper (Los Alamos NL) and coming from published MD simulations. This work resulted in a publication that has been included in the manuscript.
CEA researchers have obtained 3D experimental images of base-irradiated fuels that experienced a not negligible amount of FGR. Those images seem to indicate that inter-granular bubbles, below a certain threshold temperature, do not form an interconnected network, contrary to what was previously thought. Therefore, we have included in the model the phenomena of dynamic and thermal re-solution from inter-granular bubbles to grain boundaries, which may balance the trapping of diffusive Xe atoms on grain boundaries. A priori, this renders possible FGR by diffusion through the network of grain boundaries.
A new type of restructuring of the fuel, visible in the centre of the pellet at high burnup, and different from the so-called High Burnup Structure (HBS), has been recently discovered: it is characterized by the formation of different domains inside the original grains, where the orientation of the lattice is the same in each domain, but differs slightly between different domains. These domains are called subdomains or subgrains, and their appearance is concomitant with the formation of a second, bigger, population of intra-granular bubbles (called "precipitation bubbles") and with a higher FGR. We have then developed a modelling of the appearance and behaviour of these subdomains, subdomain boundaries, precipitation bubbles, in interaction with all the populations already present in the code.
At high temperature, thermal vacancies play a key role in the swelling process. Before the beginning of the thesis, MARGARET lacked consistency between base irradiation and high temperature (ramp test) conditions, and also between what happened on grain boundaries and inside the grain for thermal vacancies. We have then developed a new model, called "Generalized Speight model", to tackle this question.
Finally, we have proposed a description of the high temperature behaviour of the subdomains in ramp test conditions.
These new models have been implemented in the code, verified (check of the balances) and tested on a series of real irradiated rods in French PWR, and of few ramp

tests.
The model depends on a series of physical parameters among which several are really badly known. So, at this stage, a calibration process is needed. After a try and error process, we have proposed a set of parameters that gives quite good results on base irradiation. However, our results still explain the FGR by inter-granular bubble connection. A particular role of the edge bubbles (not modeled yet) may be involved in the base irradiation FGR and should be more deeply investigated.
In ramp conditions, our first test must be considered as explanatory.

Keywords: Fission Gas Release, FGR, Fission gas behaviour, Fuel Performance Code, Subdomains / Sub-domains / Subgrain / Sub-grain, Re-solution / Resolution, UO_2, Nuclear fuel

Résumé étendu

LE CONTEXTE

Le combustible le plus largement adopté dans les Réacteurs à Eau sous Pression (REP) est le dioxyde d'Uranium (UO_2), qui est un matériau céramique. Il est fabriqué, par frittage de poudres, sous forme de pastilles de combustible, d'environ 8-9 mm de diamètre, qui sont empilées les unes sur les autres à l'intérieur d'un tube en alliage métallique protecteur, appelé gaine. L'empilement de pastilles de combustible plus la gaine forment ce que l'on appelle le crayon combustible. Le cœur d'un réacteur est composé d'un grand nombre de ces crayons, entre lesquels passent un caloporteur, de l'eau dans le cas des REP, qui permet d'extraire la chaleur dégagée par les fissions dans le réacteur.

Le combustible tel que fabriqué est polycristallin, ce qui signifie qu'il est composé de différents grains séparés par des joints de grains. Le réseau cristallin à l'intérieur d'un grain a une certaine orientation, qui diffèrent de celle du grain voisin. La différence entre les phénomènes intra-granulaires, c'est-à-dire internes au grain, et les phénomènes inter-granulaires, c'est-à-dire au joint de grain, va jouer un rôle très important dans tout le travail présenté dans cette thèse.
Le combustible tel que fabriqué est un matériau faiblement poreux. Les pores de fabrication peuvent être intra- ou inter-granulaires, et sont remplis d'argon à une pression assez faible.

Après le premier démarrage du réacteur, les pastilles de combustible se fracturent à cause du gradient thermique très important, proche de 150°C/mm, et la colonne combustible peut alors être vue comme un ensemble de fragments. On a donc tout de suite une surface libre plus importante du matériau. L'ordre de grandeur de la taille des fragments est le millimètre.

Pendant le fonctionnement du réacteur, des Produits de Fission (PF) sont produits par la fission des atomes d'uranium : ce sont les deux atomes qui résultent de la fission des atomes fissiles. 15% des produits de fission sont, ou conduisent rapidement par décroissance à des isotopes de Xénon ou de Krypton, appelés gaz de fission. Le comportement du gaz de fission dans le combustible est complexe. La compréhension actuelle la plus répandue de ce comportement peut être résumée de la manière suivante : le gaz de fission, après avoir été produit par fission dans les grains se retrouve implanté dans le réseau cristallin. Mais il tend à former des bulles car il n'est pas thermodynamiquement stable dans l'UO_2. Les bulles (formées pendant l'irradiation) ou les pores (de fabrication) piègent les atomes de gaz dissous. Cependant, les atomes

de gaz peuvent aussi être remis en solution depuis ces différentes cavités vers la matrice cristalline lors d'interactions entre ces cavités et les pointes de fission (trajet des PFs très énergétiques venant d'être produits par une nouvelle fission et interagissant avec la matière) : ce phénomène est appelé « remise en solution dynamique », par opposition à la remise en solution thermique ou thermodynamique.
Aux températures de fonctionnement normal des crayons REP, les bulles ne sont pas mobiles. Seul le gaz qui n'est pas piégé dans les cavités est transporté vers les joints de grains, par diffusion. Dans les joints de grains, le gaz forme à nouveau des bulles, qui finissent par s'interconnecter et former des réseaux de tunnels s'étendant jusqu'aux surfaces libres des fragments. Le gaz contenu dans ce réseau peut alors percoler et être relâché hors du combustible. Il se retrouve alors dans les volumes libres du crayon (jeu pastille-gaine, fissures, plenum). La pression dans ces volumes libres augmente du fait de cet apport de gaz.
Or il existe un critère de sûreté à ne pas dépasser pour la pression interne du crayon, pour ne pas mettre en péril la première barrière que représente la gaine. C'est pourquoi le relâchement des gaz de fission doit être compris le mieux possible.

Les bulles formées dans le combustible ne sont pas de simples agrégats d'atomes de Xe et Kr. Des lacunes viennent aussi s'y ajouter. Dans la pratique, on constate que la présence de bulles entraine un gonflement du matériau, qui lui aussi doit être surveillé de près car il peut entrainer des interactions mécaniques pastille-gaine, une fois le jeu refermé. Les lacunes sont des défauts du réseau cristallin, par exemple la lacune appelée « défaut de Schottky », qui est un motif UO_2 manquant dans le cristal. Thermodynamiquement, pour augmenter l'entropie, un cristal contient toujours des défauts, et d'autant plus que la température est élevée.

Pendant l'irradiation, les produits de fission énergétiques interagissent non seulement avec les bulles, mais aussi avec le réseau cristallin : des défauts ponctuels surnuméraires sont produits, paires lacunes / auto-interstitiels (dites paires de Frenkel), ainsi que des boucles de dislocations interstitielles, qui finissent par former des dislocations linéaires. Ainsi, un combustible sous irradiation peut comporter beaucoup plus de défauts que le même cristal hors irradiation, et ceci est d'autant plus vrai que la température est basse. A priori, ces défauts d'irradiation jouent aussi un rôle dans la croissance des bulles : en s'y agrégeant, les lacunes peuvent les faire croitre, et les auto-interstitiels le faire décroitre.
Lorsque le combustible atteint des taux de combustion élevés (nombre de fission par atome d'Uranium initial élevé), le taux de combustion local dans la périphérie de la pastille est plus élevé que celui au centre. C'est un effet dû au spectre neutronique dans les REP. Dans ces zones périphériques de la pastille, où la température est de l'ordre de 400°C et où les fissions se sont fortement accumulées, un changement dans la microstructure du combustible se produit : les grains originaux disparaissent complètement au profit de grains beaucoup plus petits. Aucune bulle intra-granulaire n'est mesurée à l'intérieur de ces nouveaux petits grains et une nouvelle population de bulles inter-granulaires, plus grandes que ces nouveaux grains, apparaît. La porosité

augmente considérablement. Cette nouvelle microstructure est appelée High Burnup Struture (HBS) par la communauté combustible.

Pour essayer de prédire le comportement des gaz de fissions, il est indispensable de développer des modèles et de les implémenter dans un code de calcul pour mettre en orchestre tous ces phénomènes.
MARGARET [L. NOIROT 2011] est un code de comportement de gaz de fission en C++ et il est l'un des composants d'un code de performance de combustible plus large nommé ALCYONE [INTROÏNI et al. 2024], dédié au comportement thermo-mécanique et physico-chimique du combustible REP. MARGARET est développé depuis plus de vingt ans au CEA. Il modélise le comportement des gaz produits par fission dans le combustible, l'état microstructural du combustible et, intégré dans ALCYONE, prédit des quantités majeures d'intérêt telles que le relâchement des gaz de fission (RGF) et le gonflement, qui impacte la géométrie du crayon. MARGARET est un modèle local, ou "modèle de point" pour le code cible dans lequel il est implémenté (ALCYONE). Cela signifie que, à chaque point du maillage du code cible, MARGARET reçoit certaines informations (température, taux de fission, etc.) et renvoie d'autres informations (relâchement de gaz de fission, gonflement) concernant ce point macroscopique. Dans MARGARET, les comportements des différents points ne sont pas directement couplés, ce qui permet leur calcul en parallèle. Si nécessaire, MARGARET peut fournir, à chaque point macroscopique, une caractérisation fine de la situation du gaz. Pour décrire cette caractérisation fine, MARGARET traite deux échelles plus petites que celle de la pastille, typiquement celle du grain moyen et celle du fragment (pour le transport du gaz le long des joints de grains). Les deux échelles sont considérées sous les conditions de température, de taux de fission... du point macroscopique considéré.
Pour prédire le comportement des gaz de fission dans le combustible pendant l'irradiation, MARGARET utilise une représentation simplifiée du combustible (gaz et microstruture) qui se traduit par un ensemble de variables, comme la concentration de gaz dissout intra-granulaire, la concentration de bulles intra-granulaires etc... L'évolution temporelle du gaz et de la microstructure est transcrite en un système d'équations différentielles ordinaires (Ordinary Differential Equation, ODE), portant sur ces variables. Cette approche permet de prendre en compte tous les couplages entre les différents phénomènes, qui sont nombreux.
En plus du système d'ODE, MARGARET utilise une série de corrélations empiriques, qui permettent de réduire la taille du problème quand c'est possible. Cependant, comme on l'a vu, le combustible subit de tels changements qu'il n'est pas possible de le représenter de la même manière tout au long de l'irradiation. C'est pourquoi, au début de ma thèse, 3 états différents avaient déjà été définis, à savoir "état sain " (combustible tel que fabriqué), "en restructuration" et "restructuré", afin de décrire la formation progressive de l'HBS.
Dans MARGARET, lorsque le combustible passe d'un état à un autre, l'ensemble de variables considérés change et le système d'ODE change en conséquence. Le code a été conçu pour permettre ces changements facilement. Ils s'opèrent automatiquement, sur des critères physiques.

MOTIVATIONS

Un nouveau phénomène, visible au centre des pastilles à haut taux de combustion, a été récemment découvert [J. NOIROT, ZACHARIE-AUBRUN et al. 2018; ZACHARIE-AUBRUN et al. 2022] : c'est un nouveau type de restructuration du combustible, différente l'HBS. La restructuration au centre de la pastille est caractérisée par la formation de différents domaines cristallographiques (appelés sous-domaines dans la suite) à l'intérieur des grains originaux. La désorientation entre sous-domaines est faible (entre 1°-10° [ZACHARIE-AUBRUN et al. 2022]) mais augmente progressivement. La formation de ces sous-domaines est concomitante d'une accélération du relâchement gazeux [REST et al. 2019]. Ces sous-domaines nous donnent déjà un premier niveau d'explication pour l'apparition de la deuxième population des bulles, plus grosses et beaucoup moins nombreuses que les bulles nanométriques, appelées communément « les bulles de précipitation », qu'il est possible de voir au Microscope Eléctronique à Balayage (MEB) à partir de quatre cycles d'irradiation, ou bien sur coupes polies de la pastille (zone sombre centrale, ou zone « de précipitation »). Depuis seulement 2018-2022, nous savons donc que ces bulles de précipitation sont en fait placées sur les joints des sous-domaines. Cela suggère d'une part que ces joints de sous-domaines sont un lieu de ségrégation du gaz, et que le gaz peut s'y déplacer suffisamment pour y former de plus grosses bulles et à la fois atteindre plus facilement le vrai joint de grain, puisque l'apparition des sous-domaines coïncide avec un relâchement accru. Un point très important est que ces bulles de précipitation ne sont pas interconnectées entre elles.
Ce « à la fois » (à la fois précipitation de bulles isolées au joint des sous-domaines, et à la fois diffusion jusqu'au bord du grain le long des joints de sous-domaines) nous amène à révolutionner notre vision des phénomènes pouvant se passer sur des joints (de sous-domaines, mais aussi de grains, par conséquent). Jusqu'au début de ma thèse, dans MARGARET, la diffusion du gaz de fission le long des joints de grain n'était pas modélisée. Le gaz intergranulaire se retrouvait, au-delà d'un certain seuil de concentration, dans les bulles inter-granulaires et aucune remise en solution des bulles inter vers le joint de grain, ni thermique, ni dynamique n'était considérée. Ces choix de modélisation sont incompatibles avec une diffusion à longue distance du gaz de fission le long de joint de grains, ou de joints de sous-domaines. Or le comportement du gaz en présence des sous-domaines prouve que la diffusion à longue distance (en l'occurrence le rayon du grain) le long des joints des sous-domaines est compatible avec l'existence de bulles non connectées situées sur ces mêmes joints. Il faut donc remettre en question les choix de modélisation faits jusque-là.

Une autre observation récente nous pousse à remettre en question ou compléter nos choix de modélisation inter-granulaire. Au CEA Cadarache, des chercheurs ont obtenu de nouvelles images expérimentales 3D de combustibles irradiés en base [J. NOIROT, DOWEK et al. 2022], afin de recueillir des données sur les caractéristiques des bulles inter-granulaires et des bulles de précipitation. L'un des résultats les plus

surprenants publiés était l'absence de preuve de réseau de bulles inter-granulaires interconnectées, même pour les combustibles ayant subi un relâchement important de gaz de fission (jusqu'à 6,2% pour le combustible ayant le taux de combustion le plus élevé, égal à 72,7 GWd/tU). En fait, la percolation du gaz à travers un réseau de bulles interconnectées est généralement supposée, par les codes de RGF, comme étant le principal mode de relâchement de gaz de fission [REST et al. 2019], et il en était de même pour MARGARET avant le début de cette thèse. Cette vision des choses provient d'examens de fractographies, faits après des tests de rampe de puissance, où la température monte beaucoup plus haut qu'en irradiation de base (plus haut qu'en fonctionnement normal). Dans ces conditions, les fractographies montrent très clairement les réseaux de tunnels interconnectés. Les fractographies faites après irradiation de base, au contraire, ne passent pas par les joints de grains, et donc, avant que les reconstitutions 3D ne soient possibles, il était très difficile de se faire une idée claire de la morphologie des bulles inter-granulaires après irradiation de base.

Même si des images 3D analysant une plus grande partie du combustible seraient nécessaires pour confirmer l'absence de connexion des bulles inter-granulaires, ces nouveaux résultats remettent en question les hypothèses de modélisation actuelles et encouragent l'inclusion dans le code d'autres voies de relâchement des gaz de fission, négligées jusqu'à présent. Comme la cinétique de la connexion des bulles dépend de la température, il est important de noter ici que l'absence apparente de connexion des bulles dans les crayons REP qui ont subi des températures inférieures à environ 1100°C n'est pas incompatible avec les mesures post-irradiation (PI) effectuées sur des combustibles exploités à des puissances linéiques plus élevées, ou avec des mesures PI effectuées sur des combustibles ayant subi des rampes de puissance, où les bulles interconnectées sont clairement visibles.

Les deux points expérimentaux évoqués ci-dessus (restructuration en sous-domaines et diffusion de gaz à longue distance le long des joints de sous-domaines et de grains) ont été les deux motivations premières pour enclencher une thèse de modélisation, dans le but d'améliorer MARGARET.
Mais la thèse a aussi été vue comme l'opportunité d'opérer une cure de jouvence du modèle, en recherchant dans la bibliographie tous les apports possibles, en particulier ceux venant des modélisations atomistiques : Density Functionnal Theory (DFT), et dynamique Moléculaire (DM), d'une part, et en traquant toutes les incohérences pouvant se trouver dans le modèle, d'autre part. Ces incohérences peuvent provenir de l'état de l'art, qui évolue, ou de la nécessité d'obtenir un état de validation du code acceptable (comparaison calcul-mesure), même si tout n'a pas été compris. Par exemple, dans MARGARET avant le début de la thèse, il existait deux domaines de températures dans lesquels les coefficients de diffusion des lacunes utilisés étaient différents. Chaque fois que ces incohérences existent, elles montrent que le sujet doit être creusé, et la thèse était l'occasion de le faire.

TRAVAIL DE THESE

Au final, le travail que j'ai effectué pendant la thèse présente les axes suivants.

Un premier travail permettant d'obtenir un modèle de piégeage et remise en solution dynamique dans le cristal à partir de simulations en dynamique moléculaires existantes

Par une revue bibliographique sur le sujet, nous avons montré qu'il existe un flou dans la définition de la fréquence de remise en solution, lié à un sujet qui n'avait pas vraiment été abordé en tant que tel, à savoir le profil de remise en solution des atomes de gaz au voisinage de la bulle. Un travail des chercheurs américains W. Setyawan et M.W.D. Cooper [SETYAWAN et al. 2018] présentait des simulations d'interaction pointe de fission / bulle en dynamique moléculaire, à partir desquelles ils calculaient une fréquence de remise en solution [s^{-1}]. Nous avons pensé que leurs calculs pouvaient fournir plus que cela, à savoir le profil de remise en solution des atomes de gaz autour de la bulle. Nous les avons contactés pour en discuter et ceci a débouché sur une fructueuse collaboration avec M.W.D. Cooper, qui nous a fourni des informations synthétiques sur ces profils de remise en solution, qui n'avaient jamais été publiées auparavant.

Idéalement, pour bien modéliser la remise en solution et le piégeage autour des bulles, il faudrait mailler le combustible entre les bulles, introduire la remise en solution comme un terme source, dépendant de la distance aux bulles, et calculer la diffusion du gaz dans ce milieu avec une condition à la limite, au voisinage des bulles, nulle, traduisant l'insolubilité thermodynamique du gaz de fission dans le cristal.

Quand on sait qu'il y a une bulle nanométrique à peu près tous les 20nm, on comprend que ceci est absolument impossible à introduire dans MARGARET. D'ailleurs, tous les codes de RGF utilisent des modèles de piégeage et remise en solution dont les variables sont seulement deux scalaires : les concentrations moyennes de gaz dissous (C_{XeM}) et dans les bulles (C_{Xeb}), les moyennes étant à l'échelle du μm.

Notre but a été de construire un tel modèle simple à deux scalaires, mais compatible avec la fréquence de remise en solution et le profil de remise en solution calculés par M.W.D. Cooper, pour l'introduire ensuite dans MARGARET.

Pour ce faire, nous avons d'abord construit, hors MARGARET, un modèle assez détaillé : une bulle entouré d'une portion de combustible à symétrie sphérique, finement maillée. Dans le solide entourant la bulle, le terme source de remise en solution, dépendant de l'espace, et la diffusion sont bien pris en compte finement. Si l'on impose un historique de température et de taux de fission (nombre de fissions par m^3 et par s) à ce système, les concentrations moyennes de gaz dans le solide et dans la bulle, par m^3 de combustible, peuvent être calculées à chaque temps. C'est notre modèle de référence.

A partir de ce modèle, nous avons réussi à construire un modèle simple à deux scalaires, le terme de remise en solution ayant la forme $b(Setyawan) \times C_{Xeb}$, et le terme de piégeage étant de la forme $D_{Xe} \times GEOM2 \times C_{XeM}$, où $GEOM2$ est un terme géométrique faisant intervenir le rayon des bulles, leur concentration, mais aussi des grandeurs géométriques liées à la remise en solution. Nous avons montré qu'en terme

de fraction de gaz dissous, le modèle très détaillé et le modèle simple se comportent de façon très proche.

L'habituel modèle de piégeage / remise en solution que l'on trouve dans la plupart des codes de RGF, utilise un terme de piégeage égal à $4\pi R_b C_b D_{Xe} C_{XeM}$ (R_b est le rayon de la bulle, C_b est la concentration en bulle, D_{Xe} est le coefficient de diffusion du xénon dans le cristal) et un terme de remise en solution $b \times C_{Xeb}$, b étant défini comme la fréquence de remise en solution, donc s'identifiant a priori à $b(Setyawan)$. Nous avons montré que ce modèle est cohérent avec une remise en solution « en volume », c'est-à-dire uniforme dans le volume, ce qu'elle n'est pas en réalité.
Ceci dit, hors irradiation, le terme $4\pi R_b C_b D_{Xe} C_{XeM}$ est une bonne approximation du piégeage, tandis que notre terme $D_{Xe} \times GEOM2 \times C_{XeM}$ semble alors inadapté, puisqu'il contient des termes géométriques liés à la remise en solution.
Pour concilier tout cela, j'ai eu l'idée de tester un deuxième modèle simple, dont le terme de piégeage serait le terme classique $4\pi R_b C_b D_{Xe} C_{XeM}$, et le terme de remise en solution serait $b^{mod} \times C_{Xeb}$, où b^{mod} est une fréquence de remise en solution modifiée (en l'occurrence amoindrie) permettant d'obtenir les mêmes solutions en régime permanent - par exemple sur les paliers de température et taux de fission - que notre premier modèle simple.
Nous donnons l'expression qui permet de calculer b^{mod} en fonction de $b(Setyawan)$, $GEOM2$ et les caractéristiques géométriques des bulles.
Il s'est avéré que ce deuxième modèle était non seulement très proche du modèle de référence détaillé sur les paliers de température et taux de fission, mais aussi pendant les transitoires permettant de passer d'un pallier à un autre. Il a donc été retenu pour être intégré dans MARGARET.
Ce travail nous semble être une nette clarification par rapport à la littérature existante sur le sujet, et a fait l'objet d'une publication commune avec M.W.D. Cooper pendant la thèse [VERGANI et al. 2025].
C'est aussi est un exemple de la mise en pratique de la démarche multi-échelle : Nous avons obtenu une méthode pour transférer de l'information obtenue aux basses échelles en une modèle simple intégrable dans un code de RGF, lui-même intégré dans un code de performance combustible.

Un second travail sur les phénomènes diffusion à grande distance, de piégeage et remise en solution dynamique et thermique en inter-granulaire
Nous avons d'abord évalué le coefficient de diffusion à utiliser pour calculer la diffusion à grande échelle le long des joints de grain dans le fragment (ou le long des joints de sous-domaines dans le grain) dans une approche homogénéisée de la diffusion, où la géométrie compliquée des joints de grain est remplacée par une simple sphère de diffusion, et les concentrations locales aux joints de grain remplacées par des concentrations diluées dans la sphère.
Ensuite, nous avons repris et re-démontré le terme de piégeage du gaz inter-granulaire par les bulles inter-granulaires issu de la littérature, et nous nous sommes interrogés sur la façon de l'utiliser lorsque deux populations de cavités inter-granulaires

coexistent (ici les bulles, en concentration beaucoup plus grande que les pores de fabrication).
Nous avons ensuite établi, sur des considérations géométriques, des expressions pour la remise en solution dynamique inter-inter. Comme ce phénomène n'a jamais été étudié aux basses échelles, nous manquons d'information. C'est pourquoi, nous avons aussi introduit des paramètres pour pouvoir calibrer ce phénomène.
Les atomes de Xénon sont ségrégués aux joints de grains (et aux joints des sous-domaines), c'est un fait expérimental. Cela indique que le défaut « gaz » est plus stable aux joints de grains qu'en volume (dans le cristal). Or la remise en solution thermique au voisinage d'une cavité (bulle ou pore) dépend de cette plus ou moins grande stabilité du défaut « gaz » dans le milieu considéré. Dit autrement, la concentration à l'équilibre du défaut « gaz » dans un milieu au voisinage d'une cavité dépend, entre autres choses, de l'énergie du défaut « gaz » dans ce milieu, qui peut être calculée aux basses échelles. Si la remise en solution du gaz de fission dans le cristal est exclue du fait de l'énergie importante du défaut « gaz dans un Schottky », il n'est pas évident qu'elle soit aussi à exclure dans le milieu « joint de grain », plus accueillant.
C'est pourquoi, nous avons introduit dans MARGARET, de manière générale, la possibilité de remise en solution thermique au voisinage de toutes les cavités et dans tous les milieux (cristal, joints de sous-domaine, joint de grain).
L'effectivité de cette remise en solution thermique dépend des grandeurs physiques incluses dans les expressions des concentrations à l'équilibre du défaut « gaz » dans les différents milieux au voisinage d'une cavité. Ces concentrations à l'équilibre sont utilisées comme les conditions à la limite du problème de diffusion dans le milieu, à la frontière avec les cavités.
Le problème de la solubilité des lacunes thermiques et de leur interaction avec les bulles dans les différents milieux (cristal, joint de sous-domaine, joint de grain) se pose de façon très semblable.
Nous présentons pour la première fois une façon de calculer simultanément la concentration à l'équilibre du défaut « gaz dans un Schottky » et de lacunes au voisinage d'une bulle inter-granulaire, dans les deux milieux « cristal » et « joint ». Cette méthode minimise l'énergie libre d'une boite contenant du cristal, un joint de grain, et une bulle inter-granulaire, en devant respecter un certain nombre de contraintes : volume de la boite inchangé, bilan des atomes respecté. Un moyen adéquat de faire ceci est d'utiliser la méthode des multiplicateurs de Lagrange, et c'est ce que nous avons mis en œuvre.

Un troisième travail sur la modélisation des sous-domaines dans MARGARET

Ayant préparé, par le travail précédent, ce dont nous avions besoin pour le comportement du gaz au joint de grains et au joint des sous-domaines, nous avons pu introduire un nouvel état dans MARGARET : l'état « avec sous-domaines ». Il a fallu dans un premier temps définir un critère d'apparition de cet état. Nous l'avons exprimé comme un seuil de taux de combustion acquis dans une certaine plage de température. En effet, cette restructuration en sous-domaines ne semble pas se déclencher si la température est trop basse, ni si la température est trop haute, comme les américains ont pu le

constater sur leurs échantillons. Notre critère reste très empirique, à l'image de l'état de compréhension actuelle du phénomène.
Le passage de l'état "sain" au nouvel état « avec sous-domaine » entraine un changement de représentation du combustible. La diffusion du gaz se fait maintenant initialement dans le sous-domaine, dont la taille est approximativement dix fois plus petite que la taille des grains (de l'ordre du microns, comparé à 10μm pour la taille usuelle d'un grain). Une deuxième population de bulles intra-granulaires, inter-sous-domaines (les bulles « de précipitation ») est introduite avec un petit rayon initial. Les pores de fabrication intra-granulaires initiaux sont maintenant aussi considérés comme placés aux joints des sous-domaines, étant de toutes façons trop gros pour se trouver à l'intérieur d'un sous-domaine. La diffusion le long des court-circuit de diffusion que représentent les joints de sous-domaines est calculés de façon homogénéisée dans le grain. Au joint de grain, la croissance et l'interconnexion des bulles inter restent possibles, mais la diffusion à grande échelle le long des joints de grain dans le fragment l'est aussi. Ce dernier ajout a aussi été fait, en cohérence, pour l'état « sain ».

Dans ce nouvel état, le joint de sous-domaine est atteint par le gaz plus facilement, parce que proche. Comme dans notre modèle, nous considérons les joints des sous-domaines comme des voies de diffusion rapide, nous nous attendons à une augmentation du relâchement de gaz de fission concomitante avec la formation des sous-domaines. Nous espérons aussi pouvoir tester si le relâchement sans percolation est possible en irradiation de base, grâce à la diffusion à grande distance le long des joints de grains dans le fragment.
Toutes les équations décrivant le comportement du gaz de fission et des bulles dans l'état « avec sous-domaine » sont détaillées dans le manuscrit.

Un quatrième travail de mise en cohérence du comportement des lacunes thermiques dans le cristal, les joints et les joints de sous-domaines
MARGARET doit aussi pouvoir décrire les phénomènes ayant lieu à température plus élevée que la température de fonctionnement normale d'un REP, c'est-à-dire les phénomènes ayant lieux lors de tests de rampe de puissance, où la température va se situer au-delà de 1200°C et jusque vers 1800°C. Dans cette plage, les lacunes thermiques deviennent prédominantes par rapport aux lacunes produites par irradiation, et les bulles, spécialement les bulles inter-granulaires, se mettent à grossir rapidement, par apport de lacunes. Speight [SPEIGHT et al. 1974] a été le premier à proposer un modèle où des lacunes sont créées au joint de grain, mis en traction par les bulles inter-granulaires soudainement très pressurisées à cause de l'augmentation de température. Ces lacunes créées sur le joint de grain y diffusent et vont alimenter les bulles inter-granulaires, qui ainsi grossissent et relaxent leur pression interne. Mais Speight ne s'est pas préoccupé du fait que ces lacunes créées au joint pourraient aussi aller alimenter les bulles intra-granulaires, elles-aussi sur-pressurisées. Avant le début de ma thèse, MARGARET tentait de prendre ceci aussi en compte, mais l'ensemble du comportement des lacunes thermiques, au joint d'une part et dans les grains d'autre

part n'était pas complètement cohérent. De plus, il fallait réfléchir au comportement des lacunes thermiques dans le nouvel état « avec sous-domaines ».
Nous avons donc tout remis à plat et proposé un nouveau modèle pour les lacunes thermiques, que nous avons appelé « modèle de Speight généralisé », et qui décrit l'ensemble du comportement des lacunes thermiques au joint, éventuellement joint de sous-domaine et cristal de manière totalement cohérente. Pour complétion, nous avons étendu ce modèle à la structure HBS, mais à cause des températures basses dans les zones HBS, le modèle n'a aucun effet, ce qui est logique. Nous avons ajouté une formulation de type fluage d'irradiation pour expliquer le grossissement important des bulles de l'HBS, guidé en cela par le fait que les images de l'interface combustible-gaine à fort taux montrent que le combustible restructuré HBS est hautement déformable.

Un cinquième travail sur le comportement des sous-domaines portés à haute température en situation de rampe de puissance
Nous ne pouvons pas laisser le code dans l'incapacité de traiter les rampes fort taux de combustion. Malheureusement, aucun examen EBSD (Electron Back Scattering Diffraction) sur combustible fort taux de combustion après rampe n'est disponible, et nous ne savons pas ce que deviennent les sous-domaines pendant la rampe de puissance. Nous savons uniquement que les bulles intra-granulaires deviennent moins nombreuses et beaucoup plus grosses, qu'elles ne sont pas sphériques, qu'elles n'ont pas spécialement remonté le gradient de température, et que le gaz est largement relâché.
Nous avons donc imaginé un processus de re-croissance des sous-domaines, inspiré du phénomène de croissance granulaire. Les bulles inter-sous-domaines, suivant les joints de sous-domaines qui deviennent de moins en moins nombreux coalescent, et certains d'entre elles sont rejetées au joint de grain, où elles rejoignent les bulles inter, qui s'interconnectent et relâchent le gaz. C'est une proposition de modélisation exploratoire et qui demande à être confirmée ou infirmée par des examens EBSD post-rampe.

Mise en œuvre de toutes ses évolutions dans MARGARET et exercice de validation
Toutes les évolutions présentées ci-dessus ont été implémentées dans le code MARGARET, testée, et vérifiées notamment en calculant le bilan matière du gaz et en vérifiant qu'il est bien respecté.
Nous avons ensuite sélectionné la combinaison de paramètres à utiliser pour la validation, après une évaluation critique de la littérature et une procédure d'essai et d'erreur.
Pour valider le code, nous avons utilisé une gamme de crayons combustibles irradiés en base (12 crayons combustibles, avec des taux de combustion dans la plage de 13-77 GWd/tU) et des crayons combustibles ayant subi des rampes de puissance (6 crayons combustibles, avec des taux de combustion dans la plage de 27-73 GWd/tU). Nous avons comparé les prédictions de MARGARET avec un vaste ensemble de mesures : relâchement de gaz de fission, gonflement du combustible, EPMA, SIMS, porosité, taille

des bulles de précipitation. Les résultats de cette nouvelle version du code sont encourageants. En irradiation de base, MARGARET est capable de prédire correctement, avec quelques exceptions :

— Le relâchement des gaz de fission (dans une plage de ±40 %) ;
— Le gonflement du combustible ;
— La largeur de la zone de précipitation ;
— Le rayon des bulles de précipitation ;
— La porosité.

En particulier, la manière dont nous décrivons les sous-domaines nous a permis de prédire un relâchement de gaz de fission accru pour les combustibles à haut taux de combustion, même si la température vue par le combustible n'a pas augmenté, ou a même diminué, lors des derniers cycles.

Pour les tests en rampe de puissance, les résultats sont moins précis que ceux des combustibles irradiés en base et doivent être considérés principalement comme une illustration de l'état actuel du code. Néanmoins, MARGARET est capable de prédire assez correctement le relâchement de gaz de fission, l'augmentation du volume par atome dans toutes les populations de bulles, le taux couverture des joints par les bulles inter et la taille des bulles inter-granulaires.

Tous les résultats pour les combustibles irradiés en base et en rampe de puissance ont été obtenus en utilisant une seule expression pour D_{Uj} (coefficient d'autodiffusion au joint de grain, lui-même relié au coefficient de diffusion des lacunes au joint), et avec la description cohérente du comportement des lacunes thermiques présentée plus haut (modèle de Speight généralisé).

CONCLUSION ET PERSPECTIVES

Lors de la validation du code, nous avons également tenté de vérifier si cette nouvelle version de MARGARET est capable de prédire un relâchement important de gaz de fission en l'absence de connexions inter-granulaires de bulles. Pour ce faire, nous avons essayé différentes combinaisons de paramètres dans le but d'augmenter le relâchement par diffusion inter-granulaire à longue distance, mais aucune des simulations n'a prédit un relâchement suffisant de gaz de fission. Par conséquent, nous concluons que, pour le moment, le code est capable de prédire un relâchement important de gaz de fission uniquement en tenant compte de la percolation à travers un réseau de bulles inter-granulaires interconnectées.
Une calibration automatique du code est actuellement manquante et pourrait éventuellement être réalisée à l'avenir pour mieux déterminer les capacités de cette nouvelle version du code. Cela signifie également que la validation actuelle est susceptible de s'améliorer après la réalisation de cette calibration.

La validation du code a également mis en évidence des points spécifiques du mo-

dèle qui nécessitent des améliorations :

— Le volume par atome des bulles de précipitation pendant l'irradiation de base est trop faible par rapport aux mesures. Cette prédiction incorrecte peut probablement être améliorée en modifiant le volume que chaque Xénon piégé apporte aux bulles de précipitation. Dans le document de thèse, et suite à une bibliographie sur le sujet, on explique ce que ce terme d'apport de volume avec le gaz, en irradiation, recouvre réellement et pourquoi il pourrait être différent pour les bulles dans le cristal et les bulles au joint des sous-domaines ou des grains.

— La concentration de gaz dissous dans les grains de HBS semble trop faible par rapport à la ligne de base SIMS. Adopter une légère dépendance du terme "athermique" de la diffusion du xénon avec la température, comme suggéré par les calculs de dynamique moléculaire de Cooper [COOPER, STANEK et al. 2016], pourrait être, au moins en partie, une réponse à ce problème.

— La porosité dans la partie centrale des combustibles à haut taux de combustion ayant subi des rampes de puissance est trop faible par rapport aux mesures. Il est possible d'améliorer la manière dont les lacunes sont piégées par ou émises par les bulles inter-granulaires en tenant compte de leur forme allongée et non de leur rayon équivalent, comme cela est fait dans la version actuelle (pour le calcul de $C_{v,j}^{eq}(cavj)$).

— Une amélioration à court terme envisagée est de construire un modèle de piégeage / remise en solution pour les bulles inter-granulaires en suivant la même méthode que ce qui a été fait (premier travail ci-dessus) pour les bulles intra-granulaires, en supposant que le profil de remise en solution en fonction de la distance à la bulle est le même que celui fourni par M.W.D. Cooper. La principale différence serait la géométrie du problème : une géométrie plane pour le cas de la diffusion sur les joints de grains, alors qu'on utilisait une géométrie sphérique dans le cas des bulles intra-granulaires dans le cristal.

— Mieux encore, un travail en DM similaire à celui effectué par W. Setyawan et M.W.D. Cooper [SETYAWAN et al. 2018], mais où l'interaction de la pointe de fission aurait lieu avec une bulle intergranulaire, serait riche d'enseignements, et parait faisable.

— En termes d'amélioration à long terme, d'autres populations de bulles, actuellement non prises en compte, pourraient être modélisées dans une future version du code. En effet, dans MARGARET, nous ne considérons que 2 populations de bulles intra-granulaires : les nano-bulles et les bulles de précipitation. Cependant, des expériences sur des combustibles irradiés en base et ayant subi des rampes de puissance suggèrent la présence de bulles sur les dislocations, à des taux de combustion inférieurs au seuil de formation des sous-domaines

[THOMAS 1991; WHITE et al. 2006; BAKER 1977]. Ces bulles ont une taille supérieure aux nano-bulles (supérieure à quelques nanomètres). Elles semblent jouer un rôle important dans le comportement du gaz de fission sous certaines conditions, par exemple en rampe de puissance.

— Enfin, la preuve expérimentale, obtenue par les reconstitutions 3D, de l'absence de connexion des bulles inter-granulaires est claire sur les facettes des grains. Cependant, une connexion le long des joints triples ne peut être exclue expérimentalement. Ainsi, pour concilier à la fois les preuves expérimentales et les tentatives de modélisation, le scénario suivant pourrait être introduit dans le code, pour le comportement inter-granulaire des combustibles irradiés en base : diffusion (avec piégeage et remise en solution par et à partir des bulles inter-granulaires) sur les facettes, sans connexion des bulles de facettes, mais connexion plus facile des bulles de joints triples. Ce scénario impliquerait d'introduire les bulles de joints triple comme une nouvelle population dans le code.

Remerciements

I would like to thank my PhD supervisor, Laurence, for all the efforts that you put during these 3 years. You have been patient when dealing with my mistakes and willing to dedicate a great amount of time and energy answering all of my questions. Most importantly, you taught me what is like to be a researcher.

I would like to thank my PhD Director, Yves, and my head of the Lab, Michel, for all the time, help and attention that you offered me throughout my PhD.

I would like to thank Ambroise for the development of the tool for the automatic generation of most of the images used to compare MARGARET predictions and experimental data. Without your contribution, such an extensive validation would not have been possible.

I would like to thank the researchers, PhD and internship students that helped me out during the thesis, that offered me suggestions, corrected slides and asked questions. Special thanks to all the ones with whom I shared the opportunity to attend an international conference, and the ones that participated in creating such a special environment where to work.

I would like to thank the CEA, EDF and AMU, who made this thesis possible.

I would like to thank my mother, my father, my sister, and all my family at large, for more things that I can actually able to put into ink, but especially for the love, care and the patience that you have constantly proved for so many years and for the push that you gave me to leave for this adventure. Thanks to you, the word “home” has gained such a delicate and light-hearted meaning.

I would like to thank Margherita, for the love and support during the good, but also the difficult times that a PhD thesis can bring. Without those beautiful brown eyes, the work would have been much harder.

I would like to thank all my close friends, the ones that I had before coming in France, and the ones that I made along the way, for all the precious time that we have shared. You have made these three years worth remembering.

I would like to thank the various collocs that I had during my permanence in France, who endured me on a daily basis. I hope that, all things considered, it has been a

pleasure to share the same home for so much time.

Thanks to all of you. Without you, I would have not managed to be here writing these words.

Contents

Affidavit 3

Liste de publications et participation aux conférences 5

Résumé et mots clés 7

Abstract and keywords 9

Résumé étendu 11

Remerciements 25

Contents 27

List of Figures 32

List of Tables 38

Introduction 41

1. Context and Motivations 43
- 1.1. Overview of the UO_2 fuel and fission gas behaviour under irradiation . 43
- 1.2. MARGARET 45
- 1.3. Motivations 48
  - 1.3.1. New atomic scale simulations of dynamic re-solution from intra-granular bubbles 48
  - 1.3.2. Changes in the micro-structure of the fuel at high BU and in the centre of the pellet and link with greater Fission Gas Release . . 49
  - 1.3.3. Absence of evidence of inter-granular bubble interconnection in LWR fuel samples irradiated at high burnup and at temperatures lower than about 1100°C 50
  - 1.3.4. Improving the consistency of the code 53
  - 1.3.5. Building a new version of MARGARET that includes all these new modelling and validation of the new code against experimental results 54

2. A new model for the phenomena of trapping by and re-solution from intra-granular bubbles 57
- 2.1. Introduction 58

2.2. Review of existing re-solution models in the literature 60
2.2.1. Experiments used to determine the frequency of re-solution . . 60
2.2.2. MD simulations used to determine the frequency of re-solution 61
2.2.3. Analysis and comments on the threshold distance 64
2.2.4. Fission Gas Release codes 65
2.2.5. Conclusion on the literature review 66
2.3. Results 68
2.3.1. Re-solution profile derived from MD simulations 68
2.3.2. Building a trapping and re-solution model based on low-scale simulation 70
2.4. Discussion 81
2.4.1. Estimation of the re-solution frequency with a variable R_T . . . 81
2.4.2. Changes in the 2-scalar model with a variable R_T 83
2.5. Conclusion and perspectives 84

3. Long-range inter-granular gas diffusion 85
3.1. Literature review 85
3.1.1. Interconnection of inter-granular bubbles: the main way of Fission Gas Release? 85
3.1.2. Long-range inter-granular gas diffusion 87
3.2. Modelling in MARGARET 88
3.2.1. Macroscopic inter-granular diffusion coefficient to be used in an homogenized approach 88
3.2.2. 2D trapping term for two populations of cavities 90
3.2.3. Trapping term for cavities in the HBS 95
3.2.4. Total re-solution frequency from inter-granular cavities 96
3.2.5. Derivation of the re-solution frequency from inter-granular cavities to the grain boundary 96
3.2.6. Derivation of the re-solution frequency from the grain boundary to the grain 98
3.2.7. Taking into account a possible particular behaviour of re-solution on grain boundaries 99
3.2.8. Derivation of the equilibrium concentration of defects on the grain boundary near an inter-granular cavity: the thermal re-solution phenomenon 101
3.3. Conclusion 113

4. Subdomains 115
4.1. Literature Review 115
4.1.1. Experimental evidences: subdomain formation 115
4.1.2. Experimental evidences: link with higher fission gas release . . . 119
4.1.3. Possible mechanism of subdomain formation and conditions for the onset of the restructuring 122
4.1.4. What other fission gas models do in this regard 124

4.2. Description of the subdomains in MARGARET 125
4.2.1. General choices for the new "subdomain state" 125
4.2.2. New state in MARGARET: methodology to build the new ODE system 128

5. Consistent derivation of thermal vacancy trapping by cavities 131
5.1. Literature review 132
5.1.1. Classical experimental data related to the fuel swelling 132
5.1.2. Experimental values, atomic scale and cluster dynamics simulations of the volume per atom in different situations and bubble types 133
5.1.3. Volume brought with the gas atoms when they diffuse 136
5.1.4. Volume contribution to the bubbles in FGR codes 137
5.1.5. Conclusion on the literature review 139
5.2. A new model for the phenomena of trapping of thermal vacancies by cavities: the "Generalized Speight Model" 141
5.2.1. Derivation of the model for the "Sound" state 141

6. Behaviour of the subdomains during power ramps 157
6.1. Literature review 157
6.2. Subdomain growth at high temperatures 160
6.3. Loss of precipitation bubbles caused by the movement of the subdomain boundaries 160
6.3.1. First formulation 160
6.3.2. Second formulation 162

7. Validation of the code 165
7.1. Review of the main parameters used in the calculations 166
7.1.1. Diffusion coefficient of Xenon in the grain 166
7.1.2. Diffusion coefficient of Xenon along grain boundaries in UO_2 . 169
7.1.3. Diffusion coefficient of Xenon along the subdomain boundaries in UO_2 171
7.1.4. Intrinsic Uranium auto-diffusion coefficient: $D_{U,th}$ 173
7.1.5. Uranium auto-diffusion coefficient on the grain boundary: D_{Uj} 176
7.1.6. Uranium auto-diffusion coefficient on the subdomain boundary: D_{Ujsd} 177
7.1.7. Adjustment parameters for the re-solution process concerning gas dissolved on GB and SDB, $coe_{j->bulk}$ and $coe_{j->jsd}$ 178
7.1.8. Formation energies 179
7.1.9. Vibration frequencies 181
7.1.10. Parameters linked only to the subdomains 181
7.1.11. Parameters linked only to the mobility of the intra-granular bubbles 182
7.1.12. Parameters linked only to the HBS 183
7.2. Parameters used for the validation of the code 183

7.3. Comparison between measurements and predictions 187
7.3.1. Presentation of the measurements used for the validation 187
7.3.2. Base irradiation 190
7.3.3. Power Ramps 221
7.3.4. Is it possible to release without inter-granular bubble interconnection? 233
7.3.5. Conclusion to the validation of the code 236

Conclusion and perspectives **239**

Bibliography **243**

APPENDICES **255**

A. Definition and glossary of the variables used in this manuscript **257**
A.1. Definition 257
A.2. Glossary of the main variables and parameters 258

B. Version of MARGARET discussed in the current manuscript **263**

C. Thermal and irradiation vacancies **265**

D. OLANDER model implies a flat re-solution profile **269**

E. Expression of the re-solution frequency as a function of the radius of the cavities **271**

F. Derivation of the defects equilibrium concentrations in the bulk near an inter-granular bubble by considering the GB as a surface without associated volume **275**

G. Detailed description of the subdomains in MARGARET **279**
G.1. Equations of the evolution of the ODE variables in the subdomain state 279
G.1.1. Intra-subdomain 279
G.1.2. Inter-subdomain 282
G.1.3. Inter-granular 285
G.2. Intra-subdomain / inter-subdomain coupling 287
G.2.1. Calculation of the fractional coverages for the subdomain surface 287
G.3. Limit condition for the intra-subdomain diffusion problem at the vicinity of the subdomain boundary. 289
G.4. Inter-subdomain / inter-granular coupling 293
G.4.1. Relation between local concentration and concentration / m^3 of fresh fuel for the inter-subdomain gas 293

G.4.2. Calculation of the local inter-subdomain concentrations in the re-solution layers in front of the different portions of the grain boundary . . . 293
G.4.3. Calculation of the limit condition for the inter-subdomain problem of diffusion : C_{XejsdR} . . . 297
G.4.4. Expression of the gradients and the fluxes of gas along the subdomains, feeding the different populations on the grain boundary and the exterior . . . 297

H. Derivation of the "generalized Speight model" for the behaviour of thermal vacancies in the subdomain and HBS states 301
H.1. Subdomain state . . . 301
H.2. Restructured (HBS) state . . . 309

I. Creep term for HBS cavities 315

J. Derivation of the thermal vacancy contribution to the cavities in a limit scenario 317

List of Figures

1.1. Fission gas behaviour in the nuclear fuel under irradiation. 46
1.2. Schematic representation of how the code functions in relation with ALCYONE, highlighting the main inputs and outputs, the mesh of the pellet and the fine characterization of the gas situation that MARGARET can offer. T is the temperature, $\dot{F}$ is the fission rate, σ is the hydrostatic stress and ∇T is the gradient of the temperature with respect to the radius of the pellet. 47
1.3. Equilibrium concentrations that have to be calculated and used in the model. The letter "j" is an abbreviation for "joint de grain" in French, which means "Grain Boundary". 52
1.4. Synthesis of the main changes in the code carried out for this thesis. The groups of modifications that are the same in the different states have the same color. "GSM" means "Generalized Speight Model". 55

2.1. Resolution frequency as a function of the bubble radius for several values of the ratio between the thermal spike energy and the total electronic stopping power 63
2.2. Formation energy of a Schottky defect as a function of the distance to the grain boundary for the STGB (symmetric tilt grain boundary). . . . 64
2.3. Number of atoms that are found below the radius in abscissa just after the interaction with the fission spike, calculated by Molecular Dynamics. 71
2.4. Illustration of the problem. 72
2.5. Comparison between the reference model with 160 shells and 80 shells. 74
2.6. Comparison between the PHI-R5-NML model and the reference model 76
2.7. Comparison between the PHI-R5-NML-V model and the reference model. 78
2.8. Comparison between the PHI-R5-NML-VS model and the reference model. 80
2.9. Comparison of $n_{res} + \overline{n^{MD}_{displ}(R_T)}$ using $Profile(r)$ proportional to $1/r^5$ and a “No Man’s Land" equal to 0.5 nm. 82
2.10. Comparison between the PHI-R5-NML-V models with different values of the “No Man’s Land" width (dNML). 83

3.1. Representative Volume Element (RVE) used to derive the macroscopic diffusion coefficient of Xenon on the grain boundary, D^{MAC}_{Xej}, from the actual diffusion coefficient of Xenon on the grain boundary, D^{loc}_{Xej}. . . . 89
3.2. Schematic representation of the different fractions (each one facing a different object: inter-granular bubbles, inter-granular pores etc.) in which the surface of the grain is divided. 91

3.3. Schematic representation of the 2D diffusion problem with only one population of inter-granular cavities and no thermal re-solution phenomenon. 92
3.4. Values of $\frac{V_j \cap V_{res_cavj}}{V_{res_cavj}}$ for different equivalent radius of the inter-granular cavities, using $\delta = 2$ nm and $\theta = 50°$. 98
3.5. Coefficients that multiply the different re-solution frequencies of an inter-granular cavity. 99
3.6. Coefficients that multiply the different re-solution frequencies of dissolved gas atoms on the grain boundary. 101
3.7. Schematic representation of the problem used to derive the equilibrium concentration of defects on the grain boundary near an inter-granular cavity. 102
3.8. Schematic representation of the link between the surface tension gas / UO_2 and the surface energy of the grain boundary, also called surface tension UO_2 / UO_2. 107
3.9. Scheme of the two different systems used to calculate the Segregation Energy of a vacancy in the bulk. 111

4.1. Crystallographic contrast image at the limit of the precipitation zone on a 61 GWd/t_U irradiated UO_2. Image taken from [J. Noirot, L. Noirot, et al. 2004]. 116
4.2. Figure 7.3 of [Dowek 2021] (translated from French), which shows the state of the gas by radial position (r/R, where R is the radius of the fuel) of a fuel with a Burnup of 73 GWd/t_U. The gas dissolved or present in the nano-bubbles is in blue, the gas trapped in the bubbles detected by SIMS (the bigger population of precipitation bubbles, called "big" bubbles in the figure) is in red, the gas released is in grey. The longer vertical grey line represents the beginning of the precipitation zone. . . 120

5.1. Scheme that represents the production of vacancies on the GB, the moving away of the grains due to production of vacancies and the growth of the inter-granular cavities due to both the moving away of the grains (green) and the trapping of vacancies produced on the GB (yellow). The process, in reality, is continuous and everything happens at the same time.143
5.2. Scheme of the forces acting on the material near an inter-granular cavity.150

6.1. SEM image taken at the centre of the pellet of a ramped fuel after 6 cycles of base irradiation (Rod_72.93_RT of the validation base, presented in Section 7.3). Image taken at the LECA-STAR facility, Cadarache (FRANCE).158
6.2. Radial evolution of the intra-granular bubble density [bubbles / m^3 of fresh fuel] of an high burnup fuel before (Rod_72.93_IB of the validation base, presented in Section 7.3) and after a power ramp (Rod_72.93_RT of the validation base). Measurements performed at the LECA-STAR facility, Cadarache (FRANCE). 159

6.3. Radial evolution of the intra-granular bubble median size [μm] of an high burnup fuel before (Rod_72.93_IB of the validation base, presented in Section 7.3) and after a power ramp (Rod_72.93_RT of the validation base). Measurements performed at the LECA-STAR facility, Cadarache (FRANCE). 159

7.1. Expressions of D_{Xe} proposed in literature, at a fission rate $\dot{F} = 10^{19}$ [fissions / m^3 / s]. 170

7.2. Representative Volume Element (RVE) used to derive the macroscopic diffusion coefficient of Xenon on the subdomain boundary, D^{MAC}_{Xejsd}, from the diffusion coefficient of Xenon on the subdomain boundary, D^{loc}_{Xejsd}. 173

7.3. Expressions of D_U proposed in literature. Sabioni and Matthews's expressions are almost coincident. 175

7.4. Expressions of D_{Uj} proposed in literature. The line "Sabioni fit" is a linear fit of the point values of D_{Uj} proposed in [Sabioni 2000], and reported as dots in the figure. For the choice of $\varepsilon_{v,j}$, see Section 7.1.8. . 177

7.5. Expressions of D_{Xe} proposed in literature (see Section 7.1.1) in comparison with the one chosen for the validation (see table 7.4), at a fission rate $\dot{F} = 10^{19}$ [fissions / m^3 / s]. 185

7.6. Expressions of D_U proposed in literature (see Section 7.1.4) in comparison with the one chosen for the validation (see table 7.4). 185

7.7. Expressions of D_{Uj} proposed in literature (see Section 7.1.5) in comparison with the one chosen for the validation (see table 7.4). For the choice of $\varepsilon_{v,j}$, see Section 7.1.8. 186

7.8. Centerline temperature histories (from ALCYONE calculations) of the specimens analysed in [J. Noirot, Dowek, et al. 2022]. The link between those specimens and the "mother" rods used in this thesis are presented in table 7.5. The image is taken from [J. Noirot, Dowek, et al. 2022]. . . 188

7.9. Predicted fission gas release in time, measured FGR and predicted contribution of the different ways in which gas can be released. "PERC" stays for release by percolation through the interconnected inter-granular cavities, "DIFJ" stays for release by long range diffusion trough the grain boundaries, "DIRGRAIN" stays for direct release from the grain: it gathers the direct diffusion of gas to the free surfaces, coming from the sound grains, or from the subdomain boundaries arriving at the free surfaces. FGR measurement taken from [L. Noirot 2011]. 192

7.10. Predicted fission gas release in time, measured FGR and predicted contribution of the different ways in which gas can be released for one slice of the Rod_65.06_BI, slice 27/30 (3.6949 [m] $< z <$ 3.8730 [m]), 100% power. In this slice, subdomains appear after around 1280 days. 192

7.11. Predicted versus measured EPMA. Rod_57.61_BI, at 800mm from the bottom, two different input powers. Measurements from [L. Noirot 2011]. 193

7.12. Predicted versus measured EPMA. Rod_57.61_BI, at 2480mm from the bottom, two different input powers. To ensure confidentiality, the data have been rescaled using a common factor. 194
7.13. Predicted versus measured Porosity. Rod_57.61_BI, slice 7/30, 100% power. Measurements from [L. Noirot 2011]. 195
7.14. Predicted V_{at} of the intra-granular, inter-graular and precipitation bubbles for the Rod_57.61_BI, slice 7/30 (0.7314 [m] < z < 0.8604 [m]), at the end of irradiation. 197
7.15. Predicted V_{at} of the intra-granular, inter-graular and precipitation bubbles for the Rod_67.53_BI, slice 25/30 (2.9214 [m] < z < 3.0431 [m]), at the end of irradiation. 198
7.16. Predicted V_{at} of the HBS bubbles for the Rod_57.61_BI, slice 7/30 (0.7314 [m] < z < 0.8604 [m]), at the end of irradiation. 199
7.17. Predicted V_{at} of the HBS bubbles for the Rod_67.53_BI, slice 25/30 (2.9214 [m] < z < 3.0431 [m]), at the end of irradiation. 199
7.18. Predicted concentration of intra-granular bubbles. Rod_57.61_BI, slice 7/30 (0.7314 [m] < z < 0.8604 [m]), 100% power. 200
7.19. Predicted radius of the intra-granular bubbles. Rod_57.61_BI, slice 7/30 (0.7314 [m] < z < 0.8604 [m]), 100% power. 201
7.20. Predicted concentration of intra-granular bubbles. Rod_56.72_BI, slice 11/30 (1.2193 [m] < z < 1.3412 [m]), 100% power. 201
7.21. Predicted radius of the intra-granular bubbles. Rod_56.72_BI, slice 11/30 (1.2193 [m] < z < 1.3412 [m]), 100% power. 202
7.22. Predicted equivalent radius of the precipitation bubbles. Rod_57.61_BI, slice 7/30 (0.7314 [m] < z < 0.8604 [m]), 100% power. 203
7.23. Predicted equivalent radius of the precipitation bubbles. Rod_56.72_BI, slice 11/30 (1.2193 [m] < z < 1.3412 [m]), 100% power. 203
7.24. Predicted distribution of the fission gas between the different "reservoirs" in the centermost simulated point during irradiation, for the Rod_57.61_BI, slice 7/30 (0.7314 [m] < z < 0.8604 [m]), 100% power. "C_{Xe} Rel." represents the fission gas released from this particular point (total gas produced minus the gas in the different "reservoirs"). 204
7.25. Predicted distribution of the fission gas between the different "reservoirs" in the centermost simulated point during irradiation, for the Rod_65.06_BI, slice 27/30 (3.6949 [m] < z < 3.8730 [m]), 100% power. "C_{Xe} Rel." represents the fission gas released from this particular point (total gas produced minus the gas in the different "reservoirs"). 205
7.26. Predicted versus measured FGR. Measurements from [L. Noirot 2011; Zacharie-Aubrun et al. 2022]. 206
7.27. Predicted versus measured swelling of the pellet. Measurements published in [L. Noirot 2006], except for the rod Rod_76.94_BI, whose measurement is published in [J. Noirot, Aubrun, et al. 2009]. 208

7.28. Predicted versus measured EPMA. Rod_34.78_BI, two different input powers. To ensure confidentiality, the data have been rescaled using a common factor. . . . 209
7.29. Predicted versus measured EPMA. Rod_46.00_BI, first slice,three different input powers. To ensure confidentiality, the data have been rescaled using a common factor. . . . 210
7.30. Predicted versus measured EPMA. Rod_46.00_BI, second slice, three different input powers. To ensure confidentiality, the data have been rescaled using a common factor. . . . 211
7.31. Predicted versus measured EPMA. Rod_49.85_BI, two different input powers. To ensure confidentiality, the data have been rescaled using a common factor. . . . 212
7.32. Predicted versus measured EPMA. Rod_52.03_BI, two different input powers. To ensure confidentiality, the data have been rescaled using a common factor. . . . 213
7.33. Predicted versus measured EPMA. Rod_56.72_BI, three different input powers. Measurements from [Dowek 2021]. . . . 214
7.34. Predicted versus measured EPMA. Rod_65.06_BI, three different input powers. Measurements from [Dowek 2021]. . . . 215
7.35. Predicted versus measured EPMA. Rod_67.53_BI, 3 different input powers. Measurements from [Dowek 2021]. . . . 216
7.36. Predicted versus measured EPMA. Rod_76.94_BI, 3 different input powers. To ensure confidentiality, the data have been rescaled using a common factor. . . . 217
7.37. Predicted versus measured SIMS. Rod_67.53_BI, 2 different input powers. Measurements from [Dowek 2021] (the same measurements are plotted in figure 4.2). . . . 218
7.38. Predicted versus measured SIMS. Rod_76.94_BI, 3 different input powers. To ensure confidentiality, the data have been rescaled using a common factor. . . . 219
7.39. Predicted versus measured Porosity. Rod_67.53_BI, slice 25/30 (2.9214 [m] $< z <$ 3.0431 [m]), 100% power. To ensure confidentiality, the data have been rescaled using the maximum measured value. . . . 220
7.40. Predicted versus measured FGR. To ensure confidentiality, the data have been rescaled using a common factor. . . . 222
7.41. Predicted V_{at} of the intra-granular and inter-graular bubbles for the Rod_38.80_RT at the end of the power ramp. . . . 224
7.42. Predicted V_{at} of the intra-granular, inter-graular and precipitation bubbles for the Rod_63.01_RT at the end of the power ramp. . . . 225
7.43. Predicted V_{at} of the intra-granular, inter-graular and precipitation bubbles for the Rod_63.01_RT at the end of the power ramp. . . . 226
7.44. Predicted versus measured EPMA, Rod_63.01_RT. To ensure confidentiality, the data have been rescaled using a common factor. . . . 227

7.45. Predicted versus measured SIMS, Rod_63.01_RT. To ensure confidentiality, the data have been rescaled using a common factor. 228
7.46. Predicted versus measured porosity, Rod_63.01_RT. To ensure confidentiality, the data have been rescaled using a common factor. 229
7.47. Predicted versus measured size of the different bubble populations, Rod_63.01_RT. For a good comparison between predicted and measured size of the inter-granular bubbles, the measurements need to lay between the predicted bubble width ($2 \times R_{bj}$) and the predicted maximum length ($2 \times R_{bj} + L_{bj}$). To ensure confidentiality, the data have been rescaled using a common factor. 230
7.48. Predicted versus measured cover rate of the inter-granular bubbles, Rod_63.01_RT. To ensure confidentiality, the data have been rescaled using the maximum measured value. 231
7.49. Predicted concentration of precipitation bubbles at the end of the power ramp, Rod_72.93_RT, slice 1/9 of the ramp calculation (0.0 [m] $< z <$ 0.0398 [m]). 232
7.50. Predicted fission gas release in time, measured FGR and predicted contribution of the different ways in which gas can be released for the Rod_-65.06_BI, 100% power, with a change in the parameters explained in this Section. The measured FGR comes from [Dowek 2021]. 235

E.1. Example of the re-solution function to be included in MARGARET. . . . 273

F.1. Schematic representation of the problem used to derive the equilibrium concentration of defects on the grain boundary near an inter-granular cavity, considering the GB as a surface without associated volume. . . . 275

G.1. The different fractional coverage of the surface of the subdomain . . . 288
G.2. Schematic representation of the problem used to evaluate the local concentrations of gas in the limit re-solution shells facing each portion of the surface of a subdomain. 290
G.3. Interface between the subdomain boundary and the grain boundary. . 294

H.1. Growth of the HBS cavities due to the growth of the HBS grains. 309

I.1. Growth of the HBS cavities due to creep. 316

List of Tables

2.1. Characteristics of the calculation performed for the reference model. . 70
2.2. Diffusion coefficient of Xenon used. TK is the temperature in Kelvin . 70

3.1. Values of $\frac{b^{MD_Veshchunov}(\text{bubble of volume } \Omega)}{\dot{F}}$ for the different values of dNML and ζ. 98
3.2. Values of $(\frac{b^{mod}}{b})_j$ for different values of R_{cavj} and F_{cavj}, using dNML = 1 nm and $R_L - R_T = 3.5$ nm. 100

4.1. Resume of the data in literature regarding the formation of the subdomains. Ref. [1]: [Zacharie-Aubrun et al. 2022; Dowek 2021]; Ref. [2]: [Gerczak et al. 2018]; Ref. [3]: [Cappia et al. 2022]; Ref. [4]: [McKinney et al. 2023]. 123

7.1. Change in the A parameter in eq. 7.4 with temperature. 167
7.2. Parameters of the expression of D^*_{Xej} for each GB studied in [Liu et al. 2023]. 171
7.3. Formation energies used in the validation of MARGARET 180
7.4. Parameters and expression chosen for the validation of the code. "Lit." means that the expression or the value comes from the literature, and include also values chosen in a range of possible values proposed in literature. "Adj." means that the parameter has been adjusted. 184
7.5. Fuels and the corresponding measurements analyzed in this validation. The average burnup of the rod is in the name: Rod_13.17_BI has an average burnup of 13.17 [GWd/t$_U$]. The FGR measurements of power ramped fuels (with a "*" sign after the value) have been rescaled to ensure confidentiality. The FGR measurements of the base irradiated rods are published in part in [J. Noirot, Dowek, et al. 2022] and in part in [L. Noirot 2011]. [1] refers to [J. Noirot, Dowek, et al. 2022]; [2] refers to [L. Noirot 2011]; [3] refers to [NOIROT et al. 2009]. 189
7.6. Rods that undergo PI measurements to determine the real power at which they have operated (in these cases, P_{MIN}) and the corresponding powers chosen for the calculations. For the Rod_57.61_BI, another intermediate power has been treated too. 190
7.7. Parameters and expressions chosen to check if it possible to release without inter-granular bubble interconnection. 234

G.1. The different surfaces covering the subdomain 287
G.2. Concentrations in the different limit shells of the subdomain 290

G.3. Expression of the gas leaving the grain ($mol/m^3/s$) through the subdomain boundaries 299

Introduction

The reactor cores of Pressurized Water Reactors (PWR) power plants are composed of rods, made of a cladding with UO_2 pellets inside. During reactor operation, 15% of the fission products are isotopes of xenon or krypton, that are not thermodynamically stable in the UO_2 crystal. They tend to form bubbles inside the material, inducing swelling, or to escape the material. The swelling represents the relative increase of the volume of the pellet during irradiation, while the escape of gas from the fuel is called "fission gas release (FGR)" and is generally quantified as the ratio between the gas escaped over the produced gas. The result of the swelling of the fuel is the pellet-cladding mechanical interaction, while the fission gas release increases the inner pressure of the rod. Both have to be surveyed and understood as best as possible, and they are strongly coupled. That is why FGR codes are developed.
A first challenge, for these codes, is to predict the two key macroscopic quantities described above (swelling and FGR) in normal irradiation conditions (called "base irradiation" or BI in the following) up to high burnups. The burnup is the energy delivered by the nuclear fuel per unit of mass. A "high burnup fuel" has been irradiated for several years and this may induce micro-structural changes that complicate the modelling[1].
Nuclear fuels may experience incidental power increases, and this is studied through power ramp tests.
Another significant challenge is the prediction of key macroscopic quantities of both fuels irradiated in base irradiation and in power ramp conditions using a coherent model which uses less "ad-hoc" solutions as possible. To do so, a description of the behaviour of the fuel and the fission gases across all burnup that is consistent with the most up-to-date experiments and atomic scale simulations is needed.
However, recent information on the behaviour of the fuel and fission gases under all irradiation conditions [Setyawan et al. 2018; J. Noirot, Dowek, et al. 2022; Zacharie-Aubrun et al. 2022] has still to be integrated into the fission gas release code MARGARET [L. Noirot 2011], developed at CEA Cadarache.

This thesis document shows how these improvements have been introduced in the code and tested on a validation base.

1. The burnup is usually expressed in GWd/t_U. It is correlated to the number of fissions that happened per initial number of Uranium atoms, since the beginning of the irradiation.

1. Context and Motivations

Sommaire

1.1. Overview of the UO_2 fuel and fission gas behaviour under irradiation . 43
1.2. MARGARET 45
1.3. Motivations 48
1.3.1. New atomic scale simulations of dynamic re-solution from intra-granular bubbles 48
1.3.2. Changes in the micro-structure of the fuel at high BU and in the centre of the pellet and link with greater Fission Gas Release . . 49
1.3.3. Absence of evidence of inter-granular bubble interconnection in LWR fuel samples irradiated at high burnup and at temperatures lower than about 1100°C 50
1.3.4. Improving the consistency of the code 53
1.3.5. Building a new version of MARGARET that includes all these new modelling and validation of the new code against experimental results 54

1.1. Overview of the UO_2 fuel and fission gas behaviour under irradiation

The most widely adopted fuel in Light Water Reactors is the Uranium Dioxide (UO_2), which is a ceramic material. It is fabricated as fuel pellets, with diameters of about 8-9 mm, which are inserted one on top of the other inside a protective metal alloy, the cladding. The pile of fuel pellets plus the cladding form what is called the rod.
The as-fabricated fuel is poly-crystalline, which means that it is composed of different grains separated by grain boundaries. The crystal lattice inside a grain has the same orientation, while the crystal lattice of different grains has different orientations. This difference between grain and grain boundaries means that we can then talk of intra-granular entities for entities present inside the grains, and about inter-granular entities for entities present at the grain boundaries.
The as-fabricated fuel is a porous material: fabrication pores are present in the fuel as a result of the fabrication process. These pores can be intra- or inter-granular, depending if they are located inside the grains or at grain boundaries, respectively. These pores are not empty, but they are filled with Argon (still due to the fabrication process), at quite low pressure.

After the first start of the reactor, the fuel pellets fracture and can then be viewed as an ensemble of fragments. The crystal lattice of different fragments is not a continuum, in the sense that the surface of a fragment is a free surface and not a grain boundary. During the reactor operation, Fission Products (FP) are produced as a results of the fission of the Uranium atoms. 15% of the fission products are isotopes of Xenon or Krypton, called fission gas. The fission gas behaviour in the fuel is quite complex (that is why we need FGR codes, such as MARGARET, to simulate it), but can be summarized in this way: fission gas, after being produced by fission in the grains, tend to form bubbles[1] since they are not thermodynamically stable in the UO_2 crystal. Those bubbles can trap the dissolved gas atoms and from the bubbles, the atoms can re-solute back into the matrix because of the interactions of the energetic fission products with matter (this phenomenon is called dynamic re-solution). The gas that is not trapped in the bubbles diffuses toward the grain boundaries. In the grain boundaries, the gas once again forms bubbles, which, after a sufficient swelling, interconnect and release the gas to the free volumes by percolation[2]. The free volumes are the volumes in between the fuel pellets and the cladding, at which we have to sum the volume of the fractures. When the gas reaches the free surfaces, it is considered as released from the fuel.
A schematic representation of the fission gas behaviour can be seen in figure 1.1.
Xenon atoms are more stable on the grain boundaries than in the bulk, that is why they segregate there. Given this higher stability, an equilibrium may establish between the gas at the grain boundary in proximity of the inter-granular bubbles and the gas in these bubbles: this phenomenon is called thermal re-solution (see Section 1.3.3). Thermal re-solution does not happen in the bulk of the grain because of the low solubility of the fission gas in UO_2 crystal, as said before.
During irradiation, the energetic fission products interact not only with bubbles, but also with the crystal lattice. From this interaction, single and linear defects are produced: vacancies-interstitials pairs, dislocation loops and dislocation lines. In particular, the behaviour of vacancies-interstitials pairs is quite complex: they can recombine to form a normal site, interact with sinks such as bubbles and grain boundaries, form two or three dimensional defects. Moreover, they can interact with dislocation loops and dislocation lines, but also with other types of defects.
When the fuel reaches high burnups, the local burnup in the periphery of the pellet is higher than the one at the center, and a change in the fuel micro-structure happens at the periphery of the pellet: the original grains totally disappear at the benefit of much smaller ones. No intra-granular bubble is measured inside those new grains and a different population of inter-granular bubbles, larger than these new grains, appear. The porosity increases substantially. This new micro-structure is called High Burnup

1. At this point, the porosity of the fuel is due to both the fabrication pores, which now can be filled by fission gases as well, and the gas bubbles.

2. Percolation through the inter-connected inter-granular bubbles is not the only way for the fission gases to be released: they can diffuse directly to the free volumes from the grains that face a free surface (phenomenon called ejection) and they may diffuse towards the free volumes along the grain boundaries, as I will discuss in Section 1.3.3.

Structure (HBS) by the community.

1.2. MARGARET

MARGARET [L. Noirot 2011] is a C++ fission gas release code and it is a component of a wider Fuel Performance code for Light Water Reactors named ALCYONE [Introïni et al. 2024]. MARGARET models the behaviour of the gases produced by fission in the fuel, the micro-structure state of the fuel and, integrated into ALCYONE, predicts major quantities of interest such as fission gas release (FGR) and swelling, that impacts the geometry of the rod.

MARGARET is a local model. It is called a "point" model with respect to the target code in which it is implemented (ALCYONE). That is, at each point of the target code mesh, MARGARET receives certain pieces of information (temperature, fission rate, etc.) and sends back other pieces of information (fission gas release, swelling) regarding that macroscopic point. In MARGARET, the behaviour of different points is not directly coupled, which allows their computation in parallel.

If needed, MARGARET can provide, at each macroscopic point, a fine characterization of the gas situation[3]. To be able to describe this fine characterisation, we address two lower scales, typically that of the average grain and that of the fragment (for the gas transport along grain boundaries, see Section 1.3.3). Both are considered under the conditions of temperature, fission rate ... of the considered macroscopic point.

Figure 1.2 shows a schematic representation of how the code functions in relation with ALCYONE.

To predict the behaviour of the fission gases in the fuel during irradiation, MARGARET solves an Ordinary Differential Equations (ODE) system, where the variables characterize the fission gases and the micro-structure (bubbles, restructuring, fracturing ...), and the ODE characterize their behaviour, in the sense of the evolution in time of the variables. In addition to the ODE system, MARGARET uses a series of empirical correlations[4].

However, the fuel undergoes such changes that it is not possible to represent it the same way throughout irradiation.
That is why, at the beginning of my thesis, 3 different states had already been defined, namely "Sound" (fuel as-fabricated), "under Restructuring" and "Restructured", in

3. For example, MARGARET can say how much gas is in inter- or intra- granular position, how much Xenon is dissolved and how much Xe is trapped in the bubbles etc.

4. For example, empirical correlations are used to predict the morphology of the inter-granular bubble population, knowing its total volume.

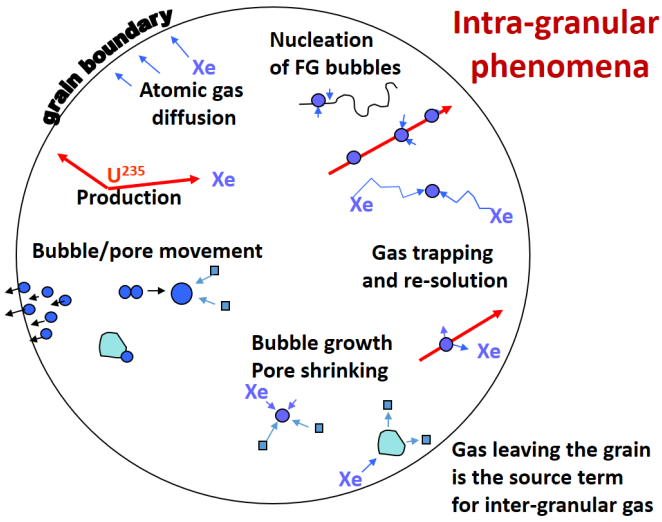

(a) Intra-granular behaviour.

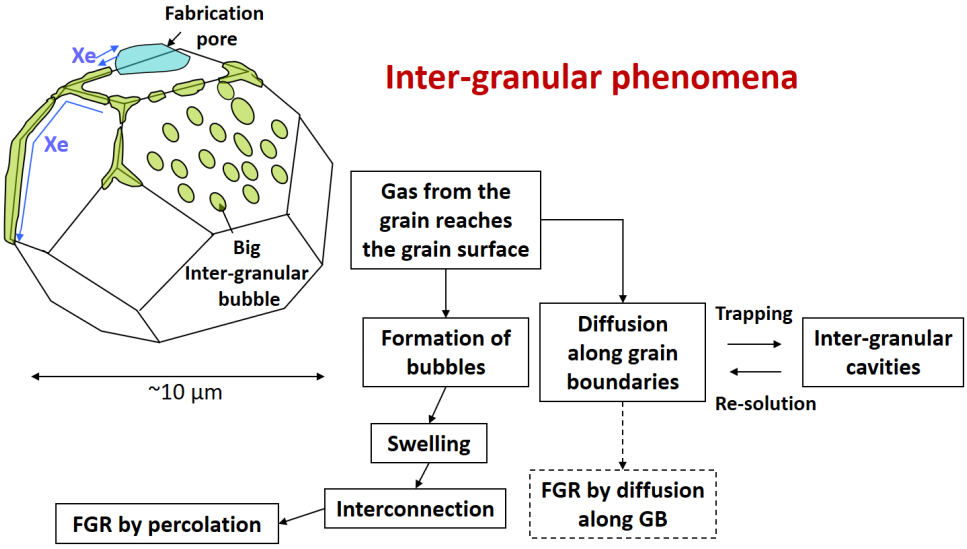

(b) Inter-granular behaviour. The fission gas release by diffusion along grain boundaries (GB) is usually not included inside FGR models, but its possible contribution to the total FGR will be discussed in this manuscript.

Figure 1.1. – Fission gas behaviour in the nuclear fuel under irradiation.

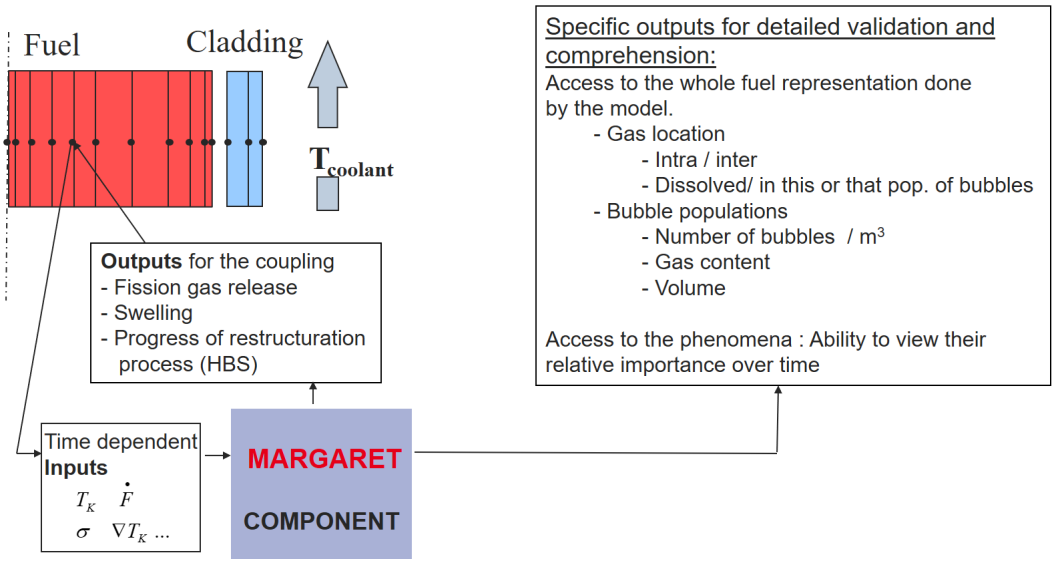

Figure 1.2. – Schematic representation of how the code functions in relation with ALCYONE, highlighting the main inputs and outputs, the mesh of the pellet and the fine characterization of the gas situation that MARGARET can offer. T is the temperature, $\dot{F}$ is the fission rate, σ is the hydrostatic stress and ∇T is the gradient of the temperature with respect to the radius of the pellet.

order to describe the progressive formation of the High Burnup Structure (HBS). The changes in the micro-structure of the fuel are such (see Section 1.1) that the restructured fuel cannot be represented by the same set of variables as the "sound" fuel. So, in MARGARET, when the fuel changes from one state to the other, the set of variables is changed and the ODE system is changed in accordance.
The code was designed to allow these changes easily[5].

A special attention is dedicated to the respect of the global balance of gases. To do so, the error on the global balance is calculated by the code and surveyed, as a way, among others, to detect possible errors in the implementation.

As the number of variables and parameters is quite large, some naming rules have been adopted in the model. They can be found in Appendix A. To help the reader, in the same Appendix, it is also possible to found a Glossary of the main variables and parameters used in this manuscript.

Few comments on the version of MARGARET used in this manuscript can be found in Appendix B.

5. There are other occasions where the set of variables and associated differential equations change, by instance the connection of part of the inter-granular bubbles to the free surface, which induces the addition of a new variable.

1.3. Motivations

As already said in the introduction, the objective of this thesis is to improve MARGARET considering recent experimental results and atomic scale simulations. The main published results that we have tried to consider and implement in MARGARET are:

— New Molecular Dynamic (MD) simulations of dynamic re-solution of gas from intra-granular bubbles;
— Recently discovered changes in micro-structure of the fuel at high BU and in the centre of the pellet;
— The absence of evidence of inter-granular bubble interconnection for fuels irradiated in base irradiation at temperatures lower than about 1100°C (centerline temperature).

Finally, the question of the consistency between base irradiation (BI) and ramp situations has been also addressed.

1.3.1. New atomic scale simulations of dynamic re-solution from intra-granular bubbles

In base irradiation, the first step of the fission gas release process is the diffusion of the dissolved gas atoms in the grains towards the grains' surface. However, this diffusion is slowed down by the trapping of the dissolved gas atoms by the intra-granular bubbles. On the other hand, the phenomenon of dynamic re-solution of the gas trapped in the intra-granular bubbles back to the lattice, caused by the interaction between the energetic fission products and the bubbles, allows part of the gas to escape from the bubbles and continue the diffusion. Since the balance between trapping and re-solution determine the percentage of gas in the grain that is dissolved in the matrix and that is able to diffuse, a correct description of this two phenomena in a fission gas release code is of absolute importance.
In the version of the MARGARET code used before the beginning of this thesis the phenomena of trapping by and re-solution from intra-granular bubbles was described using a re-solution shell around the bubbles. An hypothesis of steady state was used in this shell, where the re-solution from the bubble and the diffusion of gas from the bulk was set equal to the trapping of the gas by the bubble. The thickness of this shell was typically set equal to 2 nm. This was consistent with the fact that, as it is shown in the literature [Losonen 2017], the gas is re-dissolved from the bubbles in their proximity. The modelling used in MARGARET was different from the description generally used in other fission gas release codes [Losonen 2000; D. Olander et al. 2006; Uffelen et al. 2011; Barani et al. 2020]. In literature, the description generally involves the adoption of a trapping frequency equal to $4\pi R_b C_b D_{Xe}$ and a re-solution frequency equal to b,

where its value also depends on the radius of the bubbles. However, this description implies that the gas is re-dissolved uniformly in the solid (see Appendix D) and that is why an other approach had been implemented in MARGARET.
Recently, researchers have published new atomic scale simulations of dynamic re-solution from intra-granular bubbles [Setyawan et al. 2018]. In their paper, we can find a description of the hypothesis used in the study and a new expression of the re-solution frequency as a function of the radius of the bubbles. However, in the article, no quantitative information was given about the positions of the Xenon atoms re-dissolved in the matrix, even though they should have calculated them. So, I contacted the authors of the article [ibid.] to know more about that, and this sparked a collaboration with Dr. M.W.D. Cooper (one of the authors), which resulted in an article [Vergani et al. 2025] and in the Chapter 2 of this document. The aim was to build a simple model of trapping and re-solution based on the MD calculations, and usable in Fission Gas models such as MARGARET.

1.3.2. Changes in the micro-structure of the fuel at high BU and in the centre of the pellet and link with greater Fission Gas Release

A new phenomenon, visible in the center of the pellets at high burnup, has been recently discovered [J. Noirot, Zacharie-Aubrun, et al. 2018; Zacharie-Aubrun et al. 2022]: it can be categorized as a restructuring of the fuel, different from the restructuring that we see at the periphery of the fuel (HBS). The restructuring at the center of the pellet is characterized by the formation of different domains inside the original grains. The orientation of the lattice is the same in each domain, but differs slightly (misorientation angle between 1°-10° [Zacharie-Aubrun et al. 2022]) between different domains. These domains are called subdomains.
The formation of these subdomains is concomitant with a greater fission gas release. In fact, it seems that there is a link between these two phenomena [Rest et al. 2019]. Moreover, the new observations showed that the second, and bigger population of intra-granular bubbles (the so-called "precipitation bubbles") are placed on the subdomain boundaries. This observation gave an explanation for their appearance and also revealed that subdomain boundaries are a place where fission gases segregate. So, the idea arose that subdomain boundaries could be short cuts for diffusion in the grain, which would explain the FGR rise with burnup.
The modelling of MARGARET before the beginning of this thesis did not consider this new type of restructuring. Only the formation of the precipitation bubbles was taken into account. At the same time, MARGARET had a tendency to under-predict the fission gas release of fuels at high burnup. This is why we have worked on the introduction in MARGARET of a description of the subdomains.
In this direction, a feasibility study had been done before the beginning of this thesis to check if the dissolved gas in the subdomains could be described using only one

variable, the average concentration of dissolved gas in the subdomains, C_{XeM}, instead of discretizing the subdomains in shells and using one variable for each shell. Using only one variable to characterize the dissolved gas in the subdomains would allow to spare calculation time, which is of utmost importance for fission gas release codes. The study determined that it was possible to use only one variable, while keeping a correct description of the phenomena that happen in the subdomains, because, as the subdomain radius is about 0.5 μm [Dowek 2021], the diffusion regime inside the subdomain is close to steady state. Thus, the introduction of subdomains in MARGARET was feasible.

In Chapter 4, I present a more complete literature review on this subject (Section 4.1) and then I detail the modelling of the subdomains that we developed in MARGARET (Section 4.2).

1.3.3. Absence of evidence of inter-granular bubble interconnection in LWR fuel samples irradiated at high burnup and at temperatures lower than about 1100 °C

If subdomain boundaries behave as shortcuts for Xenon diffusion in spite of the presence of bubbles that trap the diffusing Xenon atoms, it implies that re-solution of Xenon (dynamic or thermal) from the bubbles to the subdomain boundaries is not negligible.
And if this is not negligible for subdomain boundaries, it may be not negligible for grain boundaries either.
This kind of re-solution "inter-inter" (from inter-granular bubbles to grain boundaries) had been introduced in the code before the beginning of my thesis, but never tested. It is the necessary condition for the long range diffusion along the grain boundaries.
Moreover, at CEA Cadarache, researchers have obtained new 3D experimental images of base-irradiated fuels [J. Noirot, Dowek, et al. 2022] to gather data on the characteristics of the inter-granular bubbles and the precipitation bubbles (the bigger population of intra-granular bubbles that forms at high burnup in the center of the fuel). One of the most surprising result published was the absence of evidence of a network of inter-connected inter-granular bubbles, even for fuels that experienced significant fission gas release (up to 6.2% for the fuel with the highest burnup, equal to 72.7 GWd/t$_U$). In fact, the percolation of the gas through this network is usually assumed by fission gas release codes to be the main way of fission gas release [Rest et al. 2019], and the same was true for MARGARET before the beginning of this thesis. Even if 3D experimental images that analyse a bigger part of the fuel would be needed to confirm the absence of inter-granular bubble interconnection, these new results question the current modelling assumptions and encourage the inclusion in the code of other ways for fission gas release, neglected until today.
Since the kinetic of the bubble interconnection depends on the temperature, an im-

portant thing to note here is that the apparent absence of bubble interconnections in LWR fuels that experienced centerline temperatures lower than about 1100°C is not inconsistent with Post Irradiation (PI) measurements performed on fuels operated at higher linear heat rates, or PI measurements performed on ramped fuels, where the interconnected bubbles are clearly visible.
One of the way in which Xenon can be released (apart from the direct ejection of gas from grains in the proximity of a free surface, mechanism which is already taken into account by fission gas release codes) is through diffusion along the grain boundaries. In fact, there is one experimental result that confirms this possibility. Researchers have studied Xe release from trace-irradiated UO_2 bi-crystals, at conditions where almost no inter-granular bubbles is expected to be present [D. R. Olander et al. 2001]. They concluded that lattice diffusion alone is not enough to describe the Xe release of their experiment. Even so, during in-reactor conditions, bubbles present along the grain boundaries trap the diffusing Xe and, doing so, may impede the long-range inter-granular diffusion. On the other hand, the phenomenon of dynamic (and maybe thermal) re-solution into grain boundaries may balance the trapping. Both the phenomena of dynamic and thermal re-solution into grain boundaries are usually neglected in fission gas release codes [ibid.], but we will activate them in MARGARET. In light of the recent experimental results, the long range diffusion of Xenon along grain boundaries towards the fragment surface will be modeled, as it has already been done for Helium, and an estimation of its impact to the fission gas release will be studied in this manuscript.

When the gas Helium has been introduced in MARGARET, the thermal re-solution of Helium from bubbles and pores has been introduced too (which was necessary, Helium being known to be soluble in UO_2). Again, for consistency, this phenomenon has to be taken into account for Xenon too. For intra-granular bubbles and pores no effective change is expected from this possibility, because the energy of the defect "Xe + Schottky" is high.
However, as Xe segregates on grain boundaries and subdomain boundaries, one can expect that the energy of the defect "Xe+Schottky" is lower in these places.
So, thermal re-solution of Xe from inter-granular bubbles towards grain boundary (or inter-subdomain bubbles towards subdomain boundaries) must be integrated in the model and tested. This will be incorporated in all the trapping expressions through the use of quantities of the type $C^{eq}_{Xej}(cavj)$, which is the equilibrium concentration of gas on the grain boundary (Xej, "j" standing for "joint", which means "boundary" in French) at the vicinity of the "cavj" type of inter-granular cavity.
Figure 1.3 shows the different equilibrium concentrations that have to be calculated and used in the model.

Before the beginning of the thesis, it was believed that the long-range diffusion along the grain boundaries was impossible for the gas, in the absence of the "inter-inter" re-solution. The scenario was the following: nanometric inter-granular bubbles (not modeled) would accumulate the gas, inter-connect, feed bigger bubbles and

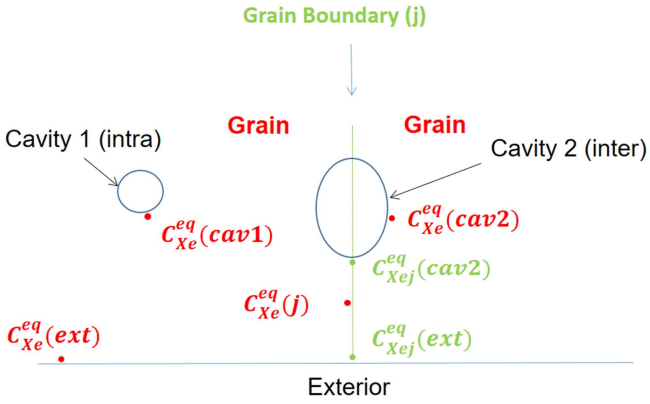

Figure 1.3. – Equilibrium concentrations that have to be calculated and used in the model. The letter "j" is an abbreviation for "joint de grain" in French, which means "Grain Boundary".

disappear periodically. As a consequence, the trapping of inter-granular gas by the inter-granular bubbles was modelled like a saturation process.
If the gas can diffuse along grain boundaries (even if it is an effective diffusion, resulting from trapping and re-solution from nano-bubbles), we have to express the trapping of gas by the bigger bubbles (those that are represented in the model) through a diffusion process, instead of a saturation one.

The description of the subdomains was our first motivation, but it implied a correct description of the behavior of the fission gas on subdomain boundaries, that is to say its trapping, re-solution and diffusion towards the grain boundary. That is why the motivation for the subdomains is presented first (Section 1.3.2) and the topic of inter-granular behavior (which serves also for the inter-subdomain behavior) is presented in a second time (Section 1.3.3). Logically, however, the Chapter presenting everything that is needed for a correct description of the inter-granular (or inter-subdomain) gas behavior (Chapter 3) is placed before the Chapter describing the “subdomain state” (Chapter 4) because the expressions derived in Chapter 3 will be used in Chapter 4.

In Chapter 3, I present a more complete literature review on this subject (Section 3.1) and then I detail the modelling of the long-range inter-granular gas diffusion present in MARGARET (Section 3.2). In particular, Section 3.2.8 is dedicated to the derivation of the equilibrium concentration of defects on the grain boundary near an inter-granular cavity.

1.3.4. Improving the consistency of the code

In the last validation of MARGARET, to avoid the formation of inter-connections at very low burnup, which would cause a release of gas by percolation, the researchers developing MARGARET chose to use an expression of the auto-diffusion coefficient of Uranium on the grain boundary, D_{Uj}, as function of the burnup. D_{Uj} is strongly linked to the formation of inter-granular bubbles inter-connections because it determines the volume contribution to the inter-granular bubbles due to the trapping of thermal vacancies on the grain boundaries.
In particular, at a given temperature (less than a threshold temperature, on which I will comment soon), the expression used for D_{Uj} determined an increase of its value spanning several orders of magnitude during irradiation.
Moreover, to adequately predict the fission gas release of both fuels irradiated under base irradiation and fuels which underwent a power ramp, two temperature domains were used: an high temperature domain (higher than 1100°C) where D_{Uj} did not depend on the burnup, and a low temperature domain where it depended on the burnup, to impede bubble inter-connection to happen too early in base irradiation, as said before.
The conclusion that had been drawn about the underlying physical phenomenon was that the modelling would have to be improved when more knowledge would be accumulated.

Another part of the MARGARET code that was inconsistent was the expression of the contribution of volume to the different cavities due to the trapping of thermal vacancies (see [L. Noirot 2011]).
In the development of MARGARET, the first hypothesis had been to say that the concentration of thermal vacancies in the bulk was the one at equilibrium with a pressure P_{hydr} (hydrostatic pressure in the solid). In base irradiation it led in practice to almost no flux to the bubbles. During power ramp conditions, on the contrary, to much swelling was obtained. So, for the ramp situation, the hypothesis of a concentration of vacancy at equilibrium with the pressure P_{hydro} was carried over to the inter-granular thermal vacancies ($C_{v,j} = C^{eq}_{v,j}(P_{hydro})$), and the intra-granular thermal vacancies were calculated analytically supposing that the flux of vacancies arriving from the grain boundary was trapped by the intra-granular bubbles. Doing so, the intra-granular swelling was adequately diminished.
However, the model lost its consistency between base irradiation and ramp conditions. Moreover, the model used to describe inter-granular swelling (namely the "White submodel") assumed that thermal vacancies were directly produced on the grain boundary due to the over-pressurization of the inter-granular bubbles, which put the grain boundary under tension [SPEIGHT et al. 1974]. Again, the consistentcy between this last approach and the hypothesis $C_{vj} = C^{eq}_{vj}(P_{hydro})$ did not exist.

In this thesis manuscript, we will illustrate our effort to obtain a more coherent description of the phenomenon of trapping of thermal vacancies by the pressurized

cavities, without loosing precision in the predictions.

The nuances of the choice of a single expression for D_{Uj} are presented in Section 7.1.5, while the literature review on the topic and the wider derivation of the contributions of volume to the different cavities due to the trapping of thermal vacancies are presented in Chapter 5.

1.3.5. Building a new version of MARGARET that includes all these new modelling and validation of the new code against experimental results

Our end goal is to obtain a code that is able to predict correctly the behaviour of the fission gas under all irradiation conditions. To do so, once we have built all the new models touched upon in the previous Sections, we need to integrate them in MARGARET. The result is a new version of MARGARET that includes all these changes (see figure 1.4).
At this point, we want to check if the predictions of this new code meet our expectations. This is done by comparing MARGARET predictions against a wide range of experimental data, such as FGR, swelling of the fuel, EPMA and SIMS measurements, measurements of the size and density of bubbles etc... . The comparisons will encompass both base irradiated and power ramped fuels. In this way, we will perform what we call the "validation" of the code.
The validation of the code will allow us also to reply to some of the questions that arose in the previous Sections, like: can the long range inter-granular diffusion contribute in relevant amount to the overall FGR? Can we predict the increase in FGR in high burnup, base irradiated fuels through a description of the subdomain formation?

Prior to exercise of validation, we need to choose the values of the set of parameters adopted in the different models present in MARGARET. This is done both by reviewing the literature (for the parameters not discussed elsewhere in the manuscript) and through a trial and error procedure.

An important point to emphasise here is that all the phenomena described in MARGARET are strongly coupled. A change in, for example, the description of the trapping and re-solution phenomena has repercussions on the overall behaviour of the fission gas. This means that each major change in the code necessitate a re-calibration of the parameters not directly involved in the modification. Hence, we think that the best way to validate the new version of MARGARET is by considering all the different modifications at the same time. This is why the comparisons between predictions and experimental data appear only in the last Chapter (Chapter 7).

Chapter 7 starts with a review of some of the major parameters that intervene in the

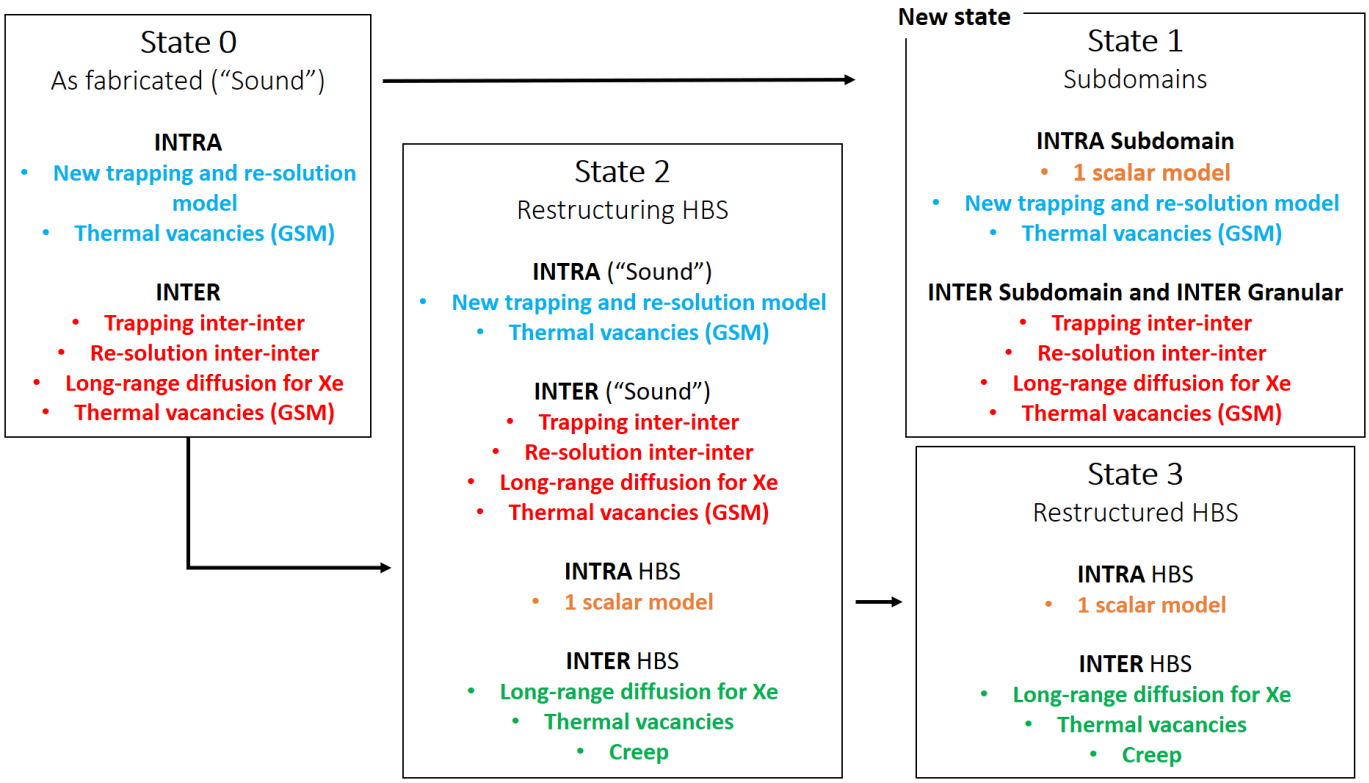

Figure 1.4. – Synthesis of the main changes in the code carried out for this thesis. The groups of modifications that are the same in the different states have the same color. "GSM" means "Generalized Speight Model".

description of the fission gas and that are not discussed elsewhere in the manuscript (Section 7.1). Then, it continuous with the presentation of the selected values of the parameters used in the different models present in MARGARET (Section 7.2). Finally, it ends with the extended validation of the new code against a wide range of experimental data (Section 7.3).

2. A new model for the phenomena of trapping by and re-solution from intra-granular bubbles

Sommaire

2.1. Introduction . . . 58
2.2. Review of existing re-solution models in the literature . . . 60
2.2.1. Experiments used to determine the frequency of re-solution . . 60
2.2.2. MD simulations used to determine the frequency of re-solution 61
2.2.3. Analysis and comments on the threshold distance . . . 64
2.2.4. Fission Gas Release codes . . . 65
2.2.5. Conclusion on the literature review . . . 66
2.3. Results . . . 68
2.3.1. Re-solution profile derived from MD simulations . . . 68
2.3.1.1. MD simulations results . . . 68
2.3.1.2. Re-solution profile derived from the MD cumulated displaced gas quantities . . . 69
2.3.2. Building a trapping and re-solution model based on low-scale simulation . . . 70
2.3.2.1. Reference model for trapping and re-solution . . . 70
2.3.2.2. The PHI-R5-NML simple model for trapping and re-solution . . . 73
2.3.2.3. The PHI-R5-NML-V simple model for trapping and re-solution . . . 77
2.3.2.4. The PHI-R5-NML-VS simple model for trapping and re-solution . . . 78
2.4. Discussion . . . 81
2.4.1. Estimation of the re-solution frequency with a variable R_T . . . 81
2.4.2. Changes in the 2-scalar model with a variable R_T . . . 83
2.5. Conclusion and perspectives . . . 84

In the first Sections of this Chapter, we copy almost [1] word for word the article [Vergani et al. 2025] born from the collaboration between L. Noirot, me, and Dr. M.W.D. Cooper (Los Alamos National Laboratory). The result of our work is a model that describes the phenomena of trapping by and re-solution from intra-granular bubbles, simple enough to be implemented in fission gas release codes such as MARGARET. In Appendix E we present the expression of the re-solution frequency as a function of the radius of the bubbles that we adopt in the version of MARGARET that we produced.

2.1. Introduction

Inside UO_2 fuels, fission gases, produced as a result of fission events, diffuse through the crystal lattice and precipitate as bubbles (both intra-granular and inter-granular). The formation of bubbles is due to the insolubility of the fission gases in the fuel matrix. Bubbles trap the diffusing fission gases and this phenomenon decreases the concentration of gas dispersed in the matrix [Rest et al. 2019]. The latter influences fission gas release: a lower concentration of fission gases in the matrix means less atoms that diffuse towards the grain surface [Hj. Matzke 1966], which would result in less or no fission gas release. Without any competing phenomenon, fission gases would mostly tend to be trapped inside bubbles, and the fission gas release would be low. However, the interaction between energetic fission products and bubbles produces re-solution events which increase the dynamic solubility of fission gases. The quantity that describes the frequency at which re-solution happens in the fuel is denoted b, the re-solution frequency. Proper knowledge of this quantity is, therefore, of utmost importance to describe the behavior of fission gases. However, in the literature, the definition of b has never been crystal clear. When it was derived from experiments by Turnbull and Cornell [J. A. Turnbull and R. M. Cornell 1970; J. A. Turnbull and R. M. Cornell 1971], it was calculated based on the shrinkage of bubbles. When it is used inside fission gas behavior models, it is generally used within the following context [Losonen 2000; D. Olander et al. 2006; Uffelen et al. 2011; Barani et al. 2020]: modelers use a trapping term of the form $4\pi D_{Xe} R_b C_b C_{Xe}$ (or, similarly: $4\pi D_{Xe}(R_b + R_g) C_b C_{Xe}$), and a re-solution term in the form: bC_{Xeb}, where D_{Xe} is the diffusion coefficient of fission gas in the fuel matrix, R_b and R_g are the radius of the population of intra-granular bubbles and of the gas atoms respectively, C_b is the concentration of intra-granular bubbles, C_{Xe} is the concentration of dispersed fission gas and C_{Xeb} is the concentration of gas in the intra-granular bubbles. This kind of approach is also used for each of the different classes of bubbles used in cluster dynamics models for intra-granular bubbles [Kim et al. 2022].

Using molecular dynamics (MD) calculations, Setyawan et al. [Setyawan et al. 2018]

1. With respect to the article, we have slightly changed the Introduction and Appendix C, so that they can fit better in the context of this thesis manuscript, we have reformulate Appendix D with the same intent, we have added footnotes 6, we have changed few words without changing the meaning of the text, and 2, and we do not have included some of the Appendix.

evaluated the re-solution frequency counting all the atoms expelled from the bubble after a re-solution event. More precisely, they counted the atoms that, at the end of the simulation, were located at a radius $r > R_T$, R_T being a threshold radius taken as $R_T = R_b + 1nm$. MD calculations rely on parameters not yet totally known, such as ζ, the fraction of the electronic stopping power deposited to the UO_2 lattice. In order to derive the value of b, then, Setyawan et al. confronted their model to experimental and empirical values of b taken from the literature, adjusted the value of ζ based on these comparisons and justified their choice also on the basis of the effective stopping power required to observe dislocations near thermal spikes.
Moreover, the question of the threshold must be explored both from its meaning and from the point of view of the associated uncertainties. Our proposal is the following: just after the fission spike/bubble interaction, within a very short time Δt_w, the Xenon atoms that are very near the bubble ($r < R_T$) would go back in the bubble because they remain within a potential well due to atom-bubble interactions. The time scale of normal diffusion would be much larger than this Δt_w. Thus a precise definition of the re-solution frequency would be that of Setyawan et al., with a R_T corresponding to the influence of the potential well around the bubble (where the choice of 1 nm in Setyawan's paper is based on a typical interaction energy distance shown by defects and interfaces, as seen in many materials). On the basis of this definition, it is not at all obvious that this value must be comparable to the values of the literature, because of the vagueness of the definitions mentioned above.

MD simulations of re-solution events, apart from calculating b, can help derive the re-solution cumulated gas quantities, which express the number of atoms re-dispersed within a certain distance from the bubble at each re-solution event. The re-solution cumulated gas quantities are a key piece of information to build a re-solution/trapping model usable in fuel performance codes and consistent with low-scale simulations.

The organization of the paper is as follows. In section 2.2, we describe the literature regarding the re-solution frequency, and we motivate why b derived in different ways should be dissimilar. In section 2.3, we present the cumulated displaced gas quantities derived from MD simulations and explain how to make use of them to construct a 2-variable model of trapping and re-solution suitable for fission gas release codes. We also validate this simple model against a reference model (with 161 variables) that describes the phenomena of trapping and re-solution consistently with the low-scale simulations. In section 2.4, we explore the possibility of changing the value of b considering the uncertainties in the process of derivation from MD calculations, and we show how the variation of b impacts the behavior of fission gas.

2.2. Review of existing re-solution models in the literature

2.2.1. Experiments used to determine the frequency of re-solution

The most recent experiments that tried directly to measure the re-solution frequency (at the present knowledge of the authors) are the ones made by Turnbull et al. [J. A. Turnbull and R. M. Cornell 1970; J. A. Turnbull and R. M. Cornell 1971] in the 70s. These experiments have shown clearly that there was an effect of reduction in the size of the bubbles or even total destruction due to re-irradiation after annealing.

The research group irradiated samples of UO_2 enriched at 5.25% and 2.5%, and then annealed them for 6 hours at 1500 °C, such that all the fission gas precipitated into intra-granular bubbles. At this point, the samples were further irradiated at a known dose of irradiation. Turnbull et al. measured both the initial and final radius of the bubbles. Using this measure, the hypothesis of mechanical equilibrium between bubbles and bulk pressure, and an equation of state (van der Waals, in Turnbull's article), it is possible to calculate the initial and final number of atoms present in each bubble. Given this information, Turnbull derived the value of the re-solution frequency. From Turnbull's article:

$$b^{Turnbull} = \frac{1}{N}\frac{dN}{dt} \qquad [1/s] \tag{2.1}$$

where N is is the number of gas atoms[2] in a bubble. If Q is the dose in $fissions/cm^3$ required to reduce the number of fission gas atoms in a bubble from N_1 to N_2 in a piece of material undergoing Φ $fissions/cm^3/s$, then

$$b^{Turnbull} = -\frac{\Phi}{Q} ln\left(\frac{N_1}{N_2}\right) \qquad [1/s] \tag{2.2}$$

If the bubbles were found as completely destroyed, N_2 was considered as equal to 1. Experiments were conducted at two different temperatures during the re-irradiation period: 200 °C and 1200 °C. They were used to give limit conditions for the value of the re-solution frequency for two different population of bubbles.
The first experiment, conducted at 200 °C, had a starting population of bubbles with a radius of about 5 - 7.5 nm. The limit conditions set by this experiment are:

$$2.6 \times 10^{-5} \quad [1/s] \quad \leq b^{Turnbull} \leq 1.2 \times 10^{-4} \quad [1/s] \tag{2.3}$$

The second experiment, conducted at 1200 °C, had a starting population of bubbles with a radius of about 2.5 - 5 nm. The limit conditions set by this experiment are:

2. The gas produced from fission: isotopes of Xenon and Krypton.

$$1.8 \times 10^{-4} \quad [1/s] \quad \leq b^{Turnbull} \leq 3.6 \times 10^{-4} \quad [1/s] \tag{2.4}$$

Let us point out that this approach, based on the bubble size, is very indirect because bubble size is driven by the absorption or emission of point defects that directly change the volume of the bubble: vacancies, self-interstitials, and different defects that include a Xenon atom, and which allow Xenon diffusion.[3]

In general, the bubble volume may vary immediately due to the interaction with the fission spike, with the appearance of point defects at the vicinity of the bubble. Then the Xenon quantity that is inside the bubble influences the inner pressure of the bubble and consequently the equilibrium concentration of these defects at the vicinity of the bubble, which gives the limit condition for the diffusion of these defects at the bubble surface. The process is quite complex, and the mechanical equilibrium is not mandatorily verified.

Moreover, during the high temperature experiment, part of the re-dispersed Xenon possibly had time to go back to the bubble by diffusion (see Appendix A in [Vergani et al. 2025]). Therefore, either the re-irradiation is done at low temperature (200°C) and one may suppose that the effects of diffusion are negligible. But in this case the hypothesis of mechanical equilibrium does not stand[4] . Or the re-irradiation is done at higher temperature (1200°C), one may suppose that the bubbles are in mechanical equilibrium[5], but the effect of diffusion is not negligible: some of the Xenon atoms had time to go back to the bubble during the re-irradiation experiment, which has not been taken into account at all in $b^{Turnbull}$.

Our conclusion is that $b^{Turnbull}$ (200°C) cannot be used (because of the mechanical equilibrium hypothesis that does not stand), and that $b^{Turnbull}$ (1200°C) should be lower than b^{MD}, which is the re-solution frequency calculated through MD simulations (like the one calculated by Setyawan et al. [Setyawan et al. 2018]), because part of Xenon atoms had time to go back by diffusion to the bubble during the re-irradiation experiment at 1200°C.

2.2.2. MD simulations used to determine the frequency of re-solution

Previous studies came up with two main mechanisms to explain re-solution:

3. Using Kröger-Vink notation [Kröger et al. 1956], and following the recent publication of Mattews et al. [C. Matthews et al. 2019], the latter would be $\{Xe_U : V_U : V_O\}$ for the preferential vacancy diffusion mechanism of Xe at high temperature and $\{Xe_U : 3V_U : 3V_O\}$ for the preferential diffusion mechanism of Xe at the intermediate irradiation-enhanced thermal diffusion regime.

4. Turnbull and Cornell [A. Turnbull et al. 1970] themselves pointed out, about their experiment at 200°C: *"Although it is a reasonable assumption that the re-solution process will be substantially temperature independent, numerical evaluation of b from low temperature experiments may be in error."*. And that is why they conducted experiments at 1200°C afterwards.

5. Even at 1200°C, mechanical equilibrium is not evident. See Appendix C on this subject.

— The first says that re-solution is caused by dissipation of fission products recoil-energy through **thermal spikes**, which is associated with the electronic part of the stopping power. From Olander's textbook [OLANDER 1976]: *"A thermal spike is an extremely hot region in the track of a fission fragment produced by the intense local heating of the solid during slowing down of the fragment. The thermal disorder created by the spike completely mixes the matrix atoms with the fission-gas atoms in the affected bubble, and, after the temperature transient has decayed, the gas atoms are considered to be frozen into the solid as atomically dispersed particles"*.
In this first case, the result is a re-solution of groups of atoms altogether. This mechanism has been named heterogeneous re-solution [D. Olander et al. 2006]. When this mechanism was presented for the first time, the idea was that small bubbles would have been entirely destroyed by an encounter with a fission spike [J. A. Turnbull 1971].
— The second mechanism says that re-solution is caused by dissipation of fission products energy through **collision cascades**, event which is associated to the ballistic part of the stopping power. In this second case, the result is a re-solution of atoms one by one.

While probably both mechanisms contribute to the phenomenon of re-solution, from the most recent literature [Setyawan et al. 2018; Schwen, Huang, et al. 2009; Govers et al. 2013; Rest et al. 2019] it seems that thermal spikes can be considered as the prevalent explanation, even if the debate is still going on in the scientific community.

In the last published MD simulation regarding re-solution, the paper of Setyawan et al. [Setyawan et al. 2018], the authors consider re-solution caused by thermal spikes. They show a dependence of the re-solution on *"bubble size, fission product track-bubble interaction geometry (e.g., off-centered distance between the axis of the thermal spike and the bubble center), and $S_{e,eff}$"*, where $S_{e,eff}$ is the effective electronic stopping power (the part of the electronic stopping power which causes heating and a rise in lattice temperature in the fission spike track).
To compute b, they used *"a realistic distribution of fission products, accounting for decay of the electronic stopping power as a function of distance for each fission product"*.
One of their most important results, the expression of the re-solution frequency as a function of the radius of the bubble, is shown in figure 2.1.

The MD simulations performed by Setyawan et al. contain information regarding the distribution of re-dispersed gas as a function of the distance from the bubble. However, this information was reduced in [ibid.] because Setyawan used only a cut off threshold. Later (Section 2.3.1.1) we present the results of reanalysing the MD simulation data to display the re-solution cumulated gas quantities. These quantities show that re-solution through thermal spikes happens in proximity of the bubbles, and not homogeneously in the bulk. This idea, already proposed in previous literature

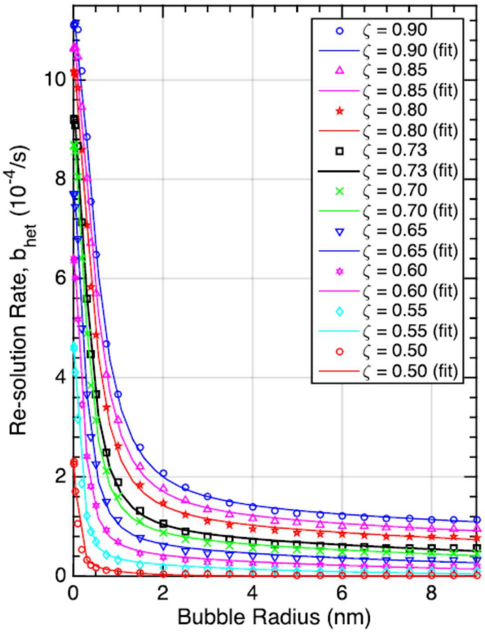

Figure 2.1. – Resolution frequency as a function of the bubble radius for several values of the ratio between the thermal spike energy and the total electronic stopping power ($\zeta = S_{e,eff}/S_e$) for a fission rate density of $10^{-8}/nm^3s$, given by the interaction bubble-thermal spike calculated through MD, according to Setyawan et al. [Setyawan et al. 2018] approach. Taken from Ref. [Setyawan et al. 2018]

[Losonen 2017], receives a further confirmation from MD simulations, and, above all, a quantification.
The fact that re-solution happens only in the vicinity of the bubbles may have a considerable influence on the behavior of fission gas in fuels under irradiation. Therefore, we would like to consider it in our models.
Examples of other re-solution models, already published, that take into account that re-solution happens only in the vicinity of the bubbles, are due to Losonen [ibid.] or Veshchunov [Veshchunov and Tarasov 2013]. Moreover, there are other works on bubbles evolution in UO_2 that consider this fact, like the Monte Carlo model of Schwen [Schwen and Averback 2010].

Setyawan et al. defined the re-dispersed atoms as those that were further than 1 nm from the initial bubble surface at the end of the MD simulation. Correspondingly, they have made the assumption that all the Xe atoms that are found no further than 1 nm from the radius of the bubble are quickly, almost instantaneously, re-trapped

by the bubble, because of the presence of a potential energy around the bubble that attracts the Xe atoms inside this threshold value. The value of this distance is taken somewhat arbitrarily, partially based on previous literature [Govers et al. 2013], partially comparing it to the distance of interaction that somewhat similar phenomena show (an example in figure 2.2).

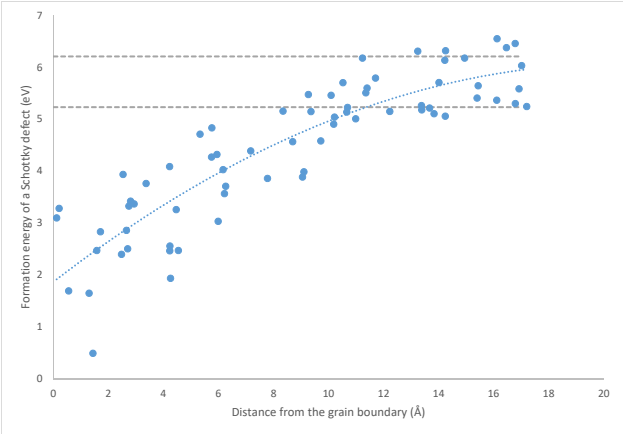

Figure 2.2. – Formation energy of a Schottky defect as a function of the distance to the grain boundary for the STGB (symmetric tilt grain boundary) around the axis [001] Σ37 (misorientation angle equal to 18.92°). Blue points represent the energy calculated in various locations. The dotted blue curve is a quadratic fit of the calculated points. The dotted grey lines correspond to the formation energy of Schottky defects in the perfect crystal. The simulation has been performed at 300 K. The image is taken from [Borde et al. 2021].

2.2.3. Analysis and comments on the threshold distance

Setyawan et al. are not the only researchers doing MD simulations who consider a threshold distance in the analysis of re-solution simulations. Apart from Setyawan's article, a 1 nm threshold distance is also used by Govers et al. [ibid.]. Huang et al. [Huang et al. 2010], instead, simply do not use any threshold distance for re-solution (threshold distance = 0). Schwen et al. [Schwen, Huang, et al. 2009] consider a threshold distance for re-solution, but with a different explanation with respect to Setyawan et al.: they propose to estimate a threshold radius by back-diffusion probability, therefore, based on a diffusion process, without taking into account any potential energy. This approach (considering back-diffusion probability) brings to a misleading definition of b, which mix the re-solution process (only due to the irradiation) with the diffusion processes around the bubble. Note that it is inconsistent

to define b including back-diffusion to the bubble and to use the same b in models that explicitly consider the diffusion with a trapping term. However, Schwen et al. were probably aware of the problem and added, in the conclusion of their article, that *"the assignment of a 'radius of influence' to determine escape from the bubble is an artificial measure to obtain a value for the re-solution parameter for comparison with previous results"*.

In any case, it makes sense to define a minimum value for the threshold distance as approximately equal to $(\frac{3}{4\pi}\Omega)^{1/3}$, which is the value of the radius of a sphere with volume equal to Ω (using the hypothesis that the volume of a Xe atom in the matrix is close to Ω[6]). The reason is that, if a Xe atom arrives at that distance from the bubbles, it can be considered as already inside the bubble. This distance can be estimated, using a value of $\Omega \approx 4.1 \times 10^{-29}\ m^3$ [Veshchunov 2000], as $\approx 0.21\ nm$. This evaluation is in line with the consideration of R_b in the Olander trapping term: $4\pi D_{Xe}(R_b + R_g)C_b C_{Xe}$.

2.2.4. Fission Gas Release codes

The frequency of re-solution is used inside fission gas release codes to model the phenomenon of re-solution of gas from the bubbles into the fuel lattice. The most common formulation of the problem of creation/trapping/re-solution of gas inside FGR codes is the following :

$$\begin{aligned} \frac{dC_{XeM}}{dt} &= -4\pi R_b C_b D_{Xe} C_{XeM} + bC_{Xeb} + \beta \\ \frac{dC_{Xeb}}{dt} &= 4\pi R_b C_b D_{Xe} C_{XeM} - bC_{Xeb} \end{aligned} \tag{2.5}$$

Where R_b is the radius of the bubble, C_b is the concentration of the bubbles, D_{Xe} is the diffusion coefficient of the gas in the solid, b is the re-solution frequency of gas in the bubble towards the solid, β is the rate of production of gas. In this formulation, the trapping term $-4\pi R_b C_b D_{Xe} C_{XeM}$ has been proposed by Ham [Ham 1958] and Olander [OLANDER 1976], and can be derived as the analytical expression of the flux at the vicinity of a bubble, in the problem of simple diffusion ($D_{Xe}\nabla^2 C = 0$), with a limit condition $C = 0$ at the surface of the bubble and $C = C_{XeM}$ at infinity (see p212 of [ibid.]). If bubbles are far from one another, C_{XeM} can also be considered as the mean concentration of gas in the solid. In the following, we will refer to this model by the name "OLANDER".

In the case of FGR codes, b is mostly a fitting parameter. It depends on the trapping model used in the code, and its value should be adequate to predict correctly the fission gas release.

It is possible to show that this 2-scalar (the Ordinary Differential Equations variables C_{Xeb} and C_{XeM}) model is equivalent to the problem of diffusion around the bubble plus a **uniform** source term coming from the re-solution of gas from the bubble (see Appendix D for this). This 2-scalar model may have driven researchers to a

6. The volume of a Schottky defect (UO_2 site missing).

definition of b that implied that the gas should be found, due to re-solution, far from the bubble. For example, a sentence from [Ronchi et al. 1986] show how the definition of b included the idea of re-solution 'in volume' for the authors: *"low-temperature destruction of bubbles by fission is not an indication that gas is being re-dissolved from the bubble"*. So, people may had a tendency to reject any definition that would count mostly Xenon atoms placed near the bubble with a very steep distribution in space.

2.2.5. Conclusion on the literature review

To conclude, what we can take for granted is :

— In the fuel during irradiation, there are interactions between fission spikes and bubbles, that produce the re-solution of gas atom from the bubbles. This phenomenon seems to be the prevalent way in which gas atoms resolute.
— The re-dispersed atoms are re-dispersed in the vicinity of the bubbles.
— A clear distinction has to be made between the re-solution itself and the diffusion processes. The R_T threshold value should be related to very short time-scale processes[7], or purely geometric considerations (like the size of a dissolved gas atom, or the size of a Schottky defect that contains a gas atom).

At the same time, we do not know which one is the most reliable value of the threshold distance of re-solution.

Moreover, we have seen how the definition of the re-solution frequency, b, is not always the same in literature:

— For Turnbull, $b^{Turnbull}$ is calculated ignoring the fact that Xe atoms can be continually re-trapped. In fact, we have seen that at 1200 °C the diffusion process could make part of the re-dissolved Xe atoms go back into the bubble.
— Following many fission gas release codes, $b^{Olander}$ should be the adequate value to predict correctly the fission gas release using a re-solution-trapping model of the kind $4\pi R_b C_b D_{Xe} C_{Xe}$ / $b^{Olander} C_{Xeb}$ for the trapping and re-solution terms respectively, or the OLANDER model, as we called it in chapter 2.2.4.
— For Setyawan (MD simulation of the fission spike), b^{MD} is calculated counting the Xe atoms re-dispersed further than a threshold distance from the original bubble surface, with the hypothesis that, within this distance, the Xe atoms are in a potential well that makes them inevitably go back into the bubble on time scale that are probably short[8] but somewhat longer that MD timescale ($\sim 100\ ps$). Moreover, the MD simulation provides the re-solution cumulated gas quantities.

In our opinion, these different frequencies have no reason to have the same values.

In line with the reasoning, we propose the following, and MD compatible, definition of b, as the ratio per second of bubble gas that is placed outside the bubble because

7. Xe atoms situated in the potential well of the bubble are probably trapped by the bubble much faster than if they would randomly diffuse
8. Short means "much faster than the bulk diffusion would do", or instantly, at the time scale of Fuel Performance Fission Gas Models

of fission spike interactions, and **that cannot go back into the bubble at a lower time scale than that of bulk diffusion**[9]. A precise definition is given in [Setyawan et al. 2018] by the equation (6) and the whole process explained in this reference. In particular, the use of a threshold R_T serves to take into account this question of "almost-immediate return" that we emphasize here.

Moreover, we should have :

$$b^{Turnbull}(1200°C) < b^{Olander} < b^{MD}$$

The first inequality is because Turnbull has not considered any back diffusion at all. The adjusted $b^{Olander}$ should be lower than b^{MD}. Otherwise, the concentration of dispersed gas predicted by the OLANDER model (which is equivalent to a uniform re-solution or 'in volume' re-solution) would be too high compared to the reality (where the re-solution profile is steep).

Let us specify that Setyawan et al. chose the parameter ζ in their article also by comparing the value of the re-solution frequency with Turnbull's estimations. But we think that they could have chosen a higher ζ or a lower threshold distance, which would have given a higher b^{MD}.

Setyawan et al. calculations - their method to calculate the value of b^{MD}, in line with our definition of the re-solution frequency, and their re-solution cumulated gas quantities - seem, therefore, the most appropriate to define a trapping/re-solution model that can be both usable in FGR models of Fuel Performance Codes, and consistent with the atomic-scale calculations. The construction of such a model is the object of the following sections.

9. Depending on the distance d of the dissolved gas atom from the radius of the bubble, this time scale can be considered equal to: $\frac{d^2}{D_{Xe}}$.

2.3. Results

In this section, we exploit the maximum of results obtained in molecular dynamics (not only b^{MD} but also the final position of Xe atoms after the interaction with the fission spike), in order to make them usable in the fission gas models of performance codes. This is typically an example of what needs to be done in the multiscale approach. First, we find a re-solution profile compatible with the MD results. Then, we build a trapping/re-solution model with only two variables (C_{XeM},C_{Xeb}), which takes this profile into account, explaining the steps to do so. We further prove that this model is suitable, by comparing it to a reference model of the bubble and its surroundings, very finely meshed.

2.3.1. Re-solution profile derived from MD simulations

2.3.1.1. MD simulations results

Setyawan et al. [Setyawan et al. 2018] have performed a series of atomistic simulations to study the behavior of Xe gas bubbles in UO_2 during the interaction with a fission spike, using the thermal spike approximation. Through the application of molecular dynamics, they have obtained the position of the Xenon atoms after the interaction between the thermal spike and the bubble. From that information, at first they deduced the number of re-dispersed (or “re-dissolved") atoms, N_{res}, and then, they determined the re-solution frequency b^{MD}. As they repeated this process for bubbles of different sizes, they obtained b^{MD} as a function of the radius of a bubble.

From the final positions of the Xenon atoms, the cumulated displaced gas quantities of Xenon can be post-treated. However, Setyawan et al. had not provided any such quantities in their article. With the permission of the authors, we have reanalysed the final atomic configuration data from those MD simulations to determine the cumulated number of gas atoms in the solid as a function of distance from the center of the bubble, $n^{MD}_{displ}(r)$. The results for a bubble of radius 1.5 nm are shown in figure 2.3. The results for bubbles of radius 0.6 and 2 nm are shown in Appendix D in [Vergani et al. 2025]. The plots show the number of gas atoms within concentric spheres of increasing radius centered at the center of the bubble: the so-called “cumulated displaced gas quantities", $n^{MD}_{displ}(r)$.
Each figure presents several curves because the simulations were repeated 5 times for each case. The solid vertical line corresponds to the position of the initial bubble radius, R_b, and the dashed vertical line corresponds to the threshold beyond which the Xenon atoms are considered as re-dispersed, called R_T (T for Threshold).
In figure 2.3, it is possible to see that no atom, or almost none, is re-dispersed further than a radius of 5 nm from the center of the bubble. We have called this outer radius “R_L" (L for re-solution Layer), and its value is assumed to be always equal to: $R_L = R_b + 3.5\ nm$. This assumption seems valid also if we analyze the data regarding bubbles with radius equal to 0.6 and 2 nm (see Appendix F in [ibid.]).

From the definitions, we have the relation below for the total number of gas atoms re-dispersed after one event, N_{res}.

$$N_{res} = n^{MD}_{displ}(R_L) - n^{MD}_{displ}(R_T) \tag{2.6}$$

2.3.1.2. Re-solution profile derived from the MD cumulated displaced gas quantities

In order to make use of the new re-solution data, we need to find a function, $Profile(r)$, compatible with those data, which will be used as the re-solution profile. The re-solution profile is the source term of re-dissolved gas, function of r, and normalized to one.
After a trial and error process, we found the profile presented below (equation 2.7).

$$\begin{aligned} Profile(r) &= 0 && R_b \leq r \leq R_T \\ Profile(r) &= \frac{G}{4\pi r^5} && R_T \leq r \leq R_L \\ Profile(r) &= 0 && r > R_L \end{aligned} \tag{2.7}$$

$Profile(r)$ is logically nil between R_b and R_T (based on a R_T threshold). G $[m^5]$ is a constant that is needed to normalize to 1 the profile on the whole domain. It is obtained using the equation 2.8 and its value is given by equation 2.9.

$$\int_{R_b}^{R_{ext}} Profile(r) 4\pi r^2 dr = \frac{4}{3}\pi(R^3_{ext} - R^3_b) \tag{2.8}$$

where R_{ext} is the limit radius of the domain considered (see equation 2.11 and figure 2.4).

$$G = \frac{2R^2_T R^2_L}{R^2_L - R^2_T} \times \frac{4}{3}\pi(R^3_{ext} - R^3_b) \tag{2.9}$$

From $Profile(r)$, we can calculate the cumulated re-dissolved gas quantities, $n_{res}(r)$, expressed in atoms, for r between R_T and R_L:

$$\begin{aligned} n_{res}(r) &= \int_{R_T}^{r} \frac{N_{res}}{\frac{4\pi}{3}(R^3_{ext} - R^3_b)} Profile(r') 4\pi r'^2 dr' \\ &= N_{res} \frac{R^2_L}{r^2} \left[\frac{r^2 - R^2_T}{R^2_L - R^2_T} \right] \end{aligned} \tag{2.10}$$

If our profile $Profile(r)$ is adequate, $n_{res}(r) + \overline{n^{MD}_{displ}(R_T)}$ should be close to $n^{MD}_{displ}(r)$ between R_T and R_L. $\overline{n^{MD}_{displ}(R_T)}$ is the mean value of the $n^{MD}_{displ}(R_T)$ obtained in the 5 simulations for the same bubble size. We see in figure 2.3 that this is the case.

2.3.2. Building a trapping and re-solution model based on low-scale simulation

Now that we have found a function that represents the re-solution profile, the aim of this section is to find the best formulation to describe the trapping/re-solution phenomena that happen in the vicinity of a bubble. This formulation should be tractable within fuel performance codes. As we also want to validate this formulation comparing it with a reference, we begin by building this detailed reference model.

2.3.2.1. Reference model for trapping and re-solution

We considered a typical nano-bubble, surrounded by an also typical spherical volume of the crystal based on the density of the nano-bubbles measured by TEM (Transmission Electron Micoscopy). The external radius of this spherical volume, R_{ext}, is related to the bubble density, C_b, by the equation 2.11.

$$C_b = \frac{1}{\frac{4}{3}\pi(R_{ext}^3 - R_b^3)} \tag{2.11}$$

We considered common conditions of temperature and fission rate, presented in the tables 2.1 and 2.2 [10].

Fission rate $(Fiss/m^3/s)$	Temperature $(°C)$	Fission yield	Radius of the bubble R_{int} (nm)	Concentration of bubbles $bubbles/m^3$	Correspondent external radius R_{ext} (nm)
10^{19}	800.	0.3	0.5	$8\,10^{23}$ [S. Kashibe 1993]	6.68346

Table 2.1. – Characteristics of the calculation performed for the reference model.

Diffusion coefficient of gas (m^2/s)	of which Thermal $5.10^{-5} \times exp(\frac{-45200.}{TK})$ [Miekeley et al. 1972]	of which Mixed $6.95\,10^{-25} \times \sqrt{\dot{F}} \times exp(\frac{-13870.}{TK})$ See footnote 10	of which Athermal $6.10^{-40} \times \dot{F}$ See footnote 10
$1.13825\,10^{-20}$	$2.5522\,5\,10^{-23}$	$5.35693\,10^{-21}$	6.10^{-21}

Table 2.2. – Diffusion coefficient of Xenon used. TK is the temperature in Kelvin

10. $D_{Xe,mix}$ and $D_{Xe,ath}$ values are taken in the set of parameters that where used for the validation of MARGARET [L. Noirot 2011] for UO_2 fuels. The form of the expressions comes from [J. A. Turnbull, Friskney, et al. 1982].

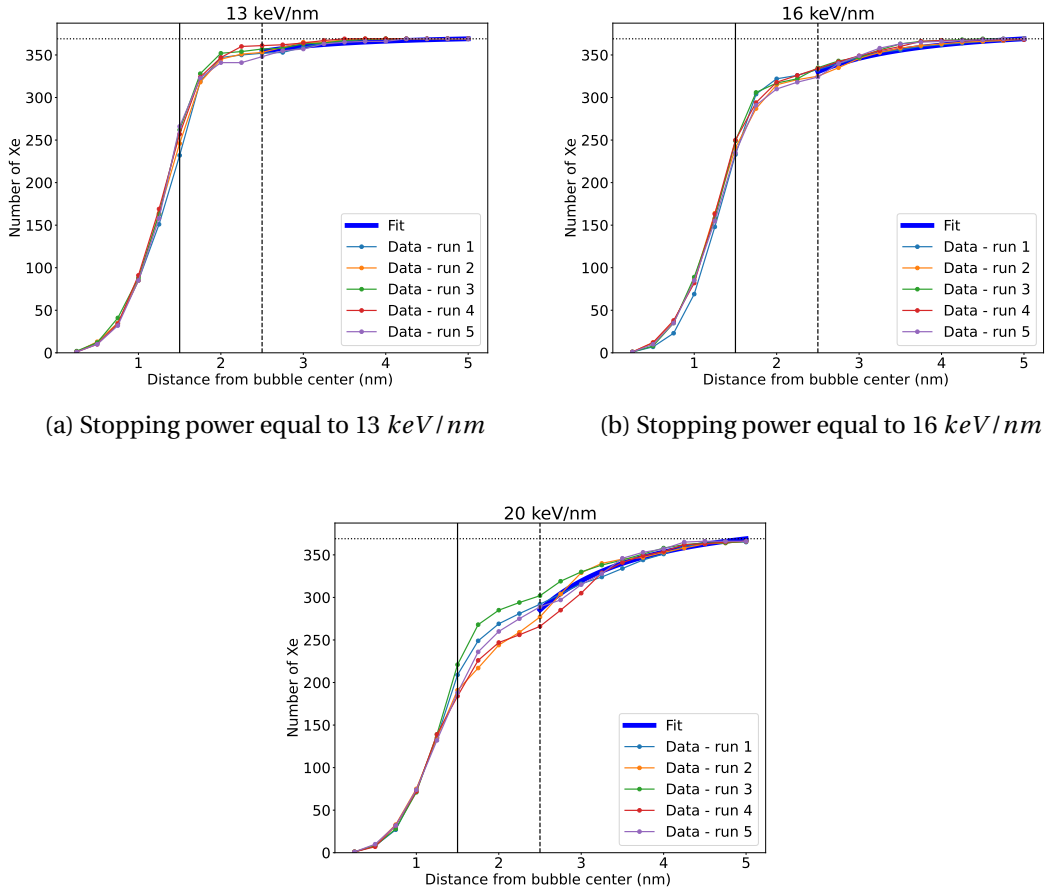

(a) Stopping power equal to 13 keV/nm

(b) Stopping power equal to 16 keV/nm

(c) Stopping power equal to 20 keV/nm

Figure 2.3. – The figure shows the number of atoms that are found below the radius in abscissa just after the interaction with the fission spike, calculated by Molecular Dynamics. The bubble radius is 1.5 nm and different stopping powers are considered. The threshold radius R_T is represented by the dashed line at 2.5 nm. The atoms that are really considered as re-dissolved are those beyond this dashed line. The blue thick lines represent $n_{res}(r) + \overline{n^{MD}_{displ}(R_T)}$, using $Profile(r)$ proportional to $1/r^5$. These figures come from a reanalysis of the work presented in [Setyawan et al. 2018].

Now we construct our reference model. If we follow Setyawan et al. assumption of a potential well for $r < R_T$, we must model the concentration of gas in the $R_b < r < R_T$ zone as permanently equal to 0, because, when a Xe atom enters in this region, it is quickly trapped by the bubble, much faster than how it would do by bulk diffusion. We have then named this zone “No Man’s Land". Since the concentration of gas in the “No Man’s Land" is equal to 0, there is no need to calculate it.
From the hypothesis of 0 concentration in the “No Man’s Land", it follows that the Xenon flux at R_T that arrives from further is directly sent to the bubble, and that the inner limit condition for the domain $R_T \leq r \leq R_{ext}$ is $C_{Xe}(R_T) = 0$. Moreover, the atoms that are produced by fissions in this zone are assumed as directly trapped by the bubble. The limit condition at $r = R_{ext}$ is “flux is equal to zero", for symmetry reasons. An illustration of the problem can be seen in figure 2.4.

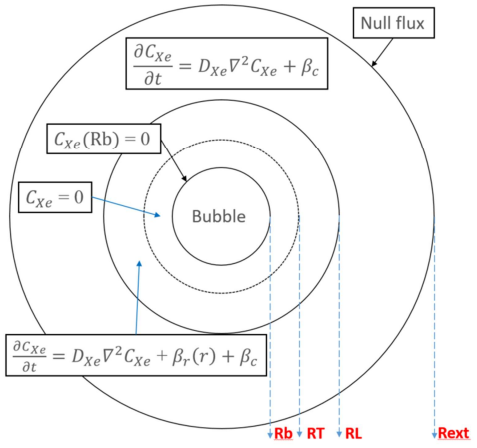

Figure 2.4. – Illustration of the problem.

The problem is expressed mathematically by the system 2.12. In the solid, we take into account the production by fissions β_c, but also the source term due to re-solution $\beta_r(r) = b^{MD} C_{Xeb} \times Profile(r)$, where $Profile(r)$ is the profile derived in section 2.3.1 and b^{MD} is the re-solution frequency obtained by Setyawan et al. [Setyawan et al. 2018]. Appendix F in [Vergani et al. 2025] shows that $\beta_r(r)$ can be locally much larger than β_c.

$$\begin{aligned} \frac{\partial C_{Xe}}{\partial t} &= D_{Xe}\nabla^2 C_{Xe} + \beta_r(r) + \beta_c \quad for\ R_T \leq r \leq R_{ext} \\ \frac{dC_{Xeb}}{dt} &= 4\pi R_T^2 D_{Xe} \frac{\partial C_{Xe}}{\partial r}\Big|_{r=R_T} \times \frac{1}{\frac{4}{3}\pi(R_{ext}^3 - R_b^3)} - b^{MD} C_{Xeb} + \beta_c \times \frac{R_T^3 - R_b^3}{R_{ext}^3 - R_b^3} \end{aligned} \tag{2.12}$$

The term $\beta_c \times \frac{R_T^3 - R_b^3}{R_{ext}^3 - R_b^3}$ represents the amount of Xe atoms produced by fissions in the "No Man's Land", that are directly trapped by the bubble.

To solve numerically this problem, the first space and time equation is discretized on a mesh of N_s concentric shells of equal width, in the domain $R_T \leq r \leq R_{ext}$, using a 1D spherical finite volume method. We thus obtain a new system of ordinary differential equations (time dependant only) of $N_s + 1$ equations and variables. This time only resulting system has the form $\frac{dY}{dt} = F(Y)$, where Y is the vector of the unknown variables. It is solved using the numerical GEAR method [Petzold 1983; Hindermarsh 1983], that has been designed to solve that kind of systems.

In order to choose the number of shells that will give a reliable solution, we considered the simple preliminary problem of production-diffusion of gas in that sphere, with null flux at the external border (for symmetry reason) and null concentration at the vicinity of the central bubble. We solved it with the same method as explained above, using different meshes in the sphere. This problem reaches a steady state in the solid that we can calculate analytically. We calculated the relative error between the numerical and analytical mean concentrations of gas in the solid, at steady state. With 160 shells, the relative error was $1.15\,10^{-3}$, which showed that this mesh could be used with confidence to obtain our reference results.

So, we have solved our reference system 2.12 with 160 shells in the domain $R_T \leq r \leq R_{ext}$ [11], and the number of variables and equations was 161. The computation is quite fast (a few minutes), even with 160 shells.

We have done an additional check to control once more if the number of shells of the reference model was enough to describe accurately the phenomena, by comparing the results given by the reference model using 80 shells and 160 shells, as it is possible to see in figure 2.5. The relative error between the reference model using 80 shells and 160 shells is always below 0.5%. The comparison indicates that dividing the number of shells by two does not vary significantly the output of the model.

2.3.2.2. The PHI-R5-NML simple model for trapping and re-solution

In a gas model intended to be included in a fuel performance code, we clearly cannot calculate the trapping by bubbles adopting a mesh so thin as the 160 shells presented above, even around a "typical intra-granular bubble". The number of variables must be kept to a minimum. Generally, models have only two variables: the average concentration of gas in the solid, C_{XeM}, and the concentration of gas in the bubbles, C_{Xeb}. The usual formulation of the problem of production/trapping/re-solution of gas has been presented in section 2.2.4. This formulation has the quality of being simple, however, it is consistent with a uniform re-solution around the bubble (see Appendix D), which is in contradiction with MD results. Here, we want to take into

11. Note that, when we have to calculate the average concentration in the solid, all the concentration profile in the solid is taken into consideration, even the 0 concentration in the "No Man's Land".

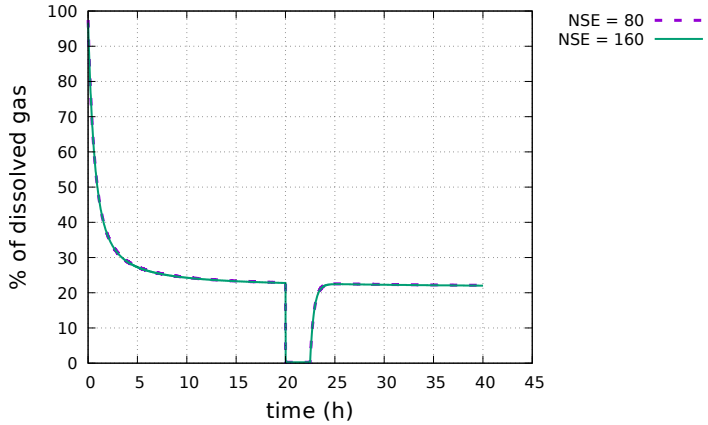

Figure 2.5. – Comparison between the reference model with 160 shells and 80 shells, using Setyawan et al. [Setyawan et al. 2018]. b^{MD} with $\zeta = 0.73$. NSE is the number of shells in the sphere.

account that re-dissolved atoms stopped in the vicinity of the bubble, following the profile determined in section 2.3.1 [12]

To construct this new model, we follow the same idea that led to the proposal of the trapping frequency $4\pi D_{Xe} R_b C_b$ by Ham. But, instead of solving analytically a pure diffusion problem, we solve analytically the steady state problem of re-solution/trapping in the vicinity of a bubble. To find this steady state solution, we consider a null flux at the exterior of the re-solution shell (at $r = R_L$), and we regard β_c as nil everywhere, because it is negligible compared to the re-solution source term β_r (see Appendix F in [Vergani et al. 2025]). Since there is no source term for $r > R_L$, the concentration outside the re-solution shell is constant. If we make the further hypothesis that inside the "No Man's Land" Xe atoms are very quickly trapped by the bubble, we can consider a constant, equal to 0, concentration profile in this layer.

In the re-solution domain ($R_T \leq r \leq R_L$), we solve the diffusion problem $D_{Xe}\nabla^2 C_{Xe} + \beta_r(r) = 0$. Here, $\beta_r(r) = \beta_{r0} \times Profile(r)$, $Profile(r)$ being the normalized profile defined in section 2.3.1.2, which is normalized to one in the $[R_b, R_{ext}]$ domain. The solution for the concentration is:

$$C_{Xe} = 0 \qquad R_b < r < R_T$$

$$C_{Xe} = \frac{\beta_{r0} G}{8\pi D_{Xe}} \left[-\frac{1}{3r^3} + \frac{1}{R_L^2 r} + \frac{1}{3R_T^3} - \frac{1}{R_L^2 R_T} \right] \qquad R_T \leq r \leq R_L$$

$$C_{Xe} = C_{Xe}(R_L) \qquad r > R_L$$

12. This problem has been also addressed by Losonen [Losonen 2017], where the author studied the time evolution of the concentration of re-dispersed gas atoms in the solid between bubbles.

G is the normalization constant defined in section 2.3.1.2 by equation 2.9.
The average concentration, C_{XeM}, can be calculated as :

$$C_{XeM} = \frac{\int_{R_b}^{R_{ext}} C_{Xe}(r) 4\pi r^2 dr}{\frac{4\pi}{3}(R_{ext}^3 - R_b^3)} = \frac{0 + \int_{R_T}^{R_L} C_{Xe}(r) 4\pi r^2 dr + \int_{R_L}^{R_{ext}} C_{Xe}(R_L) 4\pi r^2 dr}{\frac{4\pi}{3}(R_{ext}^3 - R_b^3)} \tag{2.13}$$

The concentration, and therefore also the average concentration are proportional to $\frac{\beta_{r0}}{D_{Xe}}$. We have:

$$C_{XeM} = \frac{\beta_{r0}}{D_{Xe}} \times GEOM1 \tag{2.14}$$

where $GEOM1$ is a purely geometric term with the unit of measure of m^2.

$$GEOM1 = \frac{R_T^2 R_L^2}{R_L^2 - R_T^2} \left[\begin{array}{l} -\frac{1}{3}\ln\left(\frac{R_L}{R_T}\right) + \frac{7}{18} - \frac{1}{3}\frac{R_L}{R_T} + \frac{1}{9}\frac{R_L^3}{R_T^3} - \frac{1}{6}\frac{R_T^2}{R_L^2} \\ + \frac{R_{ext}^3 - R_L^3}{3}\left(\frac{2}{3}\frac{1}{R_L^3} - \frac{1}{R_L^2 R_T} + \frac{1}{3}\frac{1}{R_T^3}\right) \end{array} \right] \tag{2.15}$$

On the other hand, as we are in steady state conditions, the trapping flux of gas in the bubble (in $mol/s/m^3$ of solid) is equal to the mean re-solution source term (in $mol/s/m^3$ of solid) β_{r0}. Replacing β_{r0} with his expression in function of C_{XeM} : $\beta_{r0} = \frac{C_{XeM} D_{Xe}}{GEOM1}$, it is possible to write the trapping flux of gas in the bubble (in $mol/s/m^3$ of solid) as a function of C_{XeM}.

$$Trapping\,flux = GEOM2 \times D_{Xe} C_{XeM} \tag{2.16}$$

where $GEOM2$ is a geometrical term with the unit of measure of m^{-2}.

$$GEOM2 = \frac{1}{GEOM1} \tag{2.17}$$

This lead us to the first 2-scalar model (PHI-R5-NML) [13]:

$$\begin{aligned} \frac{dC_{XeM}}{dt} &= -GEOM2 \times D_{Xe} C_{XeM} + b^{MD} C_{Xeb} + \beta_c \times \frac{R_{ext}^3 - R_T^3}{R_{ext}^3 - R_b^3} \\ \frac{dC_{Xeb}}{dt} &= GEOM2 \times D_{Xe} C_{XeM} - b^{MD} C_{Xeb} + \beta_c \times \frac{R_T^3 - R_b^3}{R_{ext}^3 - R_b^3} \end{aligned} \tag{2.18}$$

The term $\beta_c \frac{R_T^3 - R_b^3}{R_{ext}^3 - R_b^3}$, in the ODE equation for C_{Xeb}, is due to the fact that all the Xe atoms generated in the “No Man’s Land" are quickly trapped by the bubble, as for all

13. The name PHI-R5-NML is a mnemotechnic to remember that the model takes into account a “No Man’s Land" and a re-solution profile in r^{-5}

the other Xe atoms. The term $\beta_c \frac{R_{ext}^3 - R_T^3}{R_{ext}^3 - R_b^3}$, in the ODE equation for C_{XeM}, takes into account only the Xe atoms generated outside the “No Man’s Land". The sum of these two terms gives β_c.

In figure 2.6, we compare the PHI-R5-NML model (system of equations 2.18) and the reference model, using Setyawan’s frequency of re-solution ($b^{MD} = 3.6392 \times 10^{-4}\, s^{-1}$, with $\zeta = 0.73$). We have considered the same numerical values as in the tables 2.1 and 2.2, except for the temperature, for which we have considered an history to better study how the simplified model reproduces in time what it is calculated by the reference model. The history chosen is: $20h$ at 900 °C, $2.5h$ at 1200 °C, then again $17.5h$ at 900 °C. A change in the temperature determines a change in the diffusion coefficient, which results in a different equilibrium value for the percentage of dispersed gas.

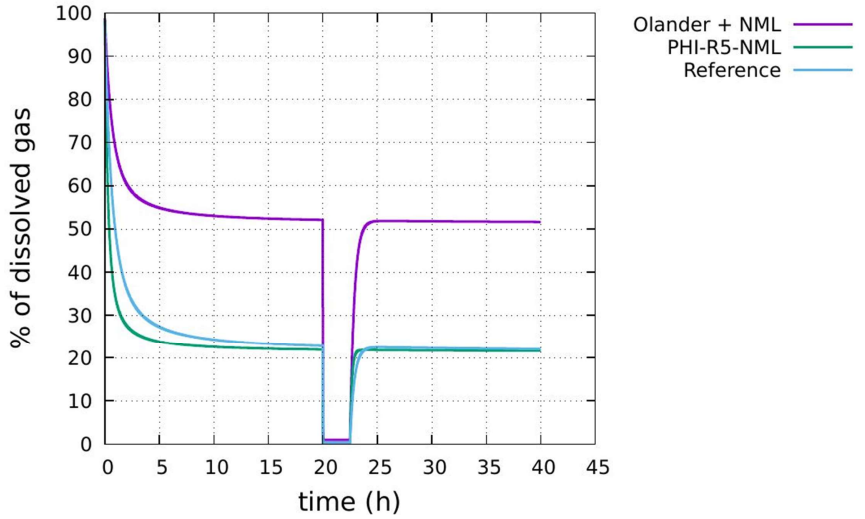

Figure 2.6. – Comparison between the PHI-R5-NML model and the reference model, using Setyawan’s b^{MD} with $\zeta = 0.73$. The history chosen is: $20h$ at 900 ° C, $2.5h$ at 1200° C, then again $17.5h$ at 900° C. We have added the comparison with “Olander+No Man’s Land" model, that would be the same as system 2.18, except that the trapping term would be $4\pi R_T C_b \times D_{Xe} C_{XeM}$ instead of $GEOM2 \times D_{Xe} C_{XeM}$.

This PHI-R5-NML model gave encouraging results when compared to the reference model, particularly on temperature plateaus (see figure 2.6). The most important result, however, is the large difference between the percentage of dissolved gas calculated with the reference model and calculated with the model that would have been written taking into consideration only the fact that there is a “No Man’s Land"

and the value of b^{MD} (model “Olander + No Man’s Land"). On the first and third temperature plateaus, for instance, the percentage of dissolved gas decreases from $50-55\%$ to $20-25\%$ when moving from the “Olander + No Man’s Land" model to the PHI-R5-NML model, which itself is very close to the reference model. Now the percentage of dissolved gas has a very great importance regarding the transport of gas from the grain to the grain boundary, because in base irradiation, only dissolved gas can diffuse. The percentage of dissolved gas is none other than $\frac{D_{Xe}^{eff}}{D_{Xe}}$, where D_{Xe}^{eff} is the effective diffusion coefficient, used in intra-granular models where bubbles are not explicitly represented. The PHI-R5-NML model is therefore already a significant improvement over “Olander + No Man’s Land" model, and allows to take into account the fact that the re-solved Xe atoms are in the vicinity of the bubble and not re-solved uniformly.

2.3.2.3. The PHI-R5-NML-V simple model for trapping and re-solution

The V in the name PHI-R5-NML-V may be for Variant or for Veshchunov because the article [Veshchunov and Tarasov 2013] gave us the idea for this variant. In a situation where we would like to simulate successive periods with and without irradiation, it may be weird to use a trapping term that includes $GEOM2$, that depends on R_T and R_L in the periods where there is no irradiation. We would prefer to use a trapping term similar to Olander’s form in these situations. However, it is crucial to maintain the progress made in predicting the level of dissolved gas percentage.

To construct our new the 2-scalar model, we want to use $GEOM2^{mod_Olander}$ instead of $GEOM2$ [14]. As previously wrote, for steady state situation, the trapping term and the re-solution term are almost equal (the terms in β_c are much lower in absolute value), and we have :

$$GEOM2 \times D_{Xe} C_{XeM} \quad = \quad b^{MD} C_{Xeb} \tag{2.19}$$

Multiplying equation 2.19 on both sides by $\frac{GEOM2^{mod_Olander}}{GEOM2}$, we get :

$$GEOM2^{mod_Olander} D_{Xe} C_{XeM} = b^{MD} \times \frac{GEOM2^{mod_Olander}}{GEOM2} C_{Xeb} = b^{mod} C_{Xeb} \tag{2.20}$$

with

$$b^{mod} = b^{MD} \times \frac{GEOM2^{mod_Olander}}{GEOM2} \tag{2.21}$$

We can then construct a new simplified model, that will behave the same way at equilibrium as the model PHI-R5-NML (eq. 2.18):

14. The $GEOM2^{mod_Olander}$ term is an improvement of the $4\pi R_T C_b$ term in the case where bubbles are close to each other. See Appendix F in [Vergani et al. 2025]

$$\begin{aligned}\frac{dC_{XeM}}{dt} &= -GEOM2^{mod_Olander} \times D_{Xe}C_{XeM} + b^{mod}C_{Xeb} + \beta_c \frac{R_{ext}^3 - R_T^3}{R_{ext}^3 - R_b^3} \\ \frac{dC_{Xeb}}{dt} &= GEOM2^{mod_Olander} \times D_{Xe}C_{XeM} - b^{mod}C_{Xeb} + \beta_c \frac{R_T^3 - R_b^3}{R_{ext}^3 - R_b^3}\end{aligned} \quad (2.22)$$

From figure 2.7, we can see that the 2-scalar PHI-R5-NML-V model approximates very well the reference case, not only on the temperature plateaus but also for the kinetics of variation of the dispersed ratio. It does it even better than the firstly built model (PHI-R5-NML). In the transient phases, the relative error between PHI-R5-NML-V and the reference model is less than 5%. On the plateaus, it is less than 1%.

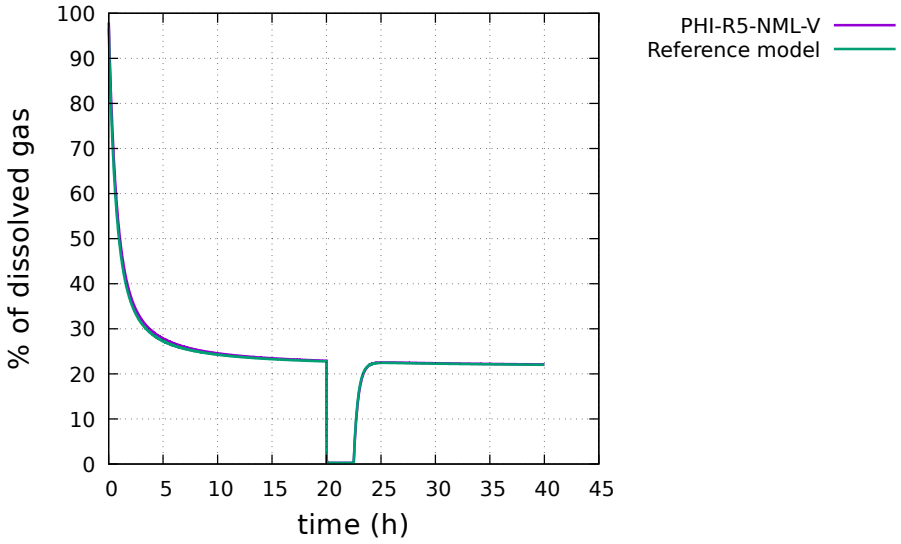

Figure 2.7. – Comparison between the PHI-R5-NML-V model and the reference model, using Setyawan et al. [Setyawan et al. 2018] b^{MD} with $\zeta = 0.73$.

These comparisons validate the whole procedure by which this model was built, and the link with low-scale simulations. So, for an intra-granular model that considers explicitly one population of bubbles, we recommend using the PHI-R5-NML-V model.

2.3.2.4. The PHI-R5-NML-VS simple model for trapping and re-solution

The theoretical assumption of our work is that the bubbles are identical, which allows to define R_{ext} from the bubble concentration C_b and bubble radius R_b. In cluster dynamics models, such as Xolotl, which is used in [Kim et al. 2022] to describe intra-granular phenomena, a whole spectrum of bubbles is modeled, and trapping and re-solution are considered for each class of bubbles. Within the framework of cluster dynamics models, the use of $GEOM2^{mod_Olander}$ instead of $4\pi R_T C_b$ appears

difficult. So, re-starting from the PHI-R5-NML model, we can imagine an intermediate model described by the system 2.23.

$$\begin{aligned}\frac{dC_{XeM}}{dt} &= -4\pi R_T C_b \times D_{Xe} C_{XeM} + b^{mod'} C_{Xeb} + \beta_c \frac{R_{ext}^3 - R_T^3}{R_{ext}^3 - R_b^3} \\ \frac{dC_{Xeb}}{dt} &= 4\pi R_T C_b \times D_{Xe} C_{XeM} - b^{mod'} C_{Xeb} + \beta_c \frac{R_T^3 - R_b^3}{R_{ext}^3 - R_b^3}\end{aligned} \tag{2.23}$$

where

$$b^{mod'} = b^{MD} \times \frac{4\pi R_T C_b}{GEOM2} \tag{2.24}$$

Now we notice that the term $\frac{4\pi R_T C_b}{GEOM2}$ does not vary much with C_b (or R_{ext}). Keeping the same characteristics of the bubble as above, except C_b, and making C_b vary between $1.1\,10^{24}$ and $1.35\,10^{20}$ bubbles/m^3 (or R_{ext} vary from 6 nm to 121 nm) gives a variation of $\frac{4\pi R_T C_b}{GEOM2}$ from 0.255 to 0.265, while the limit of $\frac{4\pi R_T C_b}{GEOM2}$, when $R_{ext} \to +\infty$, is equal to 0.265.
This leads us to the PHI-R5-NML-VS [15] model described by the system 2.25:

$$\begin{aligned}\frac{dC_{XeM}}{dt} &= -4\pi R_T C_b \times D_{Xe} C_{XeM} + b^{mod''} C_{Xeb} + \beta_c \times \left[1 - \frac{4\pi}{3}(R_T^3 - R_b^3) C_b\right] \\ \frac{dC_{Xeb}}{dt} &= 4\pi R_T C_b \times D_{Xe} C_{XeM} - b^{mod''} C_{Xeb} + \beta_c \times \frac{4\pi}{3}(R_T^3 - R_b^3) C_b\end{aligned} \tag{2.25}$$

where

$$b^{mod''} = \left[lim_{R_{ext} \to +\infty} \frac{4\pi R_T C_b}{GEOM2}\right] \times b^{MD} \tag{2.26}$$

In the system 2.25, the last terms have been re-written in function of the characteristics of the bubble population using 2.11, so that it can be easily generalized when modeling multiple classes of bubbles. Using equations 2.11 and 2.17, the expression 2.26 is transformed into :

$$b^{mod''} = \frac{R_T^3 R_L^2}{R_L^2 - R_T^2}\left[\frac{2}{3R_L^3} - \frac{1}{R_L^2 R_T} + \frac{1}{3R_T^3}\right] \times b^{MD} \tag{2.27}$$

In figure 2.8, we see that the PHI-R5-NML-VS is less accurate than PHI-R5-NML-V during the transient (up to about 25% of relative error compared to the reference model during the first transient). However, it is still a significant improvement, compared to the “Olander + NML" model.

We have obtained, with PHI-R5-NML-VS, a model that we recommend within the framework of cluster dynamics, because both trapping and re-solution terms depend only the characteristics of the considered class of bubbles.

15. The S in this name PHI-R5-NML-VS is for Simple, because the trapping term has a simpler form than in PHI-R5-NML-V.

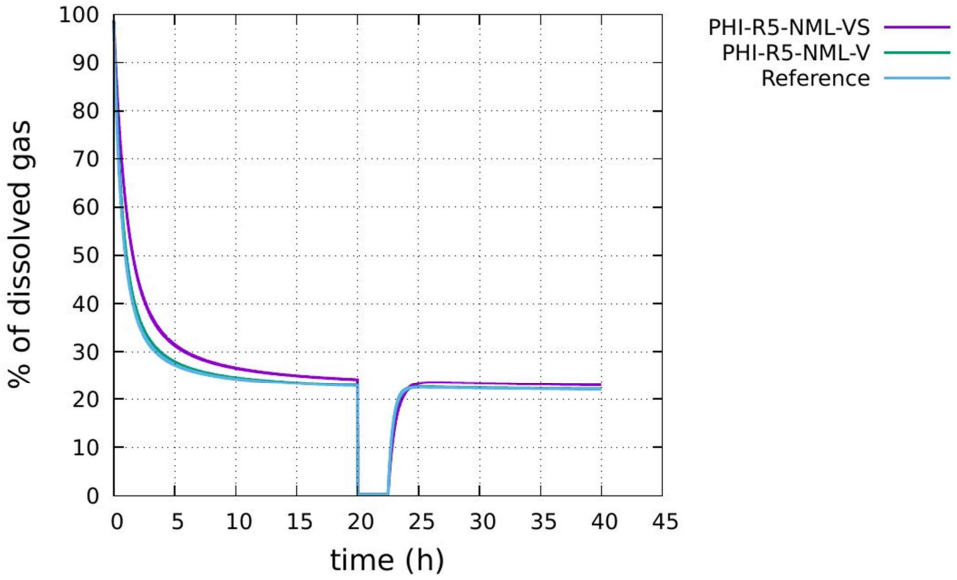

Figure 2.8. – Comparison between the PHI-R5-NML-VS model and the reference model, using Setyawan et al. [Setyawan et al. 2018] b^{MD} with $\zeta = 0.73$.

2.4. Discussion

There are two sources of uncertainty in the approach presented above. The first one is about the parameter ζ and has already been addressed in [Setyawan et al. 2018]. A change of ζ will change b^{MD} (see figure 2.1) and consequently our b^{mod}. The second source of uncertainty comes from the choice of the width of the "No Man's Land": $R_T - R_b$. Following the analysis given by Setyawan et al., in absence of more detailed information regarding the potential energy given by the presence of a bubble, we may change the value of R_T, and consider a different amount of atoms as re-solved, with respect of what Setyawan et al. did. If, for example, we diminish R_T, we would consider more atoms as resolved, and, consequently, we should increase the value of the re-solution frequency we adopt[16].
In [ibid.], Setyawan et al. have taken $R_T - R_b = 1\,nm$, and they have chosen $\zeta = 0.73$, so that b^{MD} be close to Turnbull's results. However, we have seen in section 2.2.5 that $b^{Turnbull}(1200°C)$ should be in reality lower than b^{MD}. So, ζ should be higher, or the width of the "No man's Land", $R_T - R_b$, lower.

2.4.1. Estimation of the re-solution frequency with a variable R_T

If we extend $n_{res}(r)$ in the region $r < R_T$ with the same $Profile(r)$ that we have used for the region between R_T and R_L, we can estimate a new value of the re-solution frequency that considers more atoms as effectively resolved. We call R'_T the new value of the radius below which we consider a null concentration, as previously explained. In other words, we will consider both a smaller "No Man's Land" zone and more atoms as re-dispersed (with respect to the ones considered by Setyawan et al.), increasing in this way the estimated value of b^{MD}.

In figure 2.9, it is showed one of the cumulated displaced gas quantities presented in Section 2.3.1.1 with a new distance of the "No Man's Land" equal to 0.5 nm (value chosen as an example). The comparison between the new resulting $n_{res}(r) + \overline{n^{MD}_{displ}(R_T)}$ and the MD cumulated displaced gas quantities is illustrated in figure 2.9. The comparisons for all the other data is presented in Appendix F in [Vergani et al. 2025]. In general, the comparison is not as good as the one made using a threshold distance of 1 nm, however, it shows that our $Profile(r)$ is still capable of describing in broad terms the evolution of the cumulated displaced gas quantities.

In section 2.3.1.2 we have determined an analytical expression of the re-solution profile between R_T and R_L. In this zone, the source term can be written as: $\beta_r(r) = \frac{G \times b^{MD} C_{Xeb}}{4\pi r^5}$. Let's call this zone $[R_T, R_L]$, zone 2, $G_2 = G$ and $b_2^{MD} = b^{MD}$.

16. And we should also change our GEOM2 and everything that depends on it, but this point is straightforward using the section 2.3.2.2 to 2.3.2.4.

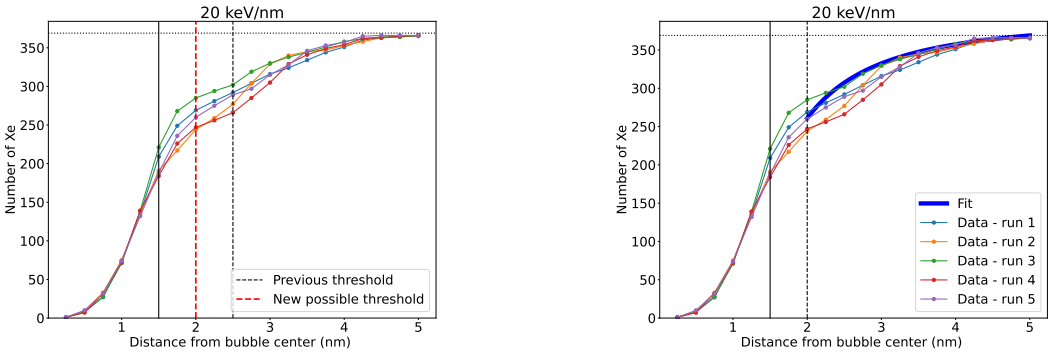

(a) Changing the width of the “No Man’s Land" from 1. nm into 0.5 nm.

(b) Comparison.

Figure 2.9. – Comparison of $n_{res} + \overline{n^{MD}_{displ}(R_T)}$ using $Profile(r)$ proportional to $1/r^5$ and a “No Man’s Land" equal to 0.5 nm. $n_{res} + \overline{n^{MD}_{displ}(R_T)}$ line is in blue. Data from the numerical experiment with a bubble of radius equal to 1.5 nm, using an electronic stopping power of 20 keV/nm.

Now, if we had considered the frequency of re-solution in the zone 1 $[R'_T, R_T]$, and calling the frequency re-solution into this zone b_1^{MD}, the mathematical derivation would have been similar, and we would have obtained a source term for re-solution occurring between R'_T and R_T : $\beta_r(r) = \frac{G_1 \times b_1^{MD} C_{Xeb}}{4\pi r^5}$.

$$G_1 = \frac{2R'^2_T R^2_T}{R^2_T - R'^2_T} \times \frac{4}{3}\pi(R^3_{ext} - R^3_b) \tag{2.28}$$

$$G_2 = \frac{2R^2_T R^2_L}{R^2_L - R^2_T} \times \frac{4}{3}\pi(R^3_{ext} - R^3_b) \tag{2.29}$$

Considering that the re-solution source term must be continuous at R_T, we have :

$$\beta_r(R_T) = \frac{G_2 \times b_2^{MD}}{4\pi R^5_T} C_{Xeb} = \frac{G_1 \times b_1^{MD}}{4\pi R^5_T} C_{Xeb} \tag{2.30}$$

It then follows that:

$$b_1^{MD} = b_2^{MD} \frac{G_2}{G_1} \tag{2.31}$$

The new total re-solution frequency is the sum of b_1^{MD} and b_2^{MD} (the total number of atoms per second which re-solute in $[R'_T, R_L]$ is given by the sum of the number of atoms per second re-dispersed between R'_T and R_T and the number of atoms per second re-dispersed between R_T and R_L):

$$b_{tot}^{MD} = b_1^{MD} + b_2^{MD} \tag{2.32}$$

In conclusion, from Setyawan et al. [Setyawan et al. 2018] re-solution frequency (b_2^{MD}), we can obtain another estimation of the re-solution process (b_{tot}^{MD}), considering a different value of the cut off distance (R_T') and supposing that the trend of the re-solution profile remains the same.

2.4.2. Changes in the 2-scalar model with a variable R_T

In figure 2.10 we can see how the predicted percentage of dispersed gas changes with a change in R_T. A lower R_T, the trapping term decreases and the re-solution term increases. The result is an increase in the percentage of dispersed gas predicted by the model, and therefore a greater tendency for the gas to escape from the grain. R_T turns out to be a very sensitive parameter since the percentage of dispersed gas can change from ≃ 22% to ≃ 62% changing the width of the “No man’s land" from 1 nm to 0.4 nm.

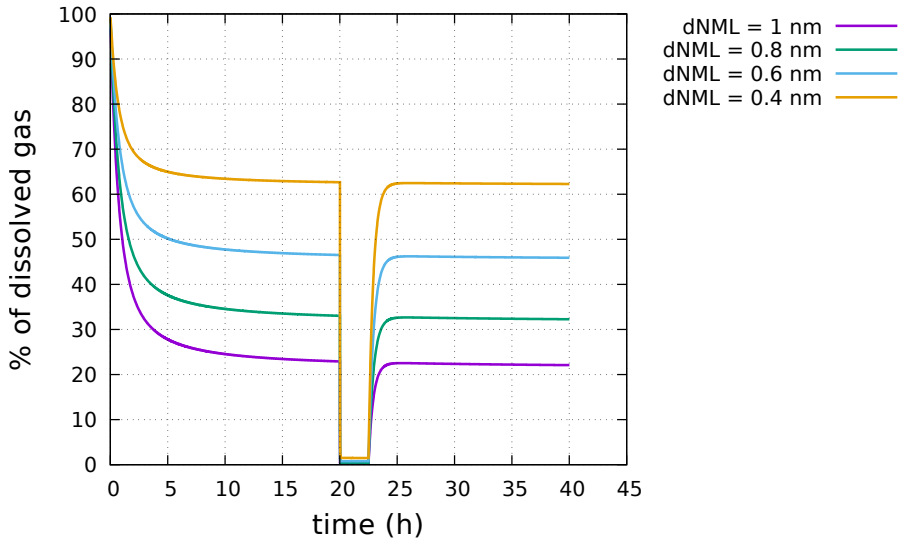

Figure 2.10. – Comparison between the PHI-R5-NML-V models with different values of the “No Man’s Land" width (dNML). When dNML = 1 nm, b^{MD} is the same as the one presented in Setyawan et al. [Setyawan et al. 2018] with $\zeta = 0.73$. The characteristics of the bubbles and the conditions are the same as in section 2.3.2.3.

2.5. Conclusion and perspectives

The definition and usage of the irradiation re-solution frequency of gas from intra-granular bubbles in the UO_2 fuel, b, in literature is blurry. When it is derived from experiments, it is calculated based on the shrinkage of bubbles. When it is used inside usual fission gas behavior models, it is generally the parameter b of the $4\pi R_b C_b D_{Xe}$ (trapping frequency) versus b (re-solution frequency) model. A more direct calculation of the re-solution frequency can be addressed using Molecular Dynamics. Looking naively at the literature, it seems that the values of b calculated in the 3 different ways have to agree between each other. We suggest, instead, that the value of b obtained through MD simulations should be higher than the one obtained through the experiments of Turnbull and the one used inside usual ($4\pi R_T C_b D_{Xe}$ versus b) models. Moreover, we propose to use the value of b obtained through Molecular Dynamics simulations inside fission gas release codes through the mediation of a reduction term, that takes into account that re-solution happens only in the vicinity of the bubbles. This reduction term also depends on the trapping term adopted in the code. We have calculated this reduction term exploiting the cumulated displaced gas quantities obtained through MD simulations, and making use of a trapping term which best considers the distance between bubbles with respect to what is commonly done in the literature. Furthermore, we have checked that this model (named PHI-R5-NML-V) is properly built.

The theoretical assumption of our work is that the bubbles are identical, which allows to define R_{ext} from the bubble concentration C_b and bubble radius R_b. The question then arose: what to do for cluster dynamics ? We proposed a second model (named PHI-R5-NML-VS), slightly degraded compared to PHI-R5-NML-V, but which still allows us to take into account the gas re-solution profile in the vicinity of the bubble, and that could be used within the cluster dynamics framework.

Looking ahead, we encourage further work on this topic at low scale, as many questions remain unanswered, particularly concerning the sensitive parameter of the width of the “No Man’s Land" that could exist for the gas at the immediate vicinity of a bubble. For example, molecular dynamics calculations could be done, placing a defect “xenon atom in a Schottky" closer and closer to a bubble, to find the distance at which xenon can no longer exist in the vicinity of a bubble.

I have implemented the PHI-R5-NML-V model in MARGARET. However, the re-solution frequencies (as a function of the radius of the bubbles) proposed in [Setyawan et al. 2018] were derived by fitting the results of MD calculations using bubbles with a radius between 0.6 and 3 [nm]. Therefore, we cannot use them with confidence for much bigger bubbles. In Appendix E, I propose an expression of the re-solution frequency that can be used for any size of the bubbles : it is based both on Setyawan’s frequencies for small bubbles and on the literature for large bubbles. I have employed this synthetic expression during the exercise of validation of the code, described in Chapter 7.

3. Long-range inter-granular gas diffusion

Sommaire

3.1. Literature review . . . 85
3.1.1. Interconnection of inter-granular bubbles: the main way of Fission Gas Release? . . . 85
3.1.2. Long-range inter-granular gas diffusion . . . 87
3.2. Modelling in MARGARET . . . 88
3.2.1. Macroscopic inter-granular diffusion coefficient to be used in an homogenized approach . . . 88
3.2.2. 2D trapping term for two populations of cavities . . . 90
3.2.3. Trapping term for cavities in the HBS . . . 95
3.2.4. Total re-solution frequency from inter-granular cavities . . . 96
3.2.5. Derivation of the re-solution frequency from inter-granular cavities to the grain boundary . . . 96
3.2.6. Derivation of the re-solution frequency from the grain boundary to the grain . . . 98
3.2.7. Taking into account a possible particular behaviour of re-solution on grain boundaries . . . 99
3.2.8. Derivation of the equilibrium concentration of defects on the grain boundary near an inter-granular cavity: the thermal re-solution phenomenon . . . 101
3.3. Conclusion . . . 113

3.1. Literature review

3.1.1. Interconnection of inter-granular bubbles: the main way of Fission Gas Release?

In Section 1.1, I have presented the current understanding of the relation between inter-granular phenomena and Fission Gas Release: after a phase of building-up of fission gases, the inter-granular bubbles interconnect and gas is released to the free volumes.
During irradiation, temperature and burnup are the main quantities that determine the formation of interconnections: The higher the burnup, the higher the quantity of

gas produced that diffuses toward the inter-granular bubbles, contributing in this way to their swelling. The higher the temperature, the higher both the diffusion coefficient of the fission gas in the lattice and the diffusion coefficient of the vacancies at the grain boundary. The flux of vacancies at the grain boundary to the inter-granular bubbles is the second main contribution to their swelling (see Section 5.1.4.2).
I will then concentrate on these two quantities (temperature and burnup) in the analysis of the experimental data on the in-pile formation of a network of interconnected bubbles and his relation to fission gas release.

Scanning Electron Microscope (SEM) and Transmission Electron Microscope (TEM) images performed on fuels that experienced centerline temperatures higher than about 1100°C confirmed the presence of interconnected cavities in the hotter parts of the fuel [White 2004; R. Cornell et al. 1969]. These type of images are one of the main evidences referred by modelers to justify the choice of considering the percolation of the fission gas through these network of cavities as the main way for the gas to be released from the fuel.

Other interesting experimental evidences of the formation of an interconnected network of inter-granular bubbles during irradiation come from the measurement of the release of short lived isotopes [Kolstad et al. 1992; J. A. Turnbull and Kolstad 2000]. These measurements show an increase in the Surface to Volume ratio of the fuel, which can be associated to bubble inter-linkage, at specific irradiation conditions, namely a temperature of the fuel higher than a certain threshold temperature.
At our knowledge, the published measurements on short lived isotopes indicate the formation of an inter-granular bubble interconnection at temperatures higher than about 1100°C. However, the fuels analyzed had burnups lower than 40 GWd/t_U, so no definitive conclusion can be drawn for fuels at higher burnups.
From these and other measurements, it was also possible to derive an empirical temperature threshold, function of the burnup, for a predicted fission gas release higher than 1% (the Vitanza threshold [Vitanza et al. 1979]). As it is usually accepted [Rest et al. 2019] that a sustained fission gas release is possible only in the presence of a network of interconnected bubbles, this 1% threshold has been linked to the formation of the network. Optical and SEM examinations on parts of fuel pellets that experienced FGR higher than 1% seem to corroborate this link [Forat et al. 1993; R. Manzel 1991]. Most importantly for us, these examinations were performed on fuels which experienced temperatures lower than 1100°C. However, we have to add that, in [Forat et al. 1993], no image that shows the interconnections were published, while in [R. Manzel 1991] the images do show the presence of interconnected bubbles on the grain edges, but, in our opinion, it's difficult to clearly assert the presence of long range bubbles interconnections.

Recently, researchers [J. Noirot, Zacharie-Aubrun, et al. 2018; J. Noirot, Dowek, et al. 2022] have performed FIB-SEM (Focused Ion Beam - Scanning Electron Microscope) 3D examinations on three standard UO_2 PWR fuel samples, with burnup ranging

between 60 and 70 GWd/t$_U$. The maximum temperatures experienced by the fuels never exceeded 1100°C, and stayed for most of the operation below 1000°C.
Some of the inter-granular bubbles examined showed signs of local inter-linkage, but, contrary to the expectations, the researchers found **no evidence** of the presence of an extended inter-granualar interconnection. At the same time, they measured a not negligible fission gas release, as high as 6% for the highest burnup fuel analyzed.
A simple explanation may arise starting from those measurements: since the formation of an inter-granular network may be reversible [Rest et al. 2019], the network may have formed at some point during irradiation, but collapsed before the end of operation. However, for similar operated fuels, it has been showed that the fission gas release fraction increases with burnup. Therefore, we cannot expect to have more interconnection at the middle of irradiation with respect to the end [J. Noirot, Dowek, et al. 2022].
Nevertheless, caution must be taken regarding the inter-granular grain edge bubbles. Long grain edge bubbles have been measured, but, as for all the other inter-granular bubbles, no signs of a long range network could be seen. However, authors report the need to analyse larger 3D volumes to clearly establish the absence of such network. Therefore, at this day, interconnections on grain edges cannot be totally excluded.

Given the absence of any definitive answer on the formation of an interconnected inter-granular network even in the presence of not negligible fission gas release, we took the opportunity to add in MARGARET one more possible way for the gas to be released: the long-range inter-granular gas diffusion.

3.1.2. Long-range inter-granular gas diffusion

There is one experimental result that shows how Xenon can be released by grain boundary diffusion. Researchers [D. R. Olander et al. 2001] have studied Xenon release from trace-irradiated UO_2 bi-crystals, at conditions where almost no inter-granular bubbles is expected to be present. They concluded that the diffusion coefficient of Xenon on the grain boundary is higher than the diffusion coefficient in the grain and that lattice diffusion alone is not enough to describe the Xenon release. Moreover, the authors gave two possible expressions of the diffusion coefficient on the grain boundaries, detailed in Section 7.1.2.
In the same paper, the authors calculated the average migration distance of the Xenon atoms in the grain boundaries in the presence of an amount of traps compatible with number densities and fractional coverage of inter-granular bubbles typical of a LWR fuel operated in base irradiation with a burnup of about 20 GWd/t$_U$. They estimated this average migration distance to be in the order of the size of the grains or less, and therefore excluded the long-grange inter-granular diffusion to be a major mechanism of fission gas release during in-reactor conditions.

In fact, even if the diffusion of Xenon is accelerated on the grain boundaries, as it appears from the analysis of the trace-irradiated specimens, during irradiation the

trapping of the diffusive Xenon by the inter-granular bubbles may impede the long-range inter-granular diffusion. On the other hand, the mechanisms of dynamic (due to the interaction bubble-fission spikes) and thermal re-solution from the inter-granular bubbles into the grain boundaries may balance the trapping. These two phenomena were not considered in [D. R. Olander et al. 2001].

In the next chapters, we will try to quantify the dynamic and thermal re-solution from the inter-granular cavities into the grain boundary (Sections 3.2.4, 3.2.5, 3.2.8), as well as the trapping frequency of the dissolved Xenon atoms by the inter-granular cavities (Section 3.2.2). Besides, to complete the description of the inter-granular phenomena, we need to estimate both the re-solution frequency from the grain boundary into the grain (Section 3.2.6) and the value of the diffusion coefficient to be use for the long-range inter-granular diffusion (Section 3.2.1). The special case of the trapping of gas on the grain boundaries of the restructured grains (HBS) by the HBS bubbles and pores is presented in Section 3.2.3.

3.2. Modelling in MARGARET

3.2.1. Macroscopic inter-granular diffusion coefficient to be used in an homogenized approach

The diffusion equation that describes the diffusion of gas on the grain boundary towards the free surfaces is modelled considering the diffusion in an equivalent homogeneous sphere. To do that, we need to link D_{Xej}^{loc}, the actual diffusion coefficient of Xenon on the grain boundary, to D_{Xej}^{MAC}, which is the macroscopic diffusion coefficient of Xenon in the homogeneous medium. The latter is the quantity that we need to describe diffusion in the equivalent homogeneous sphere.

An scheme of the problem is presented in figure 3.1.

If we define:
— V as the volume of the RVE (Representative Volume Element).
— S as the surface at the top of the RVE.
— S_j^{loc} as the surface of the grain boundary intercepted by the surface at the top of the RVE.
— V_j^{loc} as the volume of grain boundary contained in the RVE.
— C_{Xej}^{loc} as the local concentration of Xenon in the grain boundary.
— C_{Xej} as the macroscopic concentration of the inter-granular Xenon [mol/m^3 of RVE].
— h the size of the grains.

We have $S_j^{loc} \simeq 2e_{pj}h$, $S = h^2$, $V_j^{loc} \simeq 3e_{pj}h^2$, $V = h^3$, and $C_{Xej} = C_{Xej}^{loc}\frac{V_j^{loc}}{V} = C_{Xej}^{loc}\frac{3e_{pj}}{h}$.

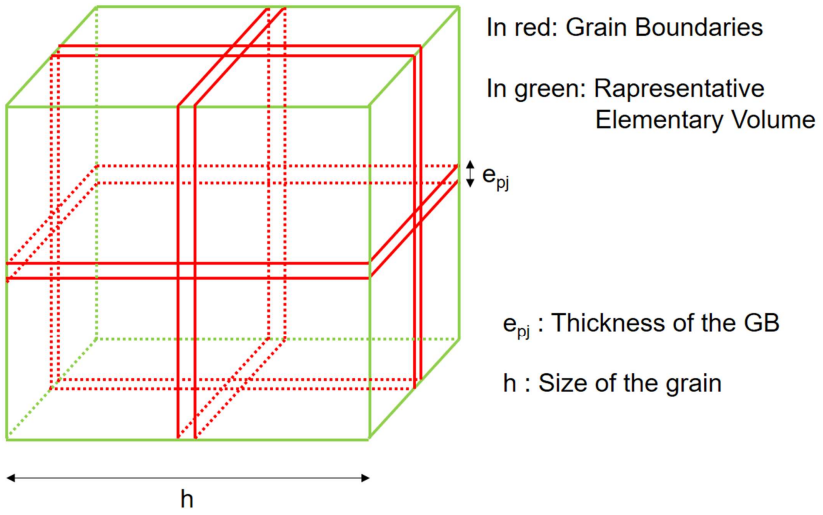

Figure 3.1. – Representative Volume Element (RVE) used to derive the macroscopic diffusion coefficient of Xenon on the grain boundary, D_{Xej}^{MAC}, from the actual diffusion coefficient of Xenon on the grain boundary, D_{Xej}^{loc}.

The last equality is due to the fact that, passing from the local (the GB) to the macroscopic (the RVE) volume, the amount of atoms do not change. Therefore, we have: $C_{Xej} \times V = C_{Xej}^{loc} \times V_j^{loc}$.
The flux of gas, Φ, in $[mol/s]$ through the surface S is equal to:

$$\begin{aligned}
\Phi &= -S_j^{loc} \times D_{Xej}^{loc} \times \vec{\nabla} C_{Xej}^{loc} \\
&= -2e_{pj}h \times D_{Xej}^{loc} \times \vec{\nabla} C_{Xej} \times \frac{h}{3e_{pj}} \\
&= -S \times \frac{2}{3} D_{Xej}^{loc} \times \vec{\nabla} C_{Xej} \\
&= -S \times D_{Xej}^{MAC} \times \vec{\nabla} C_{Xej}
\end{aligned} \tag{3.1}$$

Therefore, we can see how the macroscopic diffusion coefficient to be used in the homogeneous medium is very close ($D_{Xej}^{MAC} = \frac{2}{3} D_{Xej}^{loc}$) to the actual diffusion coefficient on the grain boundary. Given the uncertainties on the value of D_{Xej}^{loc}, we can consider $D_{Xej}^{MAC} \approx D_{Xej}^{loc}$, and just use only one symbol, D_{Xej}, for both quantities.

3.2.2. 2D trapping term for two populations of cavities

In literature we can find different expressions of the trapping term in 2D. A review of some of those can be found in [Uffelen 2000]. Alternative expressions, not cited in [ibid.], can be found in [Giorgi et al. 2022] (used for the trapping of Helium) and in chapter 3 of [D. R. Olander et al. 2001].

Before presenting the trapping term used in MARGARET, I need to add a small premise.
In the description adopted in MARGARET, the surface of the grains is split into different fractions, which are those:

- directly facing another grain (F_j);
- facing the inter-granular bubbles (F_{bj});
- facing the inter-granular pores (F_{porj});
- facing the free surface (F_{ext});
- involved in the restructured part of the fuel (fr[1]. This fraction is present only if part of the grain is restructured (HBS)).

The fractions are expressed as the corresponding part of the surface of the grain over the total surface of the grain[2].
The gas present in the bare grain boundary is considered as dissolved. The sum of the surface of the grain facing another grain and the surface of the grain facing the two population of cavities ($F_j + F_{bj} + F_{porj}$) make up the surface of the grain boundary.
In figure 3.2 it is showed the schematic representation used in MARGARET.

For the derivation of the 2D trapping term used in MARGARET, it is useful to define some more quantities first.
We call $S^{vol}_{j,tot}$ the surface of the grain boundary (which is the surface of the grain covered by cavities or by bare grain boundary) over the volume of the grain:

$$S^{vol}_{j,tot} = \frac{3(1 - fr - F_{ext})}{2A_{gg}} \tag{3.2}$$

Where A_{gg} is the radius of the grain.
We call F'_{cavj} the fraction of the grain boundary surface occupied by the cavj (bj or porj) population of inter-granular cavities:

$$F'_{cavj} = \frac{F_{cavj}}{1 - fr - F_{ext}} \tag{3.3}$$

From equations 3.2 and 3.3 we can write:

1. fr is also equal to the fraction of the volume of the grain which is restructured (HBS). In MARGARET we make the hypothesis that the surface fraction and the volume fraction are equal.
2. As an example, F_j is the surface of the grain facing another grain over the total surface of the grain

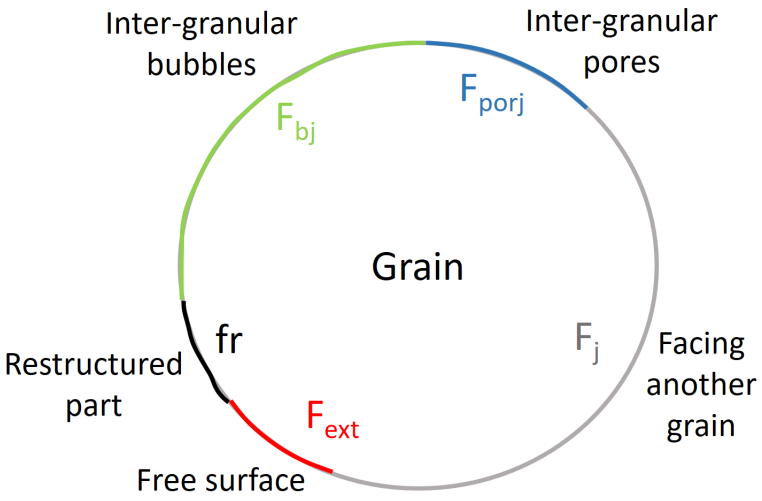

Figure 3.2. – Schematic representation of the different fractions (each one facing a different object: inter-granular bubbles, inter-granular pores etc.) in which the surface of the grain is divided.

$$S^{vol}_{j,tot} \times (1 - F'_{cavj}) = \frac{3(1 - fr - F_{ext} - F_{cavj})}{2A_{gg}} \tag{3.4}$$

Similarly to F'_{cavj}, we call F'_j the fraction of the grain boundary surface occupied by bare grain boundary:

$$F'_j = \frac{F_j}{1 - fr - F_{ext}} \tag{3.5}$$

Given the definitions above, we can also write that:

$$C_{Xej} = \underbrace{e_{pj} \times S^{vol}_{j,tot} \times F'_j}_{\text{Volume of bare grain boundary / m}^3 \text{ of fresh fuel}} \times C^{loc}_{Xej} \tag{3.6}$$

Where C_{Xej} is the "global" concentration of Xenon, expressed in [mol / m^3 of fresh fuel], C^{loc}_{Xej} is the "local" concentration of Xenon, expressed in [mol / m^3 of bare grain boundary], and e_{pj} is the width of the grain boundary.

To make the presentation clearer, we can start by considering only one population of inter-granular cavities and no thermal re-solution phenomenon.

To derive the trapping term in this special case, we solve the diffusion equation in the solid surrounding each cavity (considered as having a circular shape) with a constant production rate (gas diffusing to the grain boundaries from the grains) and with boundary conditions: 0 concentration at the surface of the bubble and null flux

at $R_{ext,cavj}$. A schematic representation of the problem can be seen in figure 3.3.

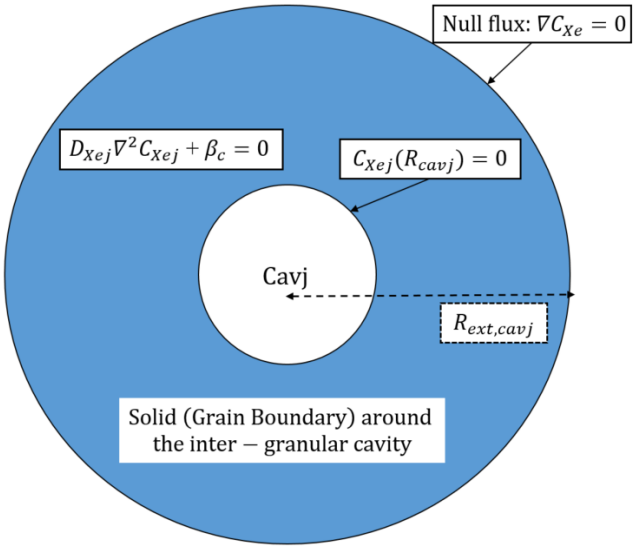

Figure 3.3. – Schematic representation of the 2D diffusion problem with only one population of inter-granular cavities and no thermal re-solution phenomenon.

$R_{ext,cavj}$ can be calculated stating that:

$$C_{cavj} \times \pi \, R^2_{ext,cavj} = S^{vol}_{j,tot} \tag{3.7}$$

The trapping term can be expressed by equation 3.8[3].

3. The derivation of equation 3.8 is as follows: After finding the concentration profile (as a function of the distance from the surface of the bubble), which is the solution to the diffusion equation, we can calculate the average concentration in the solid. Then, we can express the flux of gas [mol/s] from the solid to the bubble as a function of the average concentration of gas in the solid. Finally, we multiply by C_{cavj} to obtain the flux over all the cavities in [mol/s/m^3 of fresh fuel].

$$
\begin{aligned}
Trapping\ term\left[\frac{mol}{s\times m^3\ of\ fresh\ fuel}\right] &= \\
&= \frac{8\pi D_{Xej}\left(1-F'_{cavj}\right)^2}{\left(1-F'_{cavj}\right)\left(F'_{cavj}-3\right)-2ln\left(F'_{cavj}\right)} \times C^{surf}_{Xej,(cavj)} \times C_{cavj} \\
&= \frac{8\pi D_{Xej}\left(1-F'_{cavj}\right)^2}{\left(1-F'_{cavj}\right)\left(F'_{cavj}-3\right)-2ln\left(F'_{cavj}\right)} \times \frac{C_{Xej}}{S^{vol}_{j,tot}\left(1-F'_{cavj}\right)} \times C_{cavj} \\
&= \frac{8\pi D_{Xej}\left(1-F'_{cavj}\right)}{\left(1-F'_{cavj}\right)\left(F'_{cavj}-3\right)-2ln\left(F'_{cavj}\right)} \times \frac{C_{Xej}}{S^{vol}_{j,tot}} \times C_{cavj}
\end{aligned}
\tag{3.8}
$$

Where $C^{surf}_{Xej,(cavj)}$ is the Xenon surface concentration on the grain boundary in [mol/m^2 of grain boundary not covered by the cavj population]:

$$
C^{surf}_{Xej,(cavj)} = \frac{C_{Xej}}{S^{vol}_{j,tot}(1-F'_{cavj})} \tag{3.9}
$$

In this special case, $C^{surf}_{Xej,(cavj)} = C_{Xej} \times \frac{2A_{gg}}{3F_j}$, where $C_{Xej} \times \frac{2A_{gg}}{3F_j}$ is the average concentration of Xenon on the bare grain boundary in [mol / m^2 of bare grain boundary].

The expressions 3.8 reduce to the expression described in [Uffelen 2000] (the cell model with source term and considering a perfect trapping) and used in [J. R. Matthews et al. 1980] if we do not consider the free surface nor the HBS.

Since in MARGARET we consider 2 populations of cavities on the grain boundaries (bj and porj), we need to extend the scope of equation 3.8. We are currently not aware of a trivial way to do it.
The need to consider two populations comes from the fact that they are very different: pores are large (a few micrometer) and scarce ($\approx 10^{13}$ pores / m^3), while inter-granular bubbles are smaller and more numerous ($\approx 10^{18}$ bubbles / m^3). It is a reasonable approximation to keep equation 3.8 for the bj, as if the pores did not exist. For the pores, we could solve the diffusion equation around them by considering the grain boundary (covered with bubbles) as an homogeneous medium. In this case, the concentration of dissolved gas to be used is defined by $C^{surf}_{Xej,(porj)}$, which now is defined as:

$$
C^{surf}_{Xej,(porj)} = \frac{\text{gas situated on the bare grain boundaries}}{\text{surface of bare GB + surface covered by the inter-granular bubbles}}
$$

Expression 3.9 remains valid. However, $C^{surf}_{Xej,(cavj)} \neq C_{Xej} \times \frac{2A_{gg}}{3F_j}$.

In conclusion, equation 3.8 can be used for both populations, bubbles and pores.

Now, if we want to consider the phenomenon of thermal re-solution from the inter-granular cavities, we need to solve a diffusion equation similar to the one used to obtain the expressions 3.8, but with a different boundary condition at the surface of the cavity: this time we consider a concentration equal to the equilibrium concentration near the inter-granular cavity, $C^{eq}_{Xej}(cavj)$ (see Section 3.2.8 for the derivation this equilibrium concentration).

The resulting 2D trapping term is the following:

$$
\begin{aligned}
Trapping\ term\left[\frac{mol}{s\times m^3\ of\ fresh\ fuel}\right] = \\
&= \frac{8\pi D_{Xej}\left(1-F'_{cavj}\right)^2}{\left(1-F'_{cavj}\right)\left(F'_{cavj}-3\right)-2ln\left(F'_{cavj}\right)} \times \left(C^{surf}_{Xej,(cavj)} - C^{eq,surf}_{Xej,(cavj)}(cavj)\right) \times C_{cavj} \\
&= \frac{8\pi D_{Xej}\left(1-F'_{cavj}\right)^2}{\left(1-F'_{cavj}\right)\left(F'_{cavj}-3\right)-2ln\left(F'_{cavj}\right)} \times \frac{e_{pj}F'_j}{1-F'_{cavj}} \times \left(C^{loc}_{Xej} - C^{eq}_{Xej}(cavj)\right) \times C_{cavj} \\
&= \frac{8\pi D_{Xej}\left(1-F'_{cavj}\right)}{\left(1-F'_{cavj}\right)\left(F'_{cavj}-3\right)-2ln\left(F'_{cavj}\right)} \times \frac{\left(C_{Xej} - e_{pj}S^{vol}_{j,tot}F'_j C^{eq}_{Xej}(cavj)\right)}{S^{vol}_{j,tot}} \times C_{cavj}
\end{aligned}
\tag{3.10}
$$

Where $C^{eq,surf}_{Xej,(cavj)}(cavj)$ (which is a "diluted" concentration in the same way $C^{surf}_{Xej,(cavj)}$ is) is the equilibrium concentration near an inter-granular cavity in [mol / m^2 of grain boundary not covered by the cavj population]. We can write:

$$
C^{eq,surf}_{Xej,(cavj)}(cavj) = C^{eq}_{Xej}(cavj) \times \underbrace{\frac{F'_j}{1-F'_{cavj}}}_{\text{m}^2\text{ of bare GB / m}^2\text{ of GB not covered by the cavj population}}
\tag{3.11}
$$

We can then define the quantity $geom_{cavj}$ [m^{-2}] as:

$$
geom_{cavj} = \frac{8\pi\left(1-F'_{cavj}\right)}{\left(1-F'_{cavj}\right)\left(F'_{cavj}-3\right)-2ln\left(F'_{cavj}\right)} \frac{C_{cavj}}{S^{vol}_{j,tot}}
\tag{3.12}
$$

Using $geom_{cavj}$, the trapping term of the populations of inter-granular cavities becomes:

$$
\begin{aligned}
Trapping\ term\left[\frac{mol}{s\times m^3\ of\ fresh\ fuel}\right] &= \\
&= geom_{cavj}\times D_{Xej}\times F'_j S^{vol}_{j,tot} e_{pj}\times\left(C^{loc}_{Xej}-C^{eq}_{Xej}(cavj)\right) \\
&= geom_{cavj}\times D_{Xej}\times\left(C_{Xej}-e_{pj}S^{vol}_{j,tot}F'_j C^{eq}_{Xej}(cavj)\right)
\end{aligned}
\tag{3.13}
$$

The expressions 3.13 have been implemented in MARGARET to calculate the trapping term of the two populations of inter-granular cavities (bj and porj).

3.2.3. Trapping term for cavities in the HBS

In the HBS, the bubbles visible by optical microscopy and SEM are bigger and sparser than the bubbles present in the "sound" (not restructured) zones of the pellet. They are all inter-granular and no intra-granular bubble has been measured in the restructured grains. These bubbles are the ones modelled by MARGARET.
Given the concentration of these bubbles, and due to the fact that the restructured grains are smaller than the original grains, most restructured grains do not face any of these bubbles.
All things considered, we decided not to use a 2D trapping term for bubbles and pores in the HBS. Instead, only for the purpose of calculating a trapping term, we consider the restructured grains and their grain boundaries as an homogeneous medium.
If bubbles and pores are placed in an homogeneous medium, the trapping term that we need is the "Olander" trapping term referred to in Chapter 2 and adapted to the context:

$$
\frac{dC^{HBS}_{Xejrim}}{dt} = 4\pi D^{MAC}_{Xejrim} R_{cavrim} C^{HBS}_{cavrim} C^{HBS}_{Xejrim}
$$

Where C^{HBS}_{Xejrim} and C^{HBS}_{cavrim} are concentrations per m^3 of not-swelled, restructured fuel, D^{MAC}_{Xejrim} is the macroscopic diffusion coefficient of Xenon in the homogeneous medium. From Section 3.2.1 we have seen than we can use the diffusion coefficient on the grain boundary, D^{loc}_{Xejrim}, without modifications: $D^{MAC}_{Xejrim} \approx D^{loc}_{Xejrim}$. If we now make the further hypothesis that Xenon diffuses in a similar manner on the grain boundaries of the "sound" grains and on the grain boundaries of the HBS grains, we obtain: $D^{loc}_{Xejrim} = D^{loc}_{Xej}$.
In the code, there is also the possibility to consider the thermal re-solution in the trapping term of the HBS cavities, which becomes:

$$
\frac{dC^{HBS}_{Xejrim}}{dt} = 4\pi D_{Xej} R_{cavrim} C^{HBS}_{cavrim}\left(C^{HBS}_{Xejrim} - e_{pj}\frac{3}{2A_{pg}}F_{jrim}C^{eq}_{Xejrim}(cavrim)\right)
\tag{3.14}
$$

Where A_{pg} is the radius of the HBS grain and F_{jrim} is the fraction of the surface of

the HBS grain facing another HBS grain.
Now, if we use the concentration per m^3 of total fresh fuel, we finally obtain the term included in the ODE system:

$$\frac{dC_{Xejrim}}{dt} = 4\pi D_{Xej} R_{cavrim} \frac{C_{cavrim}}{fr} \left(C_{Xejrim} - e_{pj} S^{vol}_{jrim,tot} F_{jrim} C^{eq}_{Xejrim}(cavjrim) \right) \tag{3.15}$$

Where $S^{vol}_{jrim,tot} = \frac{3fr}{2A_{pg}}$ is the surface of total HBS grain boundary over m^3 of fresh fuel. $S^{vol}_{jrim,tot} \times F_{jrim}$ is the fraction of bare grain boundary over m^3 of fresh fuel.

$S^{vol}_{jrim,tot}$ can be found stating that:

$$S^{vol}_{jrim,tot} = \underbrace{\frac{1}{\frac{4}{3}\pi A^3_{pg}}}_{\text{Volume of an HBS grain}} \times \underbrace{4\pi A^2_{pg}}_{\text{Surface of an HBS grain}} \times \underbrace{\frac{1}{2}}_{\text{to have the surface of GB}} \times \underbrace{fr}_{\frac{\text{Volume of restructured fuel}}{\mathrm{m}^3 \text{ of fresh fuel}}} \tag{3.16}$$

3.2.4. Total re-solution frequency from inter-granular cavities

Before calculating the re-solution frequency from inter-granular cavities to the grain boundary, we need to estimate the total re-solution frequency from inter-granular cavities. This quantity can be estimated starting from the expression of the re-solution frequency as a function of the radius of the cavities presented in Appendix E, using as a radius the equivalent radius of the inter-granular cavities, $R^{eq}_{cavj} = \left(\frac{V_{cavj}}{\frac{4}{3}\pi C_{cavj}} \right)^{1/3}$. We call this total frequency $b^{MD_Veshchunov}(cavj)$ (see figure E.1).

The gas in the inter-granular cavities is assumed to be re-dissolved both towards the grain boundary and back to the grain. The total re-solution rate can be divided between the re-solution towards the grain boundary and towards the grain: $b^{MD_Veshchunov}(cavj) = b_j(cavj) + b(cavj)$.

In the rest of the manuscript, we adopt the following nomenclature: $b_x(y)$ stands for the re-solution frequency used in the equations of the ODE system, with x = arrival location, and y = departure location. Moreover, when x = grain or bulk, x is omitted.

3.2.5. Derivation of the re-solution frequency from inter-granular cavities to the grain boundary

Knowing the value of $b^{MD_Veshchunov}(cavj)$, we can derive the value of $b_j(cavj)$, the re-solution frequency from inter-granular cavities to the grain boundary, by mak-

ing some geometric considerations.
If we manage to calculate the fraction of the gas re-dissolved towards the grain boundary, we can evaluate $b_j(cavj)$.

As a first approximation, if the presence of the grain boundary do not influence "too much" re-solution events, we can make the hypothesis that atoms are homogeneously re-dissolved in the re-solution volume. Therefore, the fraction of atoms re-dissolved from inter-granular cavities that go directly to the grain boundary can be estimated as equal to:

$$\frac{V_j \cap V_{res_cavj}}{V_{res_cavj}} \tag{3.17}$$

Where V_j is the volume of the grain boundary (with width e_{pj}) and V_{res_cavj} is the re-solution volume.
If δ is the re-solution depth and R_{cavj} the radius of the intersection of the bubble with the grain boundary, we can calculate $V_j \cap V_{res_cavj}$ as:

$$V_j \cap V_{res_cavj} \approx e_{pj}\,\pi \left[(R_{cavj}+\delta)^2 - R_{cavj}^2 \right] \tag{3.18}$$

The re-solution frequency from an inter-granular bubble to the grain boundary, $b_j(cavj)$, can finally be calculated as:

$$b_j(cavj) = b^{MD_Veshchunov}(cavj) \times \frac{V_j \cap V_{res_cavj}}{V_{res_cavj}} \tag{3.19}$$

$$\approx b^{MD_Veshchunov}(cavj) \times \frac{e_{pj}\,\pi \left[(R_{cavj}+\delta)^2 - R_{cavj}^2 \right]}{\frac{4}{3}\pi \left[(R_{cavj}+\delta)^3 - R_{cavj}^3 \right] A_\theta} \tag{3.20}$$

Where A_θ takes into account that the bubble is lenticular: $A_\theta = \frac{1-\frac{3}{2}cos\theta+\frac{1}{2}cos^3\theta}{sin^3\theta}$, where θ is the angle between the bubble surface and the grain boundary. $\theta = 50°$, $A_\theta = 0.375$.

Figure 3.4 shows the values of $\frac{V_j \cap V_{res_cavj}}{V_{res_cavj}}$ for different equivalent radius of the inter-granular cavities, using $\delta = 2$ nm and $\theta = 50°$.

Then, we can evaluate $b(cavj)$ as:

$$b(cavj) = b^{MD_Veshchunov}(cavj) - b_j(cavj) \tag{3.21}$$

A similar reasoning can be applied to precipitation bubbles (described in Chapter 4) by considering the subdomain boundary as an uniform slab of thickness e_{pj}.

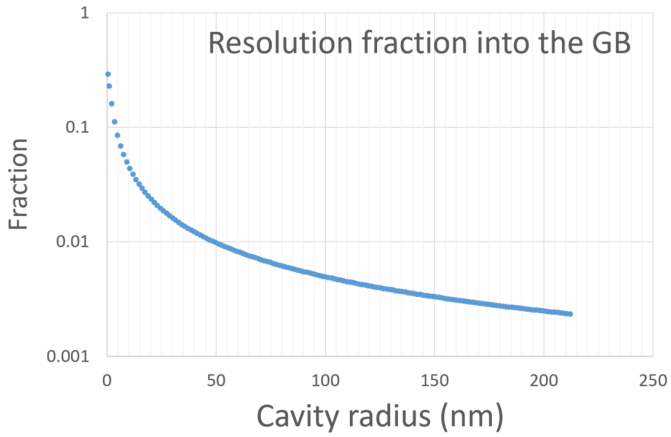

Figure 3.4. – Values of $\frac{V_j \cap V_{res_cavj}}{V_{res_cavj}}$ for different equivalent radius of the inter-granular cavities, using $\delta = 2$ nm and $\theta = 50°$.

3.2.6. Derivation of the re-solution frequency from the grain boundary to the grain

The re-solution frequency of gas dissolved in the grain boundary towards the grain, $b(j)$, can be estimated following a similar procedure as in Section 3.2.5 for $b(cavj)$, while considering the dispersed gas atoms on GB as bubbles containing only one atom and with volume equal to Ω:

$$b(j) = b^{MD_Veshchunov}(\text{bubble of volume } \Omega) \times \left(1 - \frac{V_j \cap V_{res_\Omega}}{V_{res_\Omega}}\right) \tag{3.22}$$

Table 3.1 shows the values that can assume the expression $\frac{b^{MD_Veshchunov}(\text{bubble of volume } \Omega)}{\dot{F}}$ with a change in the parameters: dNML (the width of the "No Man's Land") and ζ (the ratio between the thermal spike energy and the total electronic stopping power) (see Chapter 2 for the meaning of these two parameters).
With $\delta = 2$ nm, $e_{pj} = 1$ nm, $R_\Omega = \left(\frac{3}{4\pi}\Omega\right)^{1/3} = 0.2137$ nm, we can calculate: $\left(1 - \frac{V_j \cap V_{res_\Omega}}{V_{res_\Omega}}\right) = 0.105$.

dNML [nm] \ ζ	0.73	0.8	0.85	0.9
1	6.93×10^{-23}	8.34×10^{-23}	9.11×10^{-23}	9.77×10^{-23}
0.8	1.03×10^{-22}	1.24×10^{-22}	1.35×10^{-22}	1.45×10^{-22}
0.6	1.65×10^{-22}	1.98×10^{-22}	2.16×10^{-22}	2.32×10^{-22}
0.4	2.96×10^{-22}	3.55×10^{-22}	3.88×10^{-22}	4.16×10^{-22}

Table 3.1. – Values of $\frac{b^{MD_Veshchunov}(\text{bubble of volume } \Omega)}{\dot{F}}$ for the different values of dNML and ζ.

3.2.7. Taking into account a possible particular behaviour of re-solution on grain boundaries

We have introduced several adjustment parameters as multiplying factors of the expressions of the re-solution frequency presented above.
These coefficients affect the different re-solution frequencies as presented in figure 3.5.

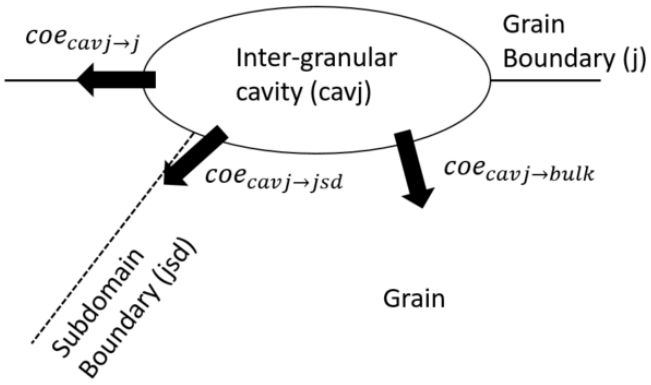

Figure 3.5. – Coefficients that multiply the different re-solution frequencies of an inter-granular cavity.

Finally, we have the following relations:

$$\begin{aligned} b(cavj) &= b^{MD_Veshchunov}(cavj) \times \left(1 - \frac{V_j \cap V_{res_cavj}}{V_{res_cavj}}\right) \times coe_{cavj->bulk} \\ b_j(cavj) &= b^{MD_Veshchunov}(cavj) \times \frac{V_j \cap V_{res_cavj}}{V_{res_cavj}} \times coe_{cavj->j} \\ b_{jsd}(cavj) &= b^{MD_Veshchunov}(cavj) \times \left(1 - \frac{V_j \cap V_{res_cavj}}{V_{res_cavj}}\right) \times R_{VDA} \times coe_{cavj->jsd} \end{aligned} \tag{3.23}$$

Where R_{VDA} is equal to the volume fraction of subdomain boundaries in the grain ($R_{VDA} = \frac{3}{2}\frac{e_{pj}}{A_{sd}}$, with e_{pj} = width of the subdomain boundaries and A_{sd} = subdomain radius. See Section G.4.1).

As the re-solution towards the grain is taken into account through the use of a small re-solution layer, $coe_{cavj->bulk}$ should be close to 1, or slightly higher. Indeed, since the expression presented in Appendix E is derived for spherical bubbles in the bulk, we need to correct that expression by considering that the bubbles on the grain boundary are elongated, and, in general, their surface over volume is higher than the one of a spherical bubble. This means that, for the same equivalent radius, the inter-granular cavities would have more interactions with energetic fission products. Moreover, the

inter-granular cavities have more atoms near the surface of the cavity with respect of their volume, increasing in this way the possibility of re-solution.

We have no indication on the influence of the grain boundary on the phenomenon of re-soution (an MD study such as Setyawan's [Setyawan et al. 2018] for intra-granular bubbles is missing). If re-solution was favored into the grain boundary, the value of $coe_{cavj->j}$ and $coe_{cavj->jsd}$ could be higher than 1. On the contrary, since the re-solution towards the grain boundaries is **not** taken into account through the use of a re-solution layer, $coe_{cavj->j}$ should take into account a reduction term similar to the one presented in Section 2.3.2.3. This attempt has **not** been pursued to favor the inter-inter re-solution.
However, we can still try to estimate this reduction term by making few considerations. The reduction term would depend on the 2D trapping term presented in Section 3.2.2 and on the re-solution profile on the grain boundary. If the grain boundary is not especially favoured, and if we follow the approach explained in Chapter 2 [4], a factor $(\frac{b^{mod}}{b})_j$ can be obtained as a function of R_{cavj} and F_{cavj}. Table 3.2 resumes the values that this factor would assume using dNML = 1 nm and $R_L - R_T = 3.5$ nm.
Even in the case of a vast population of inter-granular bubbles with radius equal to 10 nm, $(\frac{b^{mod}}{b})_j$ would be ≈ 0.4. Hence, to chose a value of one for $coe_{cavj->j}$ means favouring the GB already.

R_{cavj} \ F_{cavj}	0.1	0.5
10 nm	0.184	0.464
100 nm	2.7×10^{-2}	1.18×10^{-1}

Table 3.2. – Values of $(\frac{b^{mod}}{b})_j$ for different values of R_{cavj} and F_{cavj}, using dNML = 1 nm and $R_L - R_T = 3.5$ nm.

For the re-solution from the grain boundary to the grain and to the subdomain boundary, other adjustment parameters have been introduced, as presented in figure 3.6.

We finally obtain:

4. The approach is not detailed in the document because it is the same method as in Chapter 2. The result for $(\frac{b^{mod}}{b})_j$ is:
$(\frac{b^{mod}}{b})_j = geom_{cavj} \times \frac{1}{R_L^3 - R_T^3} \times \left[\frac{R_{ext}^2}{6}(R_L^3 - R_T^3) + \frac{R_T^2}{4}(3R_L^2 R_T - R_T^3 - 2R_L^3) - \frac{R_{ext}^2 R_T^3}{2} ln\left(\frac{R_L}{R_T}\right) \right]$
Where $R_{ext} = R_{cavj} \times \sqrt{F_{cavj}}$, $R_T = R_{cavj}$ + dNML and $R_L = R_T + (R_L - R_T)$, with $R_L - R_T = 3.5$ nm.

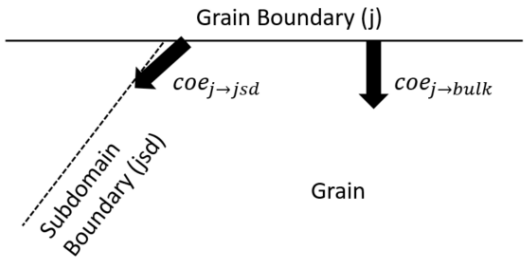

Figure 3.6. – Coefficients that multiply the different re-solution frequencies of dissolved gas atoms on the grain boundary.

$$b(j) = b^{MD_Veshchunov}(\text{bubble of volume } \Omega) \times \left(1 - \frac{V_j \cap V_{res_\Omega}}{V_{res_\Omega}}\right) \times coe_{j->bulk}$$
$$b_{j->jsd}(j) = b^{MD_Veshchunov}(\text{bubble of volume } \Omega) \times \left(1 - \frac{V_j \cap V_{res_\Omega}}{V_{res_\Omega}}\right) \times R_{VDA} \times coe_{j->jsd} \tag{3.24}$$

Where $coe_{j->bulk}$ and $coe_{j->jsd}$ should be close to 1 if the grain boundary does not especially interfere with the re-solution process, and should be smaller otherwise.

3.2.8. Derivation of the equilibrium concentration of defects on the grain boundary near an inter-granular cavity: the thermal re-solution phenomenon

To derive the equilibrium concentration of point defects (including Xenon atoms in a Schottky defect) near an inter-granular lenticular bubble we can follow the derivation presented in [L. Noirot 2014].
First of all, we consider a closed system at constant volume, V_{system}, and temperature, T. For simplicity, we consider V_{system} as a cube with side equal to L.
Then, we call s the number of normal sites[5] in the lattice, s' the number of normal sites in grain boundary, v the number of Schottky defects in the lattice, v' the number of Schottky defect on the grain boundary, x the number of gas atoms inside the bubble, p the number of Xenon atoms in a Schottky defect in the lattice, p' the number of gas atoms in a Schottky defect on the grain boundary, n the volume of the bubble divided by Ω (which represents the amount of Schottky defects that compose the bubble). We are not interested here in the concentration of interstitials.
A schematic representation of the problem can be seen in figure F.1.

Using those definitions, we can write:

5. By normal sites we mean the repetition of the primitive cell of UO_2

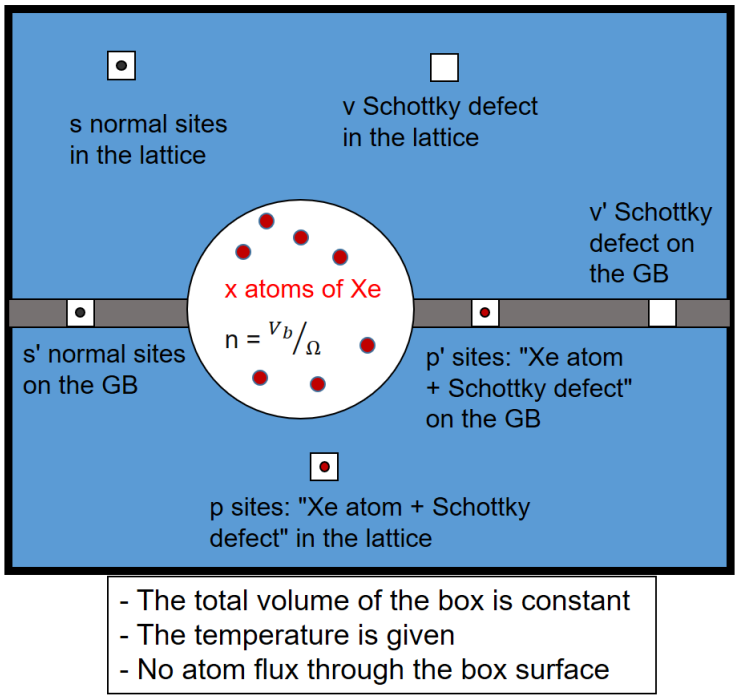

Figure 3.7. – Schematic representation of the problem used to derive the equilibrium concentration of defects on the grain boundary near an inter-granular cavity.

$$\begin{aligned} s + s' &= A\ [Total\ number\ of\ Uranium\ atoms] \\ p + p' + x &= G\ [Number\ of\ gas\ atoms] \\ (s' + v' + p') &= \frac{e_{pj}\left(L^2 - \pi R_{bj}^2\right)}{\Omega} \\ n + (v + s + p) + (s' + v' + p') &= \frac{V_{system}}{\Omega} \end{aligned} \tag{3.25}$$

Where the right hand sides are constants.

In order to find the equilibrium concentration of gas and vacancies in the bulk and on the grain boundary, we have to minimize the free energy of the system, F, taking into account the 4 constraints above.
To do that, we decided to use the Lagrange multipliers.
The total free energy of the system can be written as:

$$F = F_b + F_S + F_L + F_{L'} \tag{3.26}$$

Where F_b is the free energy of the bubble (excluding the energy of the surface of the bubble), F_S is the free energy of the surface of the bubble, F_L is the free energy of the lattice, $F_{L'}$ is the free energy of the grain boundary.

For a lenticular bubble, the volume, V_{bj}, and the surface, S_{bj}, can be calculated as:

$$V_{bj} = \frac{4}{3}\pi R_{bj}^3 \frac{1-\frac{3}{2}cos\theta_{bj}+\frac{1}{2}cos^3\theta_{bj}}{sin^3\theta_{bj}} = \frac{4}{3}\pi R_{bj}^3 A_\theta \tag{3.27}$$

$$S_{bj} = \frac{1-cos\theta}{sin^2\theta} 4\pi R_{bj}^2 = B_\theta 4\pi R_{bj}^2 \tag{3.28}$$

Where the surface is equal to the surface of two spherical caps.
We can also write that:

$$n\Omega = \frac{4}{3}\pi R_{bj}^3 A_\theta \tag{3.29}$$

$$\Omega dn = A_\theta 4\pi R_{bj}^2 dR_{bj} \tag{3.30}$$

$$dS_{bj} = B_\theta 8\pi R_{bj} dR_{bj} \tag{3.31}$$

$$\Longrightarrow dR_{bj} = \frac{\Omega dn}{A_\theta 4\pi R_{bj}^2} \tag{3.32}$$

$$\Longrightarrow dS_{bj} = \frac{B_\theta}{A_\theta}\frac{2\Omega}{R_{bj}} dn \tag{3.33}$$

dF_b can be written as:

$$dF_b = -P_b \Omega dn + \mu dx \tag{3.34}$$

Where μ is the chemical potential of the gas atoms in the bubble, which can be obtained knowing the Equation Of State of the gas in the bubble (see [L. Noirot 2014]).

F_L can be written as:

$$F_L = -kTln(Z) = -kT\left(ln(Z_1)+ln(Z_2)+ln(Z_3)\right) \tag{3.35}$$

Where Z is the partition function.
Z_1 involves the energy of the defects at 0 K:

$$ln(Z_1) = -\frac{s\varepsilon_0}{kT} - v\frac{\varepsilon_v}{kT} - p\frac{\varepsilon_p}{kT} \tag{3.36}$$

Where ε_0 is the energy of a normal site at 0 K (it is the cohesive energy of the perfect crystal divided by the number of normal sites), ε_v is the energy of a vacancy defect in the crystalline lattice at 0 K, ε_p is the energy of a 'vacancy + gas atom' site in the crystalline lattice at 0 K.

Z_2 is the configuration part of the partition function:

$$ln(Z_2) = (s+v+p)ln(s+v+p) - sln(s) - vln(v) - pln(p) \tag{3.37}$$

Z_3 is the partition function term which takes into account all the vibration modes of all the atoms:

$$\frac{\partial ln(Z3)}{\partial v} = 0 \tag{3.38}$$

$$\frac{\partial ln(Z3)}{\partial p} = ln(\mathcal{V}_{pp}) \tag{3.39}$$

$$\frac{\partial ln(Z3)}{\partial s} = ln(\mathcal{V}) \tag{3.40}$$

$$\frac{\partial ln(Z3)}{\partial n} = 0 \tag{3.41}$$

$$\frac{\partial ln(Z3)}{\partial x} = 0 \tag{3.42}$$

Where $\mathcal{V}_{pp} \approx \left(\frac{h\nu_{pp}}{kT}\right)^{-3}$ and $\mathcal{V} \approx \left(\frac{h\nu}{kT}\right)^{-3}$ are related to the vibration frequency of the gas and lattice atoms, ν_{pp} and ν. See [L. Noirot 2014, Appendix A] for the derivation of the first three terms. The last two expressions are due to the fact that a change in the number of vacancies or gas atoms in the bubble do not change the vibration modes of the atoms in the lattice.

$F_{L'}$ can be derived similarly to F_L considering s', v', p' and ε'_0, $\varepsilon_{v'}$ and $\varepsilon_{p'}$.

As there are 4 constraints, we have to introduce 4 Lagrange multipliers. The Lagrangian of the system, $\mathscr{L}$, can then be written as:

$$\begin{aligned}\mathscr{L} =& F_b + F_S + F_L + F_{L'} + \lambda_1(s+s'-A) + \lambda_2(p+x+p'-G) \\ &+ \lambda_3(n+s+v+p+v'+p'+s'-\frac{L^3}{\Omega}) + \lambda_4\left(s'+v'+p'-\frac{e_{pj}\left(L^2-\pi R_{bj}^2\right)}{\Omega}\right)\end{aligned} \tag{3.43}$$

The minimum of the free energy of the system, F, can be found imposing the partial derivatives of $\mathscr{L}$ equal to 0, for the 8 variables + 4 Lagrange multipliers:

$$\frac{\partial \mathscr{L}}{\partial \lambda_1} = s + s' - A = 0 \tag{3.44}$$
$$\frac{\partial \mathscr{L}}{\partial \lambda_2} = p + x + p' - G = 0 \tag{3.45}$$
$$\frac{\partial \mathscr{L}}{\partial \lambda_3} = n + s + v + p + v' + p' + s' - \frac{L^3}{\Omega} = 0 \tag{3.46}$$
$$\frac{\partial \mathscr{L}}{\partial \lambda_4} = s' + v' + p' - \frac{e_{pj}\left(L^2 - \pi R_{bj}^2\right)}{\Omega} = 0 \tag{3.47}$$
$$\frac{\partial \mathscr{L}}{\partial x} = \mu + \lambda_2 = 0 \tag{3.48}$$
$$\frac{\partial \mathscr{L}}{\partial n} = -P_b\Omega + \frac{2B_\theta}{A_\theta}\frac{\gamma\Omega}{R_{bj}} + \lambda_3 + \lambda_4\left(\frac{e_{pj}\pi}{\Omega} \times \frac{\Omega}{2\pi R_{bj}A_\theta}\right) = 0 \tag{3.49}$$
$$= -P_b\Omega + \frac{2B_\theta}{A_\theta}\frac{\gamma\Omega}{R_{bj}} + \lambda_3 + \lambda_4\frac{e_{pj}}{2R_{bj}A_\theta} = 0 \tag{3.50}$$
$$\frac{\partial \mathscr{L}}{\partial s} = \varepsilon_0 + kTln\left(\frac{s}{s+v+p}\right) - kTln(\mathscr{V}) + \lambda_1 + \lambda_3 = 0 \tag{3.51}$$
$$\frac{\partial \mathscr{L}}{\partial s'} = \varepsilon_0' + kTln\left(\frac{s'}{s'+v'+p'}\right) - kTln(\mathscr{V}') + \lambda_1 + \lambda_3 + \lambda_4 = 0 \tag{3.52}$$
$$\frac{\partial \mathscr{L}}{\partial v} = \varepsilon_v + kTln\left(\frac{v}{s+v+p}\right) + \lambda_3 = 0 \tag{3.53}$$
$$\frac{\partial \mathscr{L}}{\partial v'} = \varepsilon_{v'} + kTln\left(\frac{v'}{s'+v'+p'}\right) + \lambda_3 + \lambda_4 = 0 \tag{3.54}$$
$$\frac{\partial \mathscr{L}}{\partial p} = \varepsilon_p + kTln\left(\frac{p}{s+v+p}\right) - kTln(\mathscr{V}_{pp}) + \lambda_2 + \lambda_3 = 0 \tag{3.55}$$
$$\frac{\partial \mathscr{L}}{\partial p'} = \varepsilon_{p'} + kTln\left(\frac{p'}{s'+v'+p'}\right) - kTln(\mathscr{V}'_{pp}) + \lambda_2 + \lambda_3 + \lambda_4 = 0 \tag{3.56}$$

Apart from re-obtaining equations F.1, we obtain:

$$\lambda_2 = -\mu \tag{3.57}$$
$$\lambda_3 = -\varepsilon_v - kTln\left(\frac{v}{s+v+p}\right) \tag{3.58}$$
$$\lambda_4 = \varepsilon_v - \varepsilon_{v'} + kTln\left(\frac{v}{s+v+p}\right) - kTln\left(\frac{v'}{s'+v'+p'}\right) \tag{3.59}$$
$$\lambda_1 = \varepsilon_v - \varepsilon_0 + kTln\left(\frac{v}{s+v+p}\right) - kTln\left(\frac{s}{s+v+p}\right) + kTln(\mathscr{V}) \tag{3.60}$$
$$\tag{3.61}$$

Moreover, if we subtract eq. 3.51 from eq. 3.52 we obtain:

$$\varepsilon_0 - \varepsilon_0' + kTln\left(\frac{s}{s+v+p}\right) - kTln\left(\frac{s'}{s'+v'+p'}\right) - kTln(\mathcal{V}) + kTln(\mathcal{V}') = \lambda_4 \quad (3.62)$$

If we make the hypothesis that the normal sites, s and s', are the large majority of all the sites, we can write:

$$ln\left(\frac{s}{s+v+p}\right) \approx 0 \quad (3.63)$$

$$ln\left(\frac{s'}{s'+v'+p'}\right) \approx 0 \quad (3.64)$$

Moreover, if we make the further hypothesis that $\mathcal{V} \approx \mathcal{V}'$, we obtain:

$$\lambda_4 \approx \varepsilon_0 - \varepsilon_0' \quad (3.65)$$

λ_4 is then approximately equal to the difference in energy between a site in the lattice and a site on the GB.
At this point, we can relate this difference in energy with γ_j, which is the surface energy of the grain boundary [J / m^2], also called surface tension UO_2 / UO_2 [6].
The difference in the energy of two systems with the same amount of sites, where the first is composed of only normal sites, and in the other of normal sites and a grain boundary composed of s' sites, is:

$\Delta E = s' \times (\varepsilon_0' - \varepsilon_0)$

$\Delta E = \frac{S \times e_{pj}}{\Omega} \times (\varepsilon_0' - \varepsilon_0)$

Where S is the surface of the GB.
ΔE can also be written as a function of the surface energy of the grain boundary:

$\Delta E = S \times \gamma_j$

Therefore, we obtain:

$$\gamma_j = \frac{e_{pj}}{\Omega}(\varepsilon_0' - \varepsilon_0) \quad (3.66)$$

We can now express λ_4 as a function of γ_j:

$$\lambda_4 = -\frac{\gamma_j \Omega}{e_{pj}} \quad (3.67)$$

Eq. 3.49 then becomes:

6. In [Borde et al. 2021] it is called Formation energy of the GB.

$$-P_b\Omega + \frac{2B_\theta}{A_\theta}\frac{\gamma\Omega}{R_{bj}} + \lambda_3 - \frac{\gamma_j\Omega}{2\pi R_{bj}A_\theta} = 0 \tag{3.68}$$

Therefore, λ_3 is also equal to:

$$\lambda_3 = P_b\Omega - \frac{2B_\theta}{A_\theta}\frac{\gamma\Omega}{R_{bj}} + \frac{\gamma_j\Omega}{2\pi R_{bj}A_\theta} \tag{3.69}$$

From the equilibrium of the forces applied between the grain boundary and the bubble (see figure 3.8):

$$\gamma_j = 2\gamma cos\theta \tag{3.70}$$

Where γ is the surface tension gas / UO_2.

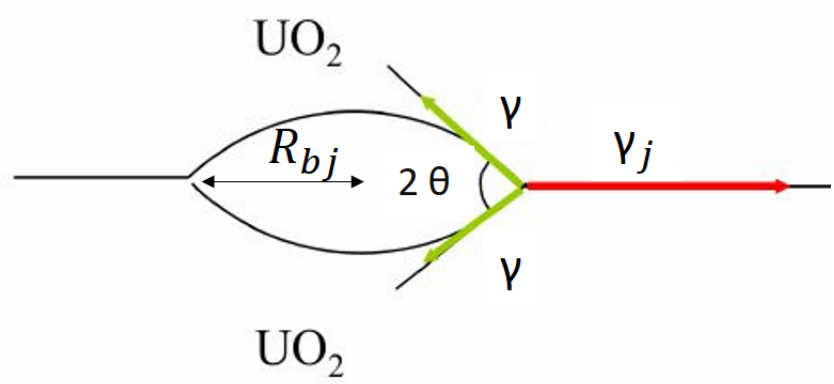

Figure 3.8. – Schematic representation of the link between the surface tension gas / UO_2 and the surface energy of the grain boundary, also called surface tension UO_2 / UO_2.

Using equations 3.53 and 3.69 we can then write:

$$\begin{aligned} kTln\left(\frac{v}{s+v+p}\right) &= -\varepsilon_v - P_b\Omega + \frac{2B_\theta}{A_\theta}\frac{\gamma\Omega}{R_{bj}} - \frac{\gamma_j\Omega}{2\pi R_{bj}A_\theta} \\ x_v^{eq} &= exp\left[-\frac{1}{kT}\left[\varepsilon_v + \Omega\left(P_b - \frac{2B_\theta - cos(\theta)}{A_\theta R_{bj}} \times \gamma\right)\right]\right] \end{aligned} \tag{3.71}$$

Where x_v^{eq} is the concentration of vacancies in the lattice in equilibrium with the inter-granular bubble in [vacancies / sites].

Using the definitions of A_θ and B_θ we can find that $\frac{2B_\theta - cos\theta}{A_\theta} = 2sin\theta$, and:

$$x_v^{eq} = exp\left[-\frac{1}{kT}\left[\varepsilon_v + \Omega\left(P_b - \gamma K_{bj}\right)\right]\right] \tag{3.72}$$

Where $K_{bj} = \frac{2}{\frac{R_{bj}}{sin(\theta)}}$ is the curvature of the bubble, because $\frac{R_{bj}}{sin(\theta)}$ is the curvature radius of the bubble.

If we divide x_v^{eq} by Ω, we obtain the equilibrium concentration of vacancies in the lattice near an inter-granular bubble in [vacancies / m^3], which is referred in the rest of the manuscript as $C_v^{eq}(bj)$:

$$C_v^{eq}(bj) = exp\left[-\frac{1}{kT}\left[\varepsilon_v + \Omega\left(P_b - \gamma K_{bj}\right)\right]\right] \times \Omega^{-1} \tag{3.73}$$

Now, if we subtract eq. 3.49 from eq. 3.55 we obtain:

$$\begin{aligned} \varepsilon_p + kTln\left(\frac{p}{s+v+p}\right) - kTln(\mathcal{V}_{pp}) - \mu &= -P_b\Omega + \frac{2B_\theta}{A_\theta}\frac{\gamma\Omega}{R_{bj}} - \frac{\gamma_j\Omega}{2\pi R_{bj}A_\theta} \\ x_p^{eq} = \frac{p}{s+v+p} &= exp\left[-\frac{1}{kT}\left[\varepsilon_p - \mu + \Omega\left(P_b - \gamma K_{bj}\right)\right]\right] \times \mathcal{V}_{pp} \end{aligned} \tag{3.74}$$

Where x_p^{eq} is the concentration of Xenon atoms in the lattice in equilibrium with the inter-granular bubble in ['Xe atom + Schottky defect' / sites].

If we divide x_p^{eq} by Ω we obtain the equilibrium concentration of Xenon in the lattice near an inter-granular bubble in [atoms / m^3], which is referred in the rest of the manuscript as $C_{Xe}^{eq}(bj)$:

$$C_{Xe}^{eq}(bj) = \frac{p}{s+v+p} = exp\left[-\frac{1}{kT}\left[\varepsilon_p - \mu + \Omega\left(P_b - \gamma K_{bj}\right)\right]\right] \times \mathcal{V}_{pp} \times \Omega^{-1} \tag{3.75}$$

If we subtract eq. 3.55 from eq. 3.56 we obtain:

$$\begin{aligned} \varepsilon_{p'} - \varepsilon_p + kTln\left(\frac{p'}{s'+v'+p'}\right) - kTln\left(x_p^{eq}\right) - kTln\left(\mathcal{V}'_{pp}\right) + kTln\left(\mathcal{V}_{pp}\right) + \lambda_4 = 0 \\ \varepsilon_{p'} - \varepsilon_p + kTln\left(\frac{p'}{s'+v'+p'}\right) - kTln\left(x_p^{eq}\right) - kTln\left(\mathcal{V}'_{pp}\right) + kTln\left(\mathcal{V}_{pp}\right) - \varepsilon'_0 + \varepsilon_0 = 0 \end{aligned} \tag{3.76}$$

If we call $\varepsilon_{Seg,Xe}$ the Segregation energy of a Xenon atom on the GB, we have:

$$\varepsilon_{Seg,Xe} = \left(\varepsilon_{p'} - \varepsilon'_0\right) - \left(\varepsilon_p - \varepsilon_0\right) \tag{3.77}$$

And we obtain:

$$\begin{aligned} x_{p'}^{eq} &= x_{p}^{eq} \times exp\left(-\frac{\varepsilon_{Seg,Xe}}{kT}\right) \times \frac{\mathcal{V}'_{pp}}{\mathcal{V}_{pp}} \\ x_{p'}^{eq} &= exp\left[-\frac{1}{kT}\left[\varepsilon_p + \varepsilon_{Seg,Xe} - \mu + \Omega\left(P_b - \gamma K_{bj}\right)\right]\right] \times \mathcal{V}'_{pp} \end{aligned} \tag{3.78}$$

Where $x_{p'}^{eq}$ is the concentration of Xenon atoms on the grain boundary in equilibrium with the inter-granular bubble in ['Xe atom + Schottky defect' / sites].
If the segregation energy is negative: $x_{Xej}^{eq} > x_{Xe}^{eq}$.

We can obtain the concentration of Xenon atoms on the grain boundary in equilibrium with the inter-granular bubble in [atoms / m^3 of grain boundary] by dividing $x_{p'}^{eq}$ by Ω. The resulting concentration is referred in the rest of the manuscript as $C_{Xej}^{eq}(bj)$:

$$\begin{aligned} C_{Xej}^{eq}(bj) &= exp\left[-\frac{1}{kT}\left[\varepsilon_p + \varepsilon_{Seg,Xe} - \mu + \Omega\left(P_b - \gamma K_{bj}\right)\right]\right] \times \mathcal{V}'_{pp} \times \Omega^{-1} \\ &= exp\left[-\frac{1}{kT}\left[\varepsilon_p + \varepsilon_{Seg,Xe} - \mu + \Omega\left(P_b - \gamma K_{bj}\right)\right]\right] \times \left(\frac{h\nu_{Xej}}{kT}\right)^{-3} \times \Omega^{-1} \end{aligned} \tag{3.79}$$

If we subtract eq. 3.53 from eq. 3.54 we obtain:

$$\varepsilon_{v'} - \varepsilon_v + kTln\left(\frac{v'}{s'+v'+p'}\right) - kTln\left(x_v^{eq}\right) - \varepsilon'_0 + \varepsilon_0 = 0 \tag{3.80}$$

If we call $\varepsilon_{Seg,v}$ the Segregation Energy of a vacancy on the GB, we obtain:

$$\varepsilon_{Seg,v} = \left(\varepsilon_{v'} - \varepsilon'_0\right) - \left(\varepsilon_v - \varepsilon_0\right) \tag{3.81}$$

And then:

$$\begin{aligned} x_{v'}^{eq} &= x_{v}^{eq} \times exp\left(-\frac{\varepsilon_{Seg,v}}{kT}\right) \\ x_{v'}^{eq} &= exp\left[-\frac{1}{kT}\left[\varepsilon_v + \varepsilon_{Seg,v} + \Omega\left(P_b - \gamma K_{bj}\right)\right]\right] \end{aligned} \tag{3.82}$$

Where $x_{v'}^{eq}$ is the concentration of vacancies on the grain boundary in equilibrium with the inter-granular bubble in [vacancies / site].
If the segregation energy is negative: $x_{v,j}^{eq} > x_{v}^{eq}$.

We can obtain the concentration of vacancies on the grain boundary in equilibrium with the inter-granular bubble in [vacancies / m^3 of grain boundary] by dividing $x_{v'}^{eq}$ by Ω. The resulting concentration is referred in the rest of the manuscript as $C_{v,j}^{eq}(bj)$:

$$C_{v,j}^{eq}(bj) = exp\left[-\frac{1}{kT}\left[\varepsilon_v + \varepsilon_{Seg,v} + \Omega\left(P_b - \gamma K_{bj}\right)\right]\right] \times \Omega^{-1} \tag{3.83}$$

Using the equations just found, we can also calculate other two equilibrium concentrations that are needed in MARGARET.

Using eq. 3.82 and considering a given concentration on the GB, $C_{v,j}^{loc}$, we can write the concentration in the lattice in equilibrium with $C_{v,j}^{loc}$, $C_v^{eq}(j)$, as:

$$C_v^{eq}(j) = C_{v,j}^{loc} \times exp\left(\frac{\varepsilon_{Seg,v}}{kT}\right) \tag{3.84}$$

Using eq. 3.78 and considering a given concentration on the GB, C_{Xej}^{loc}, we can write the concentration in the lattice in equilibrium with C_{Xej}^{loc}, $C_{Xe}^{eq}(j)$, as:

$$C_{Xe}^{eq}(j) = C_{Xej}^{loc} \times exp\left(\frac{\varepsilon_{Seg,Xe}}{kT}\right) \times \frac{\mathcal{V}_{pp}}{\mathcal{V}'_{pp}} = C_{Xej}^{loc} \times exp\left(\frac{\varepsilon_{Seg,Xe}}{kT}\right) \times \left(\frac{\nu_{Xej}}{\nu_{Xe}}\right)^3 \tag{3.85}$$

All these equilibrium concentrations at the vicinity of a bubble on the grain boundary are presented in figure 1.3 of Section 1.3.3, and serve as boundary condition for the diffusion problems.

Remark

The Segregation energy of a vacancy can be calculated as the difference in the total energy between two systems, that we can call S_1 and S_2. S_1 is composed by normal sites in the lattice, a grain boundary and a vacancy in the bulk. S_2 is composed by normal sites in the lattice, a grain boundary and a vacancy on the grain boundary. A scheme of the problem can be seen in figure 3.9.

If we call N the number of normal sites in the system S_2 and N' the number of "normal" sites on the GB in the system S_1, the total energy of S_1 is:

$(N-1)\varepsilon_0 + \varepsilon_v + N'\varepsilon'_0$

The total energy of S_2 is:

$N\varepsilon_0 + (N'-1)\varepsilon'_0 + \varepsilon_{v'}$

The difference in the total energy between the two system is:

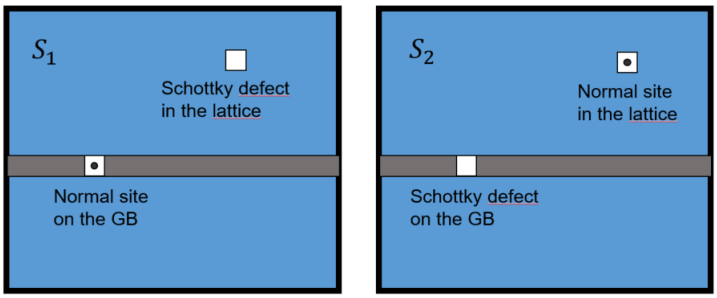

Figure 3.9. – Scheme of the two different systems used to calculate the Segregation Energy of a vacancy in the bulk.

$$E(S_2) - E(S_1) = \varepsilon_0 - \varepsilon_v - \varepsilon'_0 + \varepsilon_{v'} \tag{3.86}$$

Which is our definition of the Segregation Energy of a vacancy (bound Schottky defect).

A similar reasoning can be done with $E_{Seg,Xe}$.

If we use as a value of $\gamma_j \approx 1.3$ [J / m^2] [Borde et al. 2021] [7], the value $\varepsilon'_0 - \varepsilon_0 = \frac{\gamma_j \Omega}{e_{pj}}$ is approximately equal to 53.17×10^{-21} [J] = 0.3323 [eV].

Three final notes:

1) As for the previous chapters, a similar reasoning can be applied to the precipitation bubbles (described in Chapter 4) by considering the subdomain boundary as an uniform slab of thickness e_{pj}.

2) A different derivation of the defect equilibrium concentrations in the bulk near an inter-granular bubble ($C_v^{eq}(bj)$ and $C_{Xe}^{eq}(bj)$) can be found in Appendix F. In this case, the grain boundary is considered as surface without associated volume.
The same result is obtained.

3) The formation energy of a vacancy on the grain boundary, $\varepsilon_{v,j}$, is equal to:

$$\varepsilon_{v,j} = \varepsilon_v + E_{seg,v} \tag{3.87}$$

It can be understood thinking to the process to form a vacancy on the grain boundary:

— First: introduce a vacancy into a box S_1 with N-1 normal sites and a grain bound-

7. γ_j changes with the type of GB, from about 1 to about 1.7 [J / m^2] for the types of GB studied in [Borde et al. 2021]

ary with N' "normal" sites. It gives a box S_2 with N sites in the lattice (one being occupied by the vacancy) and N' grain boundary "normal" sites.
— Second: move the vacancy from the bulk to the grain boundary (box S_3).

We obtain:

$$E(S_2) - E(S_1) = \varepsilon_v = \text{Formation energy of a vacancy in the bulk} \tag{3.88}$$

$$E(S_3) - E(S_2) = E_{Seg,v} = \text{Segregation energy of the vacancy on the GB} \tag{3.89}$$

$$E(S_3) - E(S_1) = \varepsilon_v + E_{seg,v} = \text{Formation energy of a vacancy on the GB} = \varepsilon_{v,j} \tag{3.90}$$

Then, from eq. 3.81 we can obtain the relation between $\varepsilon_{v,j}$ and $\varepsilon_{v'}$:

$$\varepsilon_{v,j} = \varepsilon_{v'} - \left(\varepsilon'_0 - \varepsilon_0\right) \tag{3.91}$$

Finally, eq. 3.83 can then be written as :

$$C^{eq}_{v,j}(bj) = exp\left[-\frac{1}{kT}\left[\varepsilon_{v,j} + \Omega\left(P_b - \gamma K_{bj}\right)\right]\right] \times \Omega^{-1} \tag{3.92}$$

3.3. Conclusion

In this Chapter, we have:
— Derived the trapping frequency of dissolved gas at the GB by inter-granular bubbles and pores;
— Derived the trapping frequency of dissolved gas at the GB of the HBS grains by HBS bubbles and pores;
— Estimated how the gas re-dissolved from the inter-granular cavities re-distribute towards the GB and the grain;
— Derived the equilibrium concentration of defects on the grain boundary near an inter-granular cavity.

All this work is necessary to describe the behaviour of the gas at the grain boundaries, and hence to test if the long-range inter-granular diffusion can be a major way of fission gas release during base irradiation (we will address this question in Chapter 7). In addition, all the aspects treated in this Chapter will be used both in Chapter 4, to describe the behaviour of the gas at the subdomain boundaries, and in Chapter 5, to describe the behaviour of the thermal vacancies on subdomain or grain boundaries.

Both the long-range inter-granular diffusion phenomenon, as well as a term that accounted for the trapping of dissolved atoms at the GB by inter-granular cavities were already considered in MARGARET for Helium before the beginning of this thesis. However, during the thesis, I changed the trapping term and derived a more appropriate one, as detailed in this Chapter. Moreover, the direct re-solution from inter-granular cavities to the GB was previously not considered. Finally, both the estimation of the re-distribution of the re-dissolved gas and the derivation of the equilibrium concentration of defects on the grain boundary near an inter-granular cavity are new.

4. Subdomains

Sommaire

4.1. Literature Review 115
4.1.1. Experimental evidences: subdomain formation 115
4.1.2. Experimental evidences: link with higher fission gas release . . . 119
4.1.3. Possible mechanism of subdomain formation and conditions for the onset of the restructuring 122
4.1.4. What other fission gas models do in this regard 124
4.2. Description of the subdomains in MARGARET 125
4.2.1. General choices for the new "subdomain state" 125
4.2.2. New state in MARGARET: methodology to build the new ODE system 128

4.1. Literature Review

4.1.1. Experimental evidences: subdomain formation

Researchers performing post irradiation examinations on high burnup UO_2 fuels have since long noticed a change in the microstructure of the fuel towards the center of the pellet [J. Noirot, L. Noirot, et al. 2004]. The zone subjected to this change in microstructure has been called "precipitation zone", due to the formation of a bigger population of intra-granular bubbles, not present at lower burnup. Figure 4.1 shows a crystallographic contrast image at the limit of the precipitation zone on a UO_2 fuel with a burnup of 61 GWd/t_U.

However, not much more was known about this new microstructure. J. Noirot and colleagues [J. Noirot, Zacharie-Aubrun, et al. 2018] were the firsts to give a deeper insight into the characteristics of the precipitation zone. They conducted electron backscattered diffraction (EBSD) and FIB/SEM measurements on a sample with a burnup of 73 GWd/t_U and they saw that, at the center of the pellet[1], the lattice of the grains did not have a single, defined orientation, as for unirradiated and low burnup fuels. Instead, the grains were divided into different domains, called subdomains or sub-grains. Each domain has an orientation close to that of the original grain, but

1. The published EBSD map has been done at $r/R_{pellet} = 0.36$, where R_{pellet} is the radius of the pellet

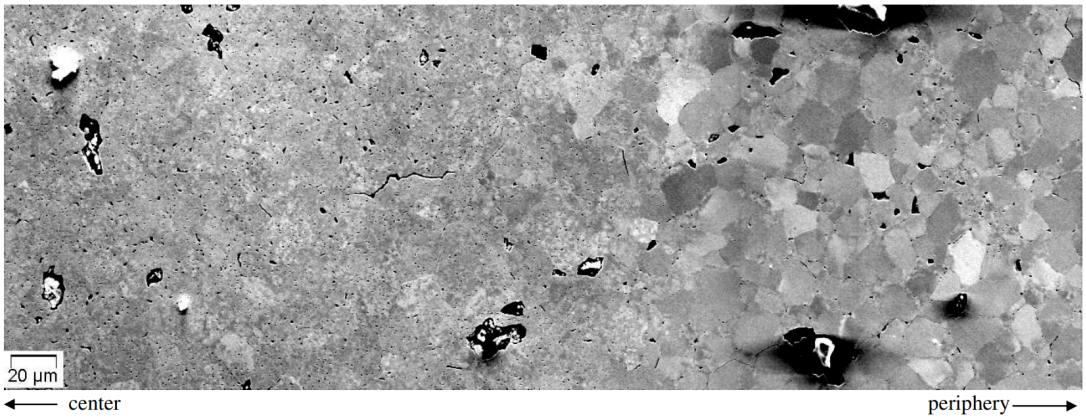

Figure 4.1. – Crystallographic contrast image at the limit of the precipitation zone on a 61 GWd/t_U irradiated UO_2. Image taken from [J. Noirot, L. Noirot, et al. 2004].

different domains (in the same grain) have a slightly different orientations[2]. Furthermore, the researchers saw that the precipitation bubbles were situated along the subdomain boundaries. They found no evidence of intra-granular bubble interconnection. Regarding the morphology of these big intra-granular bubbles, they reported shapes that are far from spherical.

After this first discovery, other researchers have analyzed high burnup specimens using EBSD and FIB/SEM measurements [J. Noirot, Dowek, et al. 2022; Zacharie-Aubrun et al. 2022; Dowek 2021; Gerczak et al. 2018; Cappia et al. 2022; McKinney et al. 2023].

J. Noirot, I. Zacharie-Aubrun, R. Dowek and other researchers [J. Noirot, Dowek, et al. 2022; Zacharie-Aubrun et al. 2022; Dowek 2021] have studied specimens taken at different radial locations of 4 fuel rods with respective burnups of 36, 61, 63 and 73 GWd/t_U (the 73 GWd/t_U fuel rod is the same rod analyzed in [J. Noirot, Zacharie-Aubrun, et al. 2018]).
The analysis of the high burnup fuel rods (61, 63 and 73 GWd/t_U) confirmed the findings of the first study [ibid.], namely: they found evidences of the subdomain formation in the central zone of the pellet; the precipitation bubbles were always situated along the subdomain boundaries; they found no evidence of intra-granular bubble interconnection; only a small part of the precipitation bubbles were found to be spherical, while the majority had flat, elongated or complex shapes. Moreover, they saw that the transition between the central restructured zone and the unrestructured mid-radial position (no subdomains, no precipitation bubbles) is very sharp.
They have also tried to quantify the progression of the restructuring. To do so, they have used 3 main indicators: average Mis2Mean, lenght of the misorientation lines,

2. In this first paper, the researchers did not quantify the difference in the orientation of the subdomains (also called misorientation angles)

and restructured fraction. The “restructured fraction 1°” is calculated as *"the surface fraction of sub-grains, with ECD < 3 μm and a threshold grain boundary angle criterion at 1°"*, where ECD is the Equivalent Circle Diameter (of the subdomains) and the threshold grain boundary angle criterion at 1° refers to the misorientation angle between adjacent subdomains. Only sub-grains enclosed with continuous boundaries between 1° and 10° were considered for the restructured fractions. The lenght of the misorientation lines is a measurement of the *"discontinuous misorientation, forming a network inside the initial grains"*. It is calculated as the lenght of the misorientation lines with misorientation angles between 1° and 10° present inside a grain over the surface of the grain [m/m^2]. Finally, the average Mis2Mean is defined as *"the mean value in an EBSD map of the Mis2Mean measurement of each pixel: first, the grains are determined in the EBSD map and then the mean orientation of the grain is calculated. Then, the minimum rotation angle, between the pixel orientation and the mean orientation of the grain is calculated for each pixel in each grain. This difference is the Mis2Mean"*. The researchers have shown that all the 3 indicators tend to increase with burnup. Therefore, it seems that this type of restructuring (the subdomain formation) is progressive.
Another interesting feature of the high burnup specimens is the not constant progression of the restructuring along the radius. For the 61 and the 63 GWd/t_U specimens, the researchers noticed a slight increase in the progression of the restructuring from the center to the outer part of the precipitation zone (the zone where the precipitation bubbles are detected, which coincides with the zone where the subdomains form). The 73 GWd/t_U sample, instead, showed a minimum in the progression of the restructuring at $0.1R_{pellet}$ (where R_{pellet} is the radius of the pellet).
Contrary to the high burnup specimens, the 36 GWd/t_U specimens showed very low indications of restructuring and no presence of precipitation bubbles.

T.J. Gerczak et al. [Gerczak et al. 2018] studied a high burnup fuel sample (72 GWd/t_U) irradiated at a linear heat rate not so dissimilar (temperature at the center of the pellet lower than 1000°C and higher than 700°C for most of the operation) to the ones undergone by the specimens of [J. Noirot, Dowek, et al. 2022; Zacharie-Aubrun et al. 2022; Dowek 2021]. They too have detected the formation of the subdomains at the central zone of the pellet. However, they did not measure any significant variation in the restructuring along the radius (unfortunately, the sample analyzed missed the innermost part of the pellet, from $r/R_{pellet} < 0.3$).

F. Cappia et al. [Cappia et al. 2022] studied a high burnup fuel sample (76 GWd/t_{HM}) that experienced an higher linear heat rate with respect to the one experienced by the fuel samples analyzed in [J. Noirot, Dowek, et al. 2022; Zacharie-Aubrun et al. 2022; Dowek 2021; Gerczak et al. 2018]. They too found an abundant presence of Low Angle Grain Boundaries (LAGB), which constitute the boundaries between subdomains, in the central region of the pellet. As for [J. Noirot, Dowek, et al. 2022; Zacharie-Aubrun et al. 2022; Dowek 2021], they measured a higher concentration of LAGB near the outer layer of the precipitation zone with respect to the most central part. A clear

transition between the precipitation zone and the unrestructured zone (at mid-radial position) is also visible.

C. Mckinney et al. [McKinney et al. 2023] studied four high burnup fuel samples with burnups of 63.5, 69, 75 and 77 GWd/t$_U$. The 63.5 GWd/t$_U$ sample came from a Boiling Water Reactor, while the other samples came from Pressurized Water Reactors. The linear heat rate history of the 63.5 GWd/t$_U$ sample is comparable with the fuel samples analyzed in J. Noirot, Dowek, et al. 2022; Zacharie-Aubrun et al. 2022; Dowek 2021; McKinney et al. 2023], while the 69, 75 and 77 GWd/t$_U$ samples seems to have experienced even higher linear heat rates than the sample studied in [Cappia et al. 2022].
The 63.5 GWd/t$_U$ sample, differently to the samples presented in [J. Noirot, Dowek, et al. 2022; Zacharie-Aubrun et al. 2022; Dowek 2021] that have a similar burnup (61 and 63 GWd/t$_U$ samples), showed a low presence of Low Angle Grain Boundaries in the central zone of the pellet, while some restructuring (formation of a not-negligible amount of LAGB) appears in the mid-radial position (r/R_{pellet} between 0.5 and 0.85). The 75 and 77 GWd/t$_U$ samples showed signs of restructuring in all the center of the pellet (the 77 GWd/t$_U$ sample missed the centermost par of the pellet, from r/R_{pellet} < 0.3), with higher restructuring towards the outer part of the precipitation zone. The 69 GWd/t$_U$ fuel sample, instead, showed almost no restructuring in the centermost part of the pellet (r/R_{pellet} < 0.3), while an abundance of LAGB was found near the outer layer of the precipitation area.
The researchers, following the analysis of these 4 specimens, proposed the existence of an unknown temperature range at which restructuring can form. Low temperatures might not be enough to *"promote sufficient xenon diffusion and intragranular fission gas bubble formation that could facilitate the formation of LAGBs"*, while high enough temperatures might *"promote thermal recovery of the microstructure as proposed by Cappia et al."* [Cappia et al. 2022].

The temperatures of the fuels considered in this manuscript are similar to the ones experienced by the samples analyzed in [J. Noirot, Dowek, et al. 2022; Zacharie-Aubrun et al. 2022; Dowek 2021], where no centermost zone without restructuring was present. Therefore, in this manuscript, we will consider a maximum temperature for the subdomain formation that is higher than the highest temperature experienced by samples analyzed in [J. Noirot, Dowek, et al. 2022; Zacharie-Aubrun et al. 2022; Dowek 2021].

As it can be noticed, all the researchers organized the data on the basis of two major variables: burnup and temperature (the temperature at which the different points analyzed operated can be found by combining the information on the radial position and the linear heat rate that the sample experienced). However, what joins all the measurements performed to study the subdomain formation is the fact that temperature and burnup do not seem the only major variables involved in the formation of the subdomains, as already highlighted by the same authors who performed the measurements [Zacharie-Aubrun et al. 2022; Dowek 2021].

In MARGARET, we need to build a condition to introduce the subdomains. This will be addressed in Sections 4.1.3 and 4.2.

4.1.2. Experimental evidences: link with higher fission gas release

A most interesting phenomenon happens at high burnup, starting from about 50 GWd/t_U: What we see is an increase in fission gas release despite the natural fall in linear heat rating as reactivity decreases with burnup [Rest et al. 2019]. This phenomenon can occur with different types of reactors and fuel cycle management [ibid.].

There are different possible explanations in literature to justify this increase in Fission Gas Release [ibid.]:

— The decrease in the fuel thermal conductivity with burnup could increase the temperature at the center of the fuel. However, even if the decrease in the fuel thermal conductivity is taken into account by ALCYONE (through the model developed by Lucuta and co-workers [Lucuta et al. 1996]), in the fuel rods considered in this manuscript temperatures generally decrease with burnup (see for example the predicted fuel centerline temperatures of the samples studied in [Zacharie-Aubrun et al. 2022]).
— The gas atoms diffusion coefficient could increase with Burnup. However, this increase seems valid only for fuels at very high burnup (higher than about 80 GWd/t_M [Spino et al. 2008]).
— Subdomain formation could create fast pathways for the gas in the grains to reach the grains' surface. In this manuscript we concentrate our attention on this last possible explanation.

A hint in this direction is that the subdomain formation is concomitant with the rise of the fission gas release.
Moreover, experiments seems to indicate that, at high burnup, most of the gas is released from the centre of the fuel [Dowek 2021], where the subdomains have formed. Figure 4.2, taken from [ibid.], shows the state of the gas by radial position of a fuel with a Burnup of 73 GWd/t_U. From this figure, it is clear how the majority of the gas is released from the centre of the pellet, where the precipitation zone is situated.

Another hint of the fact that the subdomain formation may indeed produce fast diffusion pathways for the gas in the grain to reach the grain surface comes from the behaviour of Cr-doped fuels under base irradiation. The bigger grains of the Cr-doped fuels should allow a decrease of the fission gas release with respect to UO_2 fuels irradiated at similar conditions. However, the high burnup Cr-doped fuel analyzed by Zacharie-Aubrun and colleagues [Zacharie-Aubrun et al. 2022] did not show a

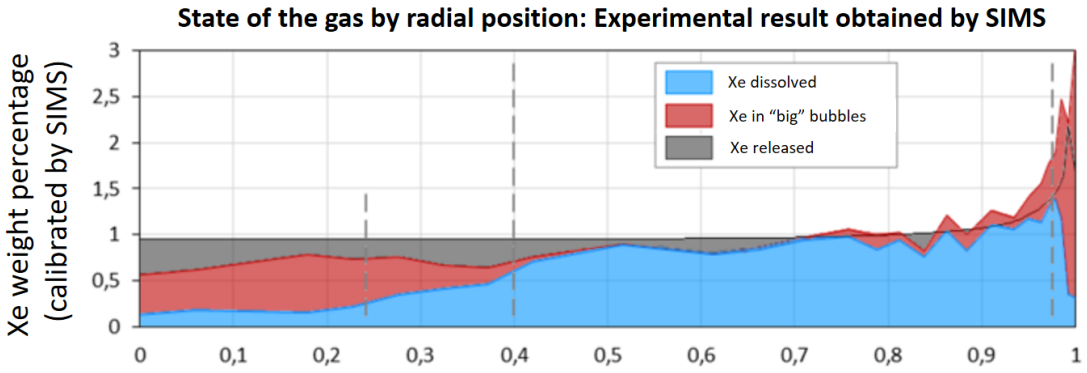

Figure 4.2. – Figure 7.3 of [Dowek 2021] (translated from French), which shows the state of the gas by radial position (r/R, where R is the radius of the fuel) of a fuel with a Burnup of 73 GWd/t$_U$. The gas dissolved or present in the nano-bubbles is in blue, the gas trapped in the bubbles detected by SIMS (the bigger population of precipitation bubbles, called "big" bubbles in the figure) is in red, the gas released is in grey. The longer vertical grey line represents the beginning of the precipitation zone.

major reduction in the fission gas release with respect to the similar burnup, standard UO_2 fuels analyzed in the same paper, even if the fuels experienced a similar irradiation history. At the same time, J. Noirot, I. Zacharie-Aubrun, R. Dowek and other researchers [Zacharie-Aubrun et al. 2022; Dowek 2021] have found out that Cr-doped fuels restructure similarly to UO_2 fuels at the center of the pellet at similar burnup.
The conclusion that we may draw is that the subdomain formation eliminates in part the benefit that comes from having larger grains because, when subdomains appear, most of the gas produced in the grains reach the grain surface by diffusion along the subdomain boundaries. In this condition, the key phenomena for the fission gas release may be the diffusion of dissolved gas from the subdomains to the subdomain boundaries, and the fact that UO_2 and Cr-doped fuels develop subdomains of comparable sizes.
In this regard, it would be interesting to model Cr-doped fuels with MARGARET considering the subdomain formation to see if it manages to predict correctly the fission gas release at high burnup.

Other results that partially corroborate this view come from the paper of S.T. Murphy [S. T. Murphy et al. 2015]. The researchers performed *"molecular dynamics simulations employing empirical potentials to investigate the diffusion of Xe atoms around edge dislocations in UO2"*. They saw that, for a certain time span at the beginning of the simulations, the dislocation enhanced the diffusion coefficient of Xe with respect to the bulk. However, after an initial increase of the Xe diffusion coefficient, the Xe atoms in the dislocation gathered into bubbles and stopped diffusing.
The authors could not consider the effect of irradiation in their study. However, we

know that, during irradiation conditions, Xe atoms trapped in the bubbles re-solute back into the matrix and, for bubbles on dislocations, also into the dislocations. Therefore, in base irradiated fuels, we can expect continuous events of bubbles formation, trapping of Xe atoms by bubbles, re-solution of Xenon from the bubbles and trapping of dissolved Xenon in the lattice by the dislocations to take place. These events, considered all together, may allow a not negligible fraction of Xe atoms to diffuse along dislocations.
Furthermore, during the MD simulation no thermal re-solution from the bubbles into the dislocation have been seen, but this phenomenon probably cannot be observed within the the short time span of a MD simulation.
Another important point to consider is the concentration of Xe atoms on the dislocations: if the concentration of dissolved Xe in the dislocations remains low (let's say less than 10^{-2} atoms/sites), it is improbable that two Xe atoms encounter to form a new bubble. It is therefore important to check if, during MARGARET calculations, the predicted concentration of Xe atoms on the subdomain boundaries remains low.
One last thing to consider is that the temperatures used in the MD simulations (from 2300 K to 3200 K) are close to or higher than the Bredig transition (≈ 2500-2600 K [Fossati et al. 2021; Dubois et al. 2024])[3], and therefore not all the deduction derived in the paper might be applicable to our temperatures of interest.

Problem with the consideration of only one population of bubbles both on the Grain Boundary and on the Subdomain Boundaries

While in the bulk the usage of only one population of bubbles to represent all the different sizes of the nano-bubbles seems reasonable, since the size of the intragranular bubbles stays between 1 and 10 nm independently on irradiation conditions and burnup (during base irradiation) [Losonen 2000], the usage of only one population of bubbles on the Grain Boundary and on the Subdomain Boundaries (SDB) seems more problematic, since we expect orders of magnitude of difference between the new nucleated bubbles on GB and SDB and the biggest inter-granular and subdomain bubbles (which can reach sizes of hundred of manometers). One of the major problems that this type of modelling produce is the difficulty to predict correctly both the swelling of the fuel, made up mostly by the biggest but less frequent bubbles, and the phenomenon of trapping of dissolved gas in the GB and SDB by the GB and SDB bubbles, at which the smaller but more frequent bubbles contribute the most. Since in MARGARET we prefer not to consider more than one population of inter-granular and inter-subdomain bubbles due to calculation time constrains, we identify the modelled bubbles with the ones that can be detected by SEM. This changes the meaning of D_{Xej} (D_{Xejsd} for the subdomains), the diffusion coefficient of gas along grain boundaries (along subdomain boundaries), that must be understood as an effective diffusion

3. Above these temperatures, the Oxygen atoms in the UO_2 fuel partially melt while the Uranium atoms retain their crystalline order [Fossati et al. 2021]. This change in the microscopic structure determines a change in the properties of the fuel [ibid.].

coefficient.

4.1.3. Possible mechanism of subdomain formation and conditions for the onset of the restructuring

A description of the possible mechanism of the subdomain formation is summarized elegantly by J. Rest et al. [Rest et al. 2019]: *"Irradiation damage causes the formation of both interstitials and vacancies in equal quantities. The precipitation of gas atoms into pores attracts vacancies from the surrounding lattice, thus causing an in-balance with the interstitial concentration. Interstitials are known to form dislocation loops that, with continuing irradiation, grow to form tangles and eventually align themselves into sub-grain boundaries and hence micro-grains"*.

MARGARET uses an ODE (Ordinary Differential Equation) to predict the dislocation density (both interstitial loops and dislocation lines), ρ_d, in the grain. Therefore, if the critical concentration of defects for the onset of the subdomain formation were to be known, MARGARET could, in theory, predict the onset of the restructuring. However, there are a few things to consider:

— As already pointed out (4.1.1), the subdomain formation seems a gradual process. On the other hand, as for the modelling of many other gradual phenomena (for example, the modelling of the release of fission gas by percolation due to the interconnection of inter-granular bubbles in other fission gas release codes [Zullo et al. 2023]), we can use a limit condition above which the effect of the phenomenon that we want to describe (the subdomain formation in this case) must be considered.

— A critical concentration of defects for the onset of the subdomain formation is not known. The subdomain formation has been discovered only recently and more studies must be done in this direction.

— The current ODE used by MARGARET to predict ρ_d is useful only to predict the formation of the HBS. Consistently, as the HBS appears in cold zones with high fission rates, the dislocation density has been made to diminish quite sharply above a temperature threshold and grow with the fission rate $\dot{F}$ [fissions / m^3 s], following Nogita and Une's correlation [Nogita et al. 1995]. On the contrary, subdomains appear above a certain temperature. Therefore, the current ODE for ρ_d cannot be used to predict the subdomains.

Since, at the moment, we cannot predict the formation of the subdomains using predictions of the concentration of defects, we must rely on the experimental information that we have. The parameters used by the researchers to classify the data on the subdomain formation are burnup and temperature, as already presented in 4.1.1.

Both are parameters at which we have access in MARGARET.
From the analysis performed in [Zacharie-Aubrun et al. 2022; Dowek 2021], we know that a fuel with burnup equal to 36 GWd/t$_U$ shows very few signs of restructuring, while at a burnup of 61 GWd/t$_U$ the subdomains have already formed (even if not with the same degree along the radius). Other Post Irradiation measurements [Gerczak et al. 2018; Cappia et al. 2022; McKinney et al. 2023] confirmed the presence of subdomains for burnup higher than 64 GWd/t$_U$. However, the 63.5 GWd/t$_U$ fuel analyzed by Mckinney [McKinney et al. 2023] is peculiar, since almost no restructuring was found in the center of the pellet. One explanation for the absence of restructuring could be due to the fact that the rod analyzed comes from a BWR reactor, instead of a PWR as all the other fuels analyzed. Another possibility is that, since the researchers used a 2° disorientation limit to classify the Low Angle Grain Boundaries as such (differently from [Zacharie-Aubrun et al. 2022; Dowek 2021] where a 1° disorientation limit was used), a not negligible amount of LAGB could be present with disorientations lower than 2°. If we consider this particular fuel as an outlier, we can conclude that the onset for the subdomain formation happens in a burnup range of 36-61 GWd/t$_U$.
A synthesis of the data in literature can be found in table 4.1.

Ref.	Average burnup [GWd/t$_U$] of the specimen	Type of reactor	Extension of the subdomain zone	Misorientation limit for classification SD	FGR	Notes
[1]	36	PWR	no SD	1°-10°	0.53	
[1]	61	PWR	0 - 0.5R_{pellet}	1°-10°	2.75	
[1]	63	PWR	0 - 0.43R_{pellet}	1°-10°	4.3	
[1]	73	PWR	0 - 0.4R_{pellet}	1°-10°	6.17	
[2]	72	PWR	0 - 0.44R_{pellet}	2°-15°	2.1	
[3]	76	PWR	0 - 0.55R_{pellet}	2°-15°	16	
[4]	63.5	BWR	0.5 - 0.85R_{pellet}	2°-15°	14.3	Few signs of restructuring
[4]	69	PWR	0.3 - 0.6R_{pellet}	2°-15°	9.8	
[4]	75	PWR	0.17 - 0.55R_{pellet}	2°-15°	12	Missing the part of the specimen at $r < 0.17R_{pellet}$
[4]	77	PWR	0.3 - 0.65R	2°-15°	16.1	Missing the part of the specimen at $r < 0.3R_{pellet}$

Table 4.1. – Resume of the data in literature regarding the formation of the subdomains. Ref. [1]: [Zacharie-Aubrun et al. 2022; Dowek 2021]; Ref. [2]: [Gerczak et al. 2018]; Ref. [3]: [Cappia et al. 2022]; Ref. [4]: [McKinney et al. 2023].

Other valuable experimental data that can help us choosing the critical value of burnup and temperature for the subdomain formation come from EPMA and SIMS

measurements. In fact, we can associate the sudden drop in the EPMA and baseline SIMS measurements at the center of the pellet with the formation of the second population of intra-granular bubbles, which trap a detectable percentage of the intra-granular Xenon. A good choice of the burnup critical value should allow us to predict correctly the start of the drop with burnup (at low burnup no sudden drop in the center is measured), while a good choice of the temperature critical value should allow us to predict correctly the precipitation radius.
Xenon depletion as seen by EPMA, or large bubble detection by SIMS are not synonimus of subdomain formation. They can be due to subdomain formation, but they can also be due to high temperature conditions because both lead to the formation of large bubbles. They can be used when we know that the temperature did not exceeded $\approx$ 1200°C.

We can also make use of the SEM (Scanning Electron Microscope) images of medium and high burnup fuels: a valuable information that we can extract is the burnup at which we detect the first precipitation bubbles.
The characterizations of high burnup fuels made by J. Noirot and colleagues [J. Noirot, L. Noirot, et al. 2004] reveal that the precipitation bubbles are detected by SEM starting from a burnup of about 45 GWd/t$_U$.

A final indication comes from fission gas release measurements: the choice of good critical values should allow us to obtain good predictions of FGR for high burnup fuels. However, the fission gas release process is complex and determined by many variables, therefore fission gas release measurements are indirect and less reliable indications for the choice of critical values.

4.1.4. What other fission gas models do in this regard

A first effort to describe the effect of the subdomain formation on the fission gas behaviour in UO_2 during base irradiation comes from a technical note written by P.-C. A. Simon et al. [Simon, Gamble, et al. 2024] and distributed during the redaction of this manuscript. In it, the part of the fuel that goes through the subdomain formation is called "Dark Zone", due to the formation of the precipitation bubbles, which, when viewed through SEM (Scanning Electron Microscope) images, look as dark spots.

The authors start by acknowledging that the mechanisms of the formation of the dark zone are still unknown.
Then, looking at the published data on the subdomain formation [J. Noirot, Zacharie-Aubrun, et al. 2018; McKinney et al. 2023], they suggest that the formation of the dark zone takes place at a burnup > 50 GWd/t$_U$ and in the range of temperature: 900 °C < T < 1100 °C. They use as the relevant parameter for the subdomain formation an effective burnup (τ_{eff}) equal to:

$$\tau_{eff} = \int f(T - T_{low}) f(T_{high} - T) d\tau \tag{4.1}$$

Where f is the Heaviside step function, T is the local temperature in Kelvin, and T_{low} = 900 °C = 1173.15 K and T_{high} = 1100 °C = 1373.15 K are the threshold temperatures in Kelvin. τ_{eff} is the burnup built up in the $[T_{low}, T_{high}]$ range.
This effective burnup is used to calculate the *"restructured volume fraction of the dark zone"*, using a formula that allows them to obtain a full developed dark zone (restructured volume fraction of the dark zone ≈ 1) at an effective burnup of about 50 GWd/t$_U$ and a restructured volume fraction of the dark zone ≈ 0.5 at about 40 GWd/t$_U$. The dark zone can overlap with the HBS zone.

The authors describe the fission gas behaviour in the dark zone in the same way as they describe the FG behaviour in the HBS (details of this last description can be found in [Simon, Aagesen, et al. 2023]). In particular, they neglect intra-granular bubbles and dislocations, the subgrains of the dark zone are assumed to have a constant radius equal to 150 nm and the inter-subgrain bubbles are considered as inter-granular bubbles.
Most importantly, in their model the only way in which gas can be released from the dark zone is through micro-cracking and no diffusion of gas through the subdomain boundaries is considered. This is coherent with the fact that there is no evidence of interconnection of precipitation bubbles, as explained in 4.1.1. However, there is no evidence that the fuels that will be used in the validation part (Chapter 7) have been subjected to micro-cracking.

The idea of an effective burnup is interesting. However, from our point of view, the idea of a restructured volume fraction is less adequate for subdomains than for the HBS formation, which instead happens by patches (the distinction between the "sound" part of the grain and the restructured part is clear). Subdomains appear more uniformly (at a given radius of the pellet) and become more and more disoriented.
So, in the model, the effective burnup could be used to trigger the subdomains onset, but also as a parameter for physical quantities related to the subdomain boundaries.

4.2. Description of the subdomains in MARGARET

4.2.1. General choices for the new "subdomain state"

In the version of MARGARET we started from, 3 possible state of the fuel were considered: the “sound” state, the restructuring state (that describes the formation of HBS at the outer zone of the pellet), and a totally restructured state (HBS). Each state has a different set of variables and associated ODEs, and incorporates different models to represent the behaviour of the fission gas and bubbles.

To describe the effect of the subdomain formation, we added one more possible state, the "subdomain state". The state of the fuel changes from the "sound" to the subdomain state once the effective burnup and temperature thresholds are reached (see Sections 4.1.3 and 4.1.4).
In practice, the effective burnup is calculated as in eq. 4.1, but with different values of the parameters T_{low} and T_{high}. These two values, together with the value of the effective burnup threshold, have been chosen during the validation of the code, following what have been written in Section 4.1.3. They are reported in Section 7.1.10.

When subdomains appear, the intra-granular ODE variables are split between variables that represent quantities in the subdomains and variables that represent quantities in the subdomain boundaries: The dissolved gas in the grain becomes dissolved gas in the subdomains, the intra-granular bubbles become intra-subdomain bubbles and the intra-granular pores become inter-subdomain pores. Moreover, in the subdomain boundaries, we consider the formation of the second population of intra-granular bubbles (the precipitation bubbles, also called inter-subdomain bubbles).
The precipitation bubbles are introduced with a size comparable to the intra-granular bubbles and then they grow more than the latter by capturing vacancies and Xenon atoms diffusing on the subdomain boundaries.

For the moment, we do not consider the effective burnup as a parameter for physical quantities related to the subdomain boundaries. Therefore, we currently do not model the effects of the increase of the disorientation of the subdomains with burnup.

In the subdomain state, the major pathway by which the gas produced in the grains reaches the grain boundaries changes: in the "sound" state, the dissolved gas in the grains[4] diffuses "directly" towards the grain boundaries.
In the subdomain state, the gas is produced in the subdomains and diffuses towards the precipitation bubbles, the inter-subdomain pores an the subdomain boundaries. The gas dissolved in the subdomain boundaries behaves similarly to the inter-granular dissolved gas: it can be re-dissolved into the subdomains by dynamic re-solution; while it diffuses in the subdomain boundaries, it can be trapped by the precipitation bubbles and the inter-subdomain pores; from those cavities it can be re-dissolved back into the subdomains and the subdomain boundaries by dynamic and thermal re-solution. Considering also the continuous contribution of the gas coming from the subdomains, a dynamic equilibrium is established between all these phenomena, and the gas who remains dissolved in the subdomains diffuses toward the grain boundaries.
Since the distance that the dissolved gas atoms have to cover to reach the grain boundaries in the "sound" state is larger than the distance that the dissolved gas atoms in the subdomains have to cover to reach the subdomain boundaries in the subdomain state, and since the diffusion coefficient of Xenon on the subdomain boundaries is

4. That is not trapped in the intra-granular bubbles

modelled as higher than the bulk diffusion coefficient, in the subdomain state, we expect that a higher flux of gas will reach the grain boundaries. Consequently, we expect, after the subdomain formation, a higher fission gas release, that could possibly also happen by long range diffusion of gas along grain boundary towards the fragment surface (see 1.3.3).

Basically, we have to model a 3-stage diffusion process:
— Subdomains to subdomain boundaries
— Subdomain boundaries of the grain to grain boundaries
— Grain boundaries of the fragment to the fragment surface

Through the usual homogenisation method the 2 last stages will be described as a diffusion process in spheres, using the concentration of gas on subdomain (or grain) boundaries diluted to become homogeneous concentrations in the respective sphere (grain or fragment).
It makes however three 1D-spheric diffusion problems to be solved, which may introduce too much variables and ODE equations and an unacceptable raise of computational time, if each sphere was meshed to resolve these problems.
In a work that preceded my thesis[5], it was studied the conditions in which a diffusion problem in a sphere may be replaced by a one-variable model, the one-variable in question being the mean concentration in the sphere.
It appeared that if the conditions are not far from the permanent diffusion regime of production / diffusion, the replacement could be done, and the way to do so was determined too.
If the characteristic time R^2_{sphere}/D (D being the diffusion coefficient) is short, the one-variable model can be used. This is the case for the diffusion of the gas in the subdomains, whose radius is about equal to 0.5 [μ m] [Dowek 2021].
In MARGARET, for each 1D-spherical problem of diffusion, a choice has been made available, to model it as a meshed problem with one variable per concentric shell in the sphere, or as a one-variable model.
In the case of the 3-stage diffusion process above, the one-variable model is used for the gas diffusion in the subdomain only, while the 2 other problems are resolved using meshes.

Post irradiation examinations [Dowek 2021] showed that the population of precipitation bubbles seems to slightly decrease with burnup: in the fuel with the highest burnup (73 GWd/t_U) the bubble concentration decreases of about one half with respect to the fuel with the lowest burnup (61 GWd/t_U) for both the 2 radius considered. The researchers [ibid.] speculate that the mechanisms involved for this decrease in the concentration of precipitation bubbles are the Ostwald ripening and the coalescence. Ostwald ripening implies re-solution combined with and advantage for bigger bubbles (i.e. less re-solution from them). The involvement of the coalescence mechanism is corroborated by the measurement of bubbles in which we can still distinguish the two

5. A feasibility study for the model developed during the thesis

former bubbles prior to the coalescence, however, this phenomenon should remain limited due to the low bubble movement during base irradiation.
Contrary to the expectations, for the fuel with a burnup in between the last two, (63 GWd/t_U) the number of bprec bubbles increased by 2 times with respect to the ones in the lowest burnup fuel (61 GWd/t_U).
From the measurements and the analysis presented in [Dowek 2021], we can then deduce that:

— The order of magnitude of the concentration of the precipitation bubbles does not change with the burnup;
— The variation in the measurements between different fuels seem more important than any indication on the decrease in the concentration with burnup;
— The mechanisms that determine the change in the concentration of the precipitation bubbles remain mostly unknown.

Therefore, in MARGARET, we considered a constant concentration of precipitation bubbles during base irradiation. This hypothesis can be changed in the future, if more experimental results are published and when the mechanisms that determine a change in the concentration of precipitation bubbles are clarified.

In the version of the code that we produced, no overlap between the HBS and the subdomain zone is considered, since in the fuels described in [J. Noirot, Dowek, et al. 2022; Zacharie-Aubrun et al. 2022; Dowek 2021] such an overlap was not present[6].

In the next Section, I outline the methodology used to build the ODE system for the subdomain state. The complete ODE system is presented in Appendix G, together with the relations at the interfaces sub-domain / sub-domain boundary and sub-domain boundary / grain boundary.

4.2.2. New state in MARGARET: methodology to build the new ODE system

In brief, the principles that led to the building up of the ODE system are the followings:

— The behaviour of the fission gas and bubbles inside the subdomains is the same as the one inside the grain in the "sound state". The only difference is that the dissolved gas is described by one scalar variable (C_{XeM}) instead of a 1D spherical field (C_{Xe} depending on the position in the grain) in the "sound state";
— The behaviour of the fission gas and bubbles on the subdomain boundaries is inspired from what had been done for the long-range diffusion along the grain

6. Subgrains separated by Low Angle Grain Boundaries (LAGB) have been detected in the HBS zone, but no subgrain separated by High Angle Grain Boundaries (HAGB) have been seen where the subdomain form.

boundaries for Helium before my thesis. However, I paid a particular attention to the inter-subdomain source term (gas coming from the subdomain), and I employed the expressions that I developed in Chapter 3 for the trapping of inter-subdomain gas into inter-subdomain bubbles, and re-solution from these bubbles into the subdomains and subdomain boundaries;

— The behaviour of fission gas and bubbles on the grain boundaries was constructed as a synthesis of what was done before in MARGARET for fission gas and Helium, the work performed in Chapter 3, plus a special attention to the intergranular source term coming from the gas diffusing along the inter-subdomain boundaries.

This new state has been implemented in the code by my supervisor. I contributed to the verification of the gas balance and the debugging process.

5. Consistent derivation of thermal vacancy trapping by cavities

Sommaire

5.1. Literature review . . . 132
5.1.1. Classical experimental data related to the fuel swelling . . . 132
5.1.2. Experimental values, atomic scale and cluster dynamics simulations of the volume per atom in different situations and bubble types . . . 133
5.1.3. Volume brought with the gas atoms when they diffuse . . . 136
5.1.4. Volume contribution to the bubbles in FGR codes . . . 137
5.1.4.1. Intra-granular bubbles . . . 137
5.1.4.2. Inter-granular bubbles . . . 137
5.1.4.3. MARGARET approach before this thesis . . . 138
5.1.5. Conclusion on the literature review . . . 139
5.2. A new model for the phenomena of trapping of thermal vacancies by cavities: the "Generalized Speight Model" . . . 141
5.2.1. Derivation of the model for the "Sound" state . . . 141

As we will see, the behaviour of the Fission Gas in general, and the fuel swelling in particular, cannot be correctly predicted without some kind of parallel description of point defects and defect clusters present in the fuel and their interactions with the gas bubbles.

The objective of this Chapter is to derive the simplest, but hopefully most consistent modelling of point defects and defect clusters as possible. To do so, we have to select the main experimental facts and atomistic simulation results regarding the in-pile and out-of-pile behaviour of bubbles and use them as a guide for our derivation.
The final purpose is to predict correctly the bubble volume evolution, and hence the fuel swelling.

After a literature review on the subject, I will present the model built to describe the behaviour of thermal vacancy developed within the framework of my thesis.

5.1. Literature review

Before passing to the critical analysis of the literature on this subject, one important point valid for all the discussion need to be addressed:

A priori, every kind of defect may be trapped by a bubble:
— Different defects that include a Xenon atom, like interstitial Xe, 'Xe atom + Schottky defect' ($\{Xe_U : 2V_O\}$, using the Kröger-Vink notation [Kröger et al. 1956]) etc... .
— A bound Schottky defect (all the 3 typologies), a small vacancy cluster.
— Auto-interstitials.
— And so on... [1].

The way all the items behave depends on the mobility of each kind of defect, on the interface conditions at each sink (for example, the equilibrium concentration of defects at the vicinity of the bubble, that depends on the bubble inner pressure, on the Laplace pressure and on the energy of each type of defect), on the relative strength of different sinks, like dislocation loops, dislocation lines, grain boundaries etc... .

However, due to the limit in the computational time, in MARGARET, we are limited in the number of variables that we can consider. Therefore, we cannot include equations that describe the evolution of all the defects (both linear and punctual) that we can find in a nuclear fuel under irradiation. We need to concentrate our attention to the least amount of defects that allow us to correctly predict the behaviour of the fission gas and the swelling in the different conditions at which the fuel can operate.

In the following bibliography Sections, I will review the "classical" experimental data related to the fuel swelling, then the cutting-edge experiences that give access to the volume per gas atom, V_{at}, in different kinds of bubbles. Then, I will summarize the indications that we have on the volume brought with the gas atoms when they diffuse, and finally how the contribution of volume to the bubbles has been modeled so far in literature , and in MARGARET in particular.

5.1.1. Classical experimental data related to the fuel swelling

There are different kinds of measurements that are linked with the swelling of the fuel:

— Density measurements of the fuel pellet, which give the total swelling of the pellet (including the solid swelling, that is to say the swelling of the solid part of

1. The list comprehends charged defects as well

the fuel).
— Porosity measurements along the radius of the pellet.
— Measurements of the relative inter- and intra- guanular porosity, which estimate the contribution to the total porosity due to the inter- or intra- granular bubbles.
— Measurements of the bubbles size
— Measurements of the radius of the cladding

First of all, what these measurements say is that the swelling of the fuel is more important than the part of the swelling determined by the increase in the number of atoms in the matrix due to fission of the Uranium atoms (solid swelling).
Then, as a general trend, it appears that the swelling tends to increase with temperature and burnup.
At high burnup, the formation of the HBS determines a considerable increase in the swelling of the fuel.
After a power ramp, both intra- and inter- granular bubbles grow substantially. Large inter-granular bubbles interconnections can be seen. Moreover, it is possible to measure a wide increase in the radius of the cladding.

Some of the measurements of the swelling of the fuel are presented in [L. Noirot 2011], while an in-depth comparison with MARGARET predictions will be performed in Chapter 7.

5.1.2. Experimental values, atomic scale and cluster dynamics simulations of the volume per atom in different situations and bubble types

The measurements of the volume per atom of the Xenon bubbles in the UO_2 fuel are rare and difficult to perform. Nonetheless, there are in literature some measurements that can give us some valuable information.

Moreover, in recent years, atomic scale and cluster dynamics simulations have been used by researchers to better understand the behaviour of Xenon bubbles under different irradiation conditions.

We can conceptually divide measurements and simulations depending on the position of the bubble analyzed (inter- or intra- granular) and on the different conditions at which the fuel specimens have been operated or simulated (base irradiation or power ramp).

Nano-bubbles during base irradiation

Experiments suggest that, throughout base irradiation and independently on the burnup of the fuel, the volume per atom, V_{at}, in intra-granular nano-bubbles stays close to Ω [Nogita et al. 1997; Nogita et al. 1998]. Ω is the volume of a Schottky defect (UO_2 site missing, equal to 40.9×10^{-30} m^3).

T. Beigbeder [Beigbeder 2023] performed MD simulations to study the behaviour of small (bubbles with a volume of 25 Ω and $R_b = 0.6$ nm) intra-granular Xenon bubbles in UO_2. One of the things that he studied was the stability of the bubbles at different xenon-vacancy compositions. He found that not all compositions are stable: bubbles with a $V_{at} < 0.7\Omega$ or with a $V_{at} > 1.25\Omega$ quickly[2] emit defects, like vacancies (for $V_{at} > 1.25\Omega$) and auto-interstitials (for $V_{at} < 0.7\Omega$), until their volume per atom falls in the stable region $0.7\Omega < V_{at} < 1.25\Omega$.

Intra-granular bubbles during power ramps

C. Cagna [Cagna 2016] performed Post Irradiation (PI) examinations on a specimen irradiated at a burnup of 39 GWd/t_U and power ramped at a linear power equal to 470 [W/cm] for 12h. She analyzed two big intra-granular bubbles in the center of the pellet (with $R_b = 1.1$ and 1.5 μm) and found a V_{at} equal to 2.2Ω and 3.5Ω (table 14 of the Ref.). She also determined an average value for the intra-granuar bubbles, equal to 2.6Ω (pag. 58 of the Ref.).

Precipitation bubbles during base irradiation

L.E. Thomas [Thomas 1991] studied spent PWR nuclear fuels with burnup ranging from 27 to 48 GWd/t_U. He analyzed bubbles on dislocations with sizes between 20 and 100 nm. Since the fuels with the highest burnup are close to or higher than what can be the threshold for the subdomains formation (see Section 4.1.3), we can say that at least some of the bubbles studied by Thomas can be listed as precipitation bubbles, and therefore we can compare MARGARET predictions with those measurements. Thomas measured a volume per atom V_{at} in all the bubbles analyzed in the order of 2 - 3 Ω.

A more in-depth analysis of the precipitation bubbles comes for the work of R. Dowek and colleagues [Dowek 2021]. They report average V_{at} in the range of 5 to 10×10^{-5} m^3/mol $\approx$ 2 to 4 Ω, with a couple of exceptions in the outside part of the precipitation zone of the 73 GWd/t_U sample, where the average V_{at} reaches values of $\approx 8\ \Omega$.

2. At a time scale that can be studied using MD simulations

Precipitation bubbles during power ramps

Unfortunately, as far as we know, there is no published measurement nor simulation of the V_{at} of precipitation bubbles after a power ramp.

Isolated inter-granular bubbles

J. Noirot and co-workers [J. Noirot, Aubrun, et al. 2009] performed PI examinations on two specimens irradiated at a burnup of 73 and 83 GWd/t$_U$. They measured a V_{at} at the center of the pellet equal to 7.9Ω, while at 0.24R equal to 4.7Ω.
However, they point out that they could not be sure that the measured bubbles were inter-granular, since, in the part of the fuel analyzed, it was difficult to distinguish between inter- and intra- granular bubbles.

C. Cagna [Cagna 2016] performed PI examinations on a specimen irradiated at a burnup equal to 73 GWd/t$_U$. At 0R, she found an average V_{at} equal to 2Ω. However, in her measurement she did not distinguished between intra- and inter- granular bubbles.

W. D. Neilson and co-workers [Neilson et al. 2024] developed a cluster dynamic model to predict the steady-state concentration of defects on the grain boundaries of the UO_2 fuels under irradiation. The model was developed to study irradiation-induced creep, but it gives also important information on the interaction between defects (vacancies and auto-interstitials) and inter-granular bubbles.
On the grain boundaries, the source of defects in their model is due to the production by ballistic cascades (directly due to irradiation) and due to the arrival of defects through diffusion from the bulk (this second source of defects comes from another model referenced in the paper). Then, defects on the grain boundary can recombine or be trapped by sinks. The prevalent sink of defect on GBs are inter-granular bubbles. The amount of Xenon in the inter-granular bubbles is considered constant (trapping = re-solution), while the amount of Schottky defects in the bubbles can change: if a bubble traps a vacancy, the bubble grows by a volume equal to Ω, while the opposite is true if a bubble traps an auto-interstitial. The ratio Xe atoms / Schottky defects in the inter-granular bubbles is tracked, and the tendency for defects to be trapped inside the bubbles changes with a change in this ratio. In practice, if bubbles are too much pressurized, the trapping of auto-interstitials is penalized, while the same is true for vacancies if bubbles are under-pressurized.
Their model shows that, at low temperatures (less than about 1600K), the source of auto-interstials to the grain boundaries is higher that that of vacancies, due to the higher mobility of auto-interstitials at low temperatures. This higher source of auto-interstitials from the grain determines an higher flux of auto-interstitials to the inter-granular bubbles, making them over-pressurized. At this point, the concentration of auto-interstitials at the GB is regulated by the presence of other sinks and by the re-combination with vacancies.
This kind of description predicts very high pressurization of the inter-granular bub-

bles. The researchers, however, add that: *"In reality a pressure relief mechanism may initiate that prevents full pressurization"* of inter-granular bubbles. This mechanism, not taken into account in the model, can very well be the production of thermal vacancies on the GB that will be described in Section 5.1.4.2, or the transformation of the auto-interstitials on GB into normal sites, which induces a swelling of the two adjacent grains, and an increase of the distance between the centers of mass of these two grains.
At high temperatures (higher than about 1600K), their model predicts that Uranium vacancies predominate and reach their equilibrium concentration.

5.1.3. Volume brought with the gas atoms when they diffuse

The bibliography on this subject gathers the articles [Perriot et al. 2019; C. Matthews et al. 2020; Cooper, C. Matthews, et al. 2025] that are presented in more details in Section 7.1.
At temperatures above ≈ 1200K, the Xe atoms trapped by intra-granular bubbles through diffusion might bring a volume of 4Ω, and 2Ω at very high temperature [C. Matthews et al. 2020].
The reason why the 4Ω clusters survive in their simulation is because auto-interstitials annihilate on sinks (bubbles).

In a recent article of the same team [Cooper, C. Matthews, et al. 2025], Cooper and co-workers explained the over-pressurization of the intra-granular bubbles below 1500K (1227°C) by the fact that irradiation-induced auto-interstitials are highly mobile relative to vacancies, and that they are trapped in larger amount by cavities, keeping the bubbles over-pressurized. Also, at $T < 1000$K (727°C), interstitials Xe is the largest contribution for Xe diffusion [ibid.]. Interstitial Xe would bring no volume when trapped by a bubble.
However, below ≈ 1000K, the a-thermal diffusion of Xe experimentally predominates. This type of diffusion can be understood as a periodically mixing of the atoms in the fission spikes. Unfortunately, the addition or removal of volume to a bubble due to an interaction with a fission spike has not been studied yet.
Moreover, these cluster dynamic simulations do not include the evolution of the bubbles and dislocation loops, so far.

What we can keep in mind from those works is that auto-interstitials may play an important part in the behaviour of bubbles during base irradiation.

5.1.4. Volume contribution to the bubbles in FGR codes

5.1.4.1. Intra-granular bubbles

Nano-bubbles

A simple way to reproduce the measured V_{at} of intra-granular nano-bubbles during base irradiation (V_{at} close to Ω, see Section 5.1.2) is to neglect the flux of vacancies (and auto-interstitials) into intra-granular bubbles, and consider a constant gas density in the nano-bubbles equal to 1 [Ω / atom] ≈ 5.4×10^3 [kg / m^3]. This is the description used by some meso-scale Fission Gas models [Pastore, Militello, et al. 2023].
However, this kind of modelling will face difficulties for high temperature conditions.

Precipitation bubbles

In [Simon, Gamble, et al. 2024], which is, at our current knowledge, the first Fission Gas model that simulate the subdomains formation, the precipitation bubbles are treated as inter-granular bubbles (see Section 4.1.4 for a more complete review of [ibid.]).

5.1.4.2. Inter-granular bubbles

Meso-scale Fission Gas models usually consider vacancies as the only other type of defect, apart from dissolved Xenon, which interacts with inter-granular bubbles.
The most widely adopted model [White 2004; Pastore, Luzzi, et al. 2013], used to describe the influence of the inter-granular vacancies to the growth of the inter-granular bubbles in UO_2 during irradiation conditions, comes from a paper of M.V. Speight and W. Beere [SPEIGHT et al. 1974], who refined an original description made by Hull and Rimmer [Hull et al. 1959]. The model is based on thermodynamics (irradiation does not play a role), so we can say that this model is about thermal vacancies. The idea is the following: cavities grow and shrink by absorbing and emitting vacancies that are generated or destroyed on the grain boundary.
If we use the further hypothesis that each vacancy gained or emitted has a volume equal to Ω, the volume flux due to vacancies at the lenticular cavities of circular projection can be written as:

$$\frac{dV_{cavj}^{vac}}{dt} = \frac{-8\pi}{(3-F_c)(1-F_c)+2ln(F_c)} \frac{D_{Uj}e_{pj}}{kT} \left(\sigma_{ext} + P_{int} - \frac{2\gamma sin\theta}{R_{cavj}}\right) \Omega C_{cavj} \quad (5.1)$$

Where D_{Uj} is the auto-diffusion coefficient of Uranium on the grain boundary, σ_{ext} is the externally applied stress (which, in MARGARET, is an input parameter given by ALCYONE at each time step), P_{int} is the pressure inside the cavity, γ is the UO_2/gas specific surface energy, $\frac{R_{cav}}{sin\theta}$ is the radius of curvature of the cavity, $\frac{2\gamma sin\theta}{R_{cav}}$ is the Laplace

pressure, F_c is the fractional coverage of the grain boundary given by the cavities.

In eq. 5.1, the first ratio is positive, and $\sigma_{ext} = -P_{hydro}$. The inter-granular cavities grow when their inner pressure minus the Laplace pressure is higher than the counter-pressure exerted on the fuel.

The rate of vacancy creation can be calculated through an energy balance, by equating the sum of the work of the external forces exerted on the solid (the internal pressure of the bubbles minus the Laplace pressure and the externally applied stress) and the chemical potential of the created (or destroyed) cavities. Equation 5.1 can then be derived by considering the flux of vacancies that arrive from the grain boundary (where they are created) to the cavities due to the difference in the chemical potential near or far from the bubbles. The kinetic of the vacancy flux is determined by D_{Uj}.

A very important point in the derivation of eq. 5.1 is that the growth of the inter-granular vacancies is the result of both:
— The flux of vacancies that arrive from the grain boundary
— The direct volume gain due to the continuous production of vacancies on the grain boundary, and the consequent moving apart of the two adjacent grains with a velocity v_{move} (see [SPEIGHT et al. 1974]).

Equation 5.1 allows to predict both that at high temperatures the growth of the inter-granular bubbles is faster than the one of the isolated intra-granular bubbles and that a higher externally applied counter-pressure limits this growth. Both of these tendencies are backed up by observations: Figure 9. of [NOIROT et al. 2009] shows how inter-granular bubbles after a power ramp are bigger than intra-granular ones, figure 6.3 (a) shows how inter-granular bubbles during base irradiation are bigger than intra-granular ones, and the works of Kashibe and co-workers [Kashibe et al. 1997; Kashibe et al. 2000] highlight how a higher externally applied counter-pressure limits the growth of inter-granular bubbles.

5.1.4.3. MARGARET approach before this thesis

In the version of MARGARET that preceded this thesis, two different contributions to the volume of the bubbles, both intra- and inter- granular, were considered:

— A contribution of $\zeta\Omega$ with each atoms of Xenon, where ζ was taken equal to 1. The historical reason for this choice is that the most favourable position for Xenon in UO_2 is the trivacancy (bound Schottky defect) and that Xe diffuses in substitution. This choice gave quite good results for the Xenon density inside the bubbles, compared to experiments.
— A different contribution due to isolated vacancies (see Section 1.3.4).
— For inter-granular bubbles, this second contribution followed the approach

described in Section 5.1.4.2. In particular, no exchange of vacancies from inter-granular pores (weakly pressurized) to inter-granular bubbles was considered.

As expressed in Section 1.3.4, the contribution due to isolated vacancies lacked coherence between base irradiation and power ramp conditions, and between the different types of cavities modelled in MARGARET.

5.1.5. Conclusion on the literature review

For nano-bubbles in base irradiation conditions, our model needs to predict a volume per Xenon atom close to Ω.
In base irradiation and for bubbles situated on subdomain and grain boundaries, the volume per Xe atom rises to a few Ω.
During power ramps (high temperatures), a large vacancy income have to happen to explain the wide inter-granular bubble interconnections and the high swelling of the fuel.

In the new modelling of MARGARET, we have kept two different terms to describe the change in the volume of the bubbles due to point defects and defect clusters: the term in $\zeta\Omega$ accompanying each Xe entering the bubble and a term due to the income of isolated vacancies. However, their new meaning is now the following:

Vacancies and auto-interstitials are produced in equal quantity by irradiation. If both were captured the same way by a bubble, it would not grow nor shrink.
However, simulations [Cooper, C. Matthews, et al. 2025] have shown that, below ≈ 1500K (1227°C), irradiation-induced auto-interstitials are highly mobile relative to vacancies. At the same time, dislocation loops are probably less attractive traps (energetically or geometrically, in the sense of the probability to encounter a bubble vs the probability to encounter a dislocation loop) for auto-intertitials compared to bubbles whose V_{at} is larger than 0.7Ω. The result is that auto-interstitials are trapped by cavities in larger amount with respect to vacancies, as soon as $V_{at} > 0.7\Omega$, keeping the bubbles over-pressurized. The auto-interstitials that cannot be trapped by bubbles (when $V_{at} < 0.7\Omega$) gather into dislocation loops or reach the grain boundaries.
This is not the whole story though, otherwise bubbles would simply gather auto-interstitials until they saturate (the point where they would re-emit any auto-interstials that they trap). The volume per atom that corresponds to this limit (0.7Ω) is lower than Ω [Cooper, C. Matthews, et al. 2025; Beigbeder 2023], which is the value that is actually measured for intra-granular bubbles. Other phenomena, active at these temperatures during irradiation, could explain this difference:

— Xe atoms may bring a volume higher than Ω to the bubbles that trap them.
— The interaction between bubbles and fission spikes may re-solute less vacancies than Xe atoms.

$V_{at} \approx \Omega$ would then be the result of the net flux of volume due to auto-interstitials

and Xenon arriving to the bubbles, and fission spikes interacting with them.
The term in $\zeta\Omega$ accompanying each Xe entering the bubble[3], with $\zeta = 1$, would then be a synthesis of this complex behaviour, and allow us to predict the correct V_{at} of the intra-granular nano-bubbles.

In the case of inter-granular bubbles during base irradiation, grain boundaries may be a stronger sink[4] than dislocation loops for auto-interstitals. If so, inter-granular bubbles would trap less auto-interstitials than intra-granular ones, and their V_{at} would then be higher.
Alternatively, temperature could have a still limited, but greater influence on inter-granular bubble growth as $D_{v,j}$ (diffusion coefficient of vacancies on the grain boundary) is higher than D_v (diffusion coefficient of vacancies on the grain boundary). This is even more true since grain boundaries can be a source of vacancies, which are produced there due to the over-pressurization of the inter-granular bubbles.

The diffusion coefficient of vacancies on dislocations is also higher than the one in the bulk, therefore we can imagine how vacancies produced on the GB can diffuse toward the precipitation bubbles, determining a non-negligible contribution to the volume of these bubbles. Otherwise, the dislocations that make up the subdomain boundaries may be a stronger competitor for auto-interstitials than dislocation loops in the bulk. Either way, we can expect a V_{at} of the precipitation bubbles higher than the one of the intra-granular bubbles.

Any way, if temperature is risen higher than about 1200°C (See Appendix C), like in ramp conditions, new vacancies, namely the thermal vacancies, become dominant, while thermal auto-interstitials are like inexistant.
This induces a totally different behaviour, dominated this time by those thermal vacancies, and that induces much more swelling.

Our second term of volume income with vacancies alone can be interpreted as the income of those thermal vacancies. We expect this term to remain negligible compared to the term in $\zeta\Omega \times \Phi_{Xe}$ (Where Φ_{Xe} is the Xenon flux towards the bubbles) in base irradiation[5], but preponderant during power ramp conditions.

The following Section and Appendix H explain how this thermal vacancy term is calculated for the "sound", subdomain and HBS states. However, we expect that, during irradiation, thermal vacancies will give a negligible contribution to the volume of HBS cavities, because of the low temperature at the periphery of the pellet. Appendix I presents a further contribution to the volume of the HBS cavities, due to irradiation induced creep.

3. And the same term accompanying each Xe emitted by re-solution.
4. Transformation of auto-interstitials on GB into normal sites, and swelling.
5. At least for bubbles imbedded in the bulk. Inter-granular and precipitation bubbles may be feeded by thermal vacancies in base irradiation too.

5.2. A new model for the phenomena of trapping of thermal vacancies by cavities: the "Generalized Speight Model"

As described in the previous Sections, the features that we would like to have in a model of the behaviour of vacancies in the nuclear fuel can be summarized in this way:

For base irradiated fuels:
— Predictions of the V_{at} of nano-bubbles in the order of Ω, and therefore a flux of thermal vacancies towards the intra-granular bubbles that is negligible.
— Predictions of the V_{at} of inter-granular bubbles and precipitation bubbles in line with experiments (2-4 Ω).

For power ramped fuels:
— Large flux of thermal vacancies towards all the populations of bubbles.

For all operating conditions, or at least at high temperature:
— The formation of vacancies on the grain boundary due to the high pressure of the inter-granular bubbles.
— Use of a coherent description of the behaviour of thermal vacancies, starting from the use of a single expression of D_{Uj}, independent of the burnup (See Section 7.1.5).

Moreover, since pores, both intra-granular and inter-granular, at the beginning of irradiation have pressures below the equilibrium pressure, we expect that a transfer of vacancies from pores to bubbles might happen due to the difference in the equilibrium vacancy concentrations near the different cavities.

In the next Section, I will derive what we call the "Generalized Speight Model" for the "sound" state. Similar derivations for the subdomain and the HBS states, considering the appropriate differences, are presented in Appendix H.

5.2.1. Derivation of the model for the "Sound" state

We start by making the hypothesis that, as for the expression derived by M.V. Speight and W. Beere [SPEIGHT et al. 1974], the vacancies can be produced and destroyed on the grain boundary. Moreover, vacancy can be "produced" at the interfaces, like at the free surfaces. In this latter case, the "production" of vacancies is expressed through the use of a limit condition.

If we call $\beta_{v,j}$ [Vacancies / m^3 of fresh fuel / s] the rate of production of vacancies per m^3 of fresh fuel and v_{move} [m / s] the velocity by which two grains that share a grain boundary move away one from the other due to the formation of vacancies on the grain boundary, we obtain the following relation:

$$v_{move} = \frac{\beta_{v,j}\Omega}{F_j \frac{3}{2A_{gg}}} \tag{5.2}$$

In the equation above, $\frac{\beta_{v,j}}{F_j \frac{3}{2A_{gg}}}$ is the rate of production of vacancies per m^2 of bare grain boundary.

Figure 5.1 shows a scheme of the process[6].

We can now write the variation of the volume of the cavities due to the behaviour of the thermal vacancies: the inter-granular cavities will grow due to both the moving away of the two nearby grains and the trapping of vacancies.
The variation of the volume of the inter-granular cavities can be written as:

$$\left.\frac{dV_{cavj}}{dt}\right|_{vac} = v_{move}\frac{3}{2A_{gg}}F_{cavj} + \Phi_{v,j->cavj} \times \Omega + \Phi_{v,bulk->cavj} \times \Omega \tag{5.3}$$

Where the first term represents the growth of the cavity due to the moving away of the two nearby grains, $\Phi_{v,j->cavj}$ [Vacancies / m^3 of fresh fuel / s] is the vacancy flux from the grain boundary to the inter-granular cavities due to the difference in the chemical potential of the vacancies on the grain boundary far from the cavities and the same chemical potential near the cavities, $\Phi_{v,bulk->cavj}$ [Vacancies / m^3 of fresh fuel / s] is the vacancy flux from the bulk to the inter-granular cavities due to the difference in the chemical potential of the vacancy on the bulk far from the cavities and the same chemical potential near the cavities.

The variation of the volume of the intra-granular cavities can be written as:

$$\left.\frac{dV_{cav}}{dt}\right|_{vac} = \Phi_{v,bulk->cav} \times \Omega \tag{5.4}$$

Where $\Phi_{v,bulk->cav}$ [Vacancies / m^3 of fresh fuel / s] is the vacancy flux from the bulk to the intra-granular cavities due to the difference in the chemical potential of the vacancies in the bulk far from the cavities and the same chemical potential near the cavities.

To calculate the different terms in equations 5.3 and 5.4 (v_{move} and all the fluxes) we need:

6. The flux of vacancies coming from the free surfaces and the exchange of vacancies with the bulk of the grain are not included in the scheme.

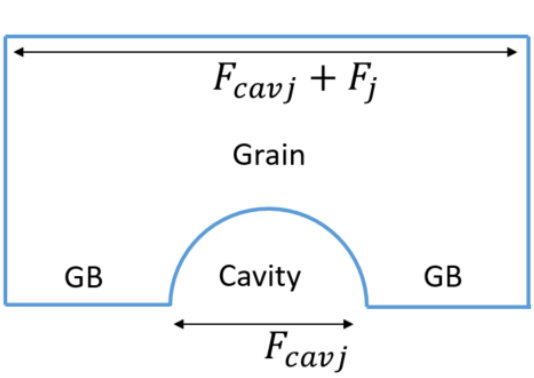

(a) Starting situation.

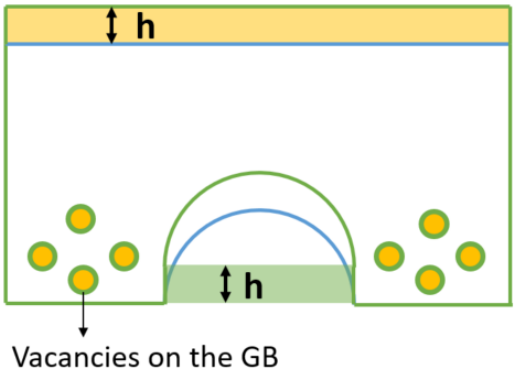

(b) Production of vacancies on the GB and moving away of the two grains (cavity growth due to the moving away of the two grains).

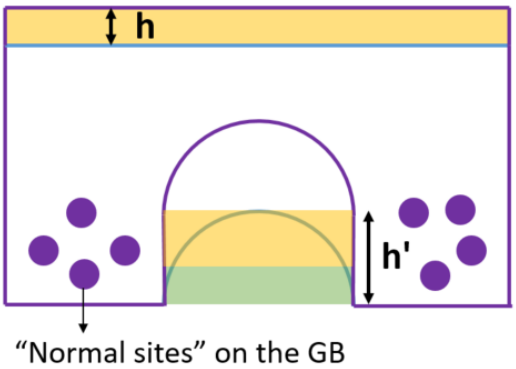

(c) Trapping of vacancies by the inter-granular cavity (cavity growth due to the trapping of vacancies). The vacancies on the GB are replaced by "normal sites" (flux of atoms opposite to the vacancy flux).

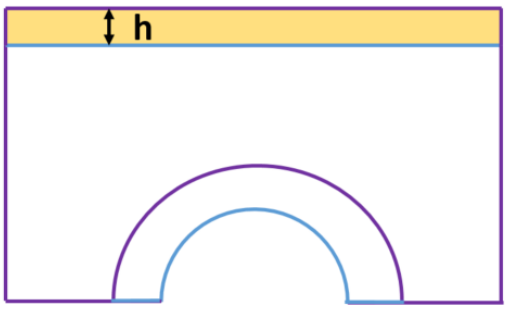

(d) Final situation. The bubble adopt an optimal shape (no change of volume).

Figure 5.1. – Scheme that represents the production of vacancies on the GB, the moving away of the grains due to production of vacancies and the growth of the inter-granular cavities due to both the moving away of the grains (green) and the trapping of vacancies produced on the GB (yellow). The process, in reality, is continuous and everything happens at the same time.

— The production rate of vacancies on the grain boundary, $\beta_{v,j}$, so that we can calculate v_{move}.
— The average concentration of vacancies on the grain boundary, $C_{v,j}$, so that we can calculate $\Phi_{v,j->cavj}$.
— The average concentration of vacancies in the bulk, C_v, so that we can calculate $\Phi_{v,bulk->cavj}$ and $\Phi_{v,bulk->cav}$.

Once we know these three quantities, we can obtain the contribution of vacancies to the growth of all the cavities in the fuel. To do that, since there are 3 unknowns, we need 3 equations.

Our model is for thermal vacancy, and consequently it does not take into account irradiation. Moreover, the only source or sink considered are the free surface, grain boundaries and cavities. Dislocations are ignored for the practical reason that they are not really included in the fuel representation for the moment[7].
The hypothesis that is behind this choice is that, in power ramp conditions (where thermal vacancies are preponderant), the bubbles are more attractive sinks for vacancies than dislocations.

This being said, we have the two balance equations for the average concentration of vacancies in the bulk, and on the grain boundary:

$$\frac{dC_v}{dt} = -\sum_{cav}\Phi_{v,bulk->cav} - \sum_{cavj}\Phi_{v,bulk->cavj} - \Phi_{v,bulk->j} \tag{5.5}$$

$$\frac{dC_{v,j}}{dt} = \beta_{v,j} - \sum_{cavj}\Phi_{v,j->cavj} - \Phi_{v,j->ext} - \Phi_{v,j->bulk} \tag{5.6}$$

Where $\Phi_{v,bulk->j}$ is the flux of vacancies from the bulk to the bare grain boundary and $\Phi_{v,j->ext}$ is the flux of vacancies from the grain boundaries far from the free surfaces to the exterior (which is the intersection of grain boundary and free surface).

We then make the further hypothesis that we are under quasi-steady state, and therefore neglect the temporal derivatives.
Using this hypothesis, we obtain:

— The permanent regime for the vacancies in the bulk:

$$\sum_{cav}\Phi_{v,bulk->cav} + \sum_{cavj}\Phi_{v,bulk->cavj} + \Phi_{v,bulk->j} = 0 \tag{5.7}$$

— The permanent regime for the vacancies on the GB:

7. An equation for the dislocation density, ρ_d, is included in the ODE system. But ρ_d serves only to trigger the HBS formation. Up to now, no explicit influence of ρ_d on bubbles, vacancies has been taken into account in the code.

$$\beta_{v,j} - \sum_{cavj} \Phi_{v,j->cavj} - \Phi_{v,j->ext} - \Phi_{v,j->bulk} = 0 \tag{5.8}$$

If we sum the above equations, we obtain:

$$\beta_{v,j} + \Phi_{v,ext->j} = \sum_{cavj} \Phi_{v,j->cavj} + \sum_{cav} \Phi_{v,bulk->cav} + \sum_{cavj} \Phi_{v,bulk->cavj} \tag{5.9}$$

Which states that the sum of the vacancies produced on the grain boundaries plus the flux of vacancies coming from the exterior is equal to the sum of the fluxes of vacancies going into the different cavities.

Remark

If we combine equations 5.3, 5.4, 5.7, 5.8 we obtain:

$$\begin{aligned} &\sum_{cavj} \frac{dV_{cavj}}{dt}\Big|_{vac} + \sum_{cav} \frac{dV_{cav}}{dt}\Big|_{vac} = \\ &= v_{move} \frac{3}{2A_{gg}} \sum_{cavj} F_{cavj} + \beta_{v,j} \times \Omega + \Phi_{v,ext->j} \times \Omega \\ &= v_{move} \frac{3}{2A_{gg}} \left(\sum_{cavj} F_{cavj} + F_j \right) + \Phi_{v,ext->j} \times \Omega \\ &= \frac{Swelling\ of\ the\ fragment}{Unit\ of\ time}\Big|_v \ [s]^{-1} \end{aligned} \tag{5.10}$$

This relation expresses that the macroscopic swelling of the fragment due to thermal vacancies is due to:

— The "production" of vacancies at the surface and the entrance of these vacancies in the material
— The production of vacancies on the GB that pushes the grains further one from the others

Moreover, this same relation says that this swelling is also equal to the swelling (due to thermal vacancies) of the cavities.
The reason behind this is that, with the permanent state hypothesis, there is no accumulation of vacancies in the solid, but only in the cavities.

Now, the last equation that we need is an energy balance. We state that the work performed by the external forces (with respect to the solid) must be equal to the energy gained by producing vacancies on the grain boundaries and by exchanging vacancies with the free surfaces and the different cavities:

$$
\begin{aligned}
-P_{Hydro} \times \frac{Swelling\ of\ the\ fragment}{Unit\ of\ time}\Big|_v & \\
+ \sum_{cavj} \left(P_{int}(cav) - \gamma K_{cavj}\right) \frac{dV_{cavj}}{dt}\Big|_{vac} & \\
+ \sum_{cav} \left(P_{int}(cav) - \gamma K_{cav}\right) \frac{dV_{cav}}{dt}\Big|_{vac} &= \beta_{v,j} \times \mu_{v,j} \\
&\quad + \Phi_{v,ext->j} \times \mu_{v,j/ext} \\
&\quad - \sum_{cavj} \Phi_{v,j->cavj} \times \mu_{v,j/cavj} \\
&\quad - \sum_{cavj} \Phi_{v,bulk->cavj} \times \mu_{v,bulk/cavj} \\
&\quad - \sum_{cav} \Phi_{v,bulk->cav} \times \mu_{v,bulk/cav}
\end{aligned}
\tag{5.11}
$$

Where the term on the left hand side is the work performed by the external forces, while the term on the right hand side is the energy gained because of the production of vacancies on the GB and the exchanges with the free surface and the cavities. γK_{cavj} is the Laplace pressure of the "cavj" cavity, K_{cavj} and K_{cav} are the curvatures of the respective cavities. We define $P_{surf}(cav)$ as: $P_{int} - \gamma K_{cavj} = P_{surf}(cavj)$. $\mu_{v,j}$ is the average vacancy chemical potential on the bare grain boundary and $\mu_{v,medium_1\,/\,medium_2}$ is the chemical potential of a vacancy in the $medium1$ in equilibrium with the $medium2$.

Starting from eq. 5.11 and using eq. 5.10, we express:

$$
\frac{Swelling\ of\ the\ fragment}{Unit\ of\ time}\Big|_v = v_{move} \frac{3}{2A_{gg}} \left(\sum_{cavj} F_{cavj} + F_j \right) + \Phi_{v,ext->j} \times \Omega \tag{5.12}
$$

And we replace $\frac{dV_{cavj}}{dt}\Big|_{vac}$ and $\frac{dV_{cav}}{dt}\Big|_{vac}$ by their expressions in function of the vacancy flux and v_{move}:

$$
\begin{aligned}
&-P_{Hydro}\left[v_{move}\frac{3}{2A_{gg}}\left(\sum_{cavj}F_{cavj}+F_j\right)+\Phi_{v,ext->j}\times\Omega\right]\\
&+\sum_{cavj}P_{surf}(cavj)\times\left[v_{move}\frac{3}{2A_{gg}}F_{cavj}+\Phi_{v,j->cavj}\times\Omega+\Phi_{v,bulk->cavj}\times\Omega\right]\\
&+\sum_{cav}P_{surf}(cav)\times\Phi_{v,bulk->cav}\times\Omega=\\
&\qquad=\beta_{v,j}\times\mu_{v,j}+\Phi_{v,ext->j}\times\mu_{v,j/ext}\\
&\qquad-\sum_{cavj}\Phi_{v,j->cavj}\times\mu_{v,j/cavj}\\
&\qquad-\sum_{cavj}\Phi_{v,bulk->cavj}\times\mu_{v,bulk/cavj}\\
&\qquad-\sum_{cav}\Phi_{v,bulk->cav}\times\mu_{v,bulk/cav}
\end{aligned}
\tag{5.13}
$$

Then, replacing v_{move} by $\frac{\beta_{v,j}\Omega}{F_j\frac{3}{2A_{gg}}}$ (see eq. 5.2), and grouping the terms depending of the fluxes, we obtain the following equation:

$$
\begin{aligned}
&\beta_{v,j}\frac{\Omega}{F_j}\left[-P_{Hydro}(\sum_{cavj}F_{cavj}+F_j)+\sum_{cavj}P_{surf}(cavj)F_{cavj}\right]=\\
&\qquad=\beta_{v,j}\times\mu_{v,j}+\Phi_{v,ext->j}\times(\mu_{v,j/ext}+P_{Hydro}\times\Omega)\\
&\qquad-\sum_{cavj}\Phi_{v,j->cavj}\times(\mu_{v,j/cavj}+P_{surf}(cavj)\times\Omega)\\
&\qquad-\sum_{cavj}\Phi_{v,bulk->cavj}\times(\mu_{v,bulk/cavj}+P_{surf}(cavj)\times\Omega)\\
&\qquad-\sum_{cav}\Phi_{v,bulk->cav}\times(\mu_{v,bulk/cav}+P_{surf}(cav)\times\Omega)
\end{aligned}
\tag{5.14}
$$

At this point, we need to evaluate all the chemical potentials.
If we follow [OLANDER 1976, p. 59]:

$$\mu_{v,medium}=\varepsilon_{v,medium}-Ts_{v,medium}+kTln\left(x_{v,medium}\right) \tag{5.15}$$

Where ε_{medium} is the formation energy of a vacancy in the medium (j or bulk), s_{medium} is the formation entropy of a vacancy in the medium and $x_{v,medium}$ is the concentration of vacancies per atomic sites in the medium.
If we neglect s_{medium} (see [ibid., p. 59]), we find:

$$\mu_{v,medium}\approx\varepsilon_{v,medium}+kTln\left(x_{v,medium}\right) \tag{5.16}$$

Then, we can also write:

$$\mu_{v,medium_1\,/\,medium_2} \approx \varepsilon_{v,medium_1} + kTln\left(x^{eq}_{v,medium_1(medium_2)}\right) \tag{5.17}$$

Where $x^{eq}_{v,medium_1(medium_2)}$ is the concentration of vacancies per atomic sites in the $medium1$ in equilibrium with the $medium2$ ($medium2$ is a cavity or the exterior). From [L. Noirot 2014] and Section 3.2.8:

$$x^{eq}_{v,medium_1(medium_2)} = exp\left(\frac{-\varepsilon_{v,medium_1}}{kT}\right)\ exp\left(\frac{-P_{surf}(medium_2)\Omega}{kT}\right) \tag{5.18}$$

We then obtain:

$$\mu_{v,medium_1\,/\,medium_2} \approx -P_{surf}(medium_2) \times \Omega \tag{5.19}$$

This means that all the terms in the equation 5.14 of the type:

$$\mu_{v,medium_1\,/\,medium_2} + P_{surf}(medium_2) \times \Omega \tag{5.20}$$

are null.

On the other hand, for the exterior the situation is more complex. In fact, the surfaces of the fragments face in part the free volumes (cracks and the fuel-cladding gap, which is closed after around 2 cycles) and in part other fragments. The part of the fragment that touches other fragments should be subjected to the hydrostatic pressure, while the other part should be subjected to the free volume pressure. However, it is impossible in our model to consider different parts of the surface of the fragment, that would be submitted to different pressures. This should change the expression of the work exerted on the fragment, but the approach that we use does not allow to take this into account. Moreover, if part of the fragment does not touch another fragment, the fragment will swell preferentially in that direction and soon touch another fragment. So, consistency imposes to calculate $\mu_{v,j\,/\,ext}$ considering that the pressure P_{hydro} is applied to the fragment surface.
Therefore, we can calculate $\mu_{v,j\,/\,ext}$ as:

$$\mu_{v,j\,/\,ext} \approx -P_{Hydro} \times \Omega \tag{5.21}$$

And therefore we obtain:

$$\mu_{v,j\,/\,ext} + P_{Hydro} \times \Omega \approx 0 \tag{5.22}$$

We can finally write the energy balance (eq. 5.14) as:

$$\beta_{v,j} \times \left[\mu_{v,j} + \frac{\Omega}{F_j} \left[P_{Hydro} \left(\sum_{cavj} F_{cavj} + F_j \right) - \sum_{cavj} P_{surf}(cavj) F_{cavj} \right] \right] = 0 \tag{5.23}$$

Equation 5.23 imposes $\mu_{v,j}$ and therefore $x_{v,j}$ (through eq. 5.16):

$$x_{v,j} = exp\left(-\frac{\varepsilon_{v,j}}{kT}\right) exp\left(-\frac{\Omega}{kTF_j} \left[P_{Hydro} \left(\sum_{cavj} F_{cavj} + F_j \right) - \sum_{cavj} P_{surf}(cavj) F_{cavj} \right] \right) \tag{5.24}$$

Where $\varepsilon_{v,j}$ is the formation energy of a vacancy on the grain boundary: $\varepsilon_{v,j} = \varepsilon_v + E_{seg,v}$ (see eq. 3.87).

If we call σ:

$$\sigma = \frac{-1}{F_j} \left[P_{Hydro} \left(\sum_{cavj} F_{cavj} + F_j \right) - \sum_{cavj} P_{surf}(cavj) F_{cavj} \right] \tag{5.25}$$

We finally obtain:

$$x_{v,j} = exp\left(\frac{-\varepsilon_{v,j}}{kT}\right) exp\left(\frac{\sigma\Omega}{kT}\right) \tag{5.26}$$

Or:

$$C_{v,j}^{loc} = exp\left(\frac{-\varepsilon_{v,j}}{kT}\right) exp\left(\frac{\sigma\Omega}{kT}\right) \times \Omega^{-1} \tag{5.27}$$

Physical meaning

Looking at figure 5.2, the balance of the forces in the vertical direction can be written as:

$$-P_{Hydro} \times S - \sigma F_j \times S + \sum_{cavj} P_{surf}(cavj) F_{cavj} \times S = 0 \tag{5.28}$$

Where S is a representative surface of the decorated GB and σ is the stress acting on the bare grain boundary. In this case, $F_j + \sum_{cavj} F_{cavj} = 1$.

By solving equation 5.28, we obtain the same σ defined in 5.25 and used in equation 5.26.
The concentration of vacancies (vacancies per site) found in equation 5.26 can then be seen as the equilibrium concentration of vacancies on a grain boundary subject to a tensile stress equal to σ.
Since we model the thermodynamic production of vacancies on the grain boundary, it makes sense that the concentration of vacancies on the grain boundary adjusts to remain equal to the equilibrium concentration.

In equation 5.26, if σ becomes too big, $x_{v,j}$ can become > 1. However, if the grain

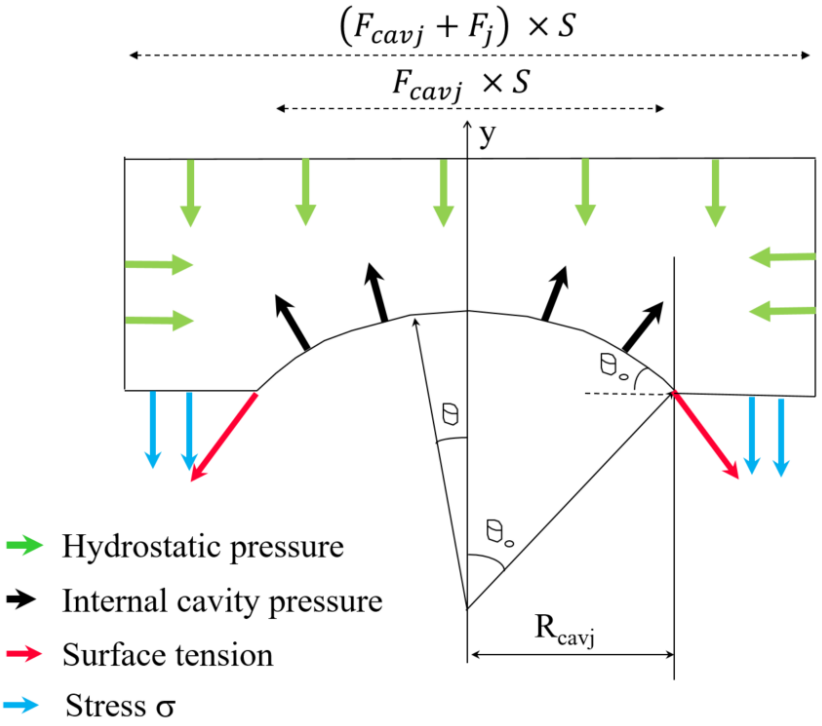

Figure 5.2. – Scheme of the forces acting on the material near an inter-granular cavity.

boundary happens to be subjected to such a tensile stress, it would probably fracture. In MARGARET, the phenomenon of fracturing is dealt by a separate model, out of the scope of this thesis.

Once $x_{v,j}$ is known (equation 5.26), using the two equations 5.7 and 5.8, we can calculate C_v and $\beta_{v,j}$.

We can write the flux of vacancies in the bulk to one type of cavity, "cav", as:

$$\Phi_{v,bulk->cav} = geom_{cav} \times D_v \left(C_v - C_v^{eq}(cav)\right) \tag{5.29}$$

Where $geom_{cav}$ is a geometrical term with dimension [m^{-2}]. In the case of spherical cavities in the bulk, $geom_{cav} = 4\pi R_{cav} C_{cav}$, where R_{cav} is the cavity radius, C_{cav} is the cavity density (cavities / m^3 of fresh fuel) [Ham 1958; OLANDER 1976] (this is the Olander expression referenced in Section 2.2.4); D_v is the vacancy diffusion coefficient.

$$\begin{aligned} \Phi_{v,bulk->j} &= \frac{15}{A_{gg}^2} \times D_v \left(C_v - C_v^{eq}(j)\right) \times F_j \\ \Phi_{v,bulk->j} &= \frac{15}{A_{gg}^2} \times D_v \left(C_v - exp\left(+\frac{E_{seg,v}}{kT}\right) C_{v,j}^{loc}\right) \times F_j \end{aligned} \tag{5.30}$$

Where $C_v^{eq}(j)$ is the concentration of vacancies in the lattice in equilibrium with the concentration of vacancies on the grain boundary. Its expression in function of $C_{v,j}^{loc}$ was derived in Section 3.2.8, eq. 3.84. The value $\frac{15}{A_{gg}^2}$ comes from the assumption of quasi-steady state of diffusion in a sphere (the grain) (see the beginning of Section G.3).

In the same way,

$$\Phi_{v,bulk->cavj} = \frac{15}{A_{gg}^2} \times D_v \left(C_v - C_v^{eq}(cavj)\right) \times F_{cavj} \tag{5.31}$$

Again, $C_v^{eq}(cavj)$ was derived in Section 3.2.8, eq. 3.73.

The permanent regime for the thermal vacancies in the bulk of the grain (eq. 5.7) gives:

$$\begin{aligned}\left[geom_{cav} + \frac{15}{A_{gg}^2}(F_j + \sum_{cavj} F_{cavj})\right] \times C_v = \\ = + \sum_{cav} geom_{cav} C_v^{eq}(cav) \\ + \frac{15}{A_{gg}^2}\left[exp\left(+\frac{E_{seg,v}}{kT}\right) C_{v,j}^{loc} \times F_j \right. \\ \left. + \sum_{cavj} F_{cavj} C_v^{eq}(cavj)\right]\end{aligned} \tag{5.32}$$

So, we can express C_v as an affine function of $C_{v,j}^{loc}$:

$$C_v = a_1 C_{v,j}^{loc} + b_1 \tag{5.33}$$

Where a_1 and b_1 depend on the geometry of the microstructure, of the temperature and equilibrium concentrations at the vicinity of the cavities:

$$a_1 = \frac{\frac{15}{A_{gg}^2} F_j \times exp\left(+\frac{E_{seg,v}}{kT}\right)}{denom_1} \; [adimensional] \tag{5.34}$$

And

$$b_1 = \frac{\sum_{cav} geom_{cav} C_v^{eq}(cav) + \frac{15}{A_{gg}^2} \sum_{cavj} F_{cavj} C_v^{eq}(cavj)}{denom_1} \; [vacancies/m^3] \tag{5.35}$$

Where

$$denom_1 = \sum_{cav} geom_{cav} + \frac{15}{A_{gg}^2}\left(F_j + \sum_{cavj} F_{cavj}\right) \tag{5.36}$$

We can now reformulate the expression of $\Phi_{bulk->j}$ from eq. 5.30 as:

$$\Phi_{bulk->j} = \alpha_1 C_{v,j}^{loc} + \beta_1 \tag{5.37}$$

Where

$$\alpha_1 = \frac{15}{A_{gg}^2} \times D_v \times F_j \left(a_1 - exp\left(+ \frac{E_{seg,v}}{kT} \right) \right) \tag{5.38}$$

and

$$\beta_1 = \frac{15}{A_{gg}^2} \times D_v \times F_j \times b_1 \tag{5.39}$$

The permanent regime for the thermal vacancies on the grain boundary (eq. 5.8) allows us to find $\beta_{v,j}$.

The flux of vacancy from the GB to the type of cavity "cavj" can be written as:

$$\Phi_{v,j->cavj} = geom_{cavj} \times D_{v,j} \times F_j' S_{jtot}^{vol} e_{pj} \left(C_{v,j}^{loc} - C_{v,j}^{eq}(cavj) \right) \tag{5.40}$$

In Section 3.2.2 we derived the same expression for Xe. $geom_{cavj}$, F_j', S_{jtot}^{vol} and e_{pj} have the same meaning and expressions as in Section 3.2.2.

The flux of vacancy from the GB to the exterior can be written as:

$$\Phi_{v,j->ext} = \frac{15}{A_{se}^2} \times D_{v,j} \times F_j' S_{jtot}^{vol} e_{pj} \left(C_{v,j}^{loc} - C_{v,j}^{eq}(ext) \right) \tag{5.41}$$

Where A_{se} is the radius of the fragment (consider as an "equivalent sphere") and $C_{v,j}^{eq}(ext)$ is the equilibrium concentration of vacancies on the grain boundary in equilibrium with the exterior: $C_{v,j}^{eq}(ext) = exp\left(\frac{-\varepsilon_{v,j}}{kT}\right) exp\left(-\frac{P_{ext}\Omega}{kT}\right) \times \Omega^{-1}$, and since we have used the hypothesis that $P_{ext} = P_{Hydro}$:

$$C_{v,j}^{eq}(ext) = exp\left(\frac{-\varepsilon_{v,j}}{kT}\right) exp\left(-\frac{P_{hydro}\Omega}{kT}\right) \times \Omega^{-1} \tag{5.42}$$

Equation 5.41 is obtained using the permanent diffusion in a sphere of radius A_{se} and the diluted concentration $C_{v,j}^{diluted} = C_{v,j}^{loc} \times F_j' S_{jtot}^{vol} e_{pj}$ in [vacancies on GB / m^3 of fresh volume], and the adequate limit condition $C_{v,j}^{eq}(ext) \times F_j' S_{jtot}^{vol} e_{pj}$. The sphere is considered as an homogeneous medium for diffusion.

The permanent regime for thermal vacancies on the GB (eq. 5.8) leads to:

$$\beta_{v,j} = \sum_{cavj} \Phi_{v,j->cavj} + \Phi_{v,j->ext} + \Phi_{v,j->bulk} \tag{5.43}$$

Which can be re-written as:

$$\beta_{v,j} = \alpha_3 C_{v,j}^{loc} + \beta_3 \tag{5.44}$$

Where

$$\alpha_3 = -\alpha_1 + D_{v,j} \times F'_j S_{jtot}^{vol} e_{pj} \left(\sum_{cavj} geom_{cavj} + \frac{15}{A_{se}^2} \right) [s^{-1}] \tag{5.45}$$

$$\beta_3 = -\beta_1 - D_{v,j} \times F'_j S_{jtot}^{vol} e_{pj} \left(\sum_{cavj} geom_{cavj} C_{v,j}^{eq}(cavj) + \frac{15}{A_{se}^2} C_{v,j}^{eq}(ext) \right) [vac/m^3/s] \tag{5.46}$$

In practice, in the code, when we need to calculate the terms of volume contribution to the cavities due to thermal vacancies:

— We calculate $C_{v,j}^{loc}$ from eq. 5.27;

— Then, we calculate a_1 and b_1, and C_v is obtained from eq. 5.33 ;

— At this point, all the terms $\frac{dV_{cav}}{dt}\Big|_{vac}$ for bulk cavities can be calculated using eq. 5.29 as:

$$\frac{dV_{cav}}{dt}\Big|_{vac} = \Phi_{v,bulk->cav} \times \Omega \tag{5.47}$$

— To calculate $\frac{dV_{cavj}}{dt}\Big|_{vac}$, v_{move} is still needed. To obtain it, α_1, β_1, α_3 and β_3 are calculated, then $\beta_{v,j}$ is obtained using eq. 5.44 and v_{move} is obtained through eq. 5.2;

— At last, $\frac{dV_{cavj}}{dt}\Big|_{vac}$ for all the inter-granular cavities can be calculated using eqs. 5.3, 5.31 and 5.40.

In the expressions of $C_{v,j}^{loc}$, $C_{v,j}^{eq}(ext)$, C_v, the Arrhenius terms $exp\left(-\frac{\varepsilon_{v,j}}{kT}\right)$ and $exp\left(-\frac{E_{seg,v}}{kT}\right)$ (where $E_{seg,v} < 0$: vacancies are segregated on the GB) decrease when T decreases.
In the expressions of the fluxes of vacancies and of $\beta_{v,j}$ (and hence v_{move}), D_v and $D_{v,j}$ are present too with their own Arrhenius terms, which also decrease when the temperature decreases.
So, the thermal vacancy contributions $\frac{dV_{cav}}{dt}\Big|_{vac}$ and $\frac{dV_{cavj}}{dt}\Big|_{vac}$ should diminish when the temperature decreases.
Our global model for the vacancy contribution to the volume of the cavities will be consistent if the vacancy contribution to the intra-granular nano-bubbles will be negligible in base irradiation.

Remarks

1) In order to calculate the fluxes of thermal vacancies from the bulk of the grain to the intra-granular bubbles, the inter-granular bubbles and the grain boundary, we need an expression for D_v, the vacancy diffusion coefficient. We can obtain D_v from the knowledge of $D_{U,th}$, the intrinsic (thermal) Uranium self-diffusion coefficient.

Since thermal auto-interstitials are negligible, D_v is obtained from $D_{U,th}$ through the relation:

$$D_{U,th} = f_v \times D_v \times x_v^{eq}(P_{surf} \approx 0) \tag{5.48}$$

Where $f_v = 0.781$ is the correlation factor for the vacancy mechanism [C. Matthews et al. 2019].
Moreover, from eq. 5.18:

$$x_v^{eq}(P_{surf} \approx 0) = exp\left(\frac{-\varepsilon_{v,bulk}}{kT}\right) \tag{5.49}$$

Eq. 5.48 expresses the fact that an uranium atom moves if there is a vacancy nearby (with probability $x_v^{eq}(P_{surf} \approx 0)$ of being there) and if the vacancy moves. It supposes that the measure was done on a sample were vacancies were at the equilibrium at atmospheric pressure (and $exp\left(\frac{-P_{atm}\Omega}{kT}\right) \approx 1$).

However, in reality, it seems that $D_{U,th}$ is driven by the mobility of $V_U^{''''}$ (Uranium vacancy, different from V_{UO_2}, which is a bound Schottky defect) [Dorado et al. 2012; C. Matthews et al. 2019]. And the equilibrium concentration of $V_U^{''''}$ cannot be expressed in the same way as 5.49. Unfortunately, as we explained at the beginning of this Chapter, we cannot track the concentration of every defects in the fuel, that is why we use equations 5.48 and 5.49 to link $D_{U,th}$ to D_v.

On the other hand, we can see how the fluxes of thermal vacancies from the bulk to the intra-granular bubbles and the inter-granular bubbles depend only on the product between D_v and $exp\left(\frac{-\varepsilon_{v,bulk}}{kT}\right)$, which is how we define $D_{U,th}$ (apart from the correlation factor).
Therefore, in practice, we only need an expression for $D_{U,th}$.

To demonstrate it, let's consider $\Phi_{bulk->cav}$ as an example:

$$\Phi_{v,bulk->cav} = geom_{cav} \times D_v \times \left(a_1 C_{v,j}^{loc} + b_1 - C_v^{eq}(cav)\right) \tag{5.50}$$

Now, $D_v \times a_1 \times C_{v,j}^{loc}$ can be written as:

$$
\begin{aligned}
D_v \times a_1 \times C_{v,j}^{loc} &= D_v \times \frac{\frac{15}{A_{gg}^2} exp\left(+\frac{E_{seg,v}}{kT}\right)}{denom_1} \times exp\left(\frac{-\varepsilon_{v,j}}{kT}\right) \times exp\left(\frac{\sigma\Omega}{kT}\right) \\
D_v \times a_1 \times C_{v,j}^{loc} &= D_v \times \frac{\frac{15}{A_{gg}^2} exp\left(-\frac{\varepsilon_v}{kT}\right)}{denom_1} \times exp\left(\frac{\sigma\Omega}{kT}\right) \\
D_v \times a_1 \times C_{v,j}^{loc} &= D_{U,th} \times \frac{\frac{15}{A_{gg}^2}}{denom_1} \times exp\left(\frac{\sigma\Omega}{kT}\right)
\end{aligned}
\tag{5.51}
$$

$D_v \times b_1$ can be written as:

$$
\begin{aligned}
D_v \times b_1 &= D_v \times \frac{\sum_{cav} geom_{cav} C_v^{eq}(cav) + \frac{15}{A_{gg}^2} \sum_{cavj} F_{cavj} C_v^{eq}(cavj)}{denom_1} \\
D_v \times b_1 &= D_v \times exp\left(-\frac{\varepsilon_v}{kT}\right) \\
&\quad \times \frac{\sum_{cav} geom_{cav} \times exp\left(\frac{(P_{cav}-\gamma K_{cav})\Omega}{kT}\right) + \frac{15}{A_{gg}^2} \sum_{cavj} F_{cavj} \times exp\left(\frac{(P_{cavj}-\gamma K_{cavj})\Omega}{kT}\right)}{denom_1} \\
D_v \times b_1 &= D_{U,th} \times \frac{\sum_{cav} geom_{cav} \times exp\left(\frac{(P_{cav}-\gamma K_{cav})\Omega}{kT}\right) + \frac{15}{A_{gg}^2} \sum_{cavj} F_{cavj} \times exp\left(\frac{(P_{cavj}-\gamma K_{cavj})\Omega}{kT}\right)}{denom_1}
\end{aligned}
\tag{5.52}
$$

And $D_v \times C_v^{eq}(cav)$ can be written as:

$$
\begin{aligned}
D_v \times C_v^{eq}(cav) &= D_v \times exp\left(-\frac{\varepsilon_v}{kT}\right) \times exp\left(\frac{\left(P_{cav} - \gamma K_{cav}\right)\Omega}{kT}\right) \\
D_v \times C_v^{eq}(cav) &= D_{U,th} \times exp\left(\frac{\left(P_{cav} - \gamma K_{cav}\right)\Omega}{kT}\right)
\end{aligned}
\tag{5.53}
$$

In Section 7.1.4, we review the literature on $D_{U,th}$.

2) In the same way[8] :

$$
D_{Uj,th} = D_{v,j} \times x_{v,j}^{eq}\left(P_{surf} \approx 0\right) \tag{5.54}
$$

8. Also $D_{Uj,th}$ seems to be driven by the mobility of $V_U^{''''}$ on the grain boundary [Galvin, Andersson, et al. 2023]. However, as we explained at the beginning of this Chapter, since we cannot track the concentration of every defects in the fuel, we use $x_{v,j}^{eq}(P_{surf} \approx 0)$ to link $D_{Uj,th}$ to $D_{v,j}$.

Now, we have to note that, in the expressions of the fluxes where $D_{v,j}$ appears, we always encounter the products: $D_{v,j} \times C_{v,j}^{loc} \times \Omega$, $D_{v,j} \times C_{v,j}^{eq}(cavj) \times \Omega$, $D_{v,j} \times C_{v,j}^{eq}(ext) \times \Omega$. Knowing the expressions of $C_{v,j}^{loc}$, $C_{v,j}^{eq}(cavj)$ and $C_{v,j}^{eq}(ext)$ (eq. 5.27, 3.83, 5.42), we can see how these products, and therefore the fluxes of vacancies towards the inter-granular cavities and the exterior, depend only on the product between $D_{v,j}$ and $exp\left(\frac{-\varepsilon_{v,j}}{kT}\right)$ (plus on σ, the pressure of the cavities and the hydrostatic pressure), which is how we define $D_{Uj,th}$.

In fact, using $\Phi_{j->cavj}$ as an example, we have:

$$
\begin{aligned}
\Phi_{v,j->cavj} &= geom_{cavj} \times D_{v,j} \times F'_j S_{jtot}^{vol} e_{pj} \times \left(C_{v,j}^{loc} - C_{v,j}^{eq}(cavj)\right) \\
\Phi_{v,j->cavj} &= geom_{cavj} \times D_{v,j} \times F'_j S_{jtot}^{vol} e_{pj} \\
&\quad \times \left(exp\left(\frac{-\varepsilon_{v,j}}{kT}\right) exp\left(\frac{\sigma\Omega}{kT}\right) - exp\left(\frac{-\varepsilon_{v,j}}{kT}\right) exp\left(\frac{\left(P_b - \gamma K_{bj}\right)\Omega}{kT}\right)\right) \times \Omega^{-1} \\
\Phi_{v,j->cavj} &= geom_{cavj} \times D_{v,j} \times exp\left(\frac{-\varepsilon_{v,j}}{kT}\right) \times F'_j S_{jtot}^{vol} e_{pj} \\
&\quad \times \left(exp\left(\frac{\sigma\Omega}{kT}\right) - exp\left(\frac{\left(P_{cavj} - \gamma K_{cavj}\right)\Omega}{kT}\right)\right) \times \Omega^{-1} \\
\Phi_{v,j->cavj} &= geom_{cavj} \times D_{Uj,th} \times F'_j S_{jtot}^{vol} e_{pj} \\
&\quad \times \left(exp\left(\frac{\sigma\Omega}{kT}\right) - exp\left(\frac{\left(P_{cavj} - \gamma K_{cavj}\right)\Omega}{kT}\right)\right) \times \Omega^{-1}
\end{aligned}
\tag{5.55}
$$

3) In Appendix J, it is presented the same derivation but in a limit case, constructed excluding any exchange of vacancies between the grain boundary and the grain (D_U tends to 0 or A_{gg} tends to $+\infty$) and any exchange of vacancies between the grain boundary and the free surfaces (A_{gg} tends to $+\infty$). Moreover, only one population of inter-granular cavities is considered.
Doing so, we obtain back eq. 5.1.
Therefore, we can say that our model is a generalization of the Speight model, that includes:

— The influence of vacancies coming from the free surface
— The link with the bulk of the grain
— With less hypothesis on the pressures

6. Behaviour of the subdomains during power ramps

Sommaire

6.1. Literature review 157
6.2. Subdomain growth at high temperatures 160
6.3. Loss of precipitation bubbles caused by the movement of the subdomain boundaries 160
6.3.1. First formulation 160
6.3.2. Second formulation 162

6.1. Literature review

The way in which subdomains form and behave seems complex and, for the moment, remains not totally understood. Despite this, EBSD measurements, performed on base irradiated fuel, allowed us to know when and where subdomains form, their size, their disorientations etc. Moreover, researchers have measured the density ([bubbles / m^3 of fresh fuel]) and size of the precipitation bubbles (see Chapter 4 for more information on base irradiated fuels).
On the contrary, we are not aware of EBSD measurements performed on ramped fuel samples with subdomains present at the beginning of the ramp. The only relevant measurements performed on power ramped fuels regard the number and size of the precipitation bubbles:

— Figure 6.1 shows a SEM image taken at the centre of the pellet of a ramped fuel after 6 cycles of base irradiation. On this image, we can see very big and scarce intra-granular bubbles, and even the absence of detectable intra-granular bubbles in some of the grains.

— Figure 6.2 shows the density of the intra-granular bubbles (the precipitation ones) of an high burnup fuel before and after a power ramp.

— Figure 6.3 shows the median diameter (D50) of the intra-granular bubbles (the precipitation ones) of an high burnup fuel before and after a power ramp.

Therefore, during a power ramp, the density of precipitation bubbles decreases and their size increases. Unfortunately, not much more is known regarding the behaviour of the subdomains when heated.

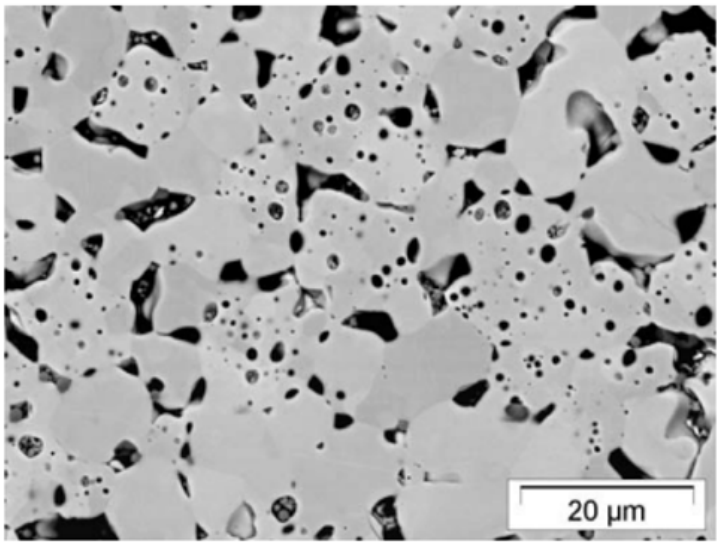

Figure 6.1. – SEM image taken at the centre of the pellet of a ramped fuel after 6 cycles of base irradiation (Rod_72.93_RT of the validation base, presented in Section 7.3). Image taken at the LECA-STAR facility, Cadarache (FRANCE).

However, we can make some reasonable assumptions: since high temperatures tend to reduce the amount of linear defects in the material (thermal recovery) [Onofri et al. 2020], we consider reasonable to predict, during a power ramp, a reduction in the number of dislocations that make up the subdomain boundaries and therefore an increase in the size of the subdomains.

With this intuition in mind, and in order to reproduce the few experimental evidences on the concentration and size of the precipitation bubbles after a power ramp, we have developed a simple model of subdomain growth at high temperatures, where the precipitation bubbles follow the movement of the subdomain boundaries. As a consequence of the subdomain growth, the bubbles located in the subdomain boundaries coalesce and some of them move towards the grain boundaries, where they are captured by the inter-granular bubbles.
The actual formulation of the model is not to be intended as a "true" description of the underlying phenomena, but more as an empirical description of the few data available at present.

In Section 6.2, I present the model of subdomain growth at high temperature, while in Section 6.3, I present the rate at which precipitation bubbles coalescence and leave the grain due to the growth of the subdomains.

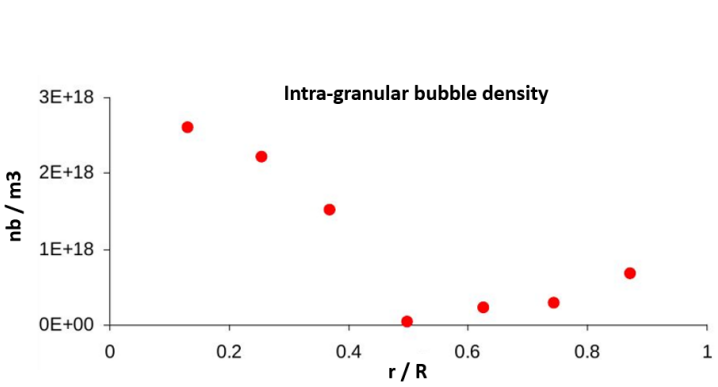

(a) After base irradiation.

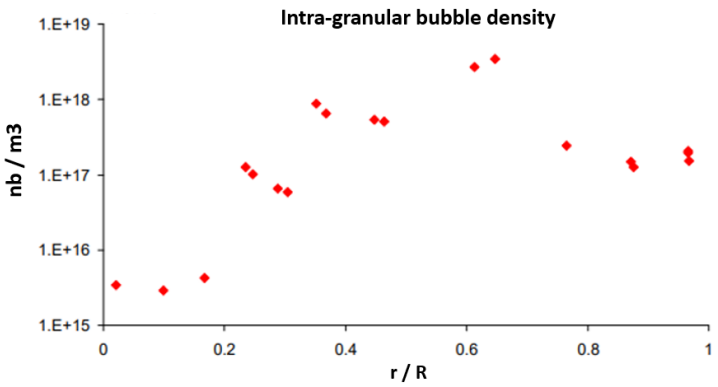

(b) After power ramp (logarithmic scale).

Figure 6.2. – Radial evolution of the intra-granular bubble density [bubbles / m^3 of fresh fuel] of an high burnup fuel before (Rod_72.93_IB of the validation base, presented in Section 7.3) and after a power ramp (Rod_72.93_RT of the validation base). Measurements performed at the LECA-STAR facility, Cadarache (FRANCE).

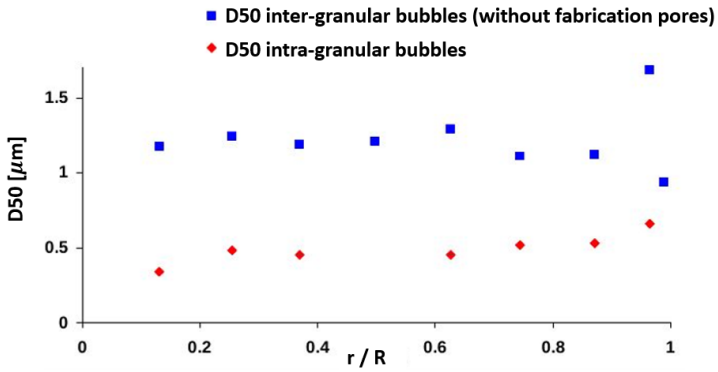

(a) After base irradiation.

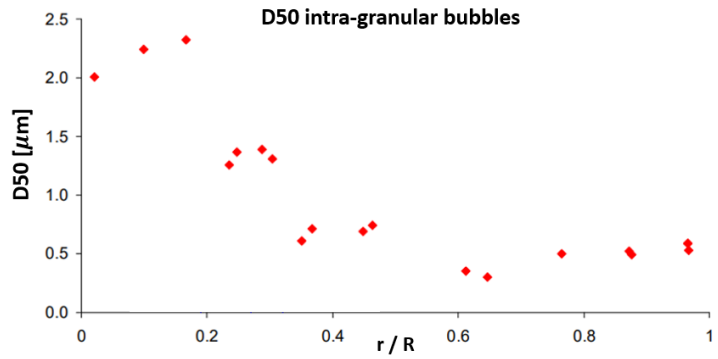

(b) After power ramp.

Figure 6.3. – Radial evolution of the intra-granular bubble median size [μm] of an high burnup fuel before (Rod_-72.93_IB of the validation base, presented in Section 7.3) and after a power ramp (Rod_72.93_RT of the validation base). Measurements performed at the LECA-STAR facility, Cadarache (FRANCE).

6.2. Subdomain growth at high temperatures

We decided to consider an exponential relation between the temperature and the growth of the volume of the subdomains:

$$\frac{dV_{sd}}{dt} = B_{growth\ sd} \times exp\left(-\frac{Ea_{growth\ sd}}{kT}\right) \tag{6.1}$$

Where V_{sd} is the volume of the subdomains, $B_{growth\ sd}$ and $Ea_{growth\ sd}$ are parameters of the model.
The form of eq. 6.1 is derived from the description of the grain growth authored by H. Stehle [Stehle 1962] and allows us to predict higher growth rate at higher temperatures.

We can also express eq. 6.1 in terms of growth rate of the radius of the subdomains:

$$\frac{dA_{sd}}{dt} = \frac{B_{growth\ sd}}{4\pi A_{sd}^2} \times exp\left(-\frac{Ea_{growth\ sd}}{kT}\right) \tag{6.2}$$

6.3. Loss of precipitation bubbles caused by the movement of the subdomain boundaries

6.3.1. First formulation

In order to derive the rate of loss of precipitation bubbles due to the growth of the subdomains at high temperature, we started by considering the phenomena of coalescence and movement towards the grain boundaries separately.

We can derive the coalescence rate by making few assumptions:

— The precipitation bubbles are placed at the subdomains "edges"
— The number of edges per subdomain is fixed

Then, the number of bubbles in a grain, $C_{bprecjsd} \times \frac{4}{3}\pi A_{gg}^3$, where $C_{bprecjsd}$ is the precipitation bubble density [bubbles / m^3 fresh fuel], is proportional to the number of subdomains:

$$\frac{4}{3}\pi A_{gg}^3 \times C_{bprecjsd} = G_1 \times N_{sd} = G_1 \times \frac{A_{gg}^3}{A_{sd}^3} \tag{6.3}$$

Where N_{sd} is the number of subdomains inside a grain and G_1 is a constant.

We then obtain:

$$C_{bprecjsd} = \frac{G_2}{A_{sd}^3} \tag{6.4}$$

Where G_2 is another constant.
If we now take the derivative of the logarithm of the above expression in time, we obtain:

$$\begin{aligned} \frac{1}{C_{bprecjsd}} \frac{dC_{bprecjsd}}{dt}\Big|_{coalescence} &= \frac{-3}{A_{sd}} \frac{dA_{sd}}{dt} \\ \frac{dC_{bprecjsd}}{dt}\Big|_{coalescence} &= C_{bprecjsd} \times \frac{-3}{A_{sd}} \frac{dA_{sd}}{dt} \end{aligned} \tag{6.5}$$

Which is the expression of the coalescence rate of the precipitation bubbles due to the growth of the subdomains.

At the same time, the subdomain boundaries loose part of them to the grain boundaries, transporting with them the precipitation bubbles towards the exterior of the grain.

For one grain, the number of bubbles that leave the grain in the unit of time can be set as proportional to the surface of the grain times the velocity at which bubbles move towards the surface:

$$\frac{4}{3}\pi A_{gg}^3 \times \frac{dC_{bprecjsd}}{dt}\Big|_{leave\ grain} = -|v_{jsd}| \times 4\pi A_{gg}^2 \times C_{bprecjsd} \tag{6.6}$$

Where $|v_{jsd}|$ is the velocity of growth of the subdomains: $|v_{jsd}| = \frac{dA_{sd}}{dt}$.
Therefore, we obtain:

$$\frac{dC_{bprecjsd}}{dt}\Big|_{leave\ grain} = -\frac{dA_{sd}}{dt} \times \frac{3}{A_{gg}} \times C_{bprecjsd} \tag{6.7}$$

Which is the rate at which precipitation bubbles leave the grain.

When bubbles leave the grain, they bring with them the gas that they contain and their volume. Therefore, we can write the total amount of Xenon in the bubbles and the total volume of the bubbles that are loss because of the growth of the subdomains in this way[1]:

$$\frac{dC_{Xebprecjsd}}{dt} = -\frac{dA_{sd}}{dt} \times \frac{3}{A_{gg}} \times C_{Xebprecjsd} \tag{6.8}$$

$$\frac{dV_{bprecjsd}}{dt} = -\frac{dA_{sd}}{dt} \times \frac{3}{A_{gg}} \times V_{bprecjsd} \tag{6.9}$$

1. The coalescence term do not contribute to the loss of gas or volume.

Finally, if we call $H(bprecjsd) = \frac{dA_{sd}}{dt} \times \frac{3}{A_{gg}}$, we obtain:

$$\frac{dC_{bprecjsd}}{dt} = -\left(\underbrace{H(bprecjsd)}_{leave\ grain} + \underbrace{\frac{3}{A_{sd}} \frac{dA_{sd}}{dt}}_{coalescence} \right) \times C_{bprecjsd} \tag{6.10}$$

$$\frac{dC_{Xebprecjsd}}{dt} = -H(bprecjsd) \times C_{Xebprecjsd} \tag{6.11}$$

$$\frac{dV_{bprecjsd}}{dt} = -H(bprecjsd) \times V_{bprecjsd} \tag{6.12}$$

For the special case of the pores on the subdomain boundaries, given their low concentration (less than one pore per grain), we impose a coalescence term equal to 0.

After trying the terms just obtained in the code, we noticed that the code had a tendency to predict a too high radius of the precipitation bubbles during power ramps. Indeed, the rate of bubble coalescence is higher than the rate at which bubbles move toward the grain boundaries. Moreover, with the terms just derived, the concentration of precipitation bubbles does not go to 0 when the radius of the subdomains approaches the radius of the grain.
This is why we have finally derived those terms in a different way, as presented in the next Section.

6.3.2. Second formulation

We can express the loss of precipitation bubbles caused by the movement of the subdomain boundaries as proportional to the loss of the subdomain surface (which is not already a grain boundary). This loss is due to both the coalescence and the movement of the precipitation bubbles from the grain to the grain boundaries.
In general, we can write:

$$\frac{dC_{bprecjsd}}{dt} = \frac{d(C^{surf}_{bprecjsd} \times S^{vol}_{sd})}{dt} \tag{6.13}$$

Where $C^{surf}_{bprecjsd}$ is the surface concentration of the precipitation bubbles [bubbles / m^2 of subdomain boundaries] and S^{vol}_{sd} is the surface of the subdomains over m^3 of fresh fuel.
If the change in the number of brecjsd is only due to the phenomenon of subdomain growth, it follows that:

$$\frac{dC_{bprecjsd}}{dt}\Big|_{change\ in\ S_{sd}} = C^{surf}_{bprecjsd}\frac{dS^{vol}_{sd}}{dt} \tag{6.14}$$

We can then write:

$$\frac{dS^{vol}_{sd}}{dt} = \frac{dN_{sd}\,4\pi A^2_{sd}(1-F_{gsd})}{dt} \times \frac{1}{\frac{4}{3}\pi A^3_{gg}} \tag{6.15}$$

Where $N_{sd} = \frac{A^3_{gg}}{A^3_{sd}}$ is the number of subdomains present in a grain and $F_{gsd} = \frac{A_{sd}}{A_{gg}}$.
We then obtain:

$$\frac{dS^{vol}_{sd}}{dt} = -\frac{3}{A^2_{sd}}\frac{dA_{sd}}{dt} \tag{6.16}$$

It is now useful to write the relation between $C^{surf}_{bprecjsd}$ and $C_{bprecjsd}$:

$$C^{surf}_{bprecjsd} = C_{bprecjsd} \times \frac{\frac{4}{3}\pi A^3_{gg}}{4\pi A^2_{sd}(1-F_{gsd})N_{sd}} \tag{6.17}$$

We can finally obtain:

$$\frac{dC_{bprecjsd}}{dt}\Big|_{change\ in\ S_{sd}} = -C^{surf}_{bprecjsd} \times \frac{3}{A^2_{sd}}\frac{dA_{sd}}{dt} \tag{6.18}$$

$$= -C_{bprecjsd} \times \frac{A_{gg}}{A_{sd}(A_{gg}-A_{sd})}\frac{dA_{sd}}{dt} \tag{6.19}$$

We have now obtained the total number of precipitation bubbles lost into the GB because of the growth of the subdomains and the linked movement of the subdomain boundaries.
A possible distribution between bubbles that have coalesced and bubbles that have reached the grain boundary can be done supposing that a proportion F_{gsd} of the total bubble lost are lost at the grain border. For small A_{sd}, this proportion is negligible, while for $A_{sd} \to A_{gg}$, it tends to 1, which make sense.

If so, we would have:

$$\frac{dC_{bprecjsd}}{dt}\Big|_{leave\ grain} = -C_{bprecjsd} \times \frac{1}{(A_{gg}-A_{sd})}\frac{dA_{sd}}{dt} \tag{6.20}$$

Which, for small A_{sd}, is similar to eq. 6.7.
Moreover, we obtain:

$$\frac{dC_{bprecjsd}}{dt}\Big|_{coalescence} = -C_{bprecjsd} \times \frac{1}{A_{sd}} \frac{dA_{sd}}{dt} \tag{6.21}$$

Which is similar to eq. 6.5.

The useful thing about eq. 6.18 is that $C_{bprecjsd}$ goes to 0 when A_{sd} goes to A_{gg}, as we would expect. In fact, in this case, the subdomain would reach the size of the initial grain and therefore no precipitation bubble is expected to be found in the grains, since no precipitation bubble is modelled outside the subdomain boundaries, which now coincides with the grain boundary.

Indeed, as:

$$\frac{A_{gg}}{A_{sd}(A_{gg} - A_{sd})} = \frac{1}{A_{sd}} + \frac{1}{A_{gg} - A_{sd}} \tag{6.22}$$

The equation 6.18 can be easily integrated. The result is that $C_{bprecjsd}$ is proportional to $\frac{A_{gg}-A_{sd}}{A_{sd}}$, which tends to zero when $A_{sd} \rightarrow A_{gg}$.

The leaving term is used also for inter-subdomain pores, but in this case we do not consider coalescence due to the low concentration of pores (less than one for each grain).

Finally, if we call $H(bprecjsd) = \frac{dA_{sd}}{dt} \times \frac{1}{(A_{gg}-A_{sd})}$, we obtain:

$$\frac{dC_{bprecjsd}}{dt} = -\left(\underbrace{H(bprecjsd)}_{leave\ grain} + \underbrace{\frac{1}{A_{sd}} \frac{dA_{sd}}{dt}}_{coalescence} \right) \times C_{bprecjsd} \tag{6.23}$$

$$\frac{dC_{Xebprecjsd}}{dt} = -H(bprecjsd) \times C_{Xebprecjsd} \tag{6.24}$$

$$\frac{dV_{bprecjsd}}{dt} = -H(bprecjsd) \times V_{bprecjsd} \tag{6.25}$$

The equations above are the expressions used in the ODE system solved by MARGARET.

7. Validation of the code

Sommaire

7.1. Review of the main parameters used in the calculations 166
7.1.1. Diffusion coefficient of Xenon in the grain 166
7.1.2. Diffusion coefficient of Xenon along grain boundaries in UO_2 . 169
7.1.3. Diffusion coefficient of Xenon along the subdomain boundaries in UO_2 171
7.1.4. Intrinsic Uranium auto-diffusion coefficient: $D_{U,th}$ 173
7.1.5. Uranium auto-diffusion coefficient on the grain boundary: D_{Uj} 176
7.1.6. Uranium auto-diffusion coefficient on the subdomain boundary: D_{Ujsd} 177
7.1.7. Adjustment parameters for the re-solution process concerning gas dissolved on GB and SDB, $coe_{j->bulk}$ and $coe_{j->jsd}$ 178
7.1.8. Formation energies 179
7.1.9. Vibration frequencies 181
7.1.10. Parameters linked only to the subdomains 181
7.1.11. Parameters linked only to the mobility of the intra-granular bubbles 182
7.1.12. Parameters linked only to the HBS 183
7.2. Parameters used for the validation of the code 183
7.3. Comparison between measurements and predictions 187
7.3.1. Presentation of the measurements used for the validation 187
7.3.2. Base irradiation 190
7.3.2.1. Detailed results on a particular rod in BI 190
7.3.2.2. Results for the other rods 206
7.3.3. Power Ramps 221
7.3.4. Is it possible to release without inter-granular bubble interconnection? 233
7.3.5. Conclusion to the validation of the code 236

In this Chapter, I present the validation of the version of the code detailed in this manuscript (Section 7.3). Prior to that (Section 7.1), I review the literature on some of the most important parameters that intervene in the behaviour of the fission gas under irradiation, and that were not discussed in the previous Chapters. This passage is essential to obtain a good comparison between MARGARET predictions and experimental data: since the phenomena described by MARGARET are strongly coupled, the usage of a "wrong" parameter could be detrimental to the overall description of the

fission gas. The literature review gives us guidelines for the choice of the parameters to be used in the exercise of validation.
After the literature review and before the validation of the code, I present the set of parameters chosen for the validation (Section 7.2).

7.1. Review of the main parameters used in the calculations

7.1.1. Diffusion coefficient of Xenon in the grain

The Xenon diffusion coefficient in the bulk, D_{Xe}, can be divided into three distinct contributions [J. A. Turnbull and R. M. Cornell 1970]: a thermal, $D_{Xe,th}$, an a-thermal, $D_{Xe,ath}$, and an irradiation-enhanced part, $D_{Xe,mix}$. The thermal part of the diffusion coefficient represents the diffusion in the absence of irradiation, and his expression is generally written as: $D_{Xe,th} = D_0 exp(-\frac{E_a}{kT})$, where D_0 is the pre-exponential term and E_a the activation energy. The irradiation-enhanced part refers to the increase in the diffusion coefficient of Xenon due to the increase in the vacancies present in the grain produced by irradiation. This part of the diffusion coefficient generally depends on the square root of the fission rate. The a-thermal part refers to the diffusion of Xenon "directly" driven by irradiation, due to the fission spikes that generate a local melting in the material and hence increase the diffusion. This part is generally expressed as proportional to the fission rate.

A review of the experiments used to determine $D_{Xe,th}$ is present in [L. Noirot 2014]. L. Noirot presented the requirements that have to be fulfilled to correctly measure $D_{Xe,th}$. Those requirements are (citing [ibid.]):

— (R1) The quantity of xenon, created or implanted, must be very low to avoid bubble nucleation.
— (R2) The atmosphere has to be controlled to avoid oxidation during annealing.
— (R3) Precise knowledge of the S/V is required to estimate D_0 properly.
— (R4) The presence of grain boundaries in the material should be avoided, because they may impact xenon transport.

L. Noirot argues that the most reliable expression is the one proposed by Davies and Long [Davies et al. 1963]:

$$D_{Xeth}(m^2/s) = 7.6\,10^{-10}\, exp\left(\frac{-3.04\ eV}{kT}\right) \tag{7.1}$$

This is the same expression for $D_{Xe,th}$ used by Turnbull [J. A. Turnbull, Friskney, et al. 1982] in 1982. In the same article, he also proposes the following a-thermal and irradiation-enhanced contributions:

$$D_{Xe,mix}(m^2/s) = 1.7 \times 10^{-25} \times \dot{F}^{0.5}\, exp\left(\frac{-1.2\ eV}{kT}\right) \tag{7.2}$$

$$D_{Xe,ath}(m^2/s) = 2 \times 10^{-40} \times \dot{F} \tag{7.3}$$

Apart from experiments, the Xenon diffusion coefficient in the bulk has been recently studied also through the exploitation of computational models.

Using the CRG (Cooper, Rushton and Grimes) empirical potential, Cooper and co-workers [Cooper, Stanek, et al. 2016] calculated the a-thermal part of the Xenon diffusion coefficient. He found:

$$D_{Xe,ath} = A \times \dot{F} \tag{7.4}$$

With A slightly depending on temperature (see table 7.1).

T [K]	A [m^3]
600	1.62×10^{-40}
1000	1.80×10^{-40}
1500	2.10×10^{-40}

Table 7.1. – Change in the A parameter in eq. 7.4 with temperature.

A value for A of $\approx 2 \times 10^{-40}$ is in line with the athermal diffusion coefficient proposed by Turnbull (eq. 7.3).

An interesting point in this article is that more than 98.5 % of the diffusivity is accounted for by electronic stopping (the fission spike, local melting of the lattice). So ballistic effects are negligible in this process. It is a similar conclusion to the findings of Setyawan for re-solution [Setyawan et al. 2018]: electronic stopping effects predominate.

The work of Perriot and co-workers [Perriot et al. 2019] focuses on the out-of-pile diffusion of Xe (and therefore on $D_{Xe,th}$). Based on DFT and Empirical Potentials (EP), they calculated the free energy of different Xe-vacancy clusters, their migration barriers and attempt frequencies. Then, $D_{Xe,th}$ was calculated as:

$$D_{Xe,th} = \sum_{\text{y} \in \text{cluster}} D_0(y) \times exp\left(-\frac{E_m(y)}{kT}\right) \times [y] \tag{7.5}$$

Where $D_0(y)$ depends on the attempt frequency of the cluster y, $E_m(y)$ is the migration barrier for the cluster y, and $[y]$ is the relative concentration of the cluster y among the clusters considered. $[y]$ is deduced from the free energy of the cluster.

Indeed, the hypothesis behind this work is a condition of thermodynamic equilibrium, which makes sense since the researcher are trying to estimate $D_{Xe,th}$.

The main conclusion of Perriot and coworkers' article are:
— Xe interstitials do not contribute to the total diffusivity in the thermal regime
— D_{Xeth} is mostly governed by Xe_{U_2O} vacancy clusters (which, in our approach - see Section 5.1.5 - could be associated to a defect '2 Schottky + Xe atom', with volume 2Ω)
— The resulting Xe diffusivity can be expressed as:

$$D_{Xe,th} = \frac{6.48 \times 10^{-7} exp\left(\frac{-3.7\,eV}{kT}\right)}{1 + 1.82 \times 10^{+4} exp\left(\frac{-1.45\,eV}{kT}\right)} \tag{7.6}$$

Expression which is in agreement with the Davies and Long's one for temperatures higher than about 1400K.

The article of Matthews and co-workers [C. Matthews et al. 2020] is the continuation of the work of Perriot (same team in both articles). This time, the aim is to provide an irradiation-enhanced term, $D_{Xe,mix}$, for the diffusion of Xenon in the presence of more defects due to irradiation.
As the thermodynamic equilibrium can not be supposed any more under irradiation, a cluster dynamic model is used to determine the cluster concentrations (the same used in [C. Matthews et al. 2019]). The thermodynamic and kinetic properties of Xenon defects are taken from Perriot's article [Perriot et al. 2019].
Under irradiation, there are much more Uranium interstitials, and they may substitute a Xenon atom in a vacancy site, kicking-out a Xenon interstitials (thermodynamically favorable reaction). The contribution to the diffusivity of Xenon given by Xe interstials can then be higher than the same contribution without irradiation, which is negligible [ibid.]. Therefore Xenon interstitials are included in the analysis.

The researchers finally give the following expression for $D_{Xe,mix}$:

$$D_{Xe,mix} = 2.82 \times 10^{-22} exp\left(\frac{-2\ eV}{kT}\right) \times \dot{F}^{0.5} \tag{7.7}$$

And explain that, under irradiation, the Xe diffusion is mainly due to $Xe_{U_4O_3}$ cluster (a cluster with 4U, 3O missing and a Xe atom).
The model seems strongly dependent on the concentration of the U_i20_i cluster (anti-Schottky defect), which can react with the $Xe_{U_4O_3}$ cluster and decrease its concentration. Since the U_i20_i cluster is highly mobile, it is quickly trapped by sinks (bubbles and dislocations, where bubbles represent the strongest sink[1]), letting the $Xe_{U_4O_3}$ cluster survive.

1. In [C. Matthews et al. 2019], the researchers assume in section 2.5 that bubbles represent the strongest sink. In [Cooper, C. Matthews, et al. 2025], page 3, they estimate the strength of the different sinks, and bubbles are the strongest.

In the article of Matthews and co-workers [C. Matthews et al. 2020], sinks are described *"as a reservoir, allowing species interaction to result in loss or gains, depending on how far away the species are from equilibrium"*.
The contribution from Xe_i to $D_{Xe,mix}$ is said *"minimal"* as *"a consequence of the fast migration mechanism for Xenon interstitials also leading to rapid reaction with sinks"*. It seems then problematic that a diffusion coefficient, calculated to be used in models where trapping of Xe by bubbles is of primary importance, ignores the contribution of Xe_i because they are rapidly trapped by bubbles.

The same team, in [Cooper, C. Matthews, et al. 2025], continues the research on Xe diffusivity through cluster dynamic studies. This time, they conclude that interstitial Xe (Xe_i), *"on the order of 1 day to 1 week, dominates diffusion below 1130 K, whereas on a 1-year timescale dominates below 1000 K"*. Again, they emphasize the role of the auto-interstitials in mantaining a low V_{at} in bubbles, up to a certain limit, based on the change in the auto-interstitials - bubble reaction energy, which is a function of the V_{at} in the bubble.

From this discussion, we have to note that Xe atoms reach bubbles with no volume (Xe_i, below $\approx 1000K$) or 4Ω (irradiation-enhanced as a $Xe_{U_4O_3}$ cluster) or $\approx 2\Omega$ (at high temperature as a Xe_{U_2O} cluster). Moreover, the behaviour of the anti-Schottky defects (auto-interstitials) has an important part to play in this respect, influencing directly the V_{at} of the bubbles.
That is the reason why we have re-interpreted our "volume contribution accompanying Xe atoms" in the cavity volume evolution equation (See Section 5.1.5).

Figure 7.1 shows the expressions of D_{Xe} proposed in literature[2].

7.1.2. Diffusion coefficient of Xenon along grain boundaries in UO_2

In the only experimental determination of D_{Xej} present in literature, the work of D.R. Olander and P. Van Uffelen [D. R. Olander et al. 2001] (discussed more thoroughly in Section 3.1.2), the researchers proposed two different expressions of D_{Xej} on the basis of two different expressions of D_{Xe}: a 'low' estimation by Davies and Long Davies et al. 1963 and an 'high' estimation by Matzke [Hj. Matzke 1990]. The expressions that they have derived are:

2. In [C. Matthews et al. 2020], they give an expression for D_{Xeth} that has the same form as in [Perriot et al. 2019], but with different coefficients. However, the expression of D_{Xeth} in [C. Matthews et al. 2020] is too high with respect to the corresponding illustration (Fig 16 of the paper) and with respect to the claim that it is close to the thermal contribution given by Turnbull [J. A. Turnbull, Friskney, et al. 1982]. So, there is probably a typo in eq. (15b) of [C. Matthews et al. 2020]. That is why we do not report it in the text, and prefer to show $D_{Xe,th}$ of Perriot [Perriot et al. 2019] and $D_{Xe,mix}$ of Matthews [C. Matthews et al. 2020].

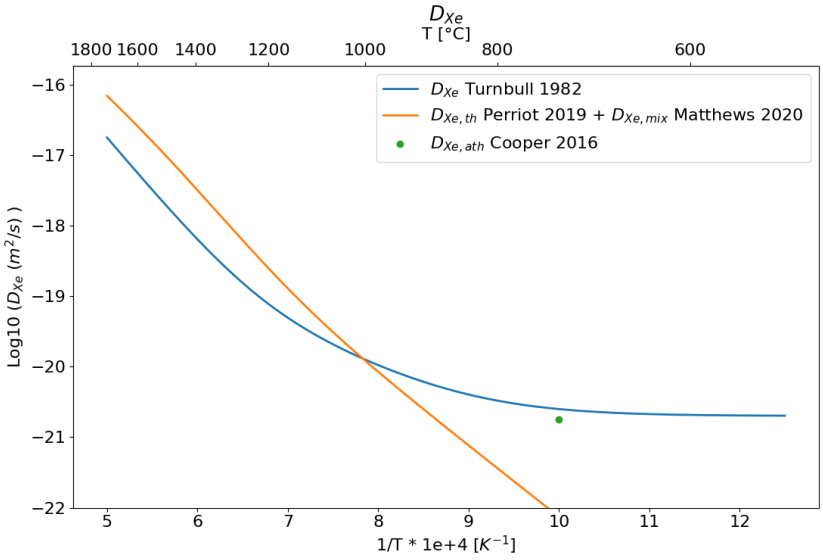

Figure 7.1. – Expressions of D_{Xe} proposed in literature, at a fission rate $\dot{F} = 10^{19}$ [fissions / m^3 / s].

$$\begin{aligned} D_{Xej}^{low\,D_{Xe}} &= 9\times10^{-8}\,exp\left(\frac{-92\ \text{kJ/mol}}{RT}\right) \quad [cm^2/s] \\ &= 9\times10^{-12}\,exp\left(\frac{-0.955\ \text{eV}}{kT}\right) \quad [m^2/s] \end{aligned} \tag{7.8}$$

$$\begin{aligned} D_{Xej}^{high\,D_{Xe}} &= 1.3\times10^{-3}\,exp\left(\frac{-272\ \text{kJ/mol}}{RT}\right) \quad [cm^2/s] \\ &= 1.3\times10^{-7}\,exp\left(\frac{-2.824\ \text{eV}}{kT}\right) \quad [m^2/s] \end{aligned} \tag{7.9}$$

Where R is the gas constant: 8.315 [J/(mol K)].
However, the researchers add that their expressions are much less reliable at temperatures far from 1773 K, which is the temperature of the experiment that they analysed.

From the analysis presented in Section 7.1.1, it seems that the most reliable measure of D_{Xe} is the one of Davies and Long [Davies et al. 1963] (see eq. 7.1), therefore, the most reliable expression for D_{Xej} should be the one derived considering the 'low' estimation of D_{Xe}.

The expression of D_{Xej} can also be derived by Molecular Dynamics. In the technical note [Liu et al. 2023], Liu and co-workers present the most recent MD simulation that tried to evaluate D_{Xej}. The authors introduced Xe atoms and vacancies on the GB,

and from the MSD (Mean Squared Displacement), they obtained D_{Xej} using:

$$MSD = 6D_{Xej}t$$

t being the duration of the simulation.

As the obtained diffusion coefficient depends on the number of vacancies introduced, the results provided by the article are presented in terms of a normalized Xe diffusion coefficient, D^*_{Xej}:

$$D^*_{Xej} = \frac{D_{Xej}}{x_{v,j}} \tag{7.10}$$

Where $x_{v,j}$ is the concentration of vacancies on the GB in [vacancies / site] and D^*_{Xej} can be expressed on the form: $D^*_{Xej} = D^{0*}_{Xej} exp(-E^*_{aXej}/kT)$.
They studied 3 different types of GBs: twist Σ5, tilt Σ5 and a random GB. For each GB, they obtained the values of D^{0*}_{Xej} and E^*_{aXej} reported in table 7.2.

Type of GB	D^{0*}_{Xej} [m^2/s]	E^*_{aXej} [eV]
twist Σ5	1.1×10^{-9}	0.39
tilt Σ5	1.2×10^{-6}	1.46
random GB	2.8×10^{-7}	1.08

Table 7.2. – Parameters of the expression of D^*_{Xej} for each GB studied in [Liu et al. 2023].

For the validation of the code, we decided to use the expression given in [D. R. Olander et al. 2001] for $D^{low\,D_{Xe}}_{Xej}$ (eq. 7.8), plus, in absence of more information in this regard, we include the same a-thermal contribution chosen for D_{Xe}.

7.1.3. Diffusion coefficient of Xenon along the subdomain boundaries in UO_2

Turnbull and Hoffman [D. Turnbull et al. 1954] propose a simple expression, later recalled by N.L. Peterson [Peterson 1986], of the auto-diffusion coefficient along Low Angle Grain Boundaries (LAGB) as a function of the misorientation angle θ and the diffusion coefficient along the dislocations that make up the LAGB, D_p, with the hypothesis that the diffusion coefficient along the dislocations is much higher that the diffusion coefficient in the bulk and that D_p is independent on the misorientation angle. By representing the subdomain boundary as a planar array of pipes of cross-sectional area A_p and spacing d, they derived the following expression:

$$D'\delta = \frac{D_p A_p}{d} = 2D_p A_p \frac{sin(\theta/2)}{b} \tag{7.11}$$

where D' is the diffusion coefficient that we would measure if we consider the LAGB as an uniform slab of thickness δ, and b is the Burgers vector of the parallel dislocations. The second equality ($d = \frac{b}{sin(2\theta/2)}$) comes from the dislocation models of crystal grain boundaries proposed by Read and Shokley [Read et al. 1950].

Using the derived expression, Turnbull and Hoffman managed to describe the rate of self-diffusion of silver in the grain boundaries of bicrystals with misorientation angles: $9° \leq \theta \leq 28°$.

In the case of auto-diffusion, the atom that diffuse are both on the LAGB and in between. So, D' is a weighted average of the diffusion coefficients in the bulk and in the dislocations.

In our case, since we are dealing with the diffusion of Xenon on the subdomain boundaries, we need to consider that Xenon atoms segregate on the dislocations that make up the subdomain boundaries. Therefore, almost all the Xenon atoms along the subdomain boundaries can be considered as concentrated in the dislocations. Then, if we consider the subdomain boundaries as an uniform slab of thickness δ (through an homogenization process similar to the one explained in Section 3.2.1), we can write:

$$D^{loc}_{Xejsd} = D^{d}_{Xejsd} \tag{7.12}$$

Where D^{loc}_{Xejsd} is the diffusion coefficient of Xenon on the subdomain boundaries and D^{d}_{Xejsd} is the diffusion coefficient of Xenon along a dislocation.

At our knowledge, the only proposed expression in the literature for D^{d}_{Xejsd} comes from [S. T. Murphy et al. 2015], expression which may not be possible to use reliably at the temperatures present in the pellet during base irradiation because it was derived for temperatures above the Bredig transition (see Section 4.1.2). Therefore, we decided to use the same expression for the Xenon diffusion coefficient on the subdomain boundaries as the one used for the Xenon diffusion coefficient on the grain boundaries: $D^{loc}_{Xejsd} = D_{Xej}$.

We now need to link D^{loc}_{Xejsd} to D^{MAC}_{Xejsd}, as in Section 3.2.1. The difference between the subdomain boundaries and the grain boundaries is that, in the subdomain boundaries, Xe diffusion is anisotropic: only one direction is subjected to an increase in the diffusion coefficient, the direction parallel to the dislocations.
To take anisotropy into account in a simple manner, we can start from the problem presented in figure 3.1, and consider that, in each subdomain boundary, diffusion happens only in one direction (see figure 7.2). If so, following the same derivation as in

Section 3.2.1, we can find: $D^{MAC}_{Xejsd} = \frac{1}{3} D^{loc}_{Xejsd}$ (instead of $D^{MAC}_{Xej} = \frac{2}{3} D^{loc}_{Xej}$). In the code, we have introduced the possibility that $D^{MAC}_{Xej} \neq D^{MAC}_{Xejsd}$. So, we can take $D^{MAC}_{Xej} = D_{Xej}$ (as explained in Section 3.2.1) and $D^{MAC}_{Xejsd} = \frac{1}{2} D_{Xej}$. D^{MAC}_{Xejsd} is simply called D_{Xejsd} in the rest of the manuscript.

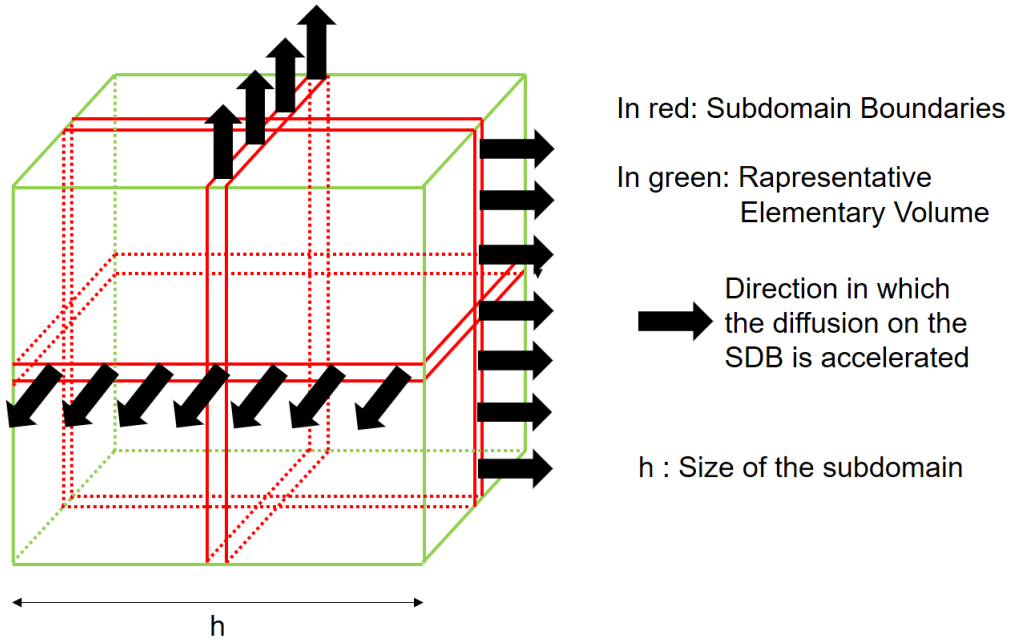

Figure 7.2. – Representative Volume Element (RVE) used to derive the macroscopic diffusion coefficient of Xenon on the subdomain boundary, D^{MAC}_{Xejsd}, from the diffusion coefficient of Xenon on the subdomain boundary, D^{loc}_{Xejsd}.

7.1.4. Intrinsic Uranium auto-diffusion coefficient: $D_{U,th}$

The Uranium self-diffusion coefficient during irradiation, similarly to the Xenon diffusion coefficient, is usually expressed using 3 different terms: the thermal part, which describes the mobility of U allowed by thermal vacancies, a radiation enhanced part, that describes the increase in the Uranium auto-diffusion coefficient caused by the presence of irradiation vacancies and auto-interstitials, and an a-thermal term, which describes the mobility of Uranium atoms due to fission spikes.
Since we are only concerned in the behaviour of thermal vacancies, as explained in Chapter 5, here we are interested only in $D_{U,th}$, the intrinsic (thermal) part of the Uranium self-diffusion coefficient.

Two of the most recent experiments performed to determine $D_{U,th}$ are the ones of Matzke [H. Matzke 1987] and Sabioni and co-workers [Sabioni et al. 1998].

Matzke derived the following expression:

$$\begin{aligned} D_{U,th}\,(m^2/s) &= 6.5\,10^{-5} exp\left(\frac{-540\ kJ/mol}{RT_K}\right) \\ &= 6.5\,10^{-5} exp\left(\frac{-5.6\ eV}{kT_K}\right) \\ &= 6.5\,10^{-5} exp\left(\frac{-64902}{T_K}\right) \end{aligned} \tag{7.13}$$

While Sabioni and co-workers the following one:

$$D_{U,th}\,(m^2/s) = 8.54\,10^{-11} exp\left(\frac{-4.4\ eV}{kT_K}\right) \tag{7.14}$$

These expressions result in diffusion coefficients orders of magnitude apart one from the other.
This is a general trend in the literature: the experimental values of $D_{U,th}$ are quite scattered and span across different orders of magnitude. A summary of other experiments can be found in the papers of Sabioni and co-workers [Sabioni et al. 1998] and of Muntaha and co-workers [Muntaha et al. 2024].
Such differences in the expressions of $D_{U,th}$ can be due to a slight difference in the stochiometry of the specimens, but also, citing [Sabioni et al. 1998], *"the nature and amount of the impurities, the characteristics of the samples, and the experimental procedures and techniques used to measure the diffusion coefficient"*.

Similarly to the thermal diffusion coefficient of Xenon, $D_{U,th}$ can also be determined using DFT and Empirical Potentials (EP), and calculating the free energy of different Uranium clusters, their migration barriers and attempt frequencies. This work has been performed by Matthews and coworkers [C. Matthews et al. 2019].
After a parametric study and a comparison with experimental values of $D_{U,th}$, passage that was needed given the uncertainty in the assumptions used to derive their model, they obtained the following expression of $D_{U,th}$:

$$D_{U,th}\,(m^2/s) = 5.24\,10^{-11} exp\left(\frac{-4.36\ eV}{kT_K}\right) \tag{7.15}$$

Which is in line with Sabioni and co-workers' result [Sabioni et al. 1998].

Finally, the activation energy of the intrinsic Uranium self-diffusion coefficient has been derived using DFT + U calculations plus a point-defect model[3] in the work of

3. The researchers modelled only single Uranium vacancies and auto-interstitials, but no defect clusters. The contribution of the defect clusters to the Uranium self-diffusion coefficient may become

Dorado and co-workers [Dorado et al. 2012]. They calculated the migration barriers of Uranium vacancies and auto-interstitials for different possible migration mechanism and found that *"the oxygen-assisted uranium vacancy mechanism emerges as the most likely mechanism for uranium diffusion in near stoichiometric UO_2, with an apparent activation energy derived from DFT that is close to that reported by Sabioni under a reducing atmosphere (4.4 eV)"* [Sabioni et al. 1998].
Moreover, they explained how the discrepancy between Sabioni and Matzke's experimental determination of $D_{U,th}$ may be due to the difference in the stoichiometry of the samples of less than 0.002. Such deviations of the stoichiometry cannot be measured by standard thermogravimetric techniques.

Unfortunately, during irradiation, we cannot be sure that the fuel remains stoichiometric, since such small variations cannot be measured during post irradiation examinations. Moreover, in ALCYONE, the Fuel Performance Code in which MARGARET is integrated, there is no model able to predict the stoichiometry of the fuel. Therefore, in the limit given by the experiments, the expression of $D_{U,th}$ to be used in the validation of the code will be chosen in such a way as to best describe the experimental data that we have on power ramped fuels.

Figure 7.3 shows the expressions of D_U proposed in literature.

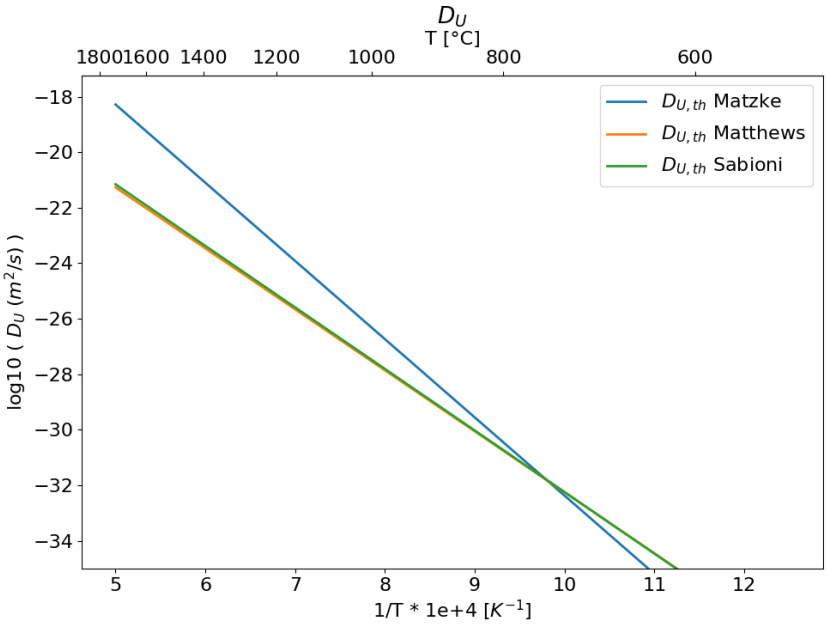

Figure 7.3. – Expressions of D_U proposed in literature. Sabioni and Matthews's expressions are almost coincident.

not negligible for non-stochiometric fuels.

7.1.5. Uranium auto-diffusion coefficient on the grain boundary: D_{Uj}

In MARGARET, we make the hypothesis that vacancies are created on the grain boundaries due to the fact that inter-granular bubbles are over-pressurized (see Section 5.1.4.2). The value of $D_{Uj} = D_{v,j} \times x_{v,j}^{eq}$ (see eq. H.35) determines the flux of vacancies created in the grain boundaries towards the inter-granular bubbles.

Experimental values of D_{Uj} have been measured by Lambert [Harding 1990], White [White 2004], Sabioni and co-workers [Sabioni 2000], Alcock and co-workers [Alcock et al. 1965], Yajima and co-workers [S. Yajima 1966].
The expression given by White [White 2004] is derived through the analysis of the swelling of inter-granular bubbles. He performed PI measurements on fuels that experienced a wide range of power histories, gathering data on the behaviour of inter-granular bubbles. Then, using the model of inter-granular bubble growth presented in Section 5.1.4.2, White derived two expression of D_{Uj}: one that best fitted the swelling data, and the other that fitted the shrinkage data. The expressions are very similar and this gave him confidence on the approach that he used to obtain them.
Sabioni and colleagues [Sabioni 2000], instead, obtained a series of values of D_{Uj} at different temperatures by measuring the diffusion of a tracer in UO_2 poly-crystals. Moreover, in the same paper, citing Matzke [Hj. Matzke 1992], the researchers wrote that the results of G.B. Alcock [Alcock et al. 1965] and of S. Yajima [S. Yajima 1966] were questionable. In fact, Sabioni and colleagues argued that the values of the diffusion coefficient reported in those articles were a result of the usage of a very high Uranium volume diffusion coefficient.

Differently from experiments, using Molecular Dynamic simulations, we can calculate directly the vacancy diffusion coefficient on grain boundaries, $D_{v,j}$. Expressions of $D_{v,j}$ can be found in [Galvin, Chakraborty, et al. 2022; Govers et al. 2013; Vincent-Aublant et al. 2009].

As introduced in Section 1.3.4, for the expression of D_{Uj} used in the last validation of MARGARET two temperature domains were adopted, in order to obtain satisfactory comparison with major experimental quantities, such as Fission Gas Release and EPMA measurements, during both base irradiation and power ramp conditions. In the low temperature domain (IB), moreover, D_{Uj} was a function of the burnup. In particular, at a given temperature, the value of the diffusion coefficient increased with burnup by several orders of magnitude.
In literature, there are nor direct nor simulation results to support such a dependence of the diffusion coefficient on the burnup and the presence of two temperature domains. On the other hand, MD simulations [Galvin, Andersson, et al. 2023] show that the value of D_{Uj} can change by few orders of magnitude with a slight change of the stoichiometry. The change in the stoichiometry can be less than the measurable limit and still produce a major change in the value of D_{Uj}. This phenomenon is amplified

at lower temperatures.
However, in the absence of a model, integrated inside Fuel Performance Codes, which predicts the stoichiometry, we prefer to try to use one single expression of D_{Uj} that does not depend on the burnup.

Figure 7.4 shows the expressions of D_{Uj} proposed in literature, plus the expressions of $D_{v,j}$ obtained by Molecular Dynamics multiplied by $x_{v,j}^{eq}$.

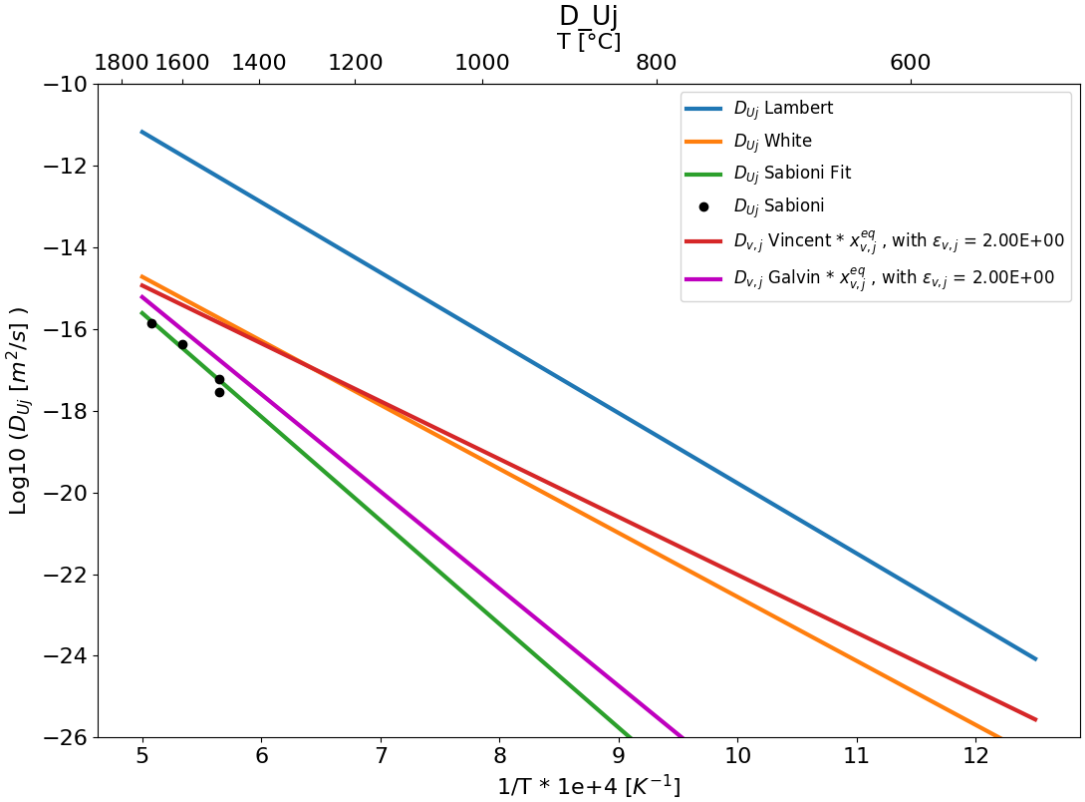

Figure 7.4. – Expressions of D_{Uj} proposed in literature. The line "Sabioni fit" is a linear fit of the point values of D_{Uj} proposed in [Sabioni 2000], and reported as dots in the figure. For the choice of $\varepsilon_{v,j}$, see Section 7.1.8.

7.1.6. Uranium auto-diffusion coefficient on the subdomain boundary: D_{Ujsd}

Following the comments on the Xenon diffusion coefficient on subdomain boundaries (Section 7.1.3), since we know that also vacancies tend to segregate on the dislocations that make up the subdomain boundaries (see Section 7.1.8), we consider:

$$D^{loc}_{Ujsd} = D^{d}_{Ujsd}$$
$$D^{MAC}_{Ujsd} = \frac{1}{2} D^{loc}_{Ujsd} \tag{7.16}$$

D^{MAC}_{Ujsd} is simply called D_{Ujsd} in the rest of the manuscript.

Moreover, in the same way as for D_U and D_{Uj}, we are interested only in the intrinsic diffusion coefficient of Uranium on subdomain boundaries, $D^{loc}_{Ujsd,th}$.

Using MD simulations, both Murphy and co-workers [S. Murphy et al. 2014] and Vincent-Aublant and co-workers [Vincent-Aublant et al. 2009] show that cations move faster along dislocations than in the bulk. Murphy and co-workers do not give an expression for the diffusion coefficient, but they calculated an Activation Energy equal to 1.57 [eV], which is much lower than the one in the bulk. Vincent-Aublant and co-workers propose the following expression: $D_{v,jsd} = 1.4e-8\ exp\left(\frac{0.81[eV]}{kT}\right)$, which is very similar to the expression that they propose for $D_{v,j}$ ($D_{v,j} = 1.8e-8\ exp\left(\frac{0.79[eV]}{kT}\right)$).

However, given the absence of strong indications on the expression of $D^{loc}_{Ujsd,th}$ to be used, we decided to use the same expression chosen for $D_{Uj,th}$ (which is also coherent with the results of [ibid.]). We then obtain: $D_{Ujsd,th} = \frac{1}{2} D_{Uj,th}$.

7.1.7. Adjustment parameters for the re-solution process concerning gas dissolved on GB and SDB, $coe_{j->bulk}$ and $coe_{j->jsd}$

At our knowledge, the only value reported in the literature for $b(j)$ is: 2×10^{-25} [m^3] $\times \dot{F}$ [Losonen 2017]. In his article, Lösönen studied the effect of $b(j)$ on the concentration of dissolved Xenon on the grain boundaries, and found a reduction of the concentration of 30-50% at 1273 K when a value of 2×10^{-25} [m^3] $\times \dot{F}$ was used, with respect of not considering at all the re-solution from grain boundaries to the grain. The reduction in the concentration diminish at higher temperatures.
Without adjustment parameters ($coe_{j->bulk} = 1$), considering dNML = 0.8, $\zeta = 0.73$, $\delta = 2$ nm, $e_{pj} = 1$ nm, $R_\Omega = \left(\frac{3}{4\pi}\Omega\right)^{1/3} = 0.2137$ nm, we can calculate a value of $b(j) \approx 1 \times 10^{-23}$ [m^3] $\times \dot{F}$ (see Section 3.2.6). So, the value of Lösönen corresponds to $coe_{j->bulk} = 0.02$, in this case.

7.1.8. Formation energies

M. Gascoin and co-workers [Gascoin et al. 2024] calculated the formation energies of the 3 bound Schottky defects in bulk UO_2 (ε_v) with Density Functional Theory (DFT) + U and found the following values: 4.30 [eV] (BSD1), 3.79 [eV] (BSD2), 3.89 [eV] (BSD3). However, these values are calculated using a box with 96 atoms, and it is known that calculations of formation energies can decrease using a box with 324 atoms, due to size effects [Burr et al. 2017; Gascoin et al. 2024].

The formation energy of a Xenon atom in the lattice can be calculated as the sum of ε_v and the incorporation energy of a Xenon in a Schottky defect. Cooper and co-workers [Cooper, Kuganathan, et al. 2016], using DFT, calculated an incorporation energy equal to 0.49 [eV]. Other values for the incorporation energy of Xe in a Schottky defect can be found in the PhD thesis of E. Vathonne [Vathonne 2014] (table 5.13): 0.45 eV for BSD1, 1.03 for BSD2 and 1.68 for BSD3. The most favorable value (0.45 [eV]) is in agreement with the value (0.49 [eV]) proposed by Cooper and co-workers [Cooper, Kuganathan, et al. 2016].

Borde and co-workers [Borde et al. 2021] studied the segregation of Schottky defects on symmetric tilt HAGB and LAGB around [001] axis. The formation energies reported in [ibid.] were calculated leveraging a classical empirical potential (CRG [Cooper, Rushton, et al. 2014] in this case). The accuracy of this method relies on the fitting procedure, and if the formation energies were not included in the fitting criteria, then their evaluation with the interatomic potential (IAP) could differ a lot from DFT results, which can be considered more accurate. This is why we have chosen to take into account the relative values of the formation energy for the calculation of the segregation energy. The formation energy of a Schottky defect in the bulk is found to be $\approx 5.5-6$ [eV], while the segregation energy depends on the misorientation angle (see figure 12 of the article): for LAGB (misorientation angle less than 15°), the segregation energy is between -2 and -3.5 [eV], while for HAGB it is between -1.5 and -3.5 [eV].

Borde and co-workers studied also the segregation of the defect 'Xenon atom in a Schottky defect' on the same types of GBs cited previously. The formation energy of a Xe atom in a Schottky defect in the bulk is found to be $\approx 8-8.5$ [eV], while the segregation energy of the same defect on the GB and in the bulk depends on the misorientation angle (see figure 16 of the article): for LAGB (misorientation angle less than 15°), the segregation energy is between -3 and -4 [eV], while for HAGB it is between -1.5 and -4 [eV].

The work of Yang and co-workers [Yang et al. 2023] showed how the incorporation energy of a Xenon atom in a Schottky defect on the grain boundary is lower than the one in the bulk for most of the sites on the grain boundary (therefore lower than 0.49 [eV] [Cooper, Kuganathan, et al. 2016]). For their work, they concentrated their atten-

tion on symmetrical tilt grain boundaries and used *"three UO_2 potentials, including the CRG* [Cooper, Rushton, et al. 2014]*, Basak* [Basak et al. 2003]*, and Morelon* [N.-D. et al. 2003] *[...] to predict the GB structures of UO_2. These three UO_2 potentials were respectively combined with the Xe-UO_2 potential of Cooper* [Cooper, Kuganathan, et al. 2016]*, iterative potential refinement (IPR)* [Thompson et al. 2014] *or Chartier* [Chartier et al. 2010] *[...] to model the interactions between Xe and UO_2 "*.

C. Chil [Chil 2025] calculated the segregation of Schottky defects in the bulk and on symmetric tilt HAGB ($\Sigma 3$, $\Sigma 5a$, $\Sigma 5b$, $\Sigma 11$) through MD, using the same procedure as in [Borde et al. 2021], but with a different interatomic potential: instead of a classical empirical interatomic potential, he used a Machine Learning numerical interatomic potential coming from [Dubois et al. 2024]. He found a value for ε_v around 3.5 [eV] and an average value for $\varepsilon_{Seg,v}$ around 1.57 [eV].

In MARGARET, we cannot differentiate between different types of grain boundaries and subdomain boundaries. Therefore, we have to choose values of the formation and segregation energies that are representative of all the grain boundaries / subdomain boundaries.
Moreover, due to the large incertitude and the significant variability associated to the values of the segregation energy, we decided to use the same segregation energy (for each type of defect) for both the grain boundaries and the subdomain boundaries.

All things considered, we decided to use for the validation of MARGARET the values of formation energies present in table 7.3. The segregation energy of a Schottky defect on the GB and SDB is between 1/3 and 1/2 of the formation energy in the bulk, while the segregation energy of a Xe atom in a Schottky defect on the GB and SDB is a bit less than 1/2 of the formation energy in the bulk. In this way, we have respected the results of Borde and co-workers [Borde et al. 2021]. Moreover, the incorporation energy of a Xenon atom in a Schottky on the GB is less than the one in the bulk, as suggested by the work of Yang and co-workers [Yang et al. 2023]. The values chosen for the Schottky defect are also in agreement with the work of Chil [Chil 2025] (with a slightly higher value for both the bulk formation energy and the segregation energy).

	Formation energy bulk [eV]	Segregation energy GB [eV]	Segregation energy SDB [eV]
SD	3.8	-1.8	-1.8
$Xe \text{ in } SD$	4.3	-2.1	-2.1

Table 7.3. – Formation energies used in the validation of MARGARET

7.1.9. Vibration frequencies

Olander [OLANDER 1976] has shown that the order of magnitude of both the vibration frequency of Xenon in the bulk, ν_p (or ν_{Xe}), and the vibration frequency of Xenon on the grain boundary, ν'_p (or ν_{Xej}) (Chapter 7.7 of [ibid.]) are approximately equal to 10^{13} [s^{-1}].
We have chosen to use the same value also for the vibration frequency of Xenon on the subdomain boundaries. These frequencies can be used as an adjustment parameter.

7.1.10. Parameters linked only to the subdomains

Initial concentration of the precipitation bubbles, $C^{in}_{bprecjsd}$

In [Dowek 2021] a value between 2 and 9 $\times 10^8$ [bubbles/mm^3] (which means 2-9 $\times 10^{17}$ [bubbles/m^3], without counting the smallest bubbles) has been measured.
For the Rod_67.53_BI of our validation database, a concentration of bubbles at the centre of precipitation zone of 2×10^{18} [bubbles / m^3] has been measured at the end of base irradiation.
So, we can take the range $2 \times 10^{17} - 2 \times 10^{18}$ [bubbles / m^3].

Initial volume of the precipitation bubbles

The precipitation bubbles are initialized with the volume (for one bubble) of 4×10^{-24} m^3 ($R_{bprecjsd} = 13.66$ nm).

Radius of the subdomains, A_{sd}

In [ibid.], R. Dowek reports values of $ECD_{50\%}$ (Median Equivalent Circular Diameter) of the subdomains between 1.1×10^{-6} [m] and 1.3×10^{-6} [m], which translates to a value for A_{sd} between 0.55×10^{-6} [m] and 0.65×10^{-6} [m].

Parameters used as a condition for the introduction of the subdomains state

The following values have been used to obtain a good comparison with experimental data (Swelling, EPMA etc.):
$\tau_{eff} = 41$ GWd/t_U
$T_{low} = 1013$ K
$T_{high} = 1473$ K

However, PI examinations performed on the high burnup fuels used for the validation of the code have always revealed the presence of the subdomains in all the central part of the pellets. Therefore, it was not possible to quantify precisely T_{high}.

7.1.11. Parameters linked only to the mobility of the intra-granular bubbles

Mechanisms of diffusion of the bubbles, D_b, and related diffusion coefficients D_S and D_U^S

The diffusion coefficient of the intra-granular bubbles can be written as:

$$D_b = \underbrace{\frac{3}{4\pi}\frac{D_U^S \Omega}{R_b^3}}_{volume\,mechanism} + \underbrace{\frac{3}{2\pi}\frac{D_S \Omega^{\frac{4}{3}}}{R_b^4} \cdot W(R_b, C_b, C_{Xeb})}_{surface\,mechanism} \tag{7.17}$$

with $W(R_b, C_b, C_{Xeb}) = \left[1 - min\left(1, \frac{Q_{vol}}{\frac{4}{3}\pi R_b^3}\right)\right]^{\frac{C_{Xeb} N_{Avogadro}}{C_b}}$

The expressions of the volume and surface mechanisms are described in [OLANDER 1976, pag. 241 and pag. 236]. The term $W(R_b, C_b, C_{Xeb})$ comes from Mikhlin [MIKHLIN 1979]. This term allows to consider the fact that, in the most dense bubbles, the jumps of the Uranium atoms at the surface of the bubble are hindered by the presence of the gas. The volume Q represents the volume without Xe atoms that is needed so that a jump of an Uranium atom at the surface of the bubble becomes possible. In [ibid.] $Q_{vol} = 1.5\,10^{-27}$ [m^3].

The value of D_S used in [Harding 1990]:

$$\begin{aligned} D_S\,(m^2/s) &= 50.exp\left(\frac{-450\,kJ/mol}{RT_K}\right) \\ &= 50.exp\left(\frac{-4.668\,eV}{kT_K}\right) \\ &= 50.exp\left(\frac{-54122}{T_K}\right) \end{aligned} \tag{7.18}$$

is very close to the expression proposed by Maiya [MAIYA 1971] and used by Mikhlin [MIKHLIN 1979].

In Nichols et al. 1986] the authors show what seems to be a *"direct evidence for in-pile mobilities comparable with surface-diffusion control predictions"* for bubbles with a diameter < 20 [nm]. They used an expression for D_S equal to:

$$\begin{aligned} D_S &= 500exp\left(-\frac{120(kcal/mol)}{RT}\right) \qquad [m^2/s] \\ D_S &= 500exp\left(-\frac{5.21(eV)}{kT}\right) \qquad [m^2/s] \end{aligned} \tag{7.19}$$

For what concern the volume term, Chkuaseli and Matzke [CHKUASELI et al. 1993] propose to use the expression of D_U^S described by Hawkins [HAWKINS et al. 1968] :

$$\begin{aligned} D_U^S\,(m^2/s) &= 1.09\,10^{-4}\,exp\left(\frac{-439.4\,kJ/mol}{RT_K}\right) \\ &= 1.09\,10^{-4}\,exp\left(\frac{-4.56\,eV}{kT_K}\right) \\ &= 1.09\,10^{-4}\,exp\left(\frac{-52848}{T_K}\right) \end{aligned} \tag{7.20}$$

Heat of transport for surface thermal self-diffusion

Olander [OLANDER 1976, pag. 238] reports that common estimates of Q_S *"include assuming it equal to the activation energy for self-diffusion 450 kJ/mole and assuming it to be 2/3 of the heat of vaporization (Q_S = 380 kJ/mole)"*.
In [Nichols et al. 1986 the authors used a value of Q_S = 120 [kcal/mol] = 8.34×10^{-19} [J/atom].

For the validation of MARGARET, we use $Q_S = 6.90 \times 10^{-19}$ [J/atom].

7.1.12. Parameters linked only to the HBS

Radius of the HBS grains

From [Dowek 2021], the $ECD_{50\%}$ of the HBS grains is between 0.5 [μm] and 0.8 [μm]. It is therefore suggested to use a value for A_{pg} between 0.25 [μm] and 0.4 [μm].

Coefficient for the HBS creep term, coe_{creep}

We take coe_{creep} in the order of magnitude of 10^{-34} [m^3 / Pa] (see Appendix I).

7.2. Parameters used for the validation of the code

In table 7.4 I resume the parameters and expressions chosen for the validation of the code. They have been chosen following the literature and adapted to obtain a good comparison with experimental data (Swelling, EPMA etc.).
Figures 7.5, 7.6 and 7.7 show the expressions of D_{Xe}, $D_{U,th}$ and $D_{Uj,th}$ chosen for the validation, in comparison with the literature ones.

Quantity	Value / Expression	Notes
$D_{Xe,th}$	$7.6\,10^{-10}\,exp\left(\frac{-3.04\ eV}{kT}\right)$ (m^2/s)	Lit.
$D_{Xe,mix}$	$3.4\times10^{-25}\times\dot{F}^{0.5}\,exp\left(\frac{-1.2\ eV}{kT}\right)$ (m^2/s)	Adj.
$D_{Xe,at}$	$4\times10^{-40}\times\dot{F}$ (m^2/s)	Adj.
D_{Xej}	$9\times10^{-12}\,exp\left(\frac{-0.955\ \text{eV}}{kT}\right)+4\times10^{-40}\times\dot{F}$ (m^2/s)	Lit. / Adj.
D_{Xejsd}	$4.5\times10^{-12}\,exp\left(\frac{-0.955\ \text{eV}}{kT}\right)+2\times10^{-40}\times\dot{F}$ (m^2/s)	$D_{Xejsd}=\frac{1}{2}D_{Xej}$
$D_{U,th}$	$2.5\times exp\left(\frac{-7.324\ eV}{kT}\right)$ (m^2/s)	Adj.
$D_{Uj,th}$	$3\times10^{-8}\,exp\left(\frac{-3.102\ eV}{kT}\right)$ (m^2/s)	Adj.
$D_{Ujsd,th}$	$1.5\times10^{-8}\,exp\left(\frac{-3.102\ eV}{kT}\right)$ (m^2/s)	$D_{Ujsd}=\frac{1}{2}D_{Uj}$
ε_v	3.8 (eV)	Lit.
ε_{Xe}	4.3 (eV)	Lit.
$\varepsilon_{v,j}$	2.0 (eV)	Lit.
ε_{Xej}	2.2 (eV)	Lit.
ν_{Xe}	10^{13} (1/s)	Lit.
ν_{Xej}	10^{13} (1/s)	Lit.
dNML	0.75×10^{-9} (m)	Adj.
ζ	0.8 (/)	Adj.
coe_j	0.3 (/)	Adj.
$coe_{cavj->bulk}$	2.5 (/)	Adj.
$coe_{cavj->j}$	1.0 (/)	Adj.
$coe_{cavj->jsd}$	2.5 (/)	Adj.
τ_{eff}	41 [GWd/t$_U$] (10.9673×10^{26} [fission / m^3])	Adj.
T_{low}	1013 [K]	Adj.
T_{high}	1473 [K]	Adj.
A_{sd}	0.6×10^{-6} [m]	Lit.
$C^{in}_{bprecjsd}$	8×10^{17} [bubbles / m^3]	Lit.
$R^{in}_{bprecjsd}$	13.66 [nm]	Choice
$Ea_{growth\ sd}$	5.991 [eV]	Adj.
$B_{growth\ sd}$	5.0e-7 [m^3/s]	Adj.
D_S	$500\times exp\left(-\frac{5.21eV}{kT}\right)$ [m^2/s]	Lit.
D^S_U	$10^{-4}\,exp\left(\frac{-4.56\,eV}{kT_K}\right)$ [m^2/s]	Lit.
Q_S	6.90×10^{-19} [J/atom]	Adj.
Q_{vol}	2.0×10^{-28} [m^3]	Adj.
A_{pg}	0.35×10^{-6} [m]	Lit.
coe_{creep}	1×10^{-35} [m^3 / Pa]	Adj.

Table 7.4. – Parameters and expression chosen for the validation of the code. "Lit." means that the expression or the value comes from the literature, and include also values chosen in a range of possible values proposed in literature. "Adj." means that the parameter has been adjusted.

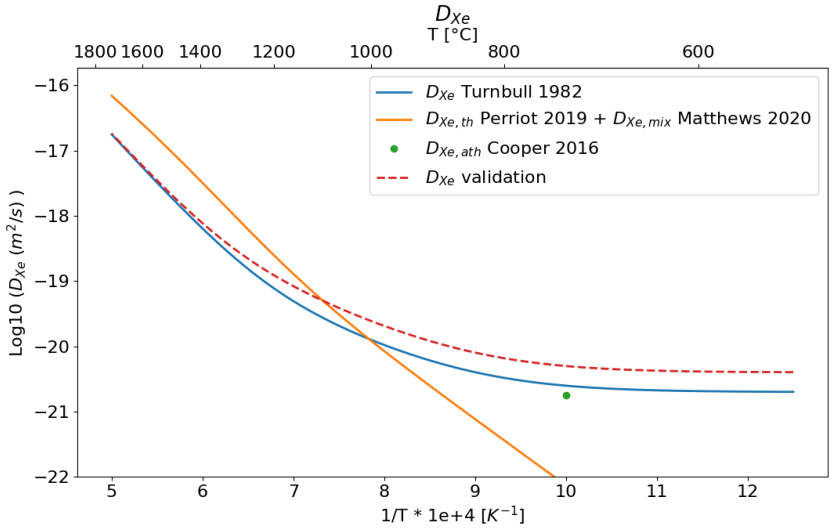

Figure 7.5. – Expressions of D_{Xe} proposed in literature (see Section 7.1.1) in comparison with the one chosen for the validation (see table 7.4), at a fission rate $\dot{F} = 10^{19}$ [fissions / m^3 / s].

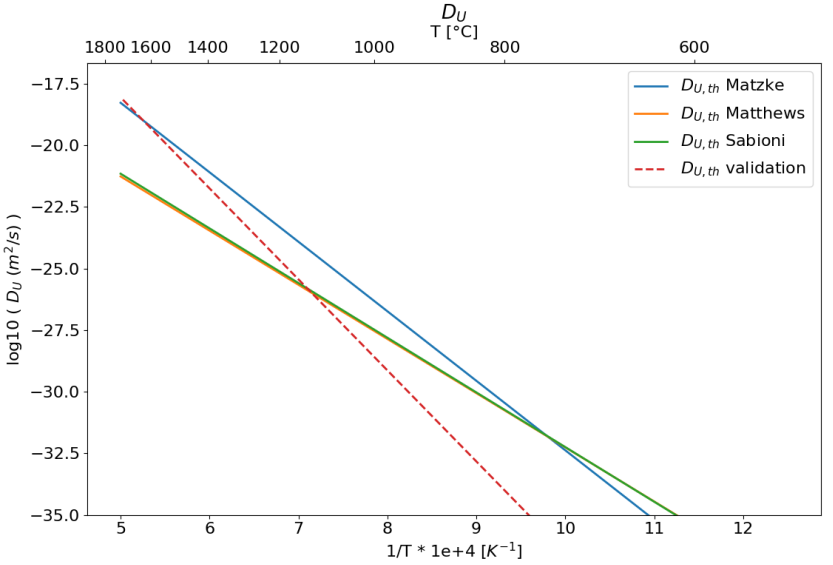

Figure 7.6. – Expressions of D_U proposed in literature (see Section 7.1.4) in comparison with the one chosen for the validation (see table 7.4).

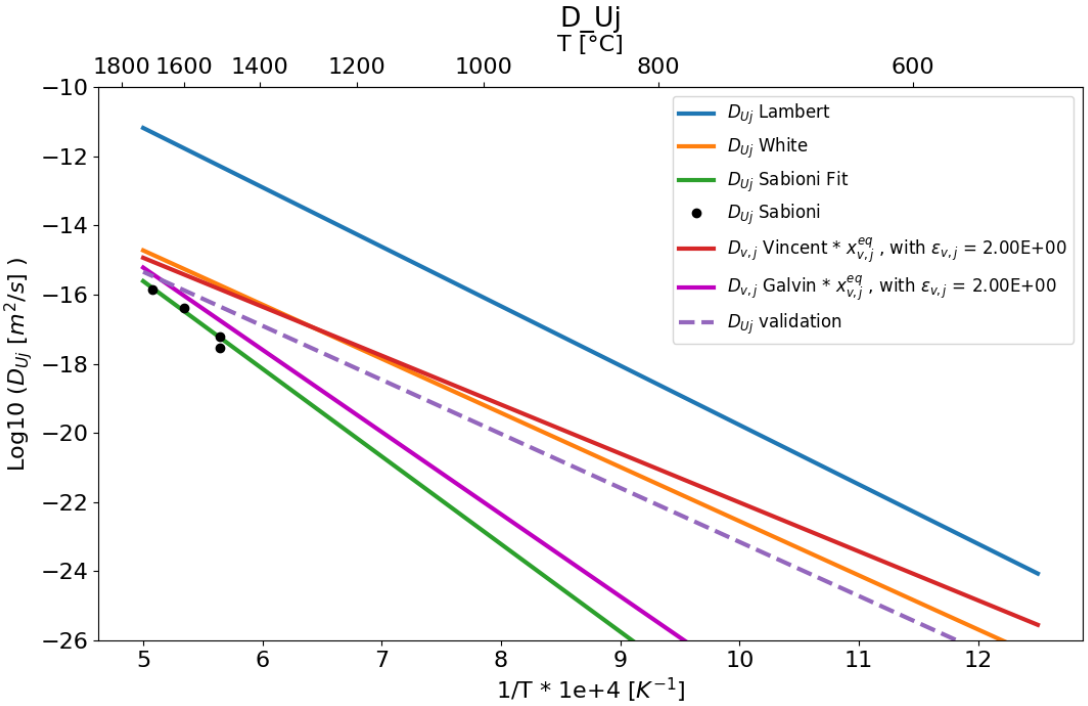

Figure 7.7. – Expressions of D_{Uj} proposed in literature (see Section 7.1.5) in comparison with the one chosen for the validation (see table 7.4). For the choice of $\varepsilon_{v,j}$, see Section 7.1.8.

7.3. Comparison between measurements and predictions

7.3.1. Presentation of the measurements used for the validation

In the following Sections, I will compare measurements and predictions of different quantities related to the behaviour of the fission gases in the nuclear fuel under irradiation.
The calculations are performed using the Fuel Performance Code ALCYONE [Introïni et al. 2024] plus MARGARET module (the version of MARGARET described in this manuscript) for the FG behaviour.
The comparison will encompass both base irradiated and power ramped fuels.

The fuels presented in this validation have been irradiated in French PWR reactors. For each fuel, we have chosen a name that represents the burnup measured at the end of irradiation, plus the sign "BI" if they have only been base irradiated, or "RT" if they underwent a power ramp.

Not all measurements reported here have already been published. When the reference on the measurements is missing, those measurements have not been subject to any prior publication. Moreover, to ensure confidentiality, some measurements and values have been rescaled using a common factor (different for each group of measurements / values). These cases are highlighted in the text.

The quantities that have been used for the validation of the code are:
— Fission Gas Release;
— Swelling of the fuel;
— Output of the Electron Probe Micro Analyzer (EPMA) of the Xe;
— Output of the Secondary Ionisation Mass Spectrometer (SIMS) of the Xe.
Moreover, we will present some insight on the behaviour of the fission gases predicted by MARGARET, like the distribution of the fission gas during irradiation (gas trapped in intra or inter-granular bubbles, gas dissolved, gas released etc.).

It is important to note that **no** automatic calibration of the parameters have been performed yet. Furthermore, the efforts done in the thesis to improve the consistency of the model result in a more demanding exercise (no "temperature domains" where the Arrhenius factors could be different, no evolution of D_{UJ} with the burnup). Therefore, the current validation of the code will probably improve in the future.

Table 7.5 shows the fuels and the corresponding measurements analyzed in this validation.
Since the temperature at which the fuels have been operated largely influences the

behaviour of the fission gas, in figure 7.8 I show the centerline temperature history predicted by ALCYONE for one slice of the Rod_56.72_BI, Rod_65.06_BI and Rod_-67.53_BI. Those slices include the height at which the specimens analyzed in [J. Noirot, Dowek, et al. 2022] have been extracted.
In general, the base irradiated fuels presented in this validation have experienced centerline temperatures lower than about 1100°C.

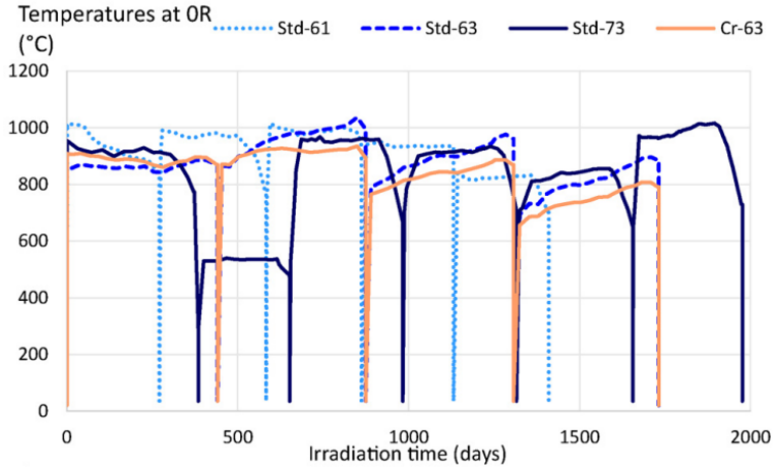

Figure 7.8. – Centerline temperature histories (from ALCYONE calculations) of the specimens analysed in [J. Noirot, Dowek, et al. 2022]. The link between those specimens and the "mother" rods used in this thesis are presented in table 7.5. The image is taken from [J. Noirot, Dowek, et al. 2022].

The calculations are based on input data given by EDF, such as the power at which the fuels have been operated. The incertitude in the power is estimated to be in the order of ±5%. Such an incertitude can have major consequences in the behaviour of the fuels, therefore, for base irradiated fuels, we have performed a sensitivity analysis on the input power: we have made the calculations with the same rod two or three times, changing each time the input power. For few of the rods presented in this validation, researchers have performed Neodymium measurements to better asses the power at which the fuel have operated. Those rods and the corresponding power chosen for those specific calculations are presented in table 7.6. For the rest of the rods, we have used a ±5% of incertitude in the input power.

In Sections 7.3.2 (base irradiated fuels) and 7.3.3 (power ramped fuels) I present the comparisons between measurements and MARGARET predictions using the parameters selected in Section 7.1. In Section 7.3.4 I try to check if the measured FGR of the fuels analyzed in [J. Noirot, Dowek, et al. 2022; Zacharie-Aubrun et al. 2022] can be explained without considering any interconnection of the inter-granular bubbles. In Section 7.3.5 I resume the conclusions that we can draw from the validation of the code.

Fuel	FGR (%)	Profilo-metry	Hydro-static density	EPMA	SIMS	V_{at} Prec. bubbles	Notes
Rod_13.17_BI	0.11	X	X	X	X	X	
Rod_25.43_BI	0.2	X	X	X	X	X	
Rod_34.78_BI	0.49	X	✓	✓	X	X	EPMA voltage: 20 keV
Rod_46.00_BI	0.8	X	X	✓	X	X	EPMA voltage: 15 keV
Rod_49.85_BI	1.47	X	✓	✓	X	X	EPMA voltage: 20 keV
Rod_52.03_BI	1.14	X	✓	✓	X	X	EPMA voltage: 15 keV
Rod_56.72_BI	2.75	X	X	✓	X	X	Std-61 in [1]. EPMA voltage: 20 keV
Rod_57.61_BI	2.59	✓	✓	✓	X	X	61 [GWd/t_U] UO_2 fuel in [2]. EPMA voltage: Slice 800 mm: 15 keV Slice 2480 mm: 20 keV
Rod_65.06_BI	4.30	X	X	X	X	✓	Std-63 in [1]. EPMA voltage: 20 keV
Rod_67.53_BI	6.17	✓	✓	✓	✓	✓	Std-73 in [1]. EPMA voltage: 15 keV
Rod_68.21_BI	5.79	X	X	X	X	X	
Rod_76.94_BI	7.31	X	✓	✓	✓	X	EPMA voltage: 15 keV
Rod_26.90_RT	1.12*	X	X	X	X	X	
Rod_38.80_RT	0.76*	X	X	X	X	X	Power ramped fuel in [3].
Rod_35.43_RT	1.72*	X	X	X	X	X	
Rod_47.00_RT	5.4*	X	X	X	X	X	
Rod_63.01_RT	2.1*	X	X	✓	✓	X	EPMA voltage: 15 keV
Rod_72.93_RT	3.72*	X	X	X	X	X	Measurements on the density and number of intra-granular bubbles are presented in Chapter 6.

Table 7.5. – Fuels and the corresponding measurements analyzed in this validation. The average burnup of the rod is in the name: Rod_13.17_BI has an average burnup of 13.17 [GWd/t_U]. The FGR measurements of power ramped fuels (with a "*" sign after the value) have been rescaled to ensure confidentiality. The FGR measurements of the base irradiated rods are published in part in [J. Noirot, Dowek, et al. 2022] and in part in [L. Noirot 2011]. [1] refers to [J. Noirot, Dowek, et al. 2022]; [2] refers to [L. Noirot 2011]; [3] refers to [NOIROT et al. 2009].

Fuel	P_{MAX}	P_{MID}	P_{MIN}
Rod_25.43_BI	100%	/	93%
Rod_34.78_BI	100%	/	93%
Rod_34.78_BI	100%	/	93%
Rod_57.61_BI	100%	95%	93%
Rod_67.53_BI	100%	/	95%

Table 7.6. – Rods that undergo PI measurements to determine the real power at which they have operated (in these cases, P_{MIN}) and the corresponding powers chosen for the calculations. For the Rod_57.61_BI, another intermediate power has been treated too.

7.3.2. Base irradiation

7.3.2.1. Detailed results on a particular rod in BI

Before the extended validation of the base irradiated fuels, I present here a detailed calculation of the Rod_57.61_BI. This rod shows clear signs of the presence of subdomains and we can compare MARGARET predictions with different kinds of measurements. Moreover, the main characteristics of the fuel pellet are published [L. Noirot 2011, table 2] [4]. It is therefore chosen as the candidate for an in-depth analysis of the outputs of the code.
Depending on the quantity being analyzed, the analysis of the rod Rod_57.61_BI will by supported by the parallel in-depth analysis of other rods of our validation base.

In practice, I will illustrate:
— The predicted versus the measured fission gas release
— The predicted contribution of the different ways in which gas can be released
— The predicted versus the measured EPMA on two different axial positions
— The predicted versus the measured porosity
— The predicted radius and concentration of the intra-granular nano-bubbles
— The predicted radius of the precipitation bubbles
— The predicted distribution of the fission gas between the different "reservoirs" (dissolved Xe in the grain, Xe trapped in the different kinds of bubbles etc.) during irradiation.

FGR

4. I resume here the temperature history in the center of the pellet of the 5 cycles: 880 - 1030 - 940 - 870 - 840 °C.

Figure 7.9 (a) shows the predicted fission gas release in time, the measured FGR at the end of irradiation and the predicted contribution of the different ways in which gas can be released, for the Rod_57.61_BI, at 100% of power.
Figure 7.9 (b) shows the same predicted quantities in time, for the slice 7/30 of the Rod_57.61_BI, at 100% of power. This slice has been chosen because the temperature history (footnote 4) as well as porosity and EPMA measurements were available in the published literature.

In figure 7.9 (b), MARGARET predicts low FGR at low and middle burnup, due to the low temperature at which the fuel has been irradiated. Then, after the formation of the subdomains, we can notice a sharp increase in the FGR, around the 1070th day, due to the increase in the flux of gas that, from the grains, reaches the grain boundaries by diffusing quickly through the subdomain boundaries. The time at which the subdomains are introduced in the calculation changes along the axis of the rod, so the effect of the subdomain formation is smoother, but clearly visible for the entire rod, in figure 7.9 (a).

We find again this behaviour by looking at the same plot for the slice 27/30 calculation of the Rod_65.06_BI, for which the temperature history is presented in figure 7.8. Figure 7.10 shows the predicted fission gas release in time, and its different contributions, for this slice at 100% of power. The subdomains appear after around 1280 days, and we can notice how, shortly after, the predicted fission gas release increases sharply, even if the temperature at the center of the fuel after the formation of the subdomains remains close or even decreases with respect to the temperature at the center of the fuel before the subdomain formation.

In both fuels, at the end of irradiation, most of the fission gas has been released by percolation through the interconnected inter-granular cavities.

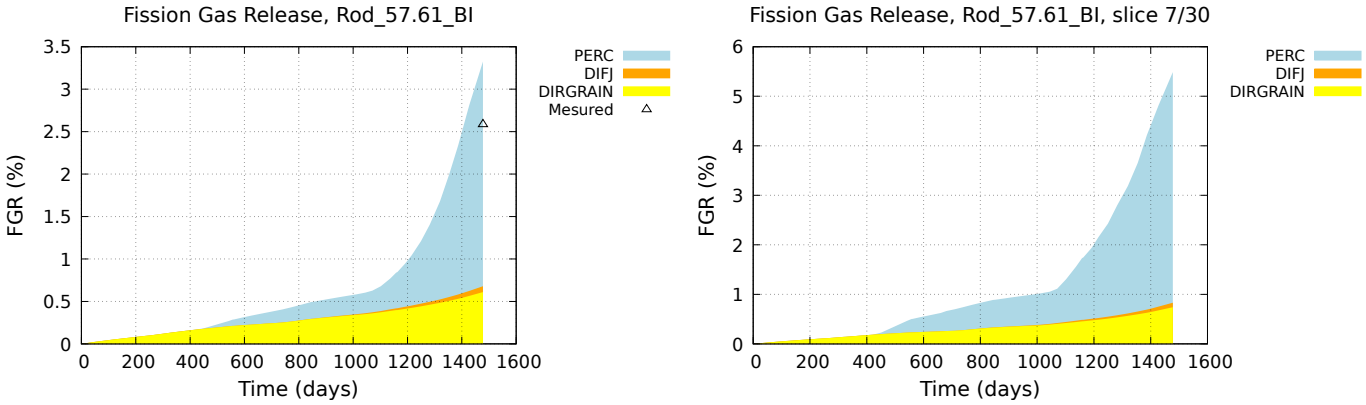

(a) Rod_57.61_BI, 100% power.

(b) Slice 7/30 (0.7314 [m] $< z <$ 0.8604 [m]) of the Rod_57.61_BI, 100% power.

Figure 7.9. – Predicted fission gas release in time, measured FGR and predicted contribution of the different ways in which gas can be released. "PERC" stays for release by percolation through the interconnected inter-granular cavities, "DIFJ" stays for release by long range diffusion trough the grain boundaries, "DIRGRAIN" stays for direct release from the grain: it gathers the direct diffusion of gas to the free surfaces, coming from the sound grains, or from the subdomain boundaries arriving at the free surfaces. FGR measurement taken from [L. Noirot 2011].

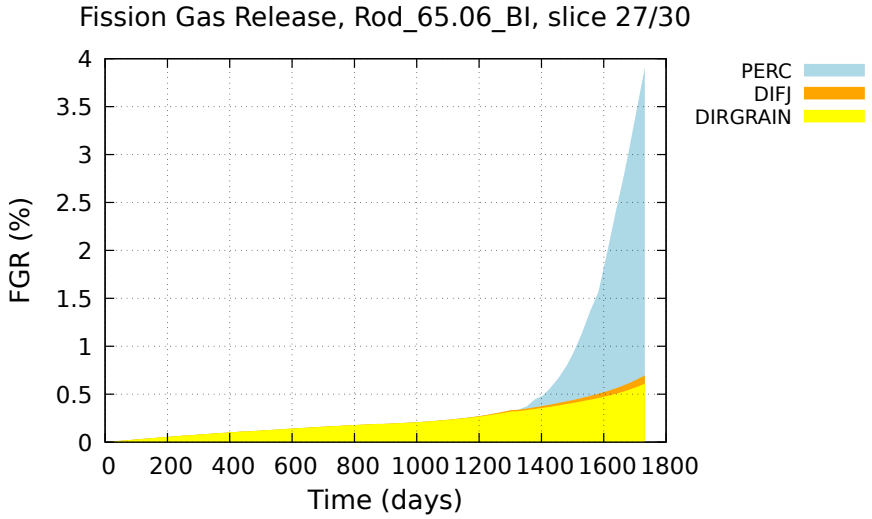

Figure 7.10. – Predicted fission gas release in time, measured FGR and predicted contribution of the different ways in which gas can be released for one slice of the Rod_65.06_BI, slice 27/30 (3.6949 [m] $< z <$ 3.8730 [m]), 100% power. In this slice, subdomains appear after around 1280 days.

EPMA

Figures 7.11 and 7.12 show the predicted versus the measured EPMA, that have been performed at two axial positions for this rod.
During the preparation of the specimen for the EPMA measurement, part of the Xenon trapped in the bubbles near the surface is lost and, therefore, it is not measured. For a reliable prediction, we need to take this fact into account. That is why we follows the work of Verwerft [Verwerft 2000]. In his work, the researcher derived an attenuation factor, function of the radius of the bubbles and the voltage of the EPMA. If we multiply this factor to the amount of Xenon in the bubbles, we can estimate the fraction of Xenon in the bubbles that is actually measured by the EPMA, and calculate from MARGARET's gas distribution a "simulated gas microprobe".

From these figures, we can see that we are able to predict quite correctly (for at least one of the input powers considered) the drop in the EPMA measurement at the center of the pellet, caused by the presence of the precipitation bubbles (see Section 4.1.3).

The rise of the simulated EPMA at the extreme periphery of the pellet is due to the fact that for the last point, a fission rate of half of the input value has been considered for gas production and local burnup, to take into account fission product implantation in the cladding. This rise is observed experimentally, but seems too high in our calculation.

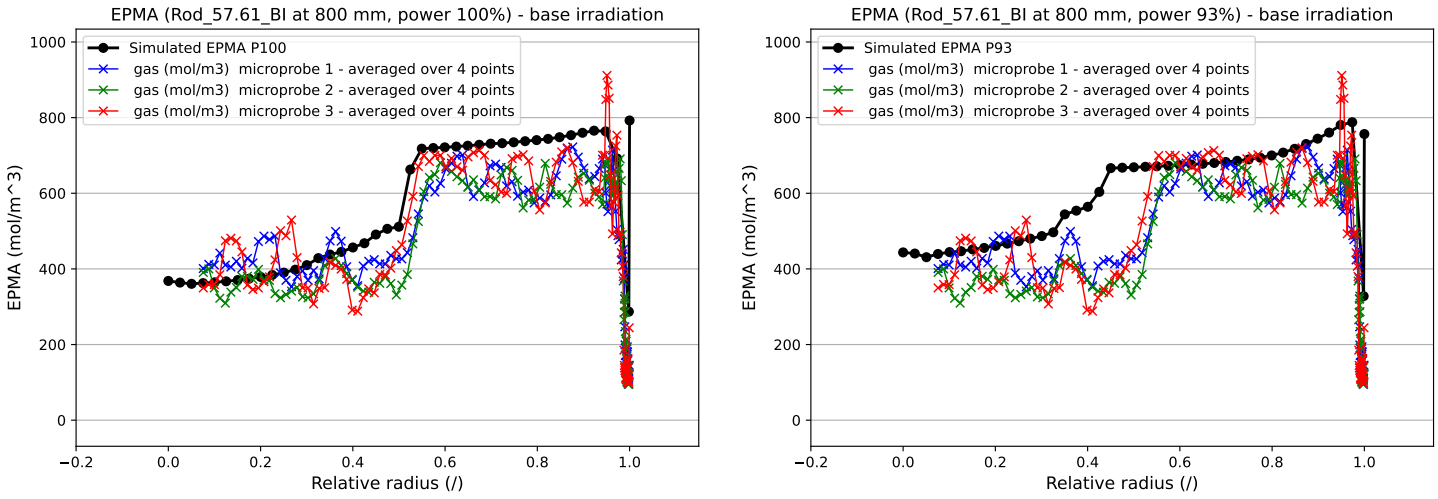

Figure 7.11. – Predicted versus measured EPMA. Rod_57.61_BI, at 800mm from the bottom, two different input powers. Measurements from [L. Noirot 2011].

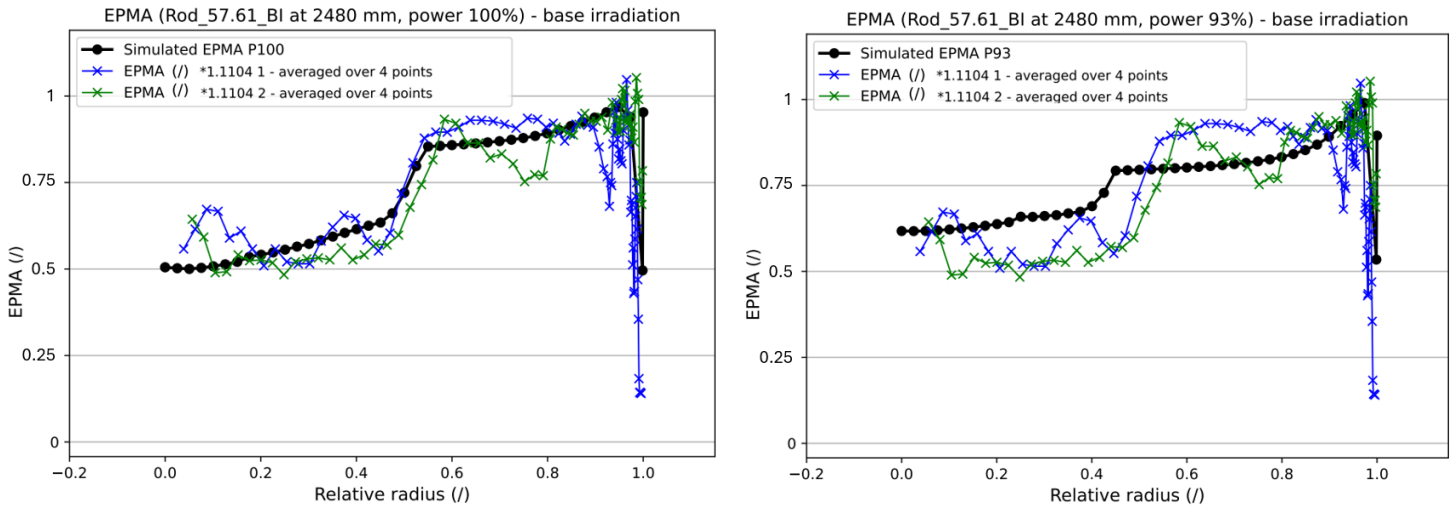

Figure 7.12. – Predicted versus measured EPMA. Rod_57.61_BI, at 2480mm from the bottom, two different input powers. To ensure confidentiality, the data have been rescaled using a common factor.

Porosity

Figure 7.13 shows the predicted versus the measured porosity along the radius of the pellet.

MARGARET predictions are close to the measurements in the center of the pellet, where the precipitation bubbles contribute to the porosity, and on the periphery, where the HBS has developed. Instead, we are currently no able to predict correctly the porosity present at a distance of around 1 mm from the outer radius of the pellet, where nor HBS nor subdomains have formed.

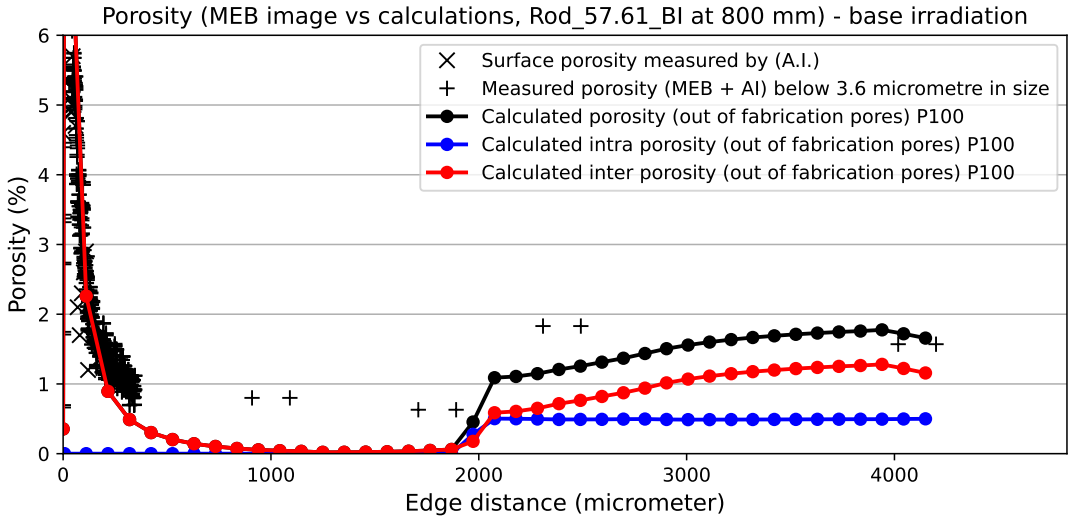

(a) Measurements on all radius except the periphery of the pellet

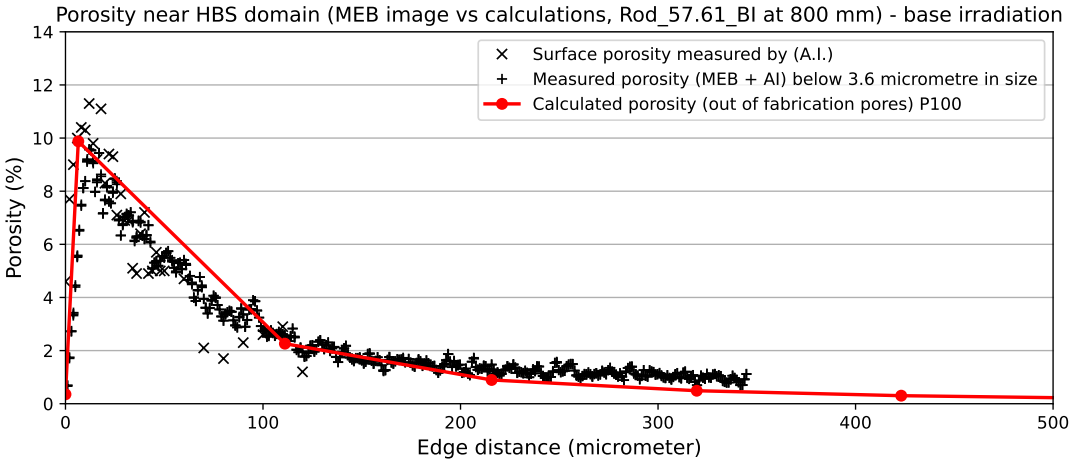

(b) Zoom on the periphery of the pellet

Figure 7.13. – Predicted versus measured Porosity. Rod_57.61_BI, slice 7/30, 100% power. Measurements from [L. Noirot 2011].

Volume per atom

Figure 7.14 shows the predicted V_{at} of the bulk[5], inter-graular and precipitation bubbles[6] at the end of irradiation, for the Rod_57.61_BI. Figure 7.16 shows the same quantity, but for the HBS bubbles.
The V_{at} of the bulk bubbles is very close to Ω throughout the radius of the pellet, as expected (see Sections 5.1.5 and 5.1.2).
The V_{at} of the precipitation bubbles increases from the outer part of the precipitation zone to the center, probably due to the increase of $D_{U,jsd}$ with the temperature. However the V_{at} remains close to Ω, and far from the measured V_{at} of the precipitation bubbles (2-4 Ω or even more, see Section 5.1.2).

The V_{at} of inter-granular bubbles reaches values close to 3 Ω in the center and stays above $\approx 1.4\Omega$ until $r = 0.6R_{pellet}$. Our prediction is therefore in line with the experiments (see Sections 5.1.5 and 5.1.2). Moreover, we can notice that, across the precipitation zone limit, there is a sudden drop in the predicted V_{at}, going towards the center. This is probably due to the fact that more atoms reaches the inter-granular bubbles in the zones where subdomains are present. At the same time, in the outer part of the precipitation zone the temperature is not high enough for the flux of thermal vacancies to compensate this increase in the flux of Xenon atoms to the inter-granular bubbles. The net effect is a decrease in the V_{at} of the inter-granular bubbles.
In the HBS region, the bubbles have a V_{at} between 2 and 3Ω, due to the creep growth phenomenon detailed in Appendix I. Near the periphery, the V_{at} is higher because the creep growth increase with the fission rate.

Figure 7.15 shows the predicted V_{at} of the bulk, inter-granular and precipitation bubbles for the Rod_67.53_BI at the end of irradiation. Figure 7.17 shows the same quantity, but for the HBS bubbles.
The values are similar to the one found for the rod Rod_57.61_BI and the conclusions that we can draw are the same.
Similar results (not plotted) are found also for the rod Rod_65.06_BI.

5. The bubbles of population "b", which are the intra-granular bubbles of the sound grains (state 0), or intra-subdomain bubbles for state (1)
6. As a reminder, the precipitation bubbles, bprecjsd, are located on the subdomain boundaries.

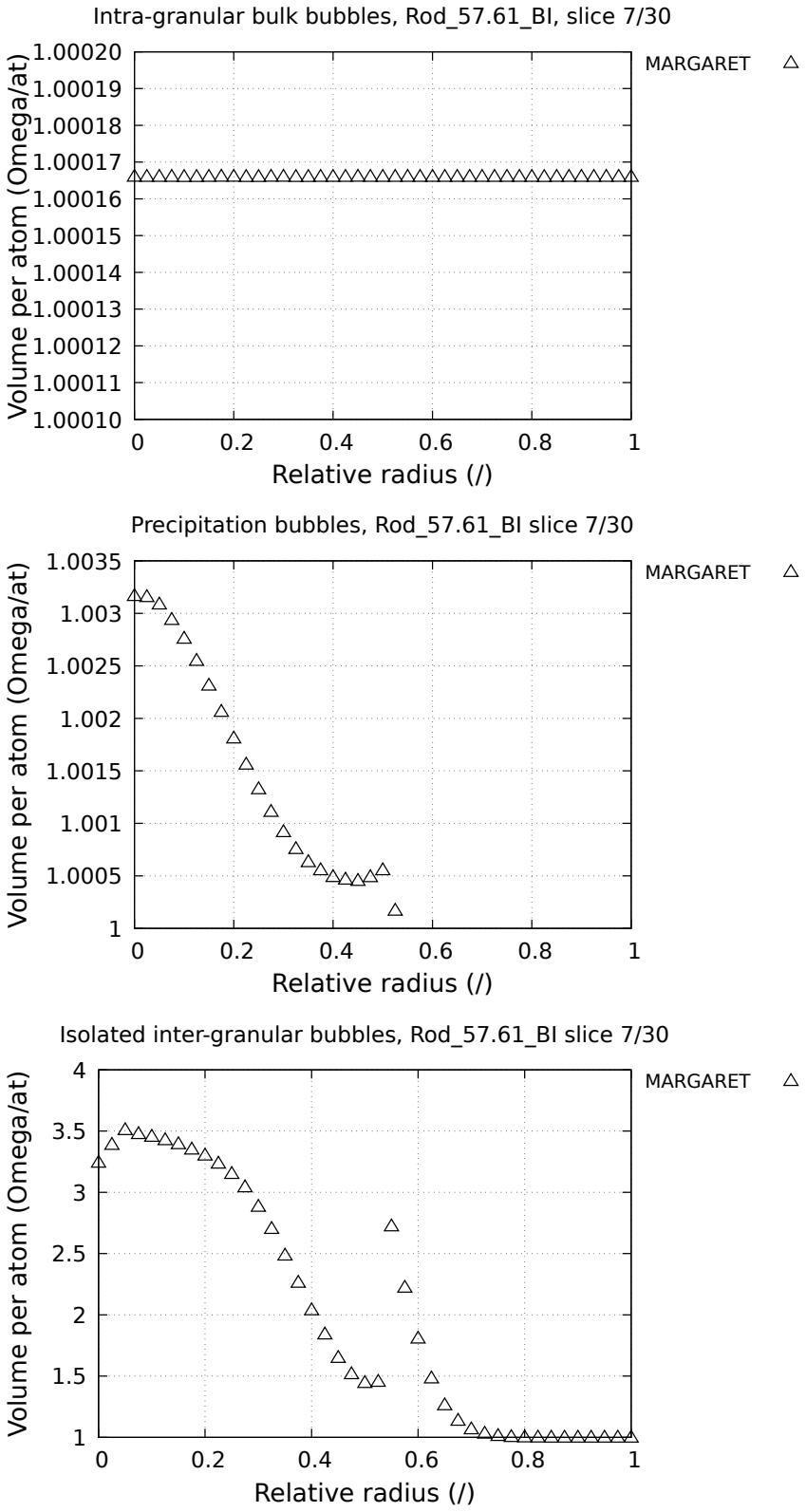

Figure 7.14. – Predicted V_{at} of the intra-granular, inter-graular and precipitation bubbles for the Rod_57.61_BI, slice 7/30 (0.7314 [m] $< z <$ 0.8604 [m]), at the end of irradiation.

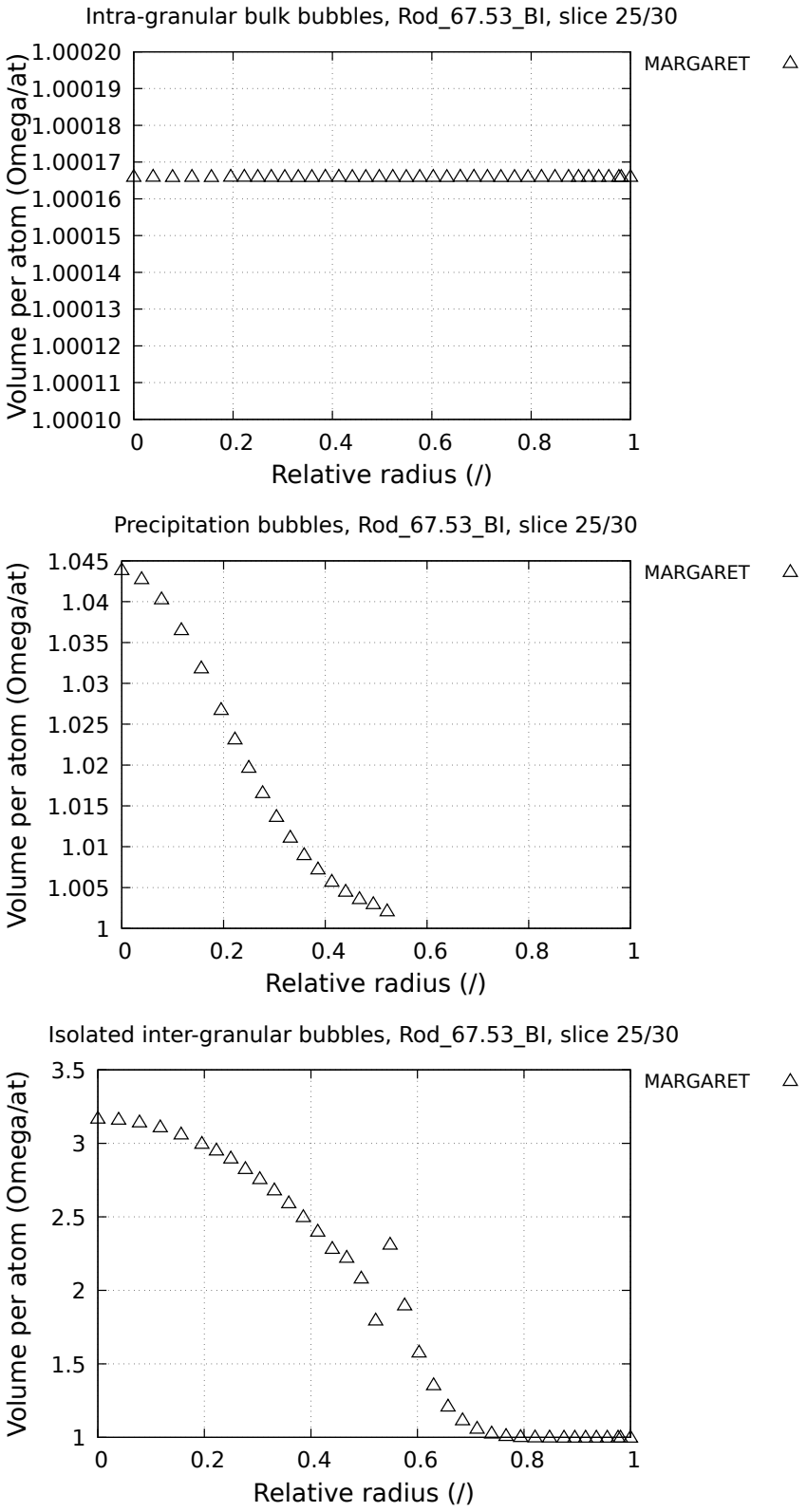

Figure 7.15. – Predicted V_{at} of the intra-granular, inter-graular and precipitation bubbles for the Rod_67.53_BI, slice 25/30 (2.9214 [m] $< z <$ 3.0431 [m]), at the end of irradiation.

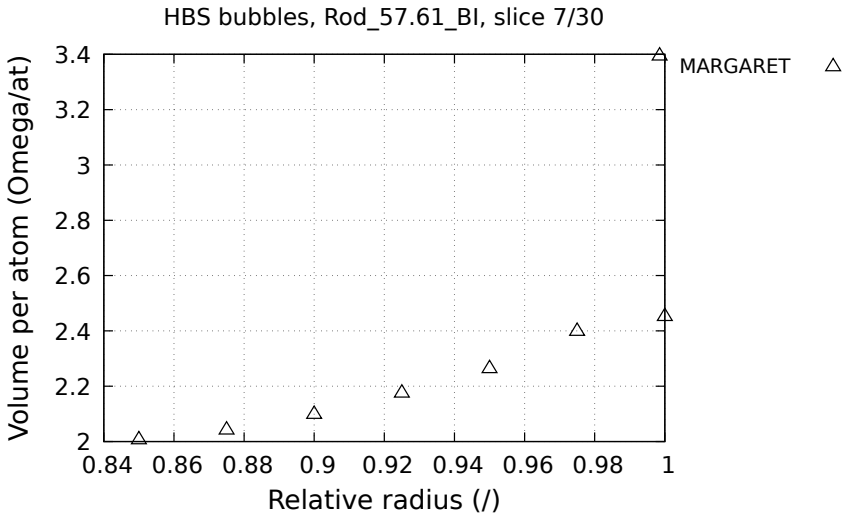

Figure 7.16. – Predicted V_{at} of the HBS bubbles for the Rod_57.61_BI, slice 7/30 (0.7314 [m] $< z <$ 0.8604 [m]), at the end of irradiation.

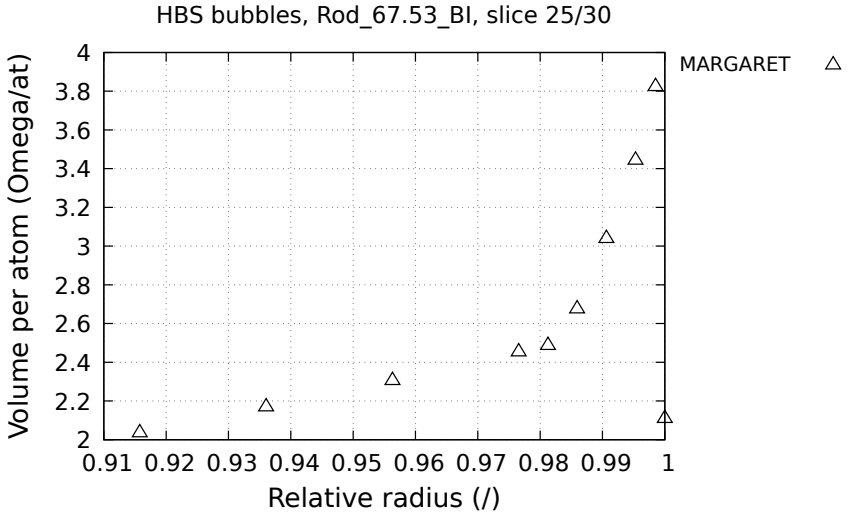

Figure 7.17. – Predicted V_{at} of the HBS bubbles for the Rod_67.53_BI, slice 25/30 (2.9214 [m] $< z <$ 3.0431 [m]), at the end of irradiation.

Concentration and radius of intra-granular bubbles, C_b and R_b

Figure 7.18 shows the predicted concentration of intra-granular bubbles for the Rod_57.61_BI at the end of irradiation (a) and how C_b changes during irradiation for the central point (b).
Figure 7.19 shows the predicted radius of intra-granular bubbles for the Rod_57.61_BI at the end of irradiation (a) and how R_b changes during irradiation (b). Similar results are obtained for rod Rod_56.72_BI (figures 7.20 and 7.21).
On this last rod, MET measurements [Angleraud 2024 (table 24)] showed the presence of sub-nanometric objects (diameter of less than 1 nm. It was not possible to characterize them to see if they have Xenon inside) with concentrations of about $10^{23} - 10^{24}$ [bubbles / m^3] and nano-bubbles with diameters of about 3-6 nm with concentrations of in the range $10^{21} - 10^{22}$ [bubbles / m^3]. MARGARET models only one bubble population in the bulk, and its predictions of the radius and concentration of the intra-granular nano-bubbles are in between the measured values of the sub-nanometric objects and the measured values of the nano-bubbles.

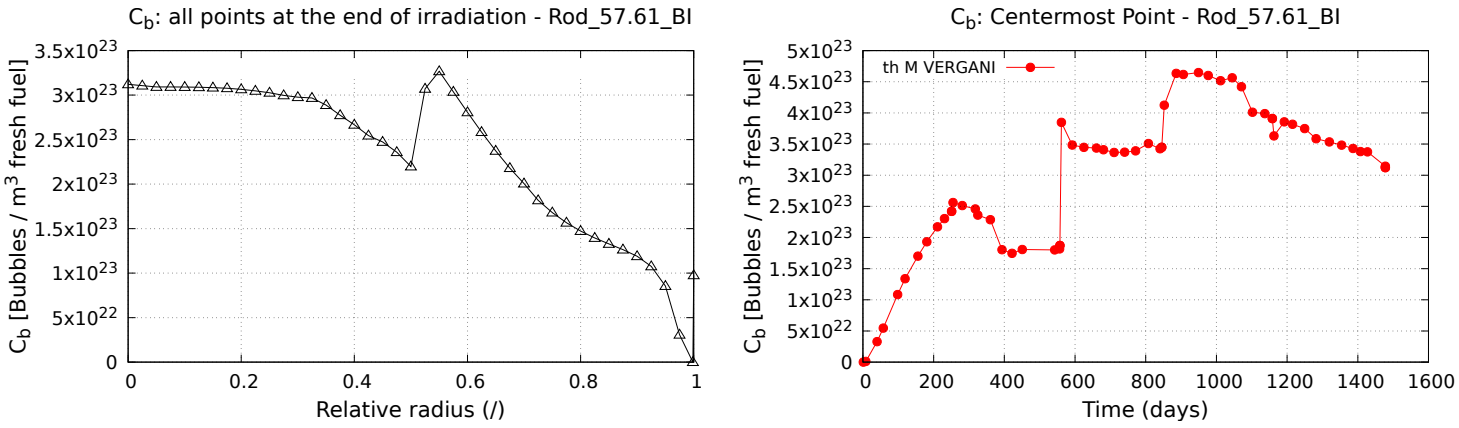

(a) All points at the end of irradiation

(b) Centermost point during irradiation

Figure 7.18. – Predicted concentration of intra-granular bubbles. Rod_57.61_BI, slice 7/30 (0.7314 [m] $< z <$ 0.8604 [m]), 100% power.

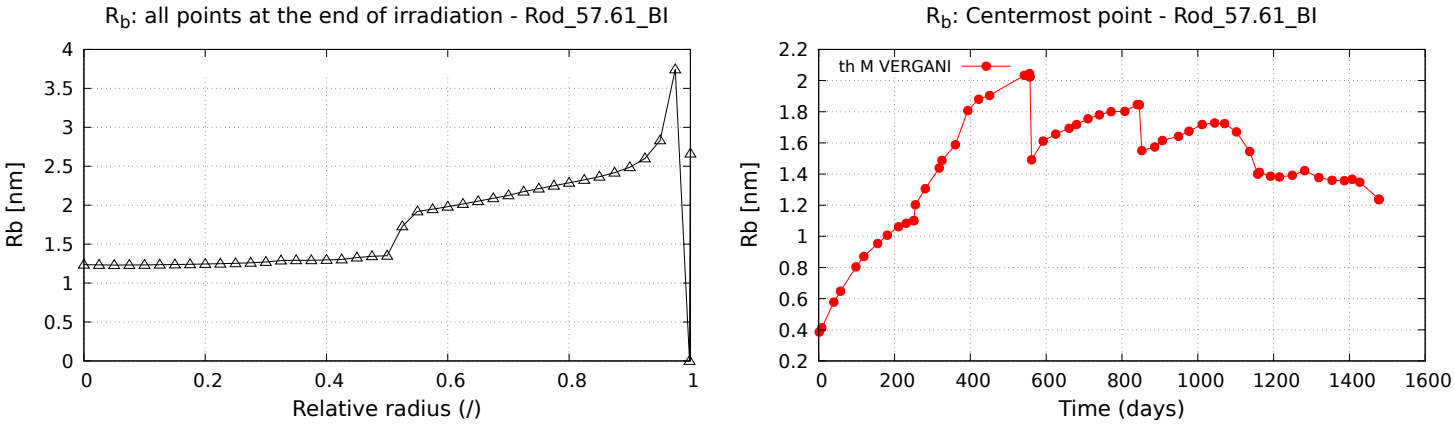

(a) All points at the end of irradiation

(b) Centermost point during irradiation

Figure 7.19. – Predicted radius of the intra-granular bubbles. Rod_57.61_BI, slice 7/30 (0.7314 [m] < z < 0.8604 [m]), 100% power.

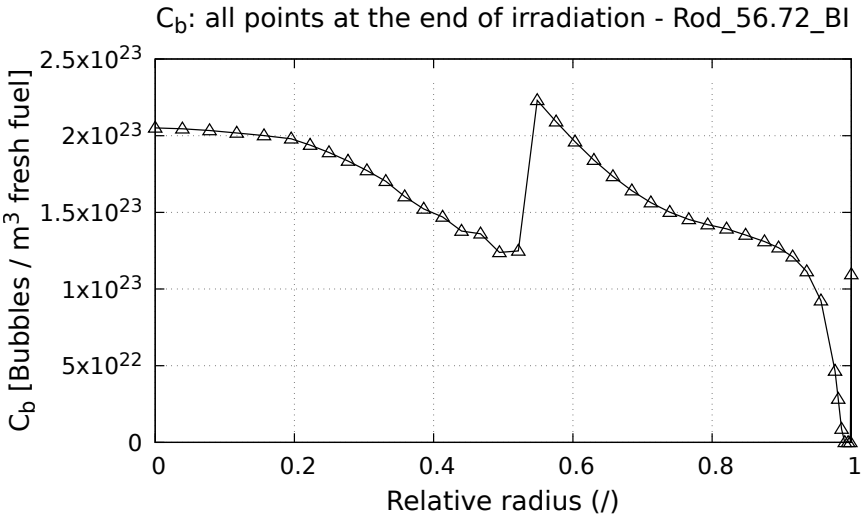

Figure 7.20. – Predicted concentration of intra-granular bubbles. Rod_56.72_BI, slice 11/30 (1.2193 [m] < z < 1.3412 [m]), 100% power.

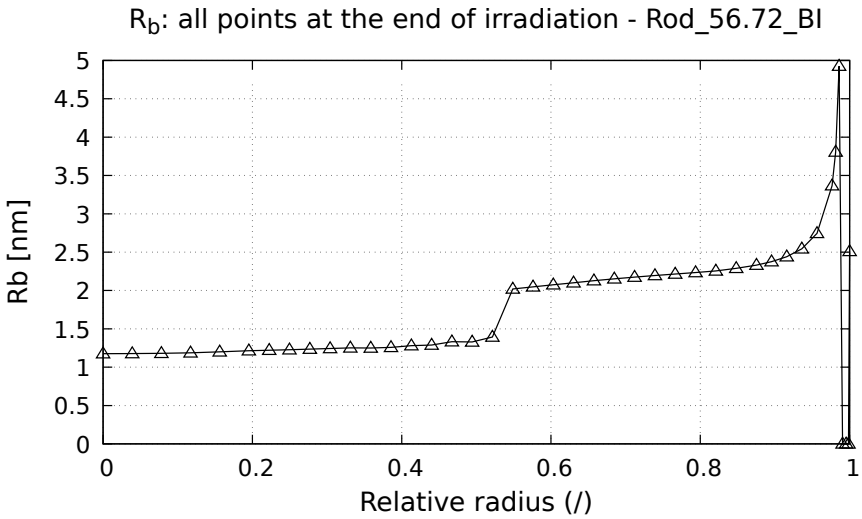

Figure 7.21. – Predicted radius of the intra-granular bubbles. Rod_56.72_BI, slice 11/30 (1.2193 [m] < z < 1.3412 [m]), 100% power.

Size of the precipitation bubbles, $R_{bprecjsd}$

Figure 7.22 shows the predicted equivalent radius of the precipitation bubbles for the Rod_57.61_BI.
Figure 7.23 shows the predicted equivalent radius of the precipitation bubbles for the Rod_56.72_BI.
As we can see from the figures, once the precipitation bubbles appear in the calculation, they quickly grow until they reach a (mostly) stable size. Their size is fairly constant throughout the precipitation zone.

In the article [J. Noirot, Dowek, et al. 2022], the researchers report values of the equivalent median diameter ($ESD_{50\%}$) of the precipitation bubbles for the Rod_56.72_-BI (Std-61 in the article) in the range 190 - 330 [nm], so 95 - 165 [nm] for the radius. In [L. Noirot 2011] the reported size of the precipitation bubbles is in the range 100 - 500 [nm], so 50 - 250 [nm] for the radius (see table 4 of [ibid.]. The sample described in this table comes from the Rod_57.61_BI, $z = 800$ mm). Both measurements are in agreement with our results, even if MARGARET is currently non able to predict changes of the radius of the precipitation bubbles along the radius of the pellet, for example a size of 100 - 300 in the center and 200 - 500 in the periphery of the precipitation zone (table 4 of [ibid.]).

I also have to add that, as I have presented in the corresponding paragraph, the predicted V_{at} of the precipitation bubbles is $\approx 1\Omega$, while it should be higher than 2Ω. Using $\zeta = 2$ instead of $\zeta = 1$ for the precipitation bubbles[7], we would obtain a doubled

7. See the equation of $\frac{dV_{cavjsd}}{dt}$ in Section G.1.2, where we could choose $\zeta = 2$ instead of $\zeta = 1$, and the discussion of Section 5.1.5.

volume of the precipitation bubbles, and therefore an equivalent radius that would be $2^{1/3} \approx 1.26$ higher. This last value would still be in agreement with the experimental data. However, we should also consider that bigger bubbles would trap more Xenon, re-solute less gas (in percentage of the total amount of gas trapped) and therefore grow even more: the whole calibration would probably need to be changed, making it difficult to asses what would be the final predicted radius of the bubbles.

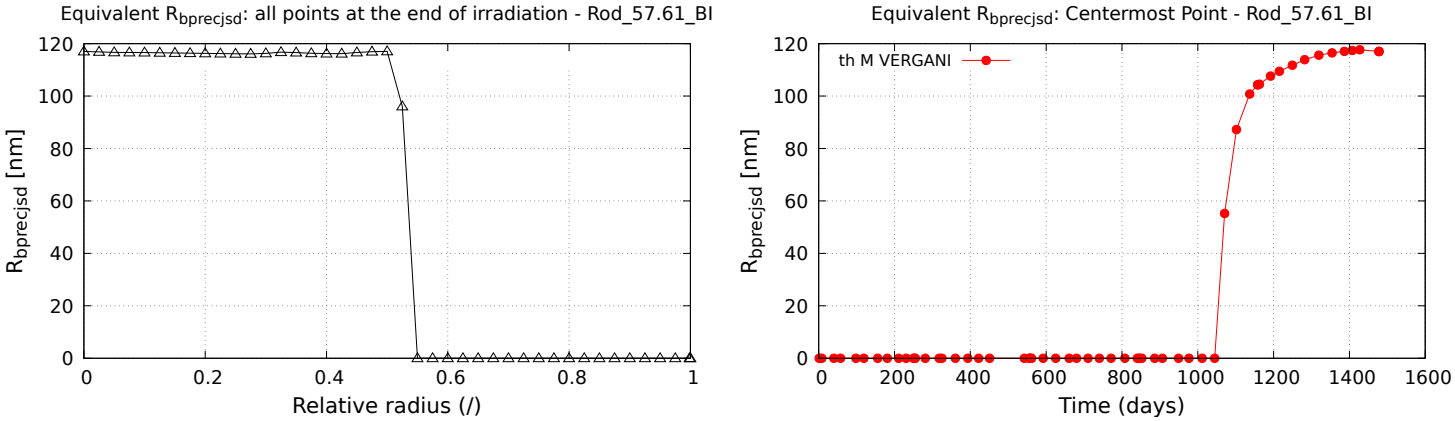

(a) All points at the end of irradiation

(b) Centermost point during irradiation

Figure 7.22. – Predicted equivalent radius of the precipitation bubbles. Rod_57.61_BI, slice 7/30 (0.7314 [m] $< z <$ 0.8604 [m]), 100% power.

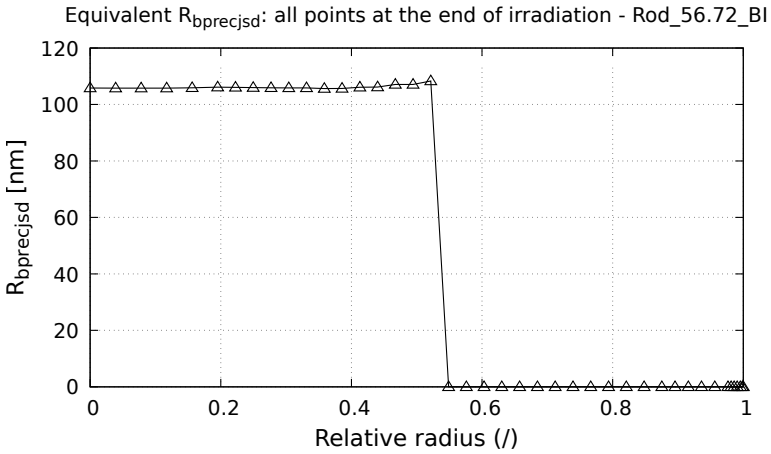

Figure 7.23. – Predicted equivalent radius of the precipitation bubbles. Rod_56.72_BI, slice 11/30 (1.2193 [m] < z < 1.3412 [m]), 100% power.

Fission gas distribution during irradiation

Figures 7.24 and 7.25 show the predicted distribution of the fission gas between the different "reservoirs" in the centermost simulated point during irradiation, for the Rod_57.61_BI and Rod_65.06_BI respectively. The nomenclature is explained in Appendix A.

These figures are really useful to understand the predictions of the code. In fact, from these figures, we can notice different things:

— The fission gas release increases after the formation of the subdomains, in agreement with the figures that showed the FGR during irradiation;

— Shortly after the formation of the subdomains, the precipitation bubbles become the major "reservoir" of the intra-granular gas;

— Looking at the change in the concentration of dissolved Xenon in time for the Rod_65.06_BI, we can clearly identify the 4 cycles experienced by the fuel;

— The concentration of dissolved gas in the grain boundaries and subdomain boundaries remains very small throughout irradiation. In fact, Xenon atoms in the subdomain boundaries quickly reach the grain boundaries or are trapped by precipitation bubbles, while Xe atoms in the grain boundaries quickly reach the free volume or are trapped by the inter-granular bubbles.

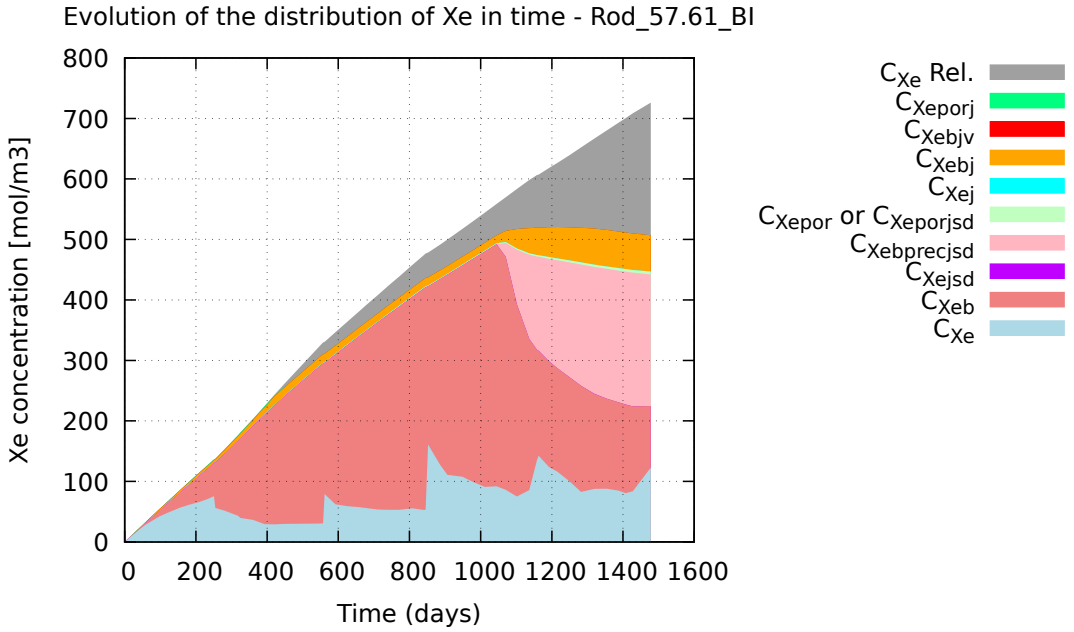

Figure 7.24. – Predicted distribution of the fission gas between the different "reservoirs" in the centermost simulated point during irradiation, for the Rod_57.61_BI, slice 7/30 (0.7314 [m] $< z <$ 0.8604 [m]), 100% power. "C_{Xe} Rel." represents the fission gas released from this particular point (total gas produced minus the gas in the different "reservoirs").

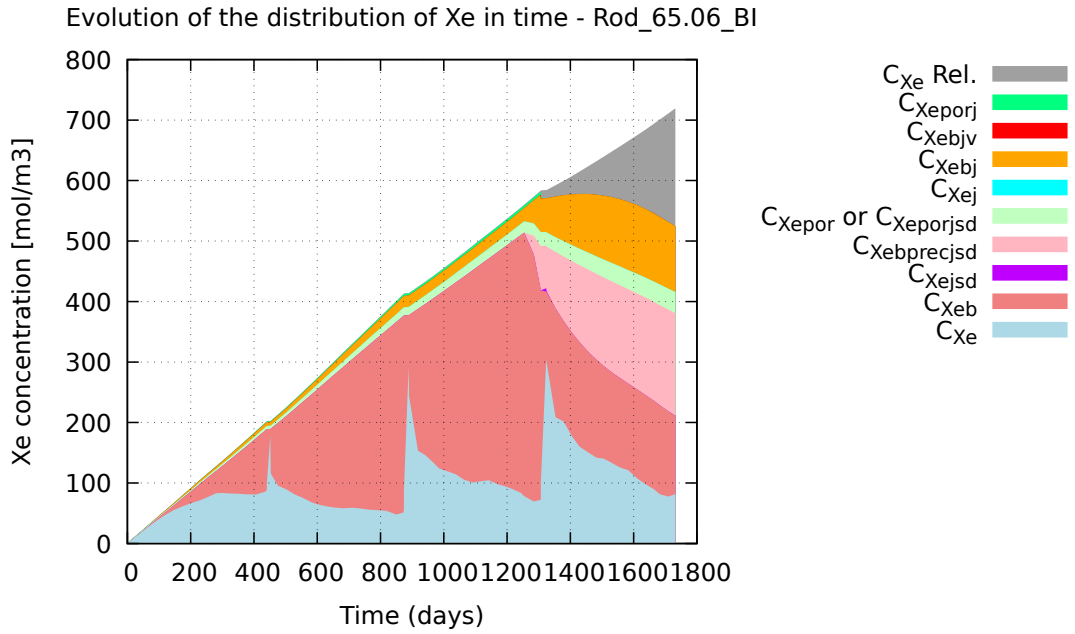

Figure 7.25. – Predicted distribution of the fission gas between the different "reservoirs" in the centermost simulated point during irradiation, for the Rod_65.06_BI, slice 27/30 (3.6949 [m] $< z <$ 3.8730 [m]), 100% power. "C_{Xe} Rel." represents the fission gas released from this particular point (total gas produced minus the gas in the different "reservoirs").

7.3.2.2. Results for the other rods

In this section, I present the extended validation of the code on the base irradiated fuels listed in table 7.5.

FGR

Figure 7.26 shows the predicted versus the measured FGR of all the base irradiated fuels.
As explained at the beginning of Section 7.3, for each fuel, we have 2-3 different predictions depending on the input power selected.

From the figure, we can see that MARGARET is able to predict quite accurately the FGR over a wide range of burnups (13 to 77 GWd/t_U).
We can also notice how much the incertitude on the input power on the high burnup fuels changes the predicted FGR.

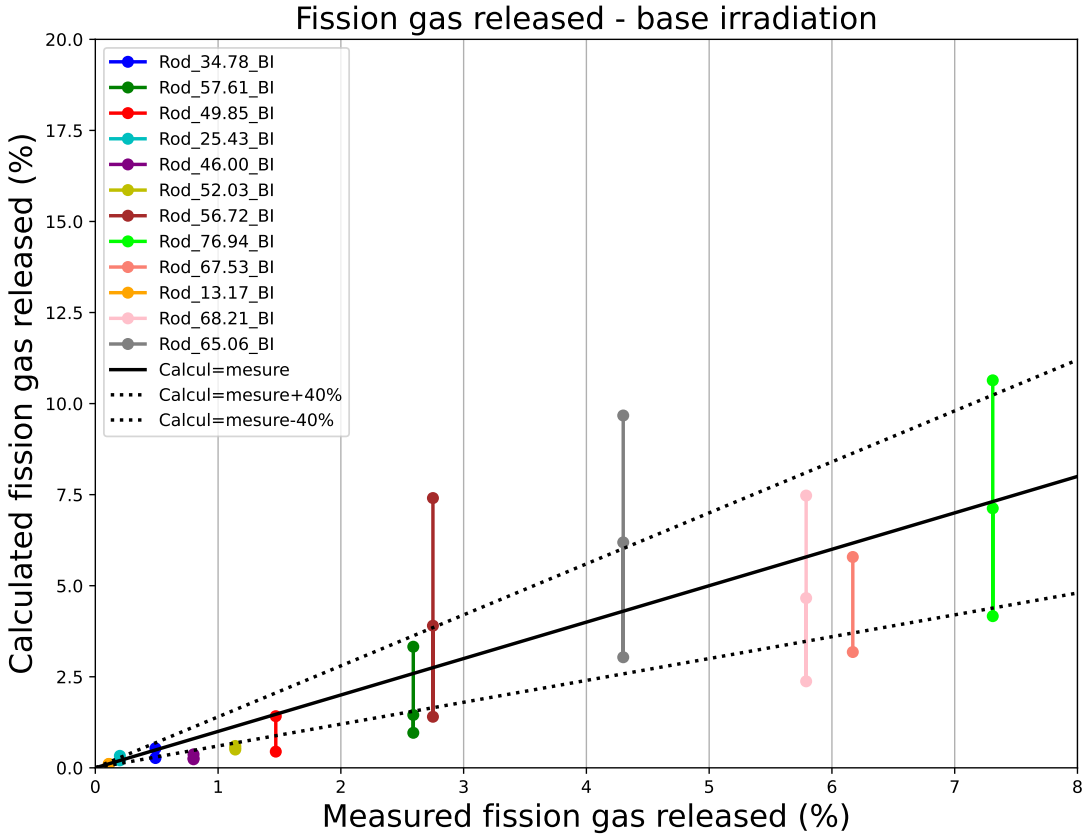

Figure 7.26. – Predicted versus measured FGR. Measurements from [L. Noirot 2011; Zacharie-Aubrun et al. 2022].

Swelling of the pellet

Figure 7.27 shows the predicted versus the measured swelling of the pellet, deduced from density measurements.

Multiple predictions are plotted for each fuel, due to different reasons:
— We have 2 or 3 different predictions depending on the input power selected.
— For the fuels that developed an HBS at the periphery of the pellet, we have two predictions: with or without counting the swelling due to the HBS. In fact, to measure the swelling, the pellet have to be estracted from the cladding, and part of the HBS may not be measured because it remains attached to it.
— For some fuels there is an uncertainty in the measurements of about 1%.
— Finally, for some fuels we have measurements on two different slices.

MARGARET predictions are quite in agreement with the measurements, but there is a general tendency to underestimate the swelling.

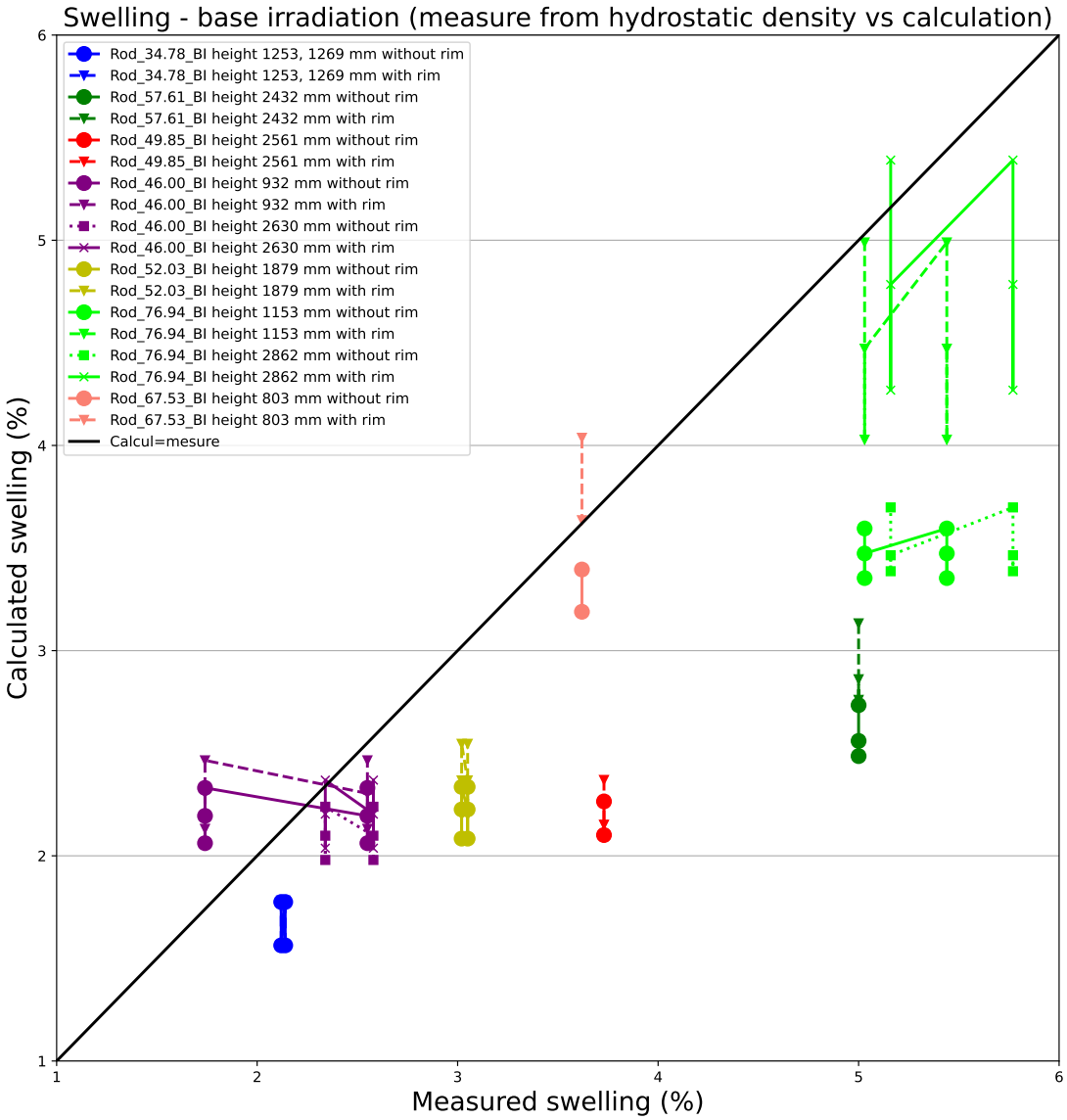

Figure 7.27. – Predicted versus measured swelling of the pellet. Measurements published in [L. Noirot 2006], except for the rod Rod_76.94_BI, whose measurement is published in [J. Noirot, Aubrun, et al. 2009].

EPMA

Figures 7.28, 7.29, 7.30, 7.31, 7.32, 7.33, 7.34, 7.35, 7.36 show the predicted versus the measured EPMA.

From these figures, we can see that we are able to predict quite correctly, for a wide variety of high burnup fuels (for at least one of the input powers considered) the drop in the EPMA measurement at the center of the pellet caused by the presence of the precipitation bubbles (see Section 4.1.3).
A few notable exceptions are Rod_52.03_BI and the highest burnup rods:

— Rod_52.03_BI is the fuel which experienced the lowest temperatures throughout irradiation, and our inability to predict the possible formation of the precipitation bubbles in this fuel highlights the limit in the formula (eq. 4.1) used for the formation of the subdomains.

— We are not able to predict the further drop in the EPMA measurement in the centermost part of the fuel of the rods Rod_67.53_BI and Rod_76.94_BI. This may be due to the fact that we consider a constant value of $C_{precjsd}$ throughout irradiation, or because we do not consider the effects of the progress in the misorientation of the subdomains during irradiation.

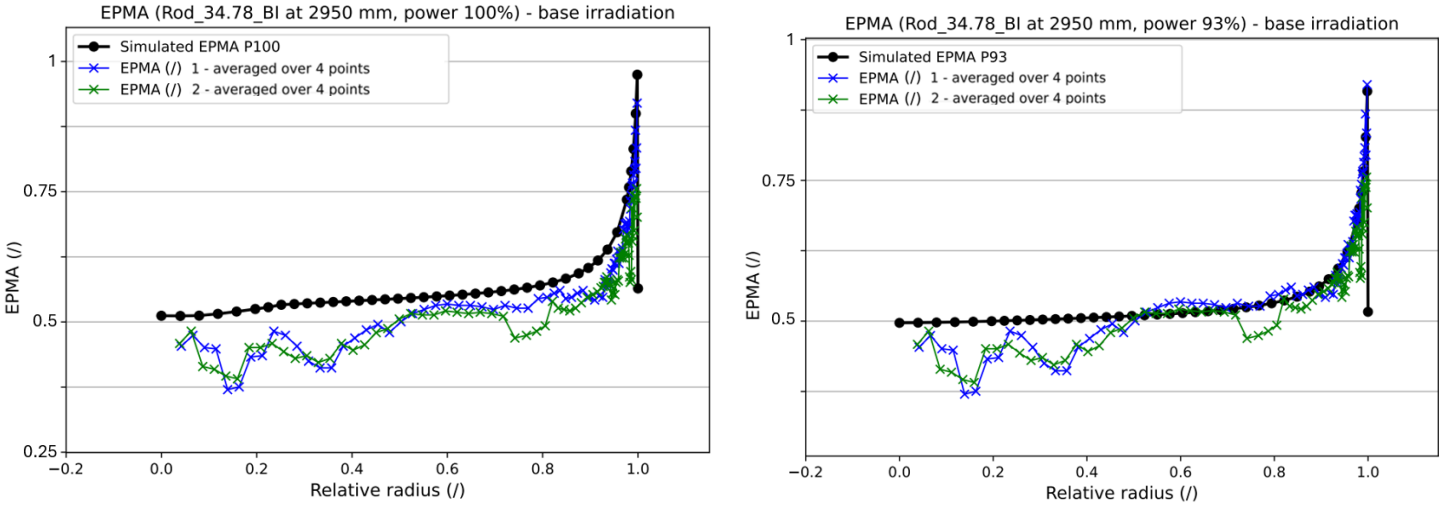

Figure 7.28. – Predicted versus measured EPMA. Rod_34.78_BI, two different input powers. To ensure confidentiality, the data have been rescaled using a common factor.

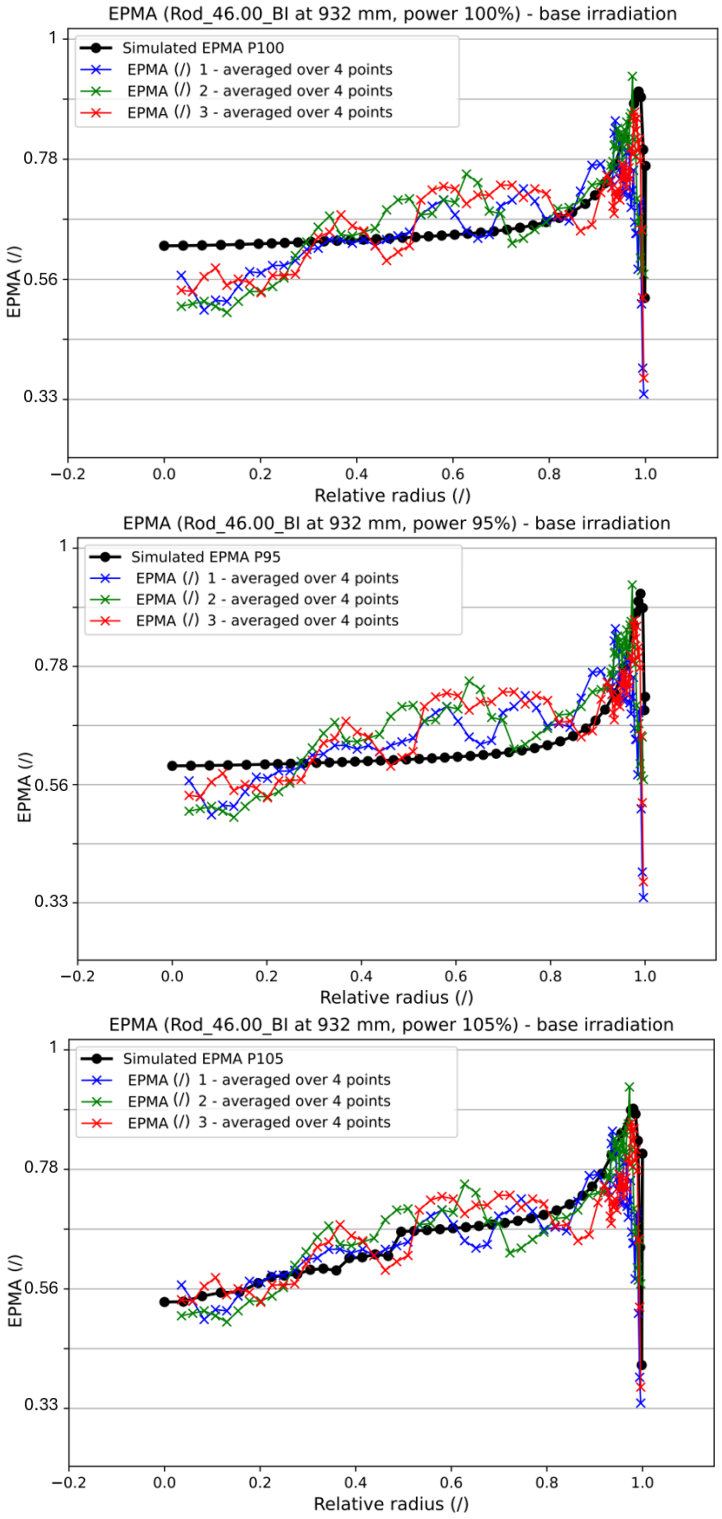

Figure 7.29. – Predicted versus measured EPMA. Rod_46.00_BI, first slice,three different input powers. To ensure confidentiality, the data have been rescaled using a common factor.

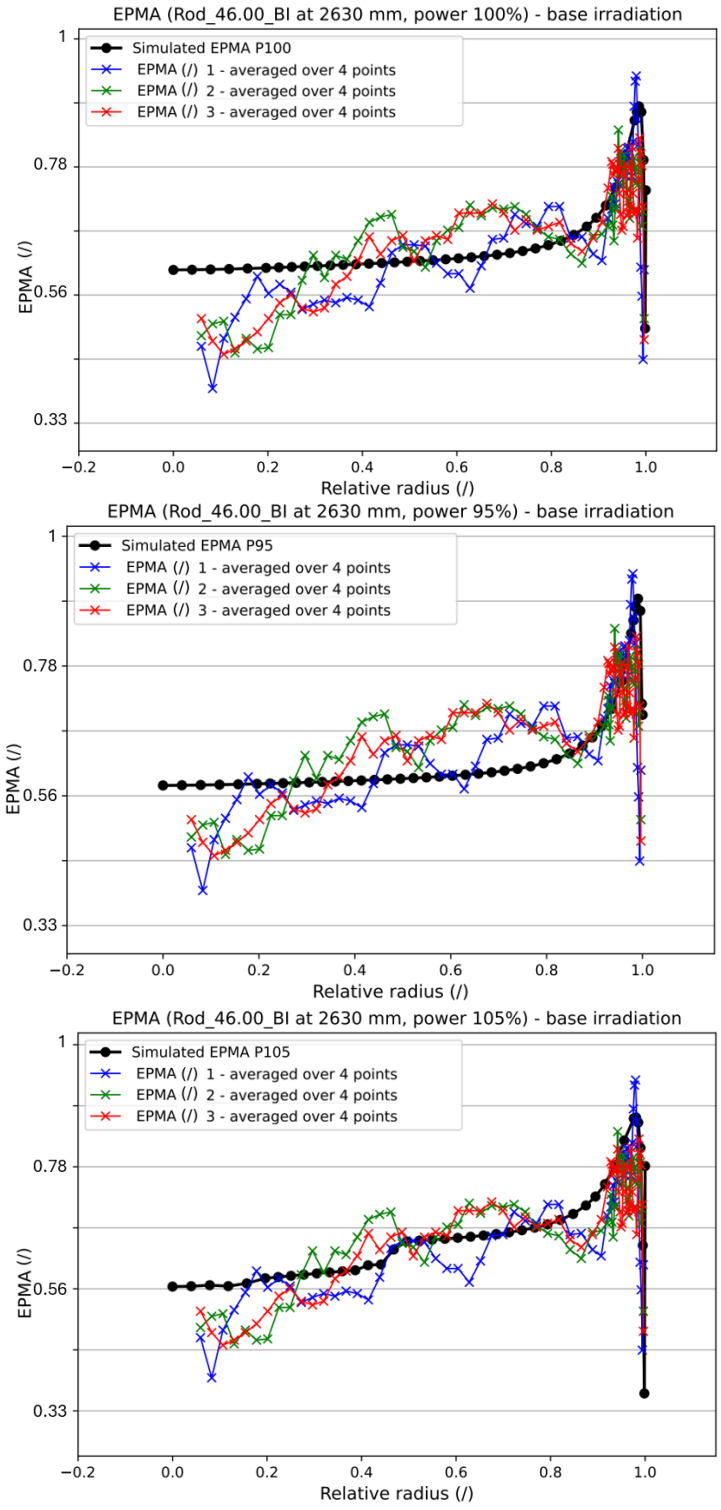

Figure 7.30. – Predicted versus measured EPMA. Rod_46.00_BI, second slice, three different input powers. To ensure confidentiality, the data have been rescaled using a common factor.

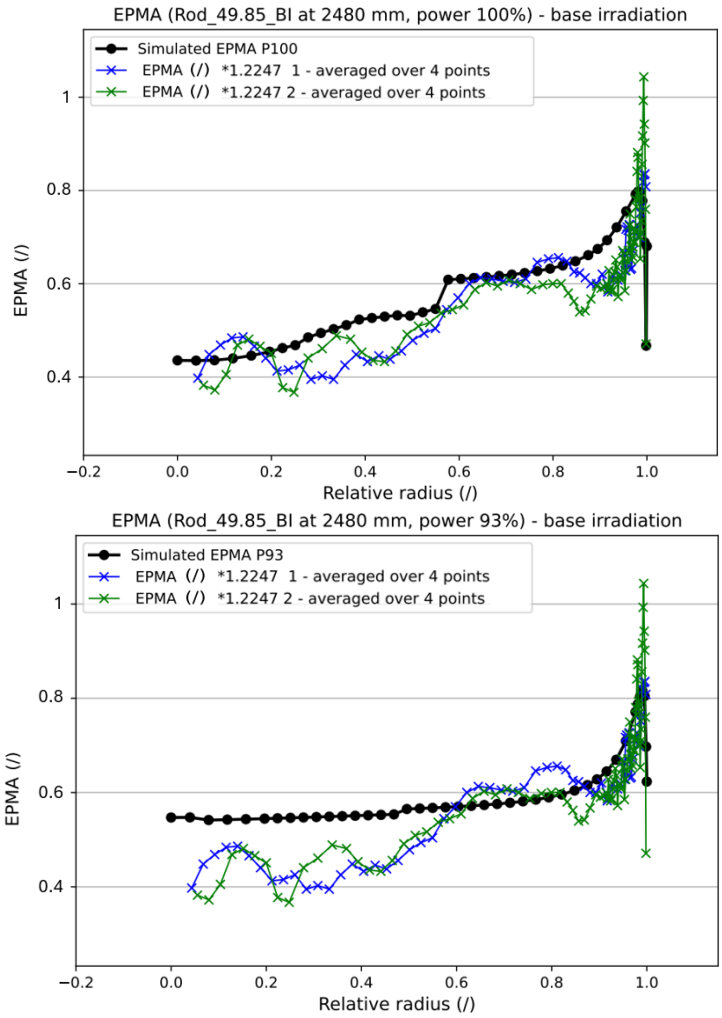

Figure 7.31. – Predicted versus measured EPMA. Rod_49.85_BI, two different input powers. To ensure confidentiality, the data have been rescaled using a common factor.

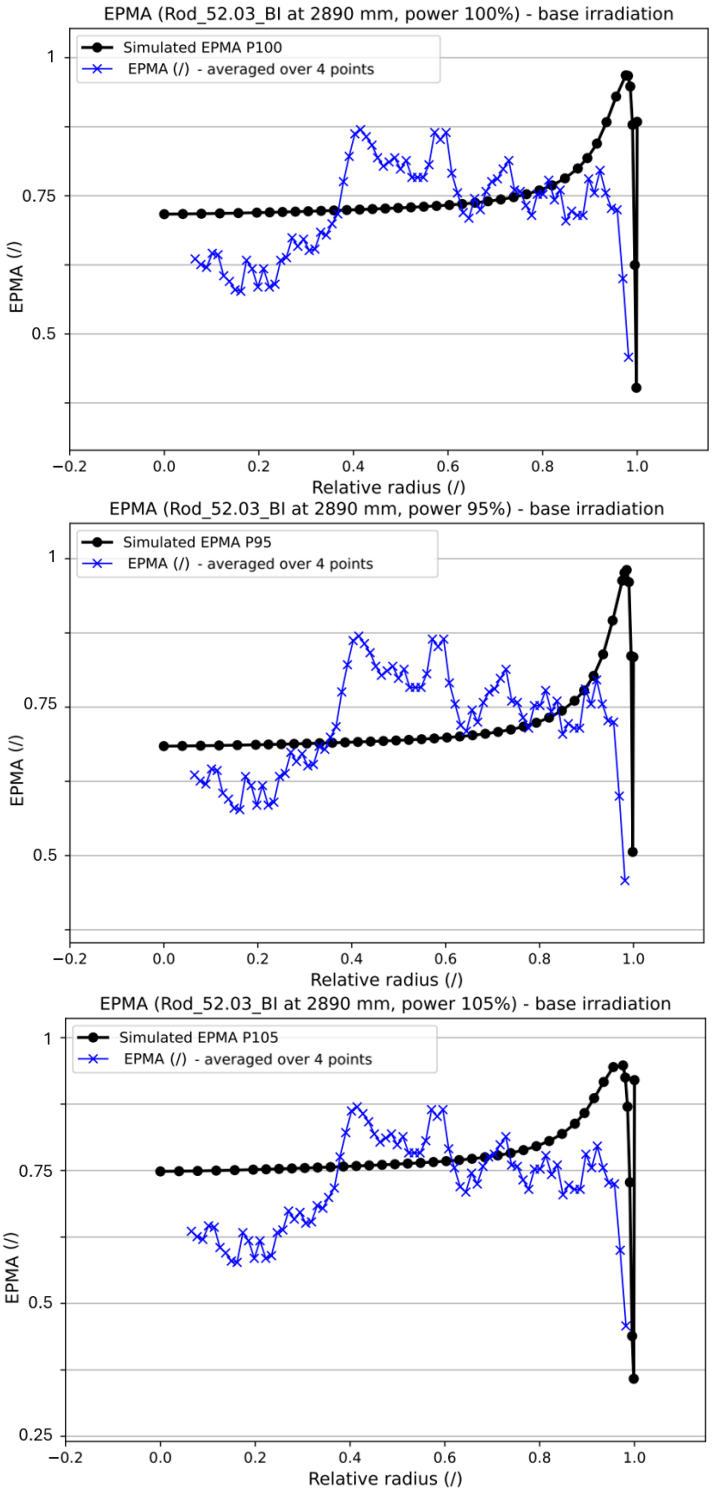

Figure 7.32. – Predicted versus measured EPMA. Rod_52.03_BI, two different input powers. To ensure confidentiality, the data have been rescaled using a common factor.

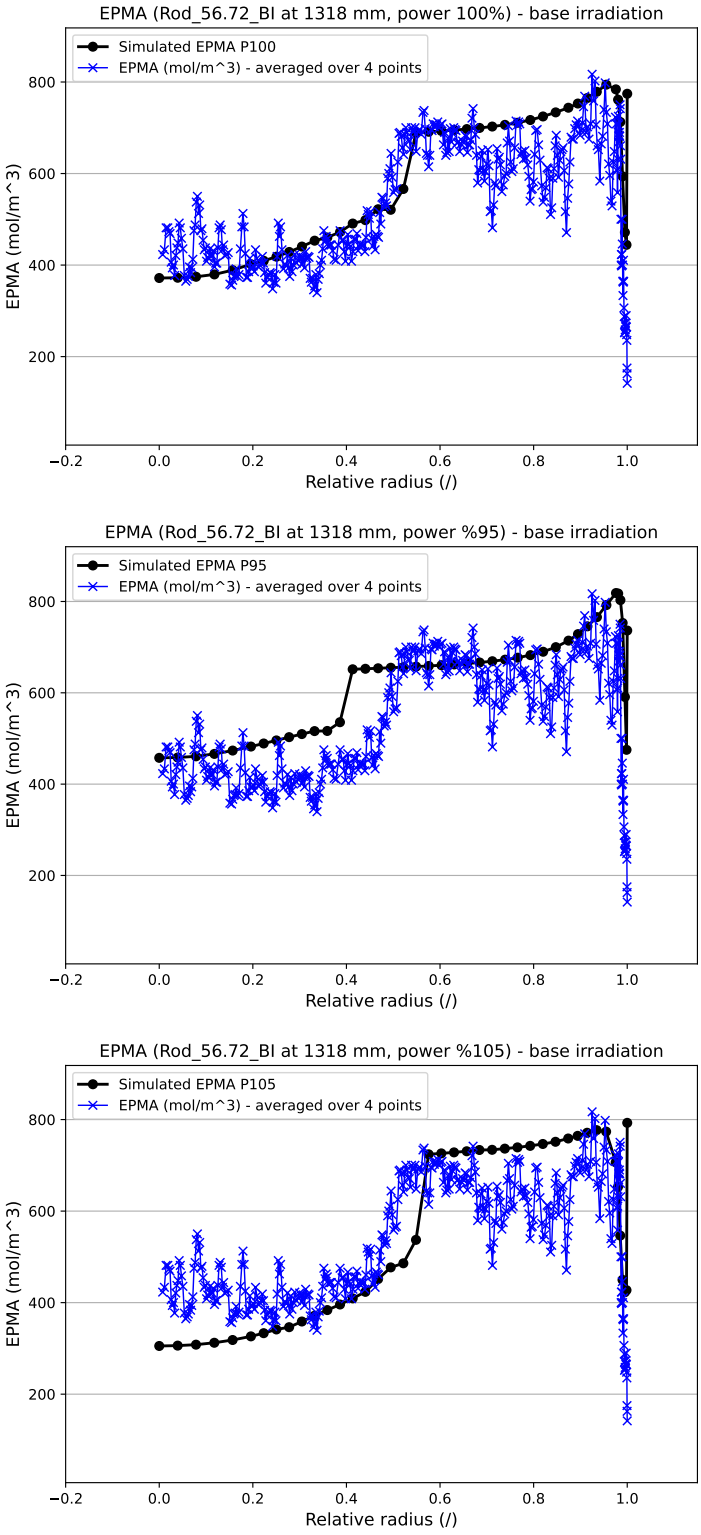

Figure 7.33. – Predicted versus measured EPMA. Rod_56.72_BI, three different input powers. Measurements from [Dowek 2021].

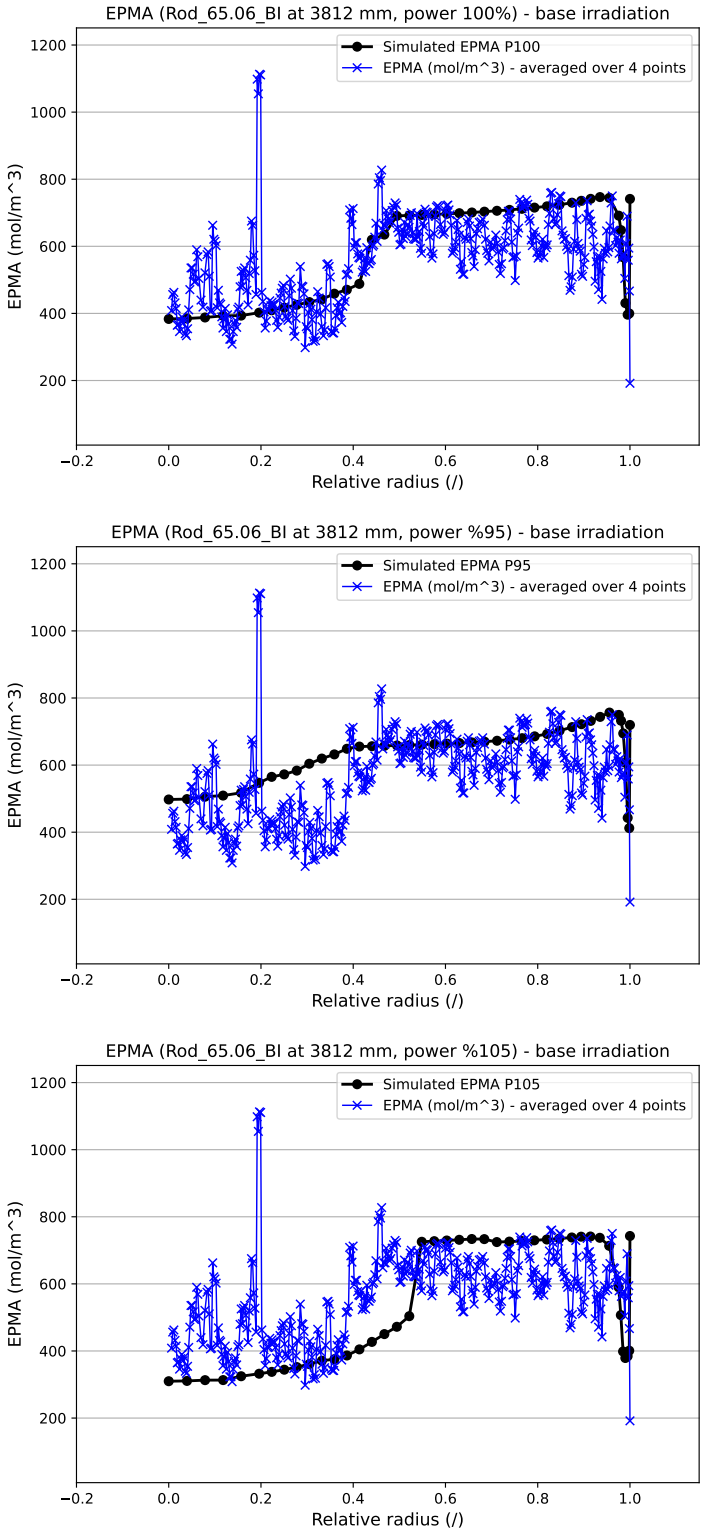

Figure 7.34. – Predicted versus measured EPMA. Rod_65.06_BI, three different input powers. Measurements from [Dowek 2021].

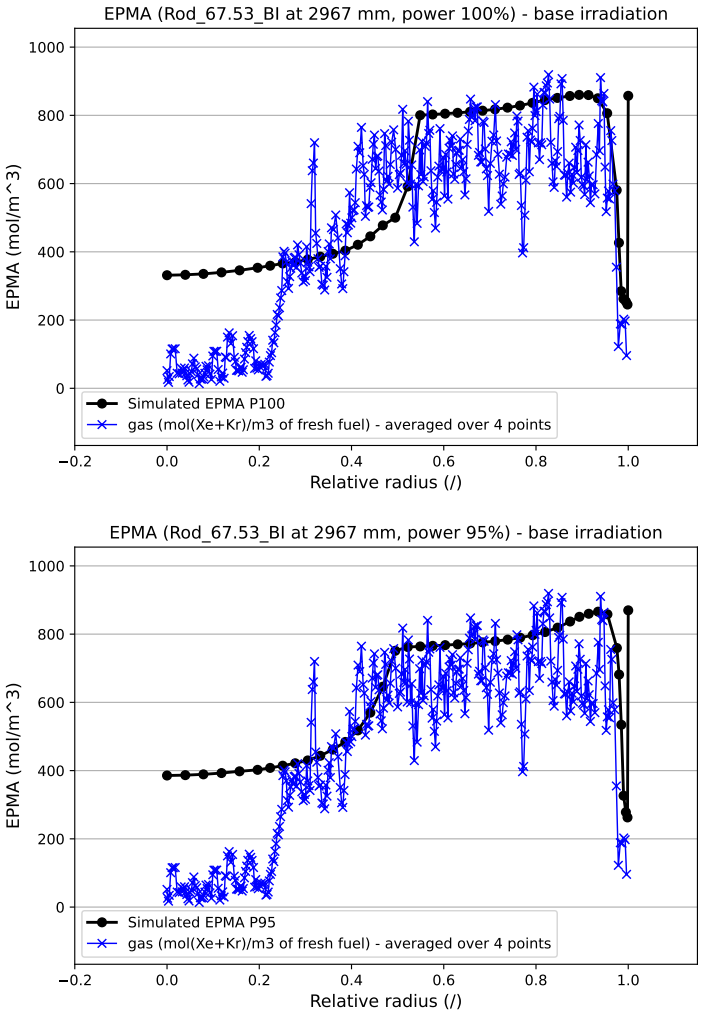

Figure 7.35. – Predicted versus measured EPMA. Rod_67.53_BI, 3 different input powers. Measurements from [Dowek 2021].

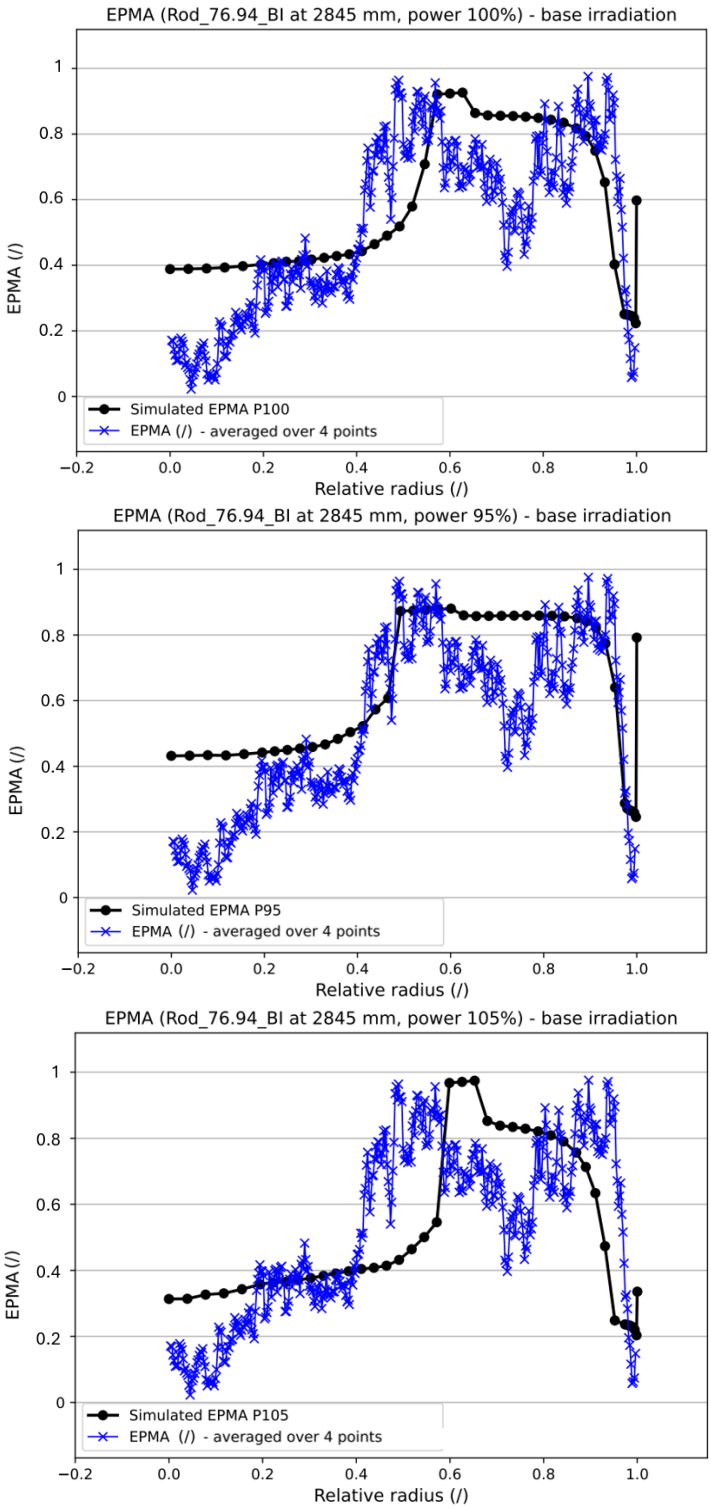

Figure 7.36. – Predicted versus measured EPMA. Rod_76.94_BI, 3 different input powers. To ensure confidentiality, the data have been rescaled using a common factor.

SIMS

Figures 7.37 and 7.38 show the predicted versus the measured SIMS. The base line SIMS measure the amount of gas dissolved in the lattice and trapped in the nanobubbles, while the total SIMS measure the total amount of gas present in the fuel, whatever its status (dissolved or trapped in the bubbles).

From these figures we can draw similar conclusions to the EPMA analysis. However, from the SIMS measurements, we can better notice MARGARET's underestimation of the amount of gas dissolved in the HBS grains.

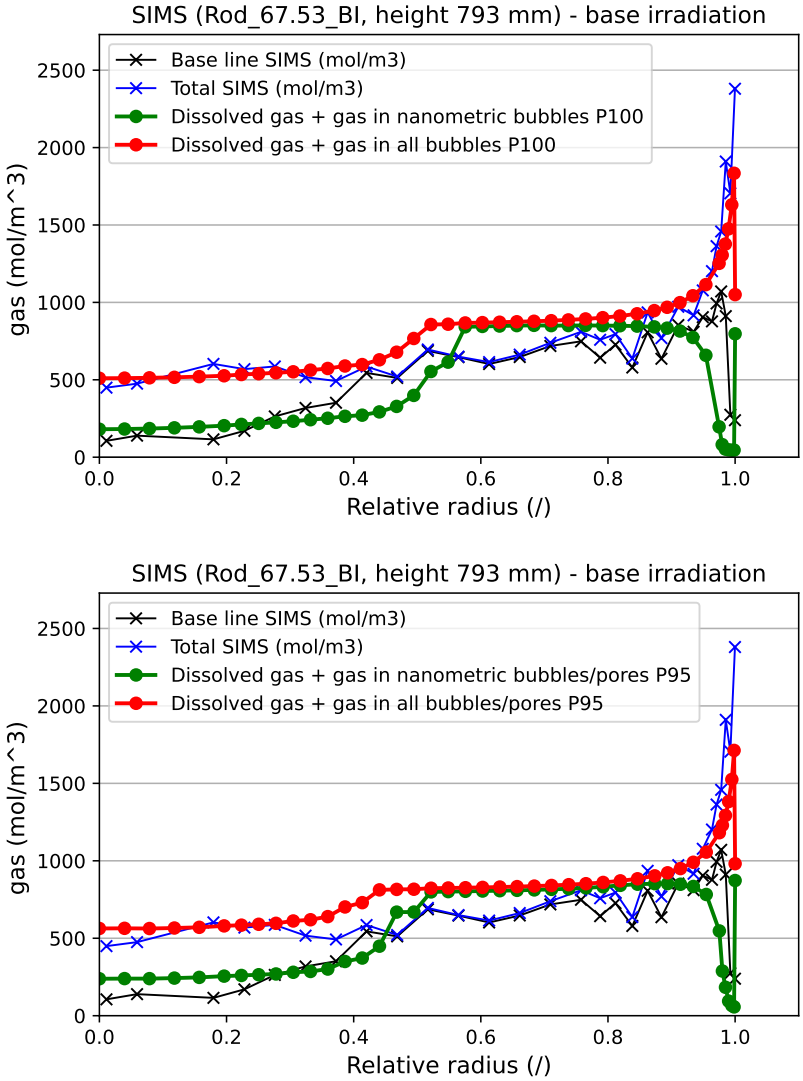

Figure 7.37. – Predicted versus measured SIMS. Rod_67.53_BI, 2 different input powers. Measurements from [Dowek 2021] (the same measurements are plotted in figure 4.2).

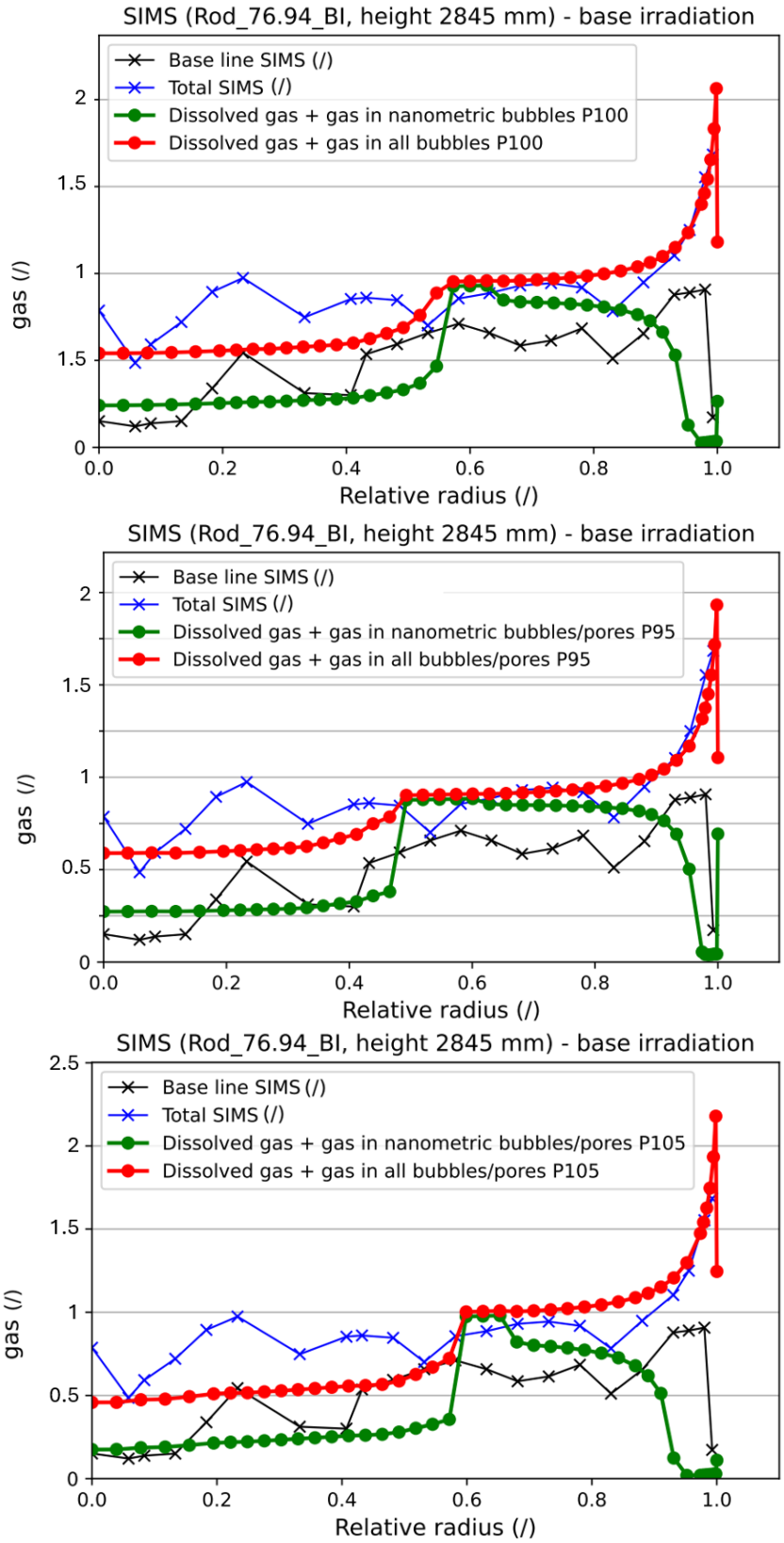

Figure 7.38. – Predicted versus measured SIMS. Rod_76.94_BI, 3 different input powers. To ensure confidentiality, the data have been rescaled using a common factor.

Porosity

Figure 7.39 shows the predicted versus the measured porosity along the radius of the pellet, for the Rod_65.06_BI.
As for the Rod_57.61_BI, MARGARET predictions are close to the measurements in the center of the pellet, where the precipitation bubbles contribute to the porosity. On the periphery, where the HBS has developed, predictions are less precise, but still close to the measurements.

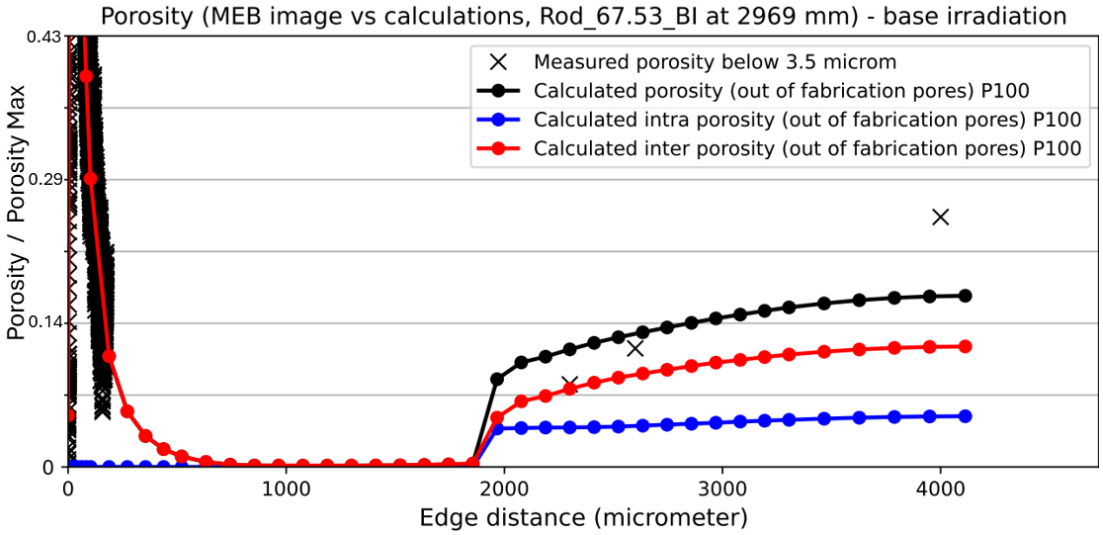

(a) All radius except the periphery of the pellet

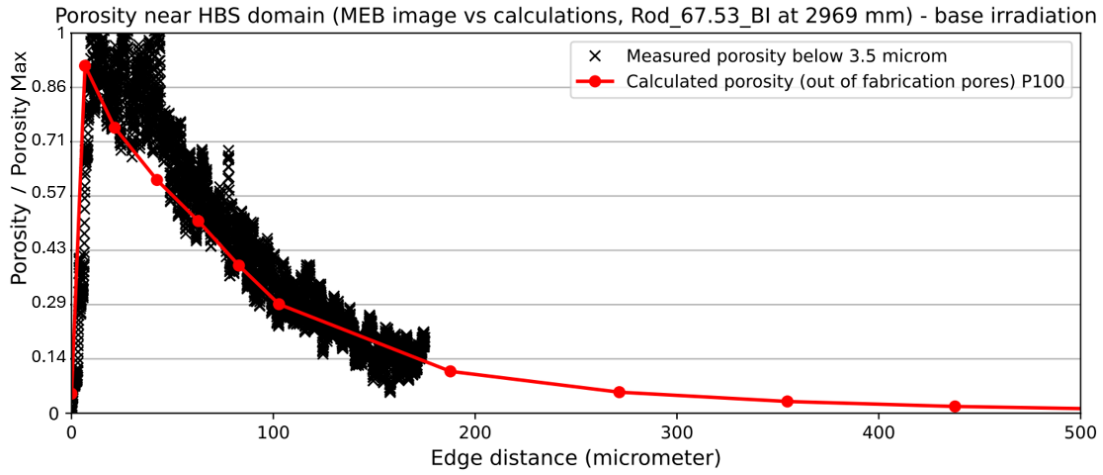

(b) Periphery of the pellet

Figure 7.39. – Predicted versus measured Porosity. Rod_67.53_BI, slice 25/30 (2.9214 [m] $< z <$ 3.0431 [m]), 100% power. To ensure confidentiality, the data have been rescaled using the maximum measured value.

7.3.3. Power Ramps

In this section, I present the validation of the code on the power ramped fuels listed in table 7.5.
Contrary to the base irradiated fuels, ramp tests are performed in dedicated facilities and the power axial profile is deduced from gamma spectrometers, therefore, there is less uncertainty on the power during a ramp test. On the contrary, uncertainty on the base irradiation power, and so on the initial state of the fuel, remains, but has not been taken into account here. All predictions are then made considering 100% power during base irradiation and 100% power during the power ramp.

FGR

Figure 7.40 shows the predicted versus the measured FGR of all the power ramped fuels.

MARGARET predictions are less accurate than the FGR predictions for the base irradiated fuels, but they remain in the range ±40% for half of the fuels and in the range ±50% for the other half. This decrease in the precision of the code is to be expected, because ramped fuels are more difficult to simulate by lack of information. For example, we have no experimental data on the behaviour of subdomains during a ramp test.

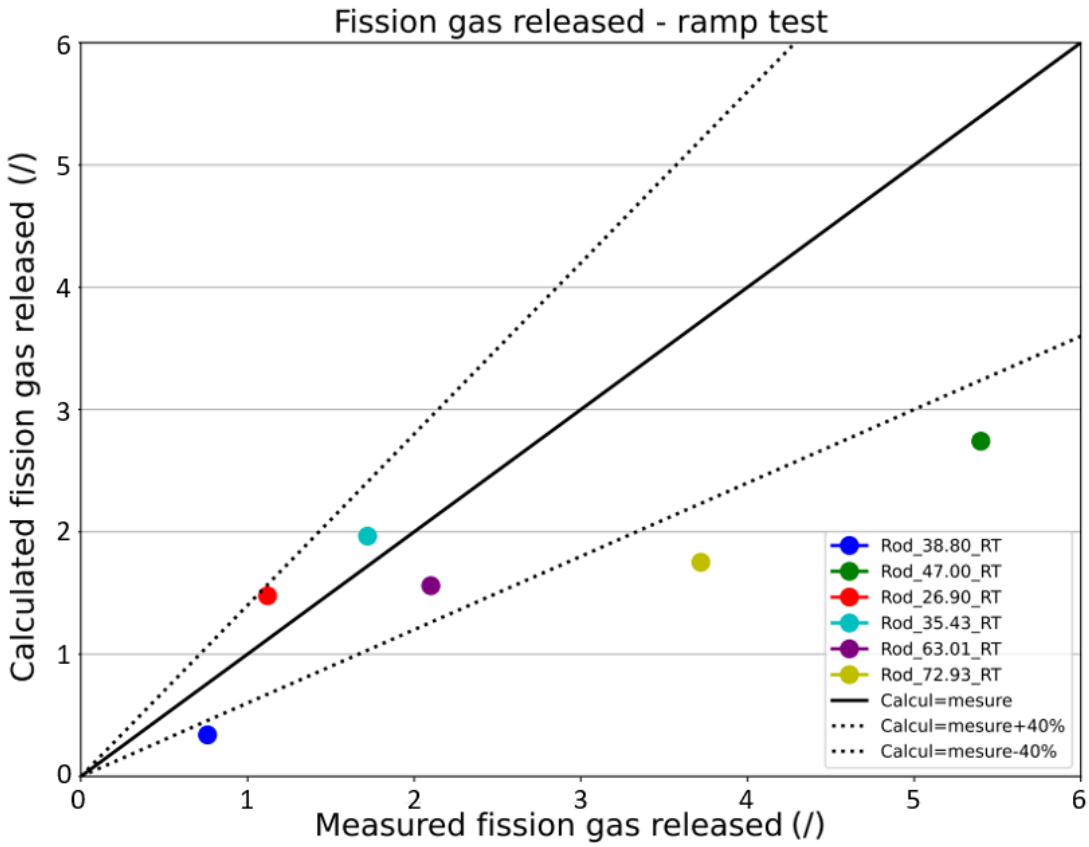

Figure 7.40. – Predicted versus measured FGR. To ensure confidentiality, the data have been rescaled using a common factor.

Volume per atom

Figures 7.41, 7.42 and 7.43 show the predicted V_{at} of the bulk, inter-granular, precipitation and HBS bubbles at the end of the power ramp, for the Rod_38.80_RT and Rod_63.01_RT.
Rod_38.80_RT does not have subdomains nor HBS, and therefore it does not have precipitation nor HBS bubbles. Concerning the inter-granular bubbles of the sound zones, we only present the V_{at} of the non-connected (isolated) bubbles.

In the Rod_38.80_RT, the V_{at} of the bulk bubbles, which started at approximately 1 Ω at the beginning of the ramp, has grown up to a value of 1.8 Ω at the center of the pellet. The V_{at} decreases quickly with the radius and stays below 1.2 Ω for a radius higher than 0.2 R_{pellet}. The value at the center of the pellet is in line with the experimental data (see Section 5.1.2), while the decrease in V_{at} is probably too fast.
The V_{at} of the inter-granular bubbles has grown up to values higher than 8 Ω for all the central part of the pellet, until $r \approx 0.5 R_{pellet}$. Towards the periphery, the V_{at} tends to reach 1 Ω: the temperature is probably not high enough for bubbles to grow by trapping of the thermal vacancies. The relative minimum in the V_{at} at $\approx 0.1 R_{pellet}$ can be explained for the following reason: in the center, the overall flux of the bulk bubbles (coming from the grain) to the inter-granular bubbles is lower than at $\approx 0.1 R_{pellet}$, due to the fact that at $\approx 0.1 R_{pellet}$ the flux of bubbles under temperature gradient is higher. The intra-granular bubbles bring a volume per Xe atom of less than 2Ω to the inter-granular bubbles, as we can see from figure 7.41 (the V_{at} at the end of the ramp is the highest throughout the ramp test). At the same time, since the temperature is lower at $\approx 0.1 R_{pellet}$, the flux of thermal vacancies to the inter-granular bubbles is lower. The overall effect is a V_{at} at $\approx 0.1 R_{pellet}$ closer to the V_{at} of the bulk bubbles than at the center. At $r \approx 0.4 R_{pellet}$, instead, the overall flux of the bulk bubbles is lower than at $\approx 0.1 R_{pellet}$, but the flux of vacancies do not decrease with the radius as fast as the decrease of the flux of bubbles. In fact, at $r \approx 0.4 R_{pellet}$, apart from the lower temperature, the V_{at} of the bulk bubbles is $\approx \Omega$, and therefore their mobility is penalized by the Mikhlin's term (see Section 7.1.11). Finally, in all of these 3 points, the contribution of volume due to the diffusion of the dissolved gas is much lower than the contributions due to thermal vacancy and the mobility of the bulk bubbles.

In the Rod_63.01_RT, the V_{at} of the bulk bubbles in the precipitation zone ($r \lesssim 0.3 R_{pellet}$) stays close to Ω, due to the fact that the pre-existing intra-granular bubbles were quickly trapped by the precipitation bubbles, and the newly formed bubbles have a $V_{at} \approx \Omega$ (at the end of the ramp test, the bulk bubbles in this zone have a radius of ≈ 0.5 nm). Just outside the precipitation zone, the V_{at} reaches a value of 6Ω and then decreases rapidly. This high value just outside the precipitation zone is due to the high value of D_U at high temperatures plus the absence of precipitation bubbles that can quickly trap the bulk bubbles.
The V_{at} of the precipitation bubbles is around 2Ω, which is probably lower then the actual value. However, the starting value at the beginning of the ramp is lower than what it should (≈ Ω, as we have seen in Section 7.3.2).

The V_{at} of the inter-granular bubbles is $\approx 2-3\Omega$ in the center of the pellet, while reaches values as high as $\approx 9\Omega$ in the mid radial position. The growth from $r \approx 0.4R_{pellet}$ to $r \approx 0.6R_{pellet}$ is due to the same phenomena that caused the growth from $r \approx 0.1R_{pellet}$ to $r \approx 0.4R_{pellet}$ in the Rod_38.80_RT. Moreover, bubbles at $r \approx 0.4R_{pellet}$ are more interconnected than bubbles at $r \approx 0.6R_{pellet}$, which means that there are less inter-granular pressurized bubbles and therefore less production of vacancies on the grain boundaries.
At the center, there is a large quantity of gas that reaches the grain boundaries inside the precipitation bubbles, because of the precipitation bubble movement. In fact, these bubbles leave the grain due to the subdomain growth at high temperatures. At the same time, an high percentage of the inter-granular bubbles are interconnected, and therefore the production of vacancies is not high enough to increase the V_{at} of isolated bubbles as high as the values predicted at mid-radial position.
Two points are missing from the graph around $r \approx 0.3R_{pellet}$ because no isolated bubble is present: all the bubbles are interconnected.
In the HBS, the bubbles remain with a $V_{at} \approx 2-3\Omega$. In fact, the temperature in the HBS region does not increase enough for the flux of thermal vacancies to be determinant.

In general, we can say that the predicted V_{at} is very sensible to the irradiation conditions (ex. the temperature in each point) and the state of the fuel (with or without subdomains).

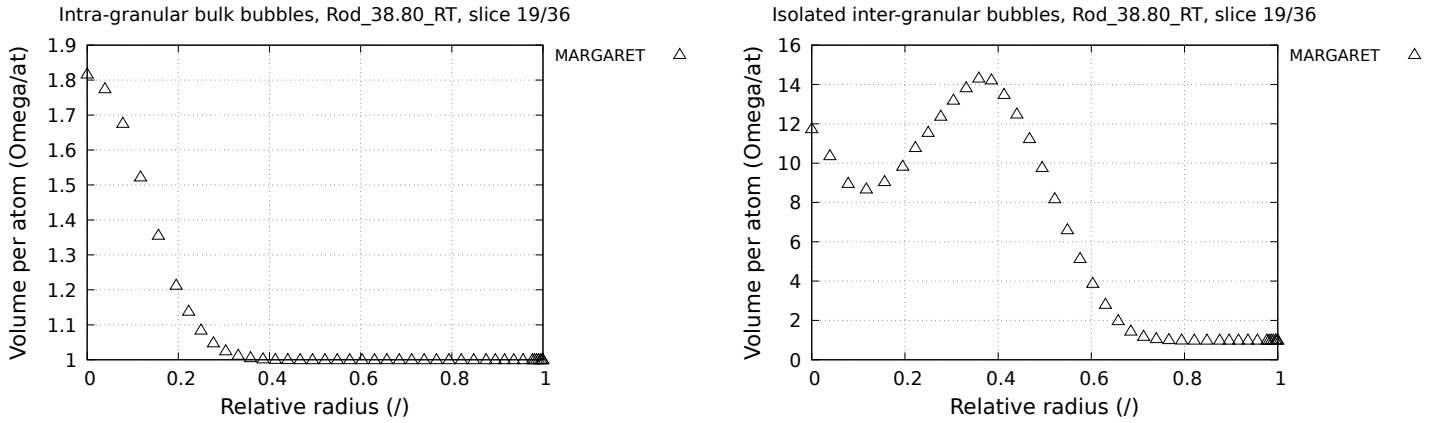

Figure 7.41. – Predicted V_{at} of the intra-granular and inter-graular bubbles for the Rod_38.80_RT at the end of the power ramp.

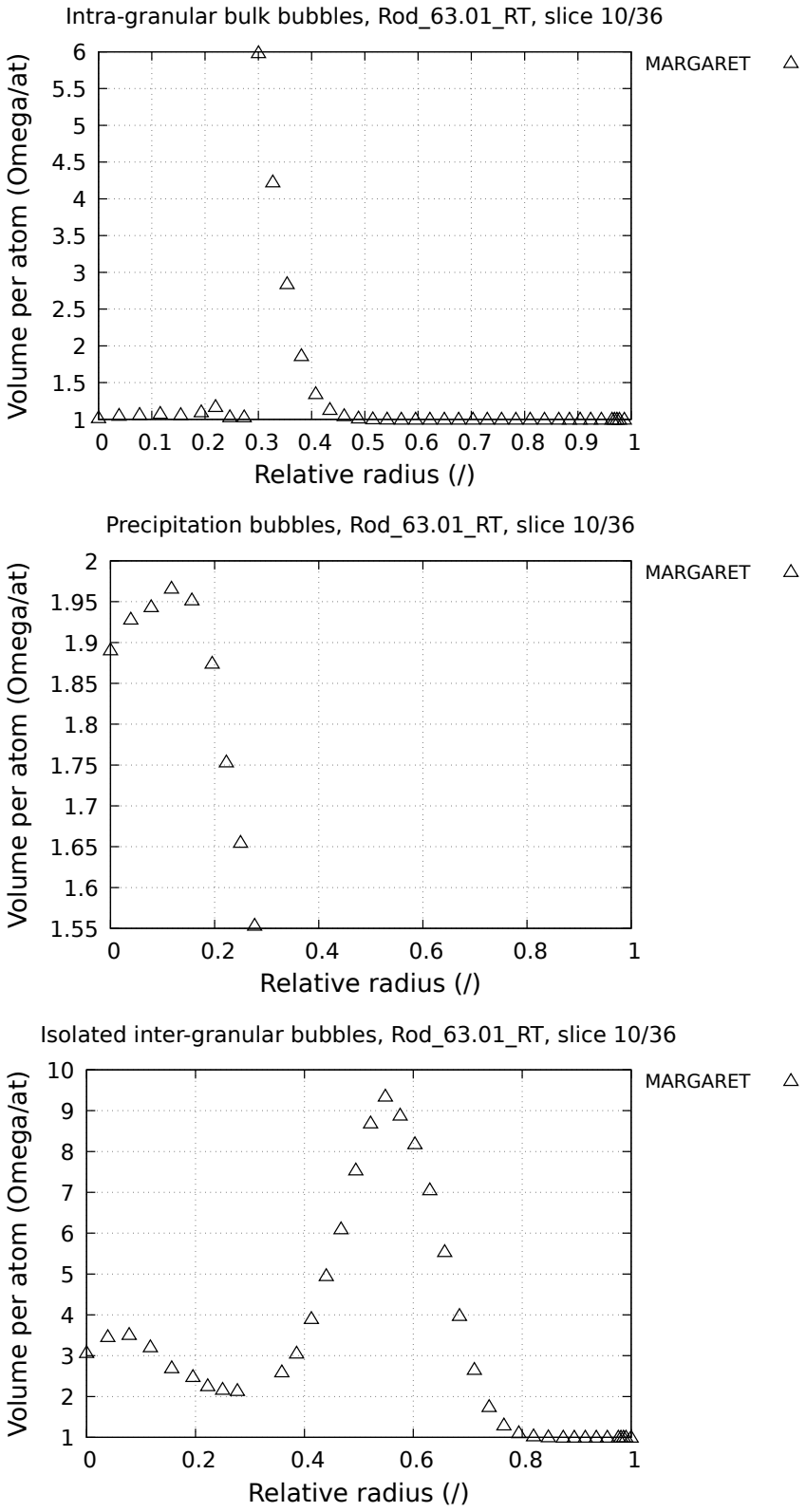

Figure 7.42. – Predicted V_{at} of the intra-granular, inter-graular and precipitation bubbles for the Rod_63.01_RT at the end of the power ramp.

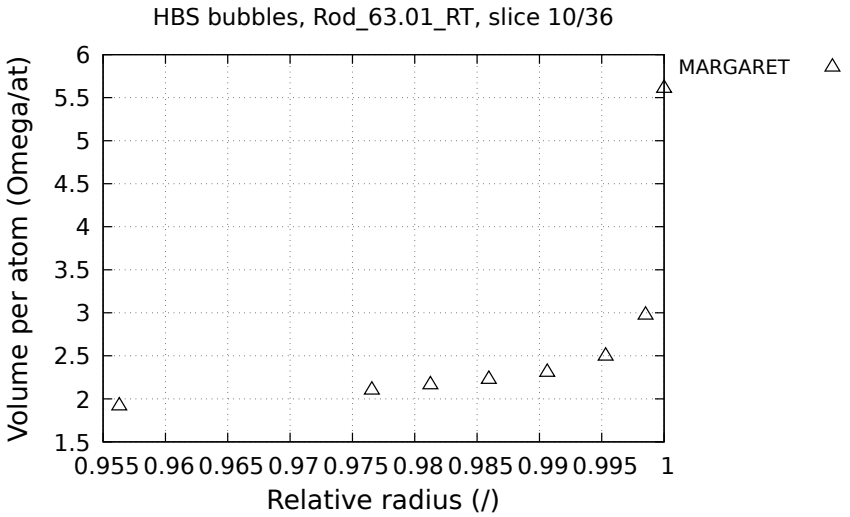

Figure 7.43. – Predicted V_{at} of the intra-granular, inter-graular and precipitation bubbles for the Rod_63.01_RT at the end of the power ramp.

EPMA

Figure 7.44 shows the predicted versus the measured EPMA for the Rod_63.01_RT. MARGARET predictions in the center of the pellet and on the periphery are in agreement with the measurements, while in the mid-radial position the predictions are too high. This is in line with the wrong prediction of the precipitation radius, as it can be better viewed by looking at the porosity measurements (figure 7.46)[8].

8. When looking at the metallographies after ramp tests, a central zone is darker because of the higher porosity. The external radius of this zone is usually called the "precipitation radius".

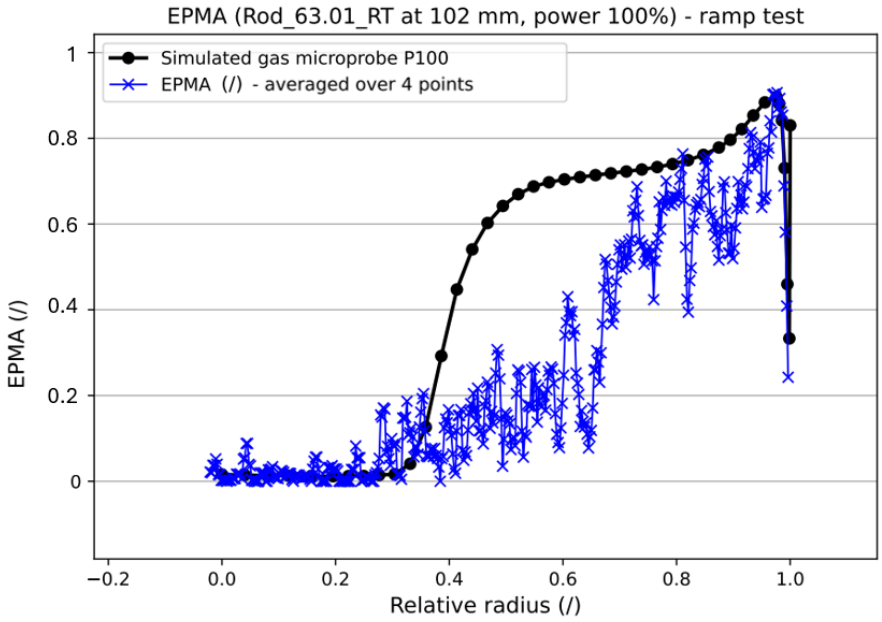

Figure 7.44. – Predicted versus measured EPMA, Rod_63.01_RT. To ensure confidentiality, the data have been rescaled using a common factor.

SIMS

Figure 7.45 shows the predicted versus the measured SIMS for the Rod_63.01_RT. From this image, we can see that the base line SIMS prediction is quite in agreement with the measurement. The sudden drop at $r \approx 0.6 R_{pellet}$ is due to the fact that, in MARGARET, we consider a cut-off value for the radius of the bubbles, under which the SIMS base line prediction sums the dissolved Xe and the gas present in the nano-bubbles (radius = 5 nm). This is done because, under a certain radius of the bubbles, the SIMS measurement cannot distinguish anymore the signal coming from the small bubbles from the signal coming from the dissolved Xenon. Since we consider only one population of bulk bubbles (the population "b" that is inside the sound grains or in subdomains), the cut-off value determines a sudden drop in the predicted base line SIMS: the bulk bubbles at $r > 0.6 R_{pellet}$ are smaller than the cut-off radius, and therefore counted together with the dissolved gas, while the inverse is true in the center.
MARGARET prediction of the total SIMS is a bit too low in the center of the pellet, meaning that too much gas has been released for this calculated slice. From figure 7.40, we see that the FGR for the Rod_63.01_RT is a bit too low with respect to the one measured. We can then deduce that MARGARET predictions of the FGR for the other slices of the same rod are probably too low.

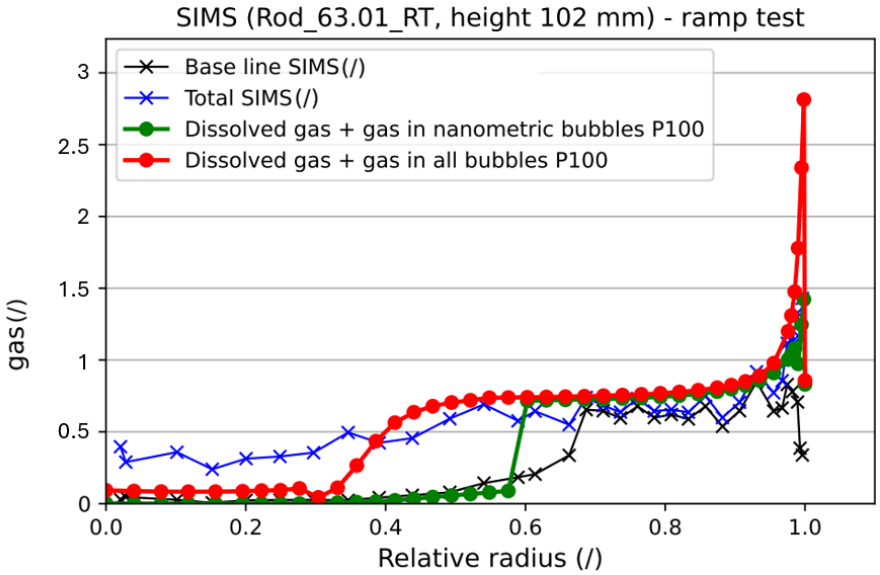

Figure 7.45. – Predicted versus measured SIMS, Rod_63.01_RT. To ensure confidentiality, the data have been rescaled using a common factor.

Porosity

Figure 7.46 shows the predicted versus the measured porosity of the Rod_63.01_-RT.

MARGARET predictions are below the measured intra- and inter-granular porosity across all the central part of the pellet, while the predictions are in agreement with the measurements in the periphery. Moreover, we can see that MARGARET does not predict correctly the precipitation radius, probably due to a D_U or D_{Uj} too low at $0.6R_{pellet}$, or not enough movement of the intra-granular sound zone bubbles (the bulk ones) due to the thermal gradient.

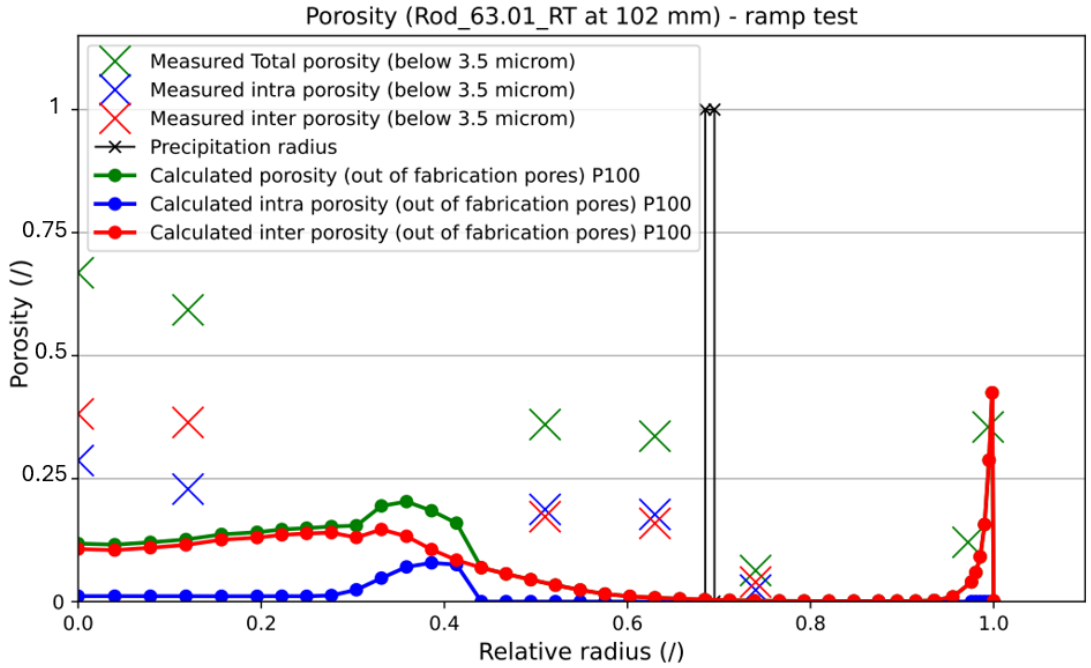

Figure 7.46. – Predicted versus measured porosity, Rod_63.01_RT. To ensure confidentiality, the data have been rescaled using a common factor.

Size of the bubbles

Figure 7.47 shows the predicted versus the measured size of the bubbles of the Rod_63.01_RT.

In the center, MARGARET overestimates the size of the precipitation bubbles, while the predictions of the size of the inter-granular bubbles are in agreement with the measurements. In the mid-radial position, the mismatch between predictions and measurements is in line with the under-estimation of the width of the precipitation zone.

The inter-granular bubble length and width are lower near the centermost part of the pellet with respect to the points around $r = 0.3R_{pellet}$. This is due to the fact that, at the center of the pellet, the volume of the inter-granular bubbles reached a maximum before the end of the ramp, while around $r = 0.3R_{pellet}$ the volume grew until the end (figures not shown here).

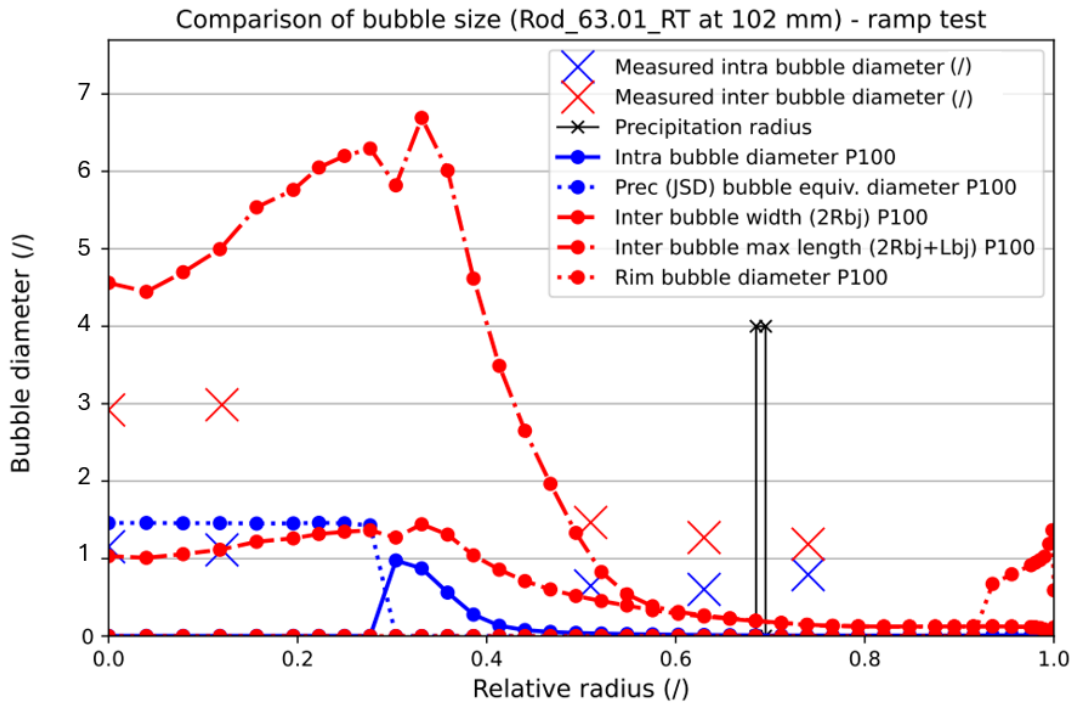

Figure 7.47. – Predicted versus measured size of the different bubble populations, Rod_63.01_RT. For a good comparison between predicted and measured size of the inter-granular bubbles, the measurements need to lay between the predicted bubble width ($2 \times R_{bj}$) and the predicted maximum length ($2 \times R_{bj} + L_{bj}$). To ensure confidentiality, the data have been rescaled using a common factor.

Cover rate of the inter-granular bubbles

Figure 7.48 shows the predicted versus the measure cover rate of the inter-granular bubbles for Rod_63.01_RT. The cover rate represents the fraction of the surface of the grain covered by inter-granular bubbles, F_{bj}. The maximal value that it can assume in the code is 0.5, as it is the maximal value measured by PI examinations.
Given the difficulties to measure F_{bj} (for example, it is measured from 2D images), the important fact, in the measure, is that F_{bj} drops drastically after $r = 0.65R_{pellet}$. In the predictions, F_{bj} rather drops at $r = 0.5R_{pellet}$, again in line with the bad prediction of the precipitation radius.

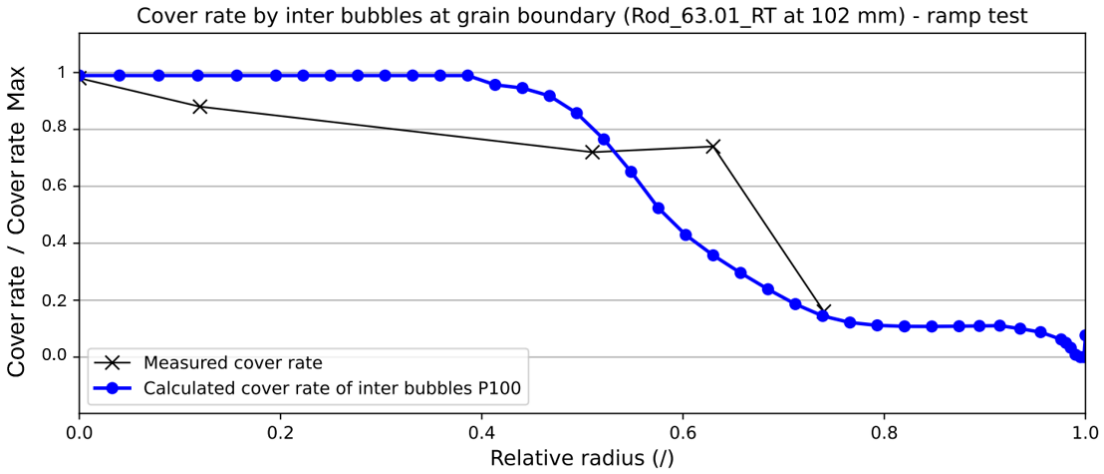

Figure 7.48. – Predicted versus measured cover rate of the inter-granular bubbles, Rod_63.01_RT. To ensure confidentiality, the data have been rescaled using the maximum measured value.

Concentration of precipitation bubbles, $C_{bprecjsd}$

Figure 7.49 shows the predicted concentration of precipitation bubbles at the end of the power ramp of another rod (Rod_72.93_RT).
We can notice that $C_{bprecjsd}$ is lower near the center of the pellet, where the temperature is higher and the subdomains have grown the most. Near the end of the precipitation zone, $C_{bprecjsd}$ is close to the value that it had at the beginning of the power ramp (8×10^{17} [bubbles/m^3]).
Despite the pronounced decrease in the concentration of precipitation bubbles in the center of the pellet, $C_{bprecjsd}$ remains approximately one order of magnitude higher than the measured value (see figure 6.2). This may in part explain the lower than measured predicted FGR for this high burnup rod (see figure 7.40).

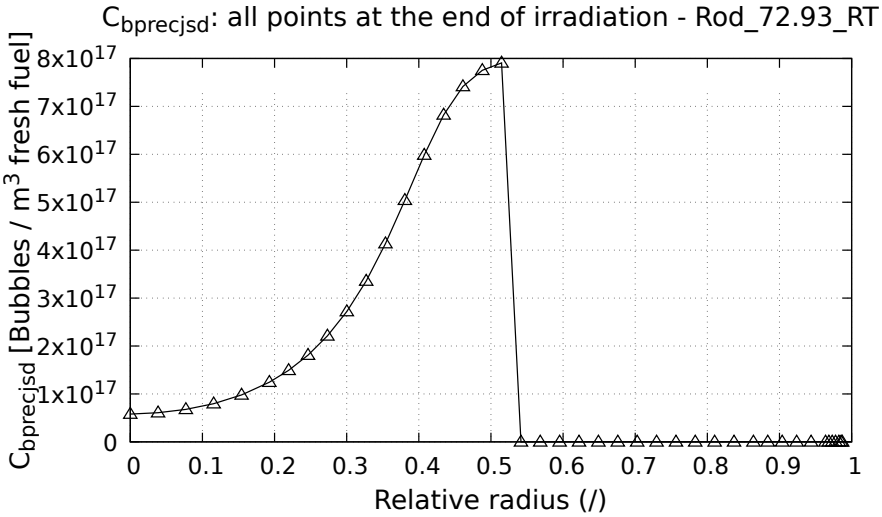

Figure 7.49. – Predicted concentration of precipitation bubbles at the end of the power ramp, Rod_72.93_RT, slice 1/9 of the ramp calculation (0.0 [m] $< z <$ 0.0398 [m]).

7.3.4. Is it possible to release without inter-granular bubble interconnection?

In Section 3, we have seen how PI measurements performed on base irradiated fuels, operated at temperatures lower than most of the fuels analyzed in literature, did not show any evidence of inter-granular bubble interconnections. Moreover, we have taken into account in the model the possible FGR through the long range diffusion through the grain boundaries. However, in the results presented before, the FGR is mainly due to inter-granular bubble interconnection. In this Section, we try answer the question: Can we explain considerable values of FGR without inter-granular bubble interconnections?

Unfortunately, without an automatic calibration of the model, we cannot be completely confident in answering this question. However, we can still present the beginning of an answer by running the simulations with a change in the values of some parameters with the direct purpose of reducing the predicted inter-granular bubble interconnection. In this way, we can check if the other ways by which fission gas can be released from the fuel, mostly ejection and long range diffusion through the grain boundaries, can explain the measured Fission Gas Release.

Using Rod_65.06_BI as a test, we have followed this logic in changing the parameters:

— To favor the inter-granular diffusion, we have chosen to increase $coe_{cavj->j}$ and D_{Xejsd}, and decrease coe_j, ν_{Xej} and ε_{Xej}. To be coherent with the value of ε_{Xej} chosen, we have also reduced the values of ε_{Xe}, ε_v and $\varepsilon_{v,j}$, so that we can keep $\varepsilon_{seg,Xe}$, $\varepsilon_{seg,v}$ and the difference between ε_{Xe} and ε_v in line with the literature.
— To impede the inter-granular bubble interconnection, we have decreased $D_{U,j}$. However, after running many simulations with different value of the parameters, we have seen that, after the formation of the subdomains, the increase in the gas that reaches the grain boundaries is high enough to cause the interconnection of the inter-granular bubbles, even if the contribution given by the thermal vacancies is negligible. Therefore, to limit the increase in the amount of gas that reaches the GB, we have chosen to increase A_{sd} and dNML, and decrease D_{Xejsd}, D_{Xemix} and ζ.

Table 7.7 shows all the parameters that have been changed and their new values / expressions.

The fission gas release in time with the set of parameters presented above is plotted in figure 7.50.

As we can see, even if the contribution of the thermal vacancies to the growth of the inter-granular bubbles is negligible, a fraction of the inter-granular bubbles interconnect and part of the gas is released by percolation. Moreover, even with the change in

Quantity	Value / Expression	Notes
$D_{Xe,mix}$	$1.7 \times 10^{-25} \times \dot{F}^{0.5}\, exp\left(\frac{-1.2\ eV}{kT}\right)$ (m^2/s)	The pre-factor is multiplied by 3 with respect to the one chosen for the extended validation.
D_{Xej}	$9 \times 10^{-11}\, exp\left(\frac{-0.955\ \text{eV}}{kT}\right) + 4 \times 10^{-40} \times \dot{F}$ (m^2/s)	The pre-factor is multiplied by 10 with respect to the one chosen for the extended validation.
D_{Xejsd}	$4.5 \times 10^{-15}\, exp\left(\frac{-0.955\ \text{eV}}{kT}\right) + 2 \times 10^{-43} \times \dot{F}$ (m^2/s)	The pre-factors are divided by 10^3 with respect to the one chosen for the extended validation.
$D_{Uj,th}$	$10^{-30}\, exp\left(\frac{-eV}{kT}\right)$ (m^2/s)	Chosen to obtain a negligible contribution of the thermal vacancies to the growth of the inter-granular bubbles
$D_{Ujsd,th}$	$10^{-30}\, exp\left(\frac{-eV}{kT}\right)$ (m^2/s)	same as $D_{Uj,th}$
ε_v	2.2 (eV)	
ε_{Xe}	2.7 (eV)	
$\varepsilon_{v,j}$	1.1 (eV)	
ε_{Xej}	1.3 (eV)	
ν_{Xej}	10^{12} (1/s)	10 times less than the one chosen for the extended validation.
dNML	1×10^{-9} (m)	
ζ	0.73 (/)	
coe_j	0.001 (/)	
$coe_{cavj->bulk}$	1 (/)	
$coe_{cavj->j}$	4 (/)	
$coe_{cavj->jsd}$	1 (/)	
A_{sd}	0.65×10^{-6} [m]	

Table 7.7. – Parameters and expressions chosen to check if it possible to release without inter-granular bubble interconnection.

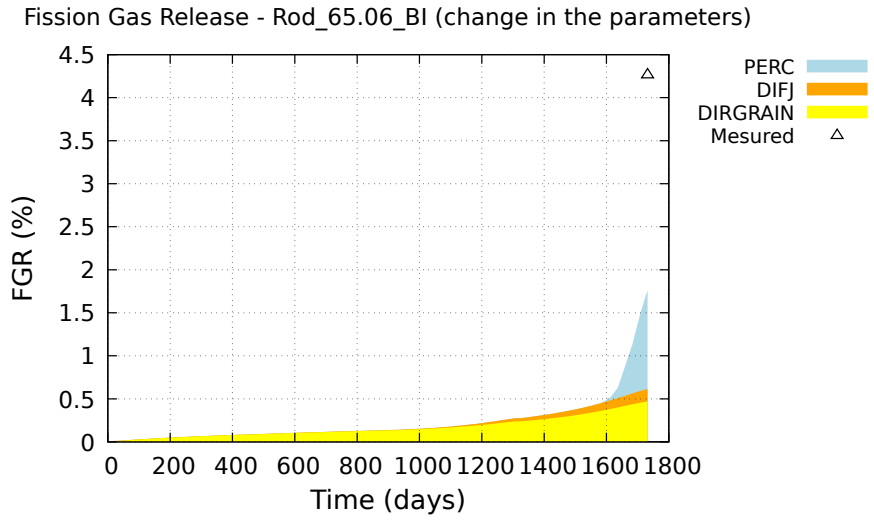

Figure 7.50. – Predicted fission gas release in time, measured FGR and predicted contribution of the different ways in which gas can be released for the Rod_65.06_BI, 100% power, with a change in the parameters explained in this Section. The measured FGR comes from [Dowek 2021].

the values of the parameters explained above, the prediction of the contribution of the long-range inter-granular diffusion remains low.

From this short analysis, we can conclude that MARGARET is, currently, not able to predict the measured FGR without considering the interconnection of inter-granular bubbles.

Moreover, we are limited in the combination of parameters that we can use: some combinations cause convergence problems, and therefore we cannot obtain a corresponding prediction.

7.3.5. Conclusion to the validation of the code

In the previous Sections, we have validated the version of the code described in this thesis manuscript on a range of base irradiated (12 fuels, burnup in the range 13-77 GWd/t$_U$) and power ramped fuels (6 fuels, burnup in the range 27-73 GWd/t$_U$). The validation on the base irradiated fuels is more extensive, due to the larger quantity of experimental data available and since it was the starting point of the thesis. The validation on the power ramps lacks the sensitivity analysis on the BI power, and the comparison with experimental data is less broad. Nonetheless, we can draw some conclusions on the state of the code for both irradiation conditions:

Even in the absence of an automatic validation, the overall results on base irradiated fuels are encouraging. MARGARET's predictions are in agreement with the measurements on the following quantities:

— Fission gas release;
— Swelling of the fuel, even if there is a general tendency to under-estimate it;
— V_{at} of bulk bubbles and inter-granular bubbles;
— Size of the precipitation bubbles ;
— Width of the precipitation zone ;
— Predictions of the porosity, except for the coldest zone of the not HBS part of the fuel;
— Predictions of the EPMA, with the notable exception of the centrmost part of the pellet in the fuel operated at the lowest power and in the two highest burnup fuels.

On the other hand, improvements are needed to correctly predict the V_{at} of the precipitation bubbles and the concentration of dissolved gas in the HBS grains.
A possible solution to better estimate the V_{at} of the precipitation bubbles is already envisaged: in the equation of $\frac{dV_{cavjsd}}{dt}$ in Section G.1.2, we could choose $\zeta = 2$ instead of $\zeta = 1$ (see the discussion of Section 5.1.5).
For what concern the concentration of dissolved gas in the HBS grains, adopting a slight dependence of the "a-thermal" term of the Xe diffusion with temperature, as suggested by Cooper's MD calculations [Cooper, Stanek, et al. 2016], may, in part, reduce the problem.

For what concerns the power ramped fuels, the predictions are less precise than the ones on the base irradiated fuels. Nevertheless, we have seen that MARGARET is able to predict rather accurately the fission gas release, the increase in the V_{at} of all the population of bubbles, the cover rate and the size of the inter-granular bubbles. On the contrary, the accuracy of the code decreases in the prediction of the porosity in all the central part of the fuel.

We can say that the model of the subdomains detailed in Chapter 4 behaved as expected. Most importantly, it allowed us to predict higher fission gas release for the

high burnup rods, even if the temperature experienced by the fuels did not increase, or even decreased, in the last cycles.
The new model of thermal vacancy, detailed in Chapter 5, together with the new meaning given to the volume contribution to the bubbles due to the trapping of Xenon atoms (see Section 5.1.5), are responsible for the good estimation of the swelling of the fuels and of the V_{at} of bulk and inter-granular bubbles during base irradiation, and the increase in V_{at} of all the population of bubbles during power ramps.
Furthermore, the code is now able to reproduce the fission gas release of both base irradiated and power ramped fuels using only one expression for D_{Uj}, and with a coherent description of the behaviour of the thermal vacancies.

Finally, in the last Section of the validation, we have tried to check if MARGARET is able to predict considerable values of FGR even in the absence of inter-granular bubble interconnections. Also in this case, an automatic calibration would be needed to better answer this question. We had no time to tempt it within the framework of this thesis. However, we have tried different combinations of the values of the parameters, with the direct intention of increasing the contribution of the long-range inter-granular diffusion to the overall fission gas release. Despite our attempts, none of these trials resulted in a sufficient increase in the FGR by inter-granular diffusion. We can then conclude that this version of MARGARET is probably not able to predict the measured values of FGR in high burnup fuels without considering the interconnection of inter-granular bubbles.

Conclusion and perspectives

Recently, new experimental results and atomic scale simulations have advanced our understanding of the behaviour of the fission gas under irradiation. With the intent of improving MARGARET's predictions on both irradiated and power ramp conditions, we have updated the code to take those results into account:

— We have built and introduced in the code a simple model for the phenomena of trapping by and re-solution from intra-granular bubbles, based on Molecular Dynamics simulations of the interaction between fission spikes and bubbles (Chapter 2). This model is the subject of an article [Vergani et al. 2025], written with the collaboration of M.W.D. Cooper, one of the authors of the MD simulations that we used to derive the model. In the article, we have also tried to clarify the relations between the value of the re-solution frequency derived in the past by experiments, the one obtained by MD simulations and the one that needs to be used by fuel performance codes.

— Researchers have recently obtained new 3D experimental images of base irradiated fuels [J. Noirot, Dowek, et al. 2022], and they found no evidence of a network of inter-connected inter-granular bubbles, even for fuels that experienced significant fission gas release. In the absence of a network of inter-connected inter-granular bubbles, the fission gas cannot be released by percolation, which is the major way of release used by fission gas models. Therefore, we have introduced in the code a description of the phenomena of thermal and dynamic re-solution from inter-granular bubbles to the grain boundaries to check if the fission gas can be released by long-range inter-granular gas diffusion (Chapter 3). In the process, we have derived the expressions for the equilibrium concentrations of both Xenon and vacancies on the grain boundary near an inter-granular bubble. We have also derived an expression to estimate the fraction of the atoms re-soluted (dynamically) from an inter-granular bubble that should remain on the grain boundaries.

— A type of restructuring of the fuel, visible in the center of the pellets at high burnup, and different from the restructuring that we see at the periphery (HBS), has been recently discovered [J. Noirot, Zacharie-Aubrun, et al. 2018; Zacharie-Aubrun et al. 2022]. This phenomenon is characterized by the formation of different domains inside the original grains, the so-called subdomains / subgrains. EBSD images have shown that the precipitation bubbles, the bigger population of intra-granular bubbles that appear at high burnup in the center

of the pellet, are placed on the boundaries of these subdomains. Furthermore, the subdomain formation is concomitant with the increase in fission gas release experienced by high burnup fuels. Given the apparent importance of this phenomenon on the behaviour of the fission gas, we have introduced in the code a description of the subdomains (Chapter 4).
In practice, we have added one more possible state of the fuel, called the subdomain state: once certain conditions of temperature and burnup (acquired in a particular temperature range) are reached, the subdomain state is introduced in the calculation. The change from the "sound" to the subdomain state determines the introduction of the second population of intra-granular bubbles (the precipitation bubbles, with a small initial radius) and a change in the schematic pathway of the fission gas from the grain, where they are produced, towards the grain boundaries: in the subdomain state, the gas is produced in the subdomains and diffuses towards the subdomain boundaries. Then, on the subdomain boundaries, the gas that it is not trapped in the precipitation bubbles diffuses towards the grain boundaries.
In our model, we consider the subdomain boundaries as fast diffusion pathways, and therefore we expect an increase in the predicted FGR after the formation of the subdomains.
All the equations that describe the behaviour of the fission gas in the subdomain state are detailed in the manuscript.

— We have built and introduced in the code a new description of the thermal vacancies, starting from the work of Speight and Beere [SPEIGHT et al. 1974] (swelling of inter-granular bubbles due to thermal vacancies), valid for all the states modelled in the code (Chapter 5). This model, coupled with a simple description of the contributions of volume to the bubbles at the temperatures where irradiation vacancies and interstitials prevail, can be used for both irradiated and power ramps conditions. The objective is to predict correctly the evolution of the volume of all the population of bubbles, and hence the fuel swelling. In the HBS, this model is not sufficient. So, we added a simple model of bubble growth due to irradiation induced creep. Indeed, in the HBS, creep is facilitated by the small size of the HBS grains.

— To predict the measured reduction in the number of precipitation bubbles and the increase in fission gas release during power ramps of high burnup fuels, we have introduced in the code a simple model of subdomain growth at high temperatures (Chapter 6).

We have then tested the code, checked that the material balances are respected and selected the combination of parameters to be used for the validation, after a critical evaluation of the literature and a trial and error procedure.
To validate the code, we have used a range of base irradiated (12 fuels, burnup in the range 13-77 GWd/t_U) and power ramped fuels (6 fuels, burnup in the range 27-73

GWd/t$_U$) (Chapter 7). We have compared MARGARET predictions with a vast series of measurements: FGR, swelling of the fuels, EPMA, SIMS, porosity, size of precipitation bubbles. Moreover, for few selected rods, we have presented a detailed characterization of the outputs of MARGARET, and compared them with the corresponding measurements, when present.
The results of this new version of the code are encouraging. In base irradiation, MARGARET is able to correctly predict, with few exceptions:

— The fission gas release (in a range of ±40%);
— The swelling of the fuels;
— The width of the precipitation zone;
— The radius of the precipitation bubbles;
— The porosity.

In particular, the way in which we describe the subdomains allowed us to predict higher fission gas release for the high burnup fuels, even if the temperature experienced by the fuels did not increase, or even decreased, in the last cycles.
For the ramp tests, the results are less precise than the ones on the base irradiated fuels, and have to be considered mostly as a display of the current state of the code. Nevertheless, MARGARET is able to predict rather accurately the fission gas release, the increase in the V_{at} of all the population of bubbles, the cover rate and the size of the inter-granular bubbles.
All the results for both base irradiated and power ramped fuels have been obtained using only one expression for D_{Uj}, and with a coherent description of the behaviour of the thermal vacancies.

During the validation of the code, we have also tried to check if this version of MARGARET is able to predict considerable fission gas release in the absence of inter-granular bubble interconnections. To do so, we have tried different combinations of the parameters with the direct purpose of increasing the release by long-range inter-granular gas diffusion, but none of the simulations predicted enough fission gas release. Therefore, we conclude that, at the moment, the code is able to predict major fission gas release only by considering the percolation through an interconnected inter-granular bubble network.

An automatic validation of the code is currently missing, and should be done in the future to better determine the capabilities of this new version of the code. This also means that the current validation is likely to improve after such a validation will be performed.
The validation of the code also highlighted specific parts of the model that need to be ameliorated:

— The V_{at} of the precipitation bubbles during base irradiation is too low with respect to the measurements. This incorrect prediction can probably be improved by changing the amount of volume that each trapped Xenon brings to the precipitation bubbles. This possibility is already considered in the code.
— The concentration of dissolved gas in the HBS grains seems too low with respect

to the baseline SIMS measurements. Adopting a slight dependence of the "athermal" term of the Xe diffusion with temperature, as suggested by Cooper's MD calculations [Cooper, Stanek, et al. 2016], may be, at least, part of the response to this problem.

— The porosity in the central part of the ramped, high burnup fuels is too low with respect to the measurements. It is possible to improve the way vacancies are trapped by of emitted from inter-granular bubbles taking into account their elongated shape and not their equivalent radius, as it is done in the present version (for the calculation of $C^{eq}_{v,j}(cavj)$).

Another short term improvement is envisaged: the same approach followed to derive the re-solution term of the intra-granular bubbles (Chapter 2) could be adopted to describe the re-solution from inter-granular bubbles to the grain boundaries. The main difference would be the geometry of the problem: a 2D geometry for the case of the grain boundary diffusion, a 3D geometry in the case of intra-granular bubbles in the bulk of the grain.

As a long term improvement, other population of bubbles, currently not considered, could be modelled in a future version of the code. In fact, in MARAGARET, we consider only 2 populations of intra-granular bubbles: the nano-bubbles and the precipitation bubbles. However, experiments on both base irradiated and power ramped fuels suggest the presence of bubbles on dislocations with a size higher than the nano-bubbles (higher than tenths of nanometers) also at burnups lower than the thershold for the subdomains formation [Thomas 1991; White et al. 2006; Baker 1977]. These bubbles seem to play an important role in the fission gas behaviour under specific conditions, such as during power ramps.

The experimental evidence of the absence of inter-connection of inter-granular bubbles is clear on the facets of the grains. But interconnection along the grain edges could not be experimentally excluded. Thus, to rationalize both the experimental evidence and the modelling attempts, the following scenario could be introduced in the code, for the base irradiation inter-granular behaviour: diffusion (with trapping and re-solution by and from the inter-granular bubbles) on the facets, without interconnection of the facet bubbles, but easier interconnection of the grain edge bubbles. This scenario would imply to introduce edge bubbles as a new population in the code.

Bibliography

[Alc+65] G.B. Alcock, R.J. Hawkins, A.W.D. Hills, et al. *A Study of Cation Diffusion in Stoichiometric UO_2 Using -Ray Spectrometry*. Symposium on Thermodynamics with Emphasis on Nuclear Materials and Atomic Transport in Solids; Vienna (Austria); 22-27 Jul 1965; IAEA-SM–66/36; ISSN 0074-1884. 1965 (cit. on p. 176).

[Ang24] M. Angleraud. "Etude par microscopie électronique en transmission des mécanismes de grossissement/croissance des bulles de gaz de fission dans le combustible nucléaire sous irradiation". PhD thesis. France: University of Toulouse, 2024 (cit. on p. 200).

[Bak77] C. Baker. "The fission gas bubble distribution in uranium dioxide from high temperature irradiated SGHWR fuel pins". In: *Journal of Nuclear Materials* 66 (1977), pp. 283–291 (cit. on pp. 23, 242).

[Bar+20] T. Barani, G. Pastore, A. Magni, et al. "Modeling intra-granular fission gas bubble evolution and coarsening in uranium dioxide during in-pile transients". In: *Journal of Nuclear Materials* 538.152195 (2020) (cit. on pp. 48, 58).

[BSK03] C.B. Basak, A.K. Sengupta, and H.S. Kamath. "Classical molecular dynamics simulation of UO_2 to predict thermophysical properties". In: *Journal of Alloys and Compounds* 360 (2003), pp. 210–216 (cit. on p. 180).

[Bei23] T. Beigbeder. "Simulations des matériaux à l'échelle atomique : étude du relâchement des gaz de fission". PhD thesis. France: University of Aix-Marseille, 2023 (cit. on pp. 134, 139).

[BGB21] M. Borde, A. Germain, and E. Bourasseau. "Molecular dynamics study of UO_2 symmetric tilt grain boundaries around [001] axis". In: *Journal of the American Ceramic Society* 104 (2021), pp. 2879–2893 (cit. on pp. 64, 106, 111, 179, 180, 261).

[BC17] P.A. Burr and M.W.D. Cooper. "Importance of elastic finite-size effects: Neutral defects in ionic compounds". In: *Phys. Rev. B* 96.094107 (2017) (cit. on p. 179).

[Cag16] C. Cagna. "Influence des gaz de fission sur l'état mécanique des combustibles oxydes irradiés". PhD thesis. France: ParisTech, 2016 (cit. on pp. 134, 135).

[Cap+22] F. Cappia, K. Wright, D. Frazer, et al. “Detailed characterization of a PWR fuel rod at high burnup in support of LOCA testing”. In: *Journal of Nuclear Materials* 569.153881 (2022) (cit. on pp. 116–118, 123).

[CBF10] A. Chartier, L. Van Brutzel, and M. Freyss. “Atomistic study of stability of xenon nanoclusters in uranium oxide”. In: *Phys. Rev. B* 81.174111 (2010) (cit. on p. 180).

[Chi25] C. Chil. *Structure des JdGs avec SNAP et énergie d’un Schottky au JdG*. Private Communication. 2025 (cit. on p. 180).

[CM93] V.F. CHKUASELI and Hj. MATZKE. “Fission gas bubble behaviour in uranium dioxide”. In: *Journal of Nuclear Materials* 201 (1993), pp. 92–96 (cit. on p. 183).

[Coo+16a] M.W.D. Cooper, N. Kuganathan, P.A. Burr, et al. “Development of Xe and Kr empirical potentials for CeO_2, ThO_2, UO_2 and PuO_2, combining DFT with high temperature MD”. In: *Journal of Physics: Condensed Matter* 28.405401 (2016) (cit. on pp. 179, 180).

[CMA25] M.W.D. Cooper, C. Matthews, and D.A. Andersson. “The role of irradiation-enhanced interstitial diffusion in over-pressurizing fission gas bubbles in UO_2”. In: *Journal of Nuclear Materials* 604.155452 (2025) (cit. on pp. 136, 139, 168, 169).

[CRG14] M.W.D. Cooper, M.J.D. Rushton, and R.W. Grimes. “A many-body potential approach to modelling the thermomechanical properties of actinide oxides”. In: *Journal of Physics: Condensed Matter* 26.105401 (2014) (cit. on pp. 179, 180).

[Coo+16b] M.W.D. Cooper, C.R. Stanek, J.A. Turnbull, et al. “Simulation of radiation driven fission gas diffusion in UO_2, ThO_2 and PuO_2”. In: *Journal of Nuclear Materials* 481 (2016), pp. 125–133 (cit. on pp. 22, 167, 236, 242).

[CSM69] R.M. Cornell, M.V. Speight, and B.C. Masters. “The role of bubbles in fission gas release from uranium dioxide”. In: *Journal of Nuclear Materials* 30 (1969), pp. 170–178 (cit. on p. 86).

[DL63] D. Davies and G. Long. *The emission of xenon-133 from lightly irradiated uranium dioxide spheroids and powders*. AERE-R 4347. 1963 (cit. on pp. 166, 169, 170, 265).

[Die77] W. Dienst. “IRRADLATION INDUCED CREEP OF CERAMIC NUCLEAR FUELS”. In: *Journal of Nuclear Materials* 65 (1977), pp. 1–8 (cit. on p. 315).

[Dor+12] B. Dorado, David A. Andersson, C. R. Stanek, et al. “First-principles calculations of uranium diffusion in uranium dioxide”. In: *Phys. Rev. B* 86.035110 (2012) (cit. on pp. 154, 175).

[Dow21] R. Dowek. “Les gaz de fission dans les combustibles REP irradiés : un état détaillé à fort taux de combustion”. PhD thesis. France: University of Aix-Marseille, 2021 (cit. on pp. 50, 116–120, 123, 127, 128, 134, 181, 183, 214–216, 218, 235).

[Dub+24] E. T. Dubois, J. Tranchida, J. Bouchet, et al. “Atomistic simulations of nuclear fuel UO_2 with machine learning interatomic potentials”. In: *PHYSICAL REVIEW MATERIALS* 8.025402 (2024) (cit. on pp. 121, 180).

[For+93] C. Forat, B. Blanpain, B. Kapusta, et al. *FISSION GAS RELEASE ENHANCEMENT AT EXTENDED BURNUP: EXPERIMENTAL EVIDENCE FROM FRENCH PWR IRRADIATION*. IAEA-TECDOC-697, p. 88. 1993 (cit. on p. 86).

[FCB21] P.C.M. Fossati, A. Chartier, and A. Boulle. “Structural Aspects of the Superionic Transition in AX_2 Compounds With the Fluorite Structure”. In: *Front. Chem.* 9.723507 (2021) (cit. on p. 121).

[Gal+23] C.0.T. Galvin, D.A. Andersson, R. Sweet, et al. *Diffusional creep in UO_2 informed by lower length scale simulations*. Technical Report: LA-UR-23-30155, OSTI Identifier: 2315683. 2023 (cit. on pp. 155, 176).

[Gal+22] C.0.T. Galvin, A. Chakraborty, D.A. Andersson, et al. *Development of a creep model informed by lower-length scale simulations to simulate creep in doped UO_2*. Technical Report: LA-UR-22-27950. 2022 (cit. on p. 176).

[GFN24] M. Gascoin, M. Freyss, and I.C. Njifon. “Trapping Properties of Iodine, Cesium, and Tellurium in Uranium Dioxide: A DFT+U Study”. In: *Inorganic Chemistry* 63 (51) (2024), pp. 24083–24095 (cit. on p. 179).

[Ger+18] T.J. Gerczak, C.M. Parish, P.D. Edmondson, et al. “Restructuring in high burnup UO2 studied using modern electron microscopy”. In: *Journal of Nuclear Materials* 509 (2018), pp. 245–259 (cit. on pp. 116, 117, 123).

[Gio+22] R. Giorgi, A. Cechet, L. Cognini, et al. “Physics-based modelling and validation of inter-granular helium behaviour in SCIANTIX”. In: *Nuclear Engineering and Technology* 54 (2022), pp. 2367–2375 (cit. on p. 90).

[GV13] K. Govers and M. Verwerft. “Classical molecular dynamics investigation of microstructure evolution and grain boundary diffusion in nano-polycrystalline UO_2”. In: *Journal of Nuclear Materials* 438 (2013), pp. 134–143 (cit. on pp. 62, 64, 176).

[Ham58] F.S. Ham. “Theory of diffusion-limited precipitation”. In: *Journal of Physics and Chemistry of Solids* 6 (1958), pp. 335–351 (cit. on pp. 65, 150).

[Har90] J.H. Harding. *Catalogue européen des propriétés de l’oxyde mixte (U,Pu)O2, Chap V : Diffusion*. NT SPU /LPCA n°02 de novembre 1990. 1990 (cit. on pp. 176, 182).

[HA68] R.J. HAWKINS and C.B. ALCOCK. “A study of cation diffusion in UO2+x and ThO2 using α-RAY spectrometry”. In: *Journal of Nuclear Materials* 26 (1968), pp. 112–122 (cit. on p. 183).

[Hin83] A.C. Hindermarsh. *ODEPACK: a systematized collection of ODE solvers*. Stepleman, R.S, et al. (Eds.), Scientific Computing. North-Holand, Amsterdam, pp. 55-64. 1983 (cit. on p. 73).

[HSA10] M. Huang, D. Schwen, and R.S. Averback. "Molecular dynamic simulation of fission fragment induced thermal spikes in UO_2: Sputtering and bubble re-solution". In: *Journal of Nuclear Materials* 399 (2010), pp. 175–180 (cit. on p. 64).

[HR59] D. Hull and D.E. Rimmer. "The growth of grain-boundary voids under stress". In: *The Philosophical Magazine: A Journal of Theoretical Experimental and Applied Physics* 4 (1959), pp. 673–687 (cit. on p. 137).

[Int+24] C. Introïni, I. Ramière, J. Sercombe, et al. "ALCYONE: the fuel performance code of the PLEIADES platform dedicated to PWR fuel rods behavior". In: *Annals of Nuclear Energy* 207.110711 (2024) (cit. on pp. 13, 45, 187).

[KU97] S. Kashibe and K. Une. "Effect of external restraint on bubble swelling in UO_2 fuels". In: *Journal of Nuclear Materials* 247 (1997), pp. 138–146 (cit. on p. 138).

[KU00] S. Kashibe and K. Une. "Fission Gas Release from Externally Restrained Uranium Dioxide Fuel". In: *Journal of NUCLEAR SCIENCE and TECHNOLOGY* 37 (2000), pp. 530–535 (cit. on p. 138).

[Kim+22] D. Kim, S. Blondel, D.E. Bernholdt, et al. "Modeling mesoscale fission gas behavior in UO_2 by directly coupling the phase field method to spatially resolved cluster dynamics". In: *Materials Theory* (2022). DOI: https://doi.org/10.1186/s41313-021-00030-8 (cit. on pp. 58, 78).

[KV92] E. Kolstad and C. Vitanza. "Fuel rod and core materials investigations related to LWR extended burnup operation". In: *Journal of Nuclear Materials* 188 (1992), pp. 104–112 (cit. on p. 86).

[KV56] F. A. Kröger and H. J. Vink. "Relations between the Concentrations of Imperfections in Crystalline Solids". In: *Solid State Physics* 3 (1956), pp. 307–435 (cit. on pp. 61, 132).

[Liu+23] X.-Y. Liu, C.0.T. Galvin, M.W.D. Cooper, et al. *Molecular dynamics simulations of fission gas xenon (Xe) diffusion at UO_2 grain-boundaries*. Technical Report: LA-UR-22-28477. 2023 (cit. on pp. 170, 171).

[Los00] P. Losonen. "On the behaviour of intragranular fission gas in UO2 fuel". In: *Journal of Nuclear Materials* 280 (2000), pp. 56–72 (cit. on pp. 48, 58, 121).

[Los17] P. Losonen. "On the effect of irradiation-induced resolution in modelling fission gas release in UO_2 LWR fuel". In: *Journal of Nuclear Materials* 496 (2017), pp. 140–156 (cit. on pp. 48, 63, 74, 178, 271).

[LMH96] P.G. Lucuta, Hj. Matzke, and I.J. Hastings. "A pragmatic approach to modelling thermal conductivity of irradiated UO_2 fuel: Review and recommendations". In: *Journal of Nuclear Materials* 232 (1996), pp. 166–180 (cit. on p. 119).

[MAI71] P.S. MAIYA. "Surface diffusion, surface free energy and grain-boundary free energy of uranium dioxide". In: *Journal of Nuclear Materials* 40 (1971), p. 57 (cit. on p. 182).

[Mat+19] C. Matthews, R. Perriot, M.W.D. Cooper, et al. "Cluster dynamics simulation of uranium self-diffusion during irradiation in UO_2". In: *Journal of Nuclear Materials* 527.151787 (2019) (cit. on pp. 61, 154, 168, 174).

[Mat+20] C. Matthews, R. Perriot, M.W.D. Cooper, et al. "Cluster dynamics simulation of xenon diffusion during irradiation in UO_2". In: *Journal of Nuclear Materials* 540.152326 (2020) (cit. on pp. 136, 168, 169).

[MW80] J. R. Matthews and M. H. Wood. "Simple operational gas release and swelling model. Pt. 2. Grain boundary gas". In: *Journal of Nuclear Materials* 91 (1980), p. 241 (cit. on p. 93).

[Mat87] H. Matzke. "Atomic transport properties in UO_2 and mixed oxides (U, Pu)O_2". In: *J. Chem. Soc., Faraday Trans. 2* 83 (1987), pp. 1121–1142 (cit. on p. 173).

[Mat66] Hj. Matzke. "Diffusion in doped UO2". In: *Nuclear applications* 2 (1966), pp. 131–137 (cit. on p. 58).

[Mat90] Hj. Matzke. "Atomic Mechanisms of mass transport in ceramic nuclear fuel materials". In: *JCSFT* 86 (1990), pp. 1243–1256 (cit. on p. 169).

[Mat92] Hj. Matzke. R.P. Argawala, (Ed.), Diffusion Processes in Nuclear Materials, Elsevier, Amsterdam, 1992, p. 9. 1992 (cit. on p. 176).

[McK+23] C. McKinney, R. Seibert, J. Werden, et al. "Characterization of the radial microstructural evolution in LWR UO2 using electron backscatter diffraction". In: *Journal of Nuclear Materials* 585.154605 (2023) (cit. on pp. 116, 118, 123, 124).

[MF72] W. Miekeley and F. W. Felix. "Effect of stoichiometry on diffusion of xenon in UO_2". In: *Journal of Nuclear Materials* 42 (1972), pp. 297–306 (cit. on p. 70).

[MIK79] E. Ya MIKHLIN. "The mobility of intra-granular gas bubbles in uranium dioxide". In: *Journal of Nuclear Materials* 87 (1979), pp. 405–408 (cit. on p. 182).

[Mun+24] M.A. Muntaha, S.Chatterjee, S. Blondel, et al. "Impact of grain boundary and surface diffusion on predicted fission gas bubble behavior and release in UO_2 fuel". In: *Journal of Nuclear Materials* 594.155032 (2024) (cit. on p. 174).

[MFG15] S. T. Murphy, P. Fossati, and R. W. Grimes. “Xe diffusion and bubble nucleation around edge dislocations in UO_2”. In: *Journal of Nuclear Materials* 466 (2015), pp. 634–637 (cit. on pp. 120, 172).

[MJG14] S.T. Murphy, E.E. Jay, and R.W. Grimes. “Pipe diffusion at dislocations in UO_2”. In: *Journal of Nuclear Materials* 447 (2014), pp. 143–149 (cit. on p. 178).

[N-D+03] Morelon N.-D., Ghaleb D., Delaye J.-M., et al. “A new empirical potential for simulating the formation of defects and their mobility in uranium dioxide”. In: *Philosophical Magazine* 83 (2003), pp. 1533–1555 (cit. on p. 180).

[Nei+24] W.D. Neilson, C.O.T. Galvin, S.J. Dillon, et al. “Irradiation-induced creep in UO2 : The role of grain boundaries”. In: *Phys. Rev. Materials* 8.103602 (2024) (cit. on pp. 135, 315).

[NR86] F.A. Nichols and C. Ronchi. *Mobility of fission gas bubbles*. Proceedings of the International Conference on the Mobility of Fission Gas Bubbles in Fission-Product Behavior in Ceramic Oxide Fuel, vol. 17, American Ceramic Society, 1986, pp. 85-93. 1986 (cit. on pp. 182, 183).

[NU95] K. Nogita and K. Une. “Irradiation induced recrystallization in high burnup fuel”. In: *Journal of Nuclear Materials* 226 (1995), pp. 305–310 (cit. on p. 122).

[NU97] K. Nogita and K. Une. “High resolution TEM of high burnup UO_2 fuel”. In: *Journal of Nuclear Materials* 250 (1997), pp. 244–249 (cit. on p. 134).

[NU98] K. Nogita and K. Une. “High resolution TEM observation and density estimation of Xe bubbles in high burnup UO_2 fuels”. In: *Nuclear Instruments and Methods in Physics Research B* 141 (1998), pp. 481–486 (cit. on p. 134).

[Noi+09] J. Noirot, I Aubrun, L. Desgranges, et al. “HIGH BURNUP CHANGES IN UO_2 FUELS IRRADIATED UP TO 83 GWd/t IN M5 ® CLADDINGS”. In: *Nuclear Engineering and Technology* 41.2 (2009) (cit. on pp. 135, 208).

[Noi+22] J. Noirot, R. Dowek, I. Zacharie-Aubrun, et al. “Restructuring in high burnup pressurized water reactor UO_2 fuel central parts: Experimental 3D characterization by focused ion beam-scanning electron microscopy”. In: *Journal of Applied Physics* 132.195902 (2022) (cit. on pp. 14, 41, 50, 86, 87, 116–118, 128, 188, 189, 202, 239).

[NOI+09] J. NOIROT, C. GONNIER, L. DESGRANGES, et al. *LWR FUEL GAS CHARACTERIZATION AT CEA CADARACHE LECA-STAR HOT LABORATORY*. IAEA-TECDOC-CD-1635, 2009. 2009 (cit. on pp. 138, 189).

[NNa04] J. Noirot, L. Noirot, and L. Desgranges et al. *Fission gas inventory in PWR high burnup fuel. Experimental characterisation and modelling*. Proceedings of the 2004 International Meeting on LWR Fuel Performance. 2004 (cit. on pp. 115, 116, 124).

[NZB18] J. Noirot, I. Zacharie-Aubrun, and T. Blay. “Focused ion beam–scanning electron microscope examination of high burn-up UO 2 in the center of a pellet”. In: *Nuclear Engineering and Technology* 50 (2018), pp. 259–267 (cit. on pp. 14, 49, 86, 115, 116, 124, 239).

[Noi06] L. Noirot. “MARGARET: An Advanced Mechanistic Model of Fission Gas Behavior in Nuclear Fuel”. In: *Journal of NUCLEAR SCIENCE and TECHNOLOGY* 43 - No. 9 (2006), pp. 1149–1160 (cit. on p. 208).

[Noi11] L. Noirot. “MARGARET : A comprehensive code for the description of fission gas behavior”. In: *NED* 241 (2011), pp. 2099–2118 (cit. on pp. 13, 41, 45, 53, 70, 133, 189, 190, 192, 193, 195, 202, 206, 273, 279–281, 285, 286).

[Noi14] L. Noirot. “A method to calculate equilibrium concentrations of gas and defects in the vicinity of an over-pressured bubble in UO_2”. In: *Journal of Nuclear Materials* 447 (2014), pp. 166–178 (cit. on pp. 101, 103, 104, 148, 166, 279).

[Nor29] F. H. Norton. *The creep of steel at high temperatures*. McGraw-Hill Book Company, Incorporated. (No. 35). 1929 (cit. on p. 315).

[OLA76] D. R. OLANDER. *Fundamental Aspects of Nuclear Reactor Fuel Elements*. TID-26711-P1 Technical Information Center, Office of Public Affairs - Energy Research and Development Administration. 1976 (cit. on pp. 62, 65, 147, 150, 181–183).

[OU01] D. R. Olander and P. Van Uffelen. “On the role of grain boundary diffusion in fission gas release”. In: *Journal of Nuclear Materials* 288 (2001), pp. 137–147 (cit. on pp. 51, 87, 88, 90, 169, 171).

[OW06] D.R. Olander and D. Wongsawaeng. “Re-solution of fission gas - A review: Part I. Intragranular bubbles”. In: *Journal of Nuclear Materials* 354 (2006), pp. 94–109 (cit. on pp. 48, 58, 62).

[Ono+20] C. Onofri, C. Sabathier, C. Baumier, et al. “Extended defect change in UO_2 during in situ TEM annealing”. In: *Acta Materialia* 196 (2020), pp. 240–251 (cit. on p. 158).

[Pas+13] G. Pastore, L. Luzzi, V. Di Marcello, et al. “Physics-based modelling of fission gas swelling and release in UO_2 applied to integral fuel rod analysis”. In: *Nuclear Engineering and Design* 256 (2013), pp. 75–86 (cit. on p. 137).

[Pas+23] G. Pastore, N. Militello, S. Blondel, et al. “Single-size and cluster dynamics modeling of intra-granular fission gas bubbles in UO_2”. In: *Journal of Nuclear Materials* 583.154453 (2023) (cit. on p. 137).

[Per+19] R. Perriot, C. Matthews, M W.D. Cooper, et al. “Atomistic modeling of out-of-pile xenon diffusion by vacancy clusters in UO_2”. In: *Journal of Nuclear Materials* 520 (2019), pp. 96–109 (cit. on pp. 136, 167–169).

[Pet86] N.L. Peterson. “Diffusion mechanisms and structural effects in grain boundaries”. In: *Journal of Vacuum Science & Technology A* 4 (1986), pp. 3066–3070 (cit. on p. 171).

[Pet83] L.R. Petzold. *Automatic selection of methods for solving stiff and nonstiff systems of ordinary differential equations*. SIAM J. Sci. Stat. Comput. 4, 136-148. 1983 (cit. on p. 73).

[R M91] H. Eberle R. Manzel. Proc. ANS/ENS Int. Top. Meet. On LWR Fuel Performance, Avignon, France, p. 528. 1991 (cit. on p. 86).

[RS50] W.T. Read and W. Shockley. “Dislocation models of crystal grain boundaries”. In: *Phys Rev* 78 (1950), p. 275 (cit. on p. 172).

[Res+19] J. Rest, M.W.D. Cooper, J. Spino, et al. “Fission gas release from UO2 nuclear fuel: A review”. In: *Journal of Nuclear Materials* 513 (2019), pp. 310–345 (cit. on pp. 14, 15, 49, 50, 58, 62, 86, 87, 119, 122).

[Rie86] H. Riedel. *Fracture at high temperatures*. Springer Berlin Heidelberg. Berlin, Heidelberg - 1987. 1986 (cit. on p. 315).

[RE86] C. Ronchi and P. T. Elton. “Radiation re-solution of fission gas in uranium dioxide and carbide”. In: *Journal of Nuclear Materials* 140 (1986), pp. 228–244 (cit. on p. 66).

[S K93] K. Nogita S. Kashibe K. Une. “Formation and growth of intragranular fission gas bubles in UO_2 fuels with burnup of 6-83 GWd/t”. In: *Journal of Nuclear Materials* 206 (1993), pp. 22–34 (cit. on p. 70).

[S Y66] T. Hirai S. Yajima H. Faruya. “Lattice and grain-boundary diffusion in UO_2”. In: *Journal of Nuclear Materials* 20 (1966), p. 162 (cit. on p. 176).

[Sab00] A.C.S. Sabioni. “Effect of grain-boundaries on uranium and oxygen diffusion in polycrystalline UO_2”. In: *Journal of Nuclear Materials* 278 (2000), pp. 364–369 (cit. on pp. 176, 177).

[SFM98] A.C.S. Sabioni, W.B. Ferraz, and F. Millot. “First study of uranium self-diffusion in UO_2 by SIMS”. In: *Journal of Nuclear Materials* 257 (1998), pp. 180–184 (cit. on pp. 173–175).

[SA10] D. Schwen and R.S. Averback. “Intragranular Xe bubble population evolution in UO_2 : A firts passage Monte Carlo simulation approach”. In: *Journal of Nuclear Materials* 402 (2010), pp. 116–123 (cit. on p. 63).

[Sch+09] D. Schwen, M. Huang, P. Bellon, et al. “Molecular dynamics simulation of intragranular Xe bubble re-solution in UO_2”. In: *Journal of Nuclear Materials* 392 (2009), pp. 35–39 (cit. on pp. 62, 64).

[Set+18] W. Setyawan, M.W.D. Cooper, K.J. Roche, et al. “Atomistic model of xenon gas bubble re-solution rate due to thermal spike in uranium oxide”. In: *Journal of Applied Physics* 124.075107 (2018). DOI: 10.1063/1.5042770 (cit. on pp. 16, 22, 41, 49, 58, 61–63, 67, 68, 71, 72, 74, 78, 80, 81, 83, 84, 100, 167, 258, 271–273).

[Sim+23] P.-C. A. Simon, L. K. Aagesen, Nathan Capps, et al. *Compare Predictions of Transient Fission Gas Release by Empirical and Mechanistic Models to Experiments in High-Burnup UO_2 Fuel*. INL/RPT-23-75026 Rev. 000. 2023 (cit. on p. 125).

[Sim+24] P.-C. A. Simon, K. Gamble, A. Pagani, et al. *Deployment of BISON models of fuel restructuring at high burnup and related fission gas behavior in UO_2*. Technical report: INL/RPT-24-81422-Rev000. 2024 (cit. on pp. 124, 137).

[SB74] M.V. SPEIGHT and W. BEERE. "Vacancy potential and void growth on grain boundaries". In: *Metal Science* 329 (1974), pp. 190–191 (cit. on pp. 19, 53, 137, 138, 141, 240).

[SP08] J. Spino and P. Peerani. "Oxygen stoichiometry shift of irradiated LWR-fuels at high burn-ups: Review of data and alternative interpretation of recently published results". In: *Journal of Nuclear Materials* 375 (2008), pp. 8–25 (cit. on p. 119).

[Ste62] H. Stehle. paper presented to Deutsche Gesellschaft für Metallkunde and Deutsche Keramische Gesellschaft, Baden-Baden (1962). 1962 (cit. on p. 160).

[Tho91] L.E. Thomas. *Condensed-phase xenon and krypton in UO_2 spent fuel*. Fundamental Aspects of Inert Gases in Solids, Ed by S.E. Donelly and J.H. Evans, Plenum Press, New York. 1991 (cit. on pp. 23, 134, 242).

[TMW14] A.E. Thompson, B. Meredig, and C. Wolverton. "An improved interatomic potential for xenon in UO_2: a combined density functional theory/genetic algorithm approach". In: *Journal of Physics: Condensed Matter* 26.105501 (2014) (cit. on p. 180).

[TC70a] A. Turnbull and R. M. Cornell. *Observations demonstrating the re-solution of gas from bubbles and sintering pores during the irradiation of UO_2 at a high temperature*. CEGB Report RD/B/N 1716. 1970 (cit. on p. 61).

[TH54] D. Turnbull and R.E. Hoffman. "The effect of relative crystal and boundary orientations on grain boundary diffusion rates". In: *Acta Metallurgica* 2 (1954), pp. 419–426 (cit. on p. 171).

[Tur71] J. A. Turnbull. "The distribution of intragranular fission gas bubble in UO_2 during irradiation". In: *Journal of Nuclear Materials* 38 (1971), pp. 203–212 (cit. on p. 62).

[Tur80] J. A. Turnbull. "A review of irradiation induced re-solution in oxide fuels". In: *Radiation Effects* 53 (1980), pp. 243–250 (cit. on pp. 271, 273).

[TC70b] J. A. Turnbull and R. M. Cornell. "The re-solution of gas atoms from bubbles during the irradiation of UO_2". In: *Journal of Nuclear Materials* 36 (1970), pp. 161–168 (cit. on pp. 58, 60, 166).

[TC71] J. A. Turnbull and R. M. Cornell. “The re-solution of fission-gas atoms from bubbles during the irradiation of UO_2 at an elevated temperature”. In: *Journal of Nuclear Materials* 41 (1971), pp. 156–160 (cit. on pp. 58, 60).

[Tur+82] J. A. Turnbull, C.A. Friskney, J. R. Findlay, et al. “The diffusion coefficients of gaseous and volatile species during the irradiation of uranium dioxide”. In: *Journal of Nuclear Materials* 107 (1982), pp. 168–184 (cit. on pp. 70, 166, 169, 265, 266).

[TK00] J. A. Turnbull and E. Kolstad. *Investigations on radioactive and stable gas release behaviour at the Halden reactor*. Fission gas behaviour in Water Reactor Fuels, Cadarache, France, 26-29 September. 2000 (cit. on p. 86).

[Uff00] P. Van Uffelen. “Modelling the variable precipitation of fission products at grain boundaries”. In: *Journal of Nuclear Materials* 280 (2000), pp. 275–284 (cit. on pp. 90, 93).

[Uff+11] P. Van Uffelen, G. Pastore, V. Di Marcello, et al. “Multiscale modelling for the fission gas behaviour in the TRANSURANUS code”. In: *Nuclear Engineering and Technology* 43 (2011), pp. 477–488 (cit. on pp. 48, 58).

[Vat14] E. Vathonne. “Etude par calcul de structure électronique des dégâts d’irradiation dans le combustible nucléaire $U0_2$: comportement des défauts ponctuels et gaz de fission”. PhD thesis. France: University of Aix-Marseille, 2014 (cit. on p. 179).

[VCN25] M. Vergani, M.W.D. Cooper, and L. Noirot. “A model for trapping and re-solution regarding intra-granular bubbles in UO_2, linked to atomic-scale simulations”. In: *Journal of Nuclear Materials* 605.155562 (2025) (cit. on pp. 5, 17, 49, 58, 61, 68, 72, 74, 77, 81, 239).

[Ver00] M. Verwerft. “Multiple voltage electron probe microanalysis of fission gas bubbles in irradiated nuclear fuel”. In: *Journal of Nuclear Materials* 282 (2000), pp. 97–111 (cit. on p. 193).

[Ves00] M. S. Veshchunov. “On the theory of fission gas bubble evolution in irradiated UO_2 fuel”. In: *Journal of Nuclear Materials* 277 (2000), pp. 67–81 (cit. on p. 65).

[VT13] M. S. Veshchunov and V. I. Tarasov. “Modelling of irradiated UO_2 fuel behaviour under transient conditions”. In: *Journal of Nuclear Materials* 437 (2013), pp. 250–260 (cit. on pp. 63, 77, 271, 272).

[VDB09] E. Vincent-Aublant, J-M. Delaye, and L. Van Brutzel. “Self-diffusion near symmetrical tilt grain boundaries in UO_2 matrix: A molecular dynamics simulation study”. In: *Journal of Nuclear Materials* 392 (2009), pp. 114–120 (cit. on pp. 176, 178).

[VKG79] C. Vitanza, E. Kolstad, and C. Graziani. *Fission Gas Release from UO_2 Pellet at High Burnup*. American Nuclear Society, Topical Meeting on Light Water Reactor Fuel Performance, Portland, Oregon. 1979 (cit. on p. 86).

[Whi04] R.J. White. “The development of grain-face porosity in irradiated oxide fuel”. In: *Journal of Nuclear Materials* 325 (2004), pp. 61–77 (cit. on pp. 86, 137, 176).

[WCB06] R.J. White, R.C. Corcoran, and P.J. Barnes. *A summary of swelling data obtained from the AGR/halden ramp test programme*. Tech. Rep. R&T/NG/EXT/REP/0206/02. 2006 (cit. on pp. 23, 242).

[YW23] L. Yang and B.D. Wirth. “Tilt grain boundary stability in uranium dioxide and effect on xenon segregation”. In: *Journal of Nuclear Materials* 577.154302 (2023) (cit. on pp. 179, 180).

[Zac+22] I. Zacharie-Aubrun, J. Noirot, R. Dowek, et al. “Restructuring in high burnup UO2 fuels: Experimental characterization by electron backscattered diffraction”. In: *Journal of Applied Physics* 132.195903 (2022) (cit. on pp. 14, 41, 49, 116–120, 123, 128, 188, 206, 239).

[ZPL23] G. Zullo, D. Pizzocri, and L. Luzzi. “The SCIANTIX code for fission gas behaviour: Status, upgrades, separate-effect validation, and future developments”. In: *Journal of Nuclear Materials* 587.154744 (2023) (cit. on p. 122).

APPENDICES

A. Definition and glossary of the variables used in this manuscript

A.1. Definition

MARGARET characterizes the gas and micro-structure situation by means of a series of mathematical variables. Variables are denominated obeying to the following nomenclature. C means a concentration per / m^3 of initial fuel. The index Xe means that the variable deals with fission gas (Xe + Kr in reality). The index cav is for any type of cavities (bubbles or as-fabricated pores). The index b is for bubble. The index por is for the as-fabricated pores. The index j is for grain boundary (preferred to gb to avoid confusion with the b of bubble). The index jsd is for the boundaries of subdomains. The index $bprecjsd$ is dedicated to the second intra-granular bubble population of the precipitation area, because these bubbles are located on the boundaries of subdomains (See Section 1.3.2). The index v (for vented) is used for the inter-granular bubbles connected with the outside. For example, C_{Xebjv} is the concentration of fission gas in inter-granular bubbles connected with the outside.

In the analyses made in chapter 7, we sometimes have called “bulk bubbles” the bubbles that are surrounded by crystal, that is to say, the intra-granular bubbles of sound grains or the bubbles inside the subdomains. This population is always the population designed by the index “b”.

The volumetric quantities in the ODE system are always reduced to m^3 of fresh fuel. They are therefore not to be confused with local concentrations in the "sound" zones only or in the restructured zones only of the "under restructuring" state.
The local volumetric values inside "sound" zones = Global value (per m^3 of fresh fuel) / (1-fr), where fr is the fraction of restructured volume.
The local volumetric values inside Restructured zones = Global value (per m^3 of fresh fuel) / fr, where fr is the fraction of restructured volume.

Moreover, throughout the manuscript, there will be a constant switch between local concentrations, useful to describe physical phenomena, like the concentration of Xenon on the grain boundary in [mol / m^3 of grain boundary], C^{loc}_{Xej}, and global concentrations, like the concentration of Xenon on the grain boundary in [mol / m^3

of fresh fuel], C_{Xej}, used in the ODE system. A clear distinction between those two different concentrations is highlighted in the text.

A.2. Glossary of the main variables and parameters

Variable [unit of measure]	**Meaning**	**Notes**
A_{gg} [m]	Radius of the "sound" grain.	
A_{pg} [m]	Radius of the HBS grain.	
A_{sd} [m]	Radius of the subdomain.	
$b_x(y)$ [s^{-1}]	Re-solution frequency of gas used in the ODE system, with x = arrival location, and y = departure location. Moreover, when x = grain or bulk, x is omitted.	$b(cav)$, for small bubbles, is equal to b^{mod} defined in Chapter 2 (eq. 2.21). For bigger bubbles, b^{MD} in eq. 2.21 (the value of b^{MD} comes from [Setyawan et al. 2018]) is substituted by the more general expression derived in Appendix E. $b(b)$ (the re-solution frequency from bulk bubbles) consider also the possibility of bubble destruction by fission spikes. For bubbles at GBs and SDBs, we start by calculating the total re-solution frequency, called $b^{MD_Veshchunov}(y)$ (where y is either "cavj" or "cavjsd". See Section 3.2.4 for a more detailed explanation in the case of bubbles on GBs), and then we distribute the re-dissolved gas atoms to the different locations (GB, bulk etc.) following Section 3.2.5. Finally, we correct the resulting values following Section 3.2.7. $b(j)$, the re-solution frequency of gas dissolved in the grain boundary towards the grain, is estimated in Section 3.2.6.

b^{mod} [s^{-1}]	Modified re-solution frequency to be used by FGR models, like MARGARET, to take into account that gas atoms are re-dissolved near the cavities.	It is used to calculate $b(cav)$. See Chapter 2.
b^{MD} [s^{-1}]	Re-solution frequency calculated by Molecular Dynamics.	See Chapter 2.
$C_{xy}^{eq}(z)$ [mol / m^3]	Equilibrium concentration of the specie x (x = gas atoms, Xe, or vacancies, v) in the medium y (bulk, GB, SDB) in equilibrium with the medium z (intra-granular, inter-granular and inter-subdomain cavities, GB, SDB, exterior). When y = grain or bulk, y is omitted.	
$coe_{y->z}$ [/]	Adjustment parameters used to calculate the re-solution frequency of gas from the medium y (inter-granular or inter-subdomain cavities, GB or SDB) towards the medium z (GB, SDB or bulk).	See Section 3.2.7.
D_{xy} [m^2/s]	Diffusion coefficient of the specie x in the medium y. When y = grain or bulk, y is omitted. For example, D_{Xej} is the diffusion coefficient of Xenon at the GB.	For the diffusion of species (x = gas atoms, Xe, or vacancies, v) at the grain boundaries, in MARGARET we make the hypothesis that $D_{xj}^{MAC} \approx D_{xj}^{loc}$ (see Section 3.2.1). D_{xj} is then used with the meaning of both "local" (actual diffusion coefficient in the medium) and "global" (macroscopic diffusion coefficient in the homogeneous medium) variable. For the diffusion of species (x = gas atoms or vacancies) at the subdomain boundaries, in MARGARET we make the hypothesis that $D_{xjsd}^{MAC} \approx \frac{1}{2} D_{xjsd}^{loc}$ (see Section 7.1.3). We have then chosen to make D_{xjsd} synonymous of D_{xjsd}^{MAC}.

dNML [m]	Width of the lattice region around the bulk cavities where the Xenon atoms are quickly trapped by the cavities, much faster than how they would do by bulk diffusion.	See Chapter 2.
e_{pj} [m]	Width of the GB and SDB.	
F_x [/]	Fraction of the "sound" or HBS grain surface, or fraction of the subdomain surface that face the x element (bare grain boundary, cavity, exterior etc.). For example, F_{bj} is the fraction of the surface of the grain that faces the inter-granular bubbles.	See Section 3.2.2 for the "sound" grains and Appendix G.2.1 for the subdomains. It is not to be confused with the free energy, used in Section 3.2.8.
F'_x [/]	Fraction of the grain or subdomain boundary surface occupied by the x element (either bare grain boundary or one of the population of GB or SDB cavities).	See Section 3.2.2 for the "sound" grains (a similar derivation can be done for both HBS grains and subdomains).
fr [/]	Fraction of the volume of the grain that is restructured (HBS).	It is also equal to the fraction of the surface of the grain involved in the HBS (see Section 3.2.2).
$GEOM2^{mod_Olander}$ [m^{-2}]	Geometric term, function of R_{cav} (the radius of the cavities) and C_{cav} (the cavity density [cav / m^3 of fresh fuel]). It is used to calculate the flux of dissolved Xe atoms in the bulk towards the bulk cavities.	See Chapter 2. In Appendix G, it is named $geom_{cav}$ to be coherent with the term $geom_{cavj}$.
$geom_{cav}$ [m^{-2}]	Geometric term, function of R_{cav} (the radius of the cavities) and C_{cav} (the cavity density [cav / m^3 of fresh fuel]). It is used to calculate the flux of dissolved Xe atoms in the bulk towards the bulk cavities.	See Appendix G. In Chapter 2, it is named $GEOM2^{mod_Olander}$.
$geom_{cavj}$ [m^{-2}]	Geometric term used to calculate the flux of both dissolved Xe atoms and vacancies at the GB and SDB towards the inter-granular and inter-subdomain cavities.	See eq. 3.12.
K_y [m^{-1}]	Curvature of the y cavity.	$K_y = 2 \times \left(\frac{R_y}{sin(\theta)}\right)^{-1}$, where R_y is the radius of the y cavity.

P_{Hydro} [Pa]	Hydrostatic pressure in the material in the point where MARGARET is running.	It is an input parameter for MARGARET. Its value is calculated by ALCYONE.
$P_{int}(y)$ [Pa]	Pressure of the gas inside the y population of cavities	
$P_{surf}(y)$ [Pa]	Pressure of the gas inside the y population of cavities minus the Laplace pressure (γK_y).	
$S^{vol}_{j,tot}$ [m^2 of GB / m^3 of fresh fuel]	Surface of the grain boundary (which is the surface of the grain covered by cavities or by bare grain boundary) over the volume of the grain.	See eq. 3.2 (a similar derivation can be done for both HBS grains and subdomains).
T_{high} [K]	Parameter used in eq. 4.1 to calculate τ_{eff}.	
T_{low} [K]	Parameter used in eq. 4.1 to calculate τ_{eff}.	
V_{at} [m^3 / atom]	Volume per atom in a cavity.	In this manuscript, it is usually expressed in [Ω / atom].
v_{move} [m / s]	Velocity by which two grains that share a grain boundary move away one from the other due to the formation of vacancies on the grain boundary.	See Section 5.2.1.
$\beta_{v,j}$ [Vacancies / m^3 of fresh fuel / s]	Rate of production of vacancies per m^3 of fresh fuel.	See Section 5.2.1.
γ [J / m^2]	Surface tension gas / UO_2.	
γ_j [J / m^2]	Surface energy of the grain boundary, also called surface tension UO_2 / UO_2 [1].	$\gamma_j = 2\gamma cos\theta$ (see eq. 3.70 and Figure 3.8).
ε_{xy} [eV]	Formation energy of the specie x (x = gas atoms, Xe, or vacancies, v) in the medium y. When y = grain or bulk, y is omitted.	
$\varepsilon_{Seg,xy}$ [eV]	Segregation energy of the specie x (x = gas atoms, Xe, or vacancies, v) in the medium y (GB or SDB). When y = GB, y can be omitted.	

1. In [Borde et al. 2021] it is called Formation energy of the GB.

ζ [/]	It has two meanings, depending on the context: 1) Fraction of the electronic stopping power deposited to the UO_2 lattice by a fission fragment (alternative definition: ratio between the thermal spike energy and the total electronic stopping power). 2) Adimensional parameter (that multiplies Ω) used to determine the volume contribution to the cavities given by the trapping and resolution of Xe atoms.	For 1): see Chapter 2. For 2): see Section 5.1.4.3.
θ [°]	Angle between the cavity surface and the GB or SDB.	It is not used in the case of bulk bubbles, because they are considered spherical ($\theta = 90°$).
$\mu_{v,y}$ [eV / atom]	Chemical potential of the vacancies in the medium y.	
$\mu_{v,y/z}$ [eV / atom]	Chemical potential of the vacancies in the medium y, in equilibrium with the medium z.	See eq. 5.17.
ν_p (or ν_{Xe}) [s^{-1}]	Vibration frequency of Xenon in the bulk.	
ν'_p (or ν_{Xej}) [s^{-1}]	Vibration frequency of Xenon at the GB.	
τ_{eff} [GWd/t_U]	It is the burnup built up in the $[T_{low}, T_{high}]$ range, in the point where MARGARET is running.	It is used as a condition to determine when the subdomains appear. See Section 4.1.4.
$\Phi_{v,y->z} = -\Phi_{v,z->y}$ [Vacancies / m^3 of fresh fuel / s]	Vacancy flux from the medium y (GB, SDB, bulk) to the medium z (bulk cavities, inter-granular cavities, inter-subdomain cavities, exterior) due to the difference in the chemical potential of the vacancies on the medium y far from the medium z and the same chemical potential near the medium z.	
Ω [m^3]	Volume of a Schottky defect (UO_2 site missing, equal to 40.9×10^{-30} m^3).	

B. Version of MARGARET discussed in the current manuscript

The version of MARGARET described in this thesis manuscript has been built as a separate "branch" with respect to the version of MARGARET used as a default in ALCYONE.
The name of this branch is th_M_VERGANI.
The objective is to replace the current default version of MARGARET with the one described in these pages.

C. Thermal and irradiation vacancies

Below a certain temperature (during base irradiation), vacancies produced by irradiation dominate over equilibrium vacancies. We can demonstrate this using the thermal and mix diffusion coefficient of Xe.
An evaluation of the thermal diffusion coefficient has been performed by Davies and Long Davies et al. 1963, while an evaluation of the irradiation-enhanced diffusion coefficient has been obtained by Turnbull J. A. Turnbull, Friskney, et al. 1982. If we use the relation between the diffusion coefficient and the jump frequency, we find $D_{Xeth} = s^2 j_{Xe} C_v^{eq}$ and $D_{Xemix} = s^2 j_{Xe} C_v^{irr}$, where s is the jump distance, j_{Xe} is the jump frequency of Xenon from a vacancy site to a near vacancy site, C_v^{eq} is the vacancy concentration at equilibrium in the bulk (with $P = 0$), in fraction of sites, and C_v^{irr} is the vacancy concentration in fraction of sites due to irradiation, and resulting from the equilibrium between production/ recombination/interactions with the different traps.
The fraction C_v^{irr}/C_v^{eq} can be calculated as a function of T and $\dot{F}$:

$$\frac{C_v^{irr}}{C_v^{eq}} = \frac{1.7\,10^{-25}\sqrt{\dot{F}}exp\left(\frac{-1.197eV}{kT}\right)}{7.6\,10^{-10}exp\left(\frac{-3.04eV}{kT}\right)} = 2.237\,10^{-16}\sqrt{\dot{F}}exp\left(\frac{+1.843eV}{kT}\right) \tag{C.1}$$

The order of magnitude of $\dot{F}$ is typically $10^{19}\ fissions/m^3/s$, which allows to obtain :

$$\frac{C_v^{irr}}{C_v^{eq}} = 7.074\,10^{-7}exp\left(\frac{+1.843eV}{kT}\right) = 7.074\,10^{-7}exp\left(\frac{21368}{T}\right) \tag{C.2}$$

Below $1508K = 1235°C$**, irradiation vacancies predominate, while the thermal behavior prevails above.**

We can now write a simple model for defects:

$$\frac{dC_v}{dt} = G - RC_iC_v \tag{C.3}$$
$$- \sum_{cav} 4\pi R_{cav} C_{cav} D_v \left(C_v - C_v^{eq}(P_{cav} - \frac{2\gamma}{R_{cav}}) \right) - T_v^{disloc}$$
$$- \frac{15}{A_g^2} D_v \left(C_v - C_v^{eq}(j) \right)$$
$$\frac{dC_i}{dt} = G - RC_iC_v \tag{C.4}$$
$$- \sum_{cav} 4\pi R_{cav} C_{cav} D_i \left(C_i - C_i^{eq}(P_{cav} - \frac{2\gamma}{R_{cav}}) \right) - T_i^{disloc}$$
$$- \frac{15}{A_g^2} D_i \left(C_i - C_i^{eq}(j) \right)$$

Where defect production and short range recombination is on the first line, trapping by bubbles and dislocations on the second line, and trapping by the grain surface is on the third line. $C_v^{eq}(P_{cav} - \frac{2\gamma}{R_{cav}})$ is the vacancy concentration in the crystal at the vicinity of a cavity (bubble or fabrication pore) of inner pressure P_{cav} and radius R_{cav} (curvature $\frac{2}{R_{cav}}$). $C_v^{eq}(j)$ is the vacancy concentration in the crystal at the vicinity of the grain surface (hydrostatic pressure, no curvature).

The expected behavior of point defects, if we follow the assumptions behind Turnbull's second term, should be as follows:

— Turnbull J. A. Turnbull, Friskney, et al. 1982 suggests that, in the range where irradiation vacancies predominate ($T < 1235°C$), we are in a near-permanent regime where concentrations of vacancies and interstitials are mostly determined by the terms G and RC_iC_v. In this case $C_v^{irr} \simeq C_i^{irr}$ is proportional to the square root of the fission rate. It means that D_v and D_i are too low for the trapping by extended defects to have an influence. In this situation the bubbles may remain out of equilibrium.

— In the range where thermal vacancies prevail ($T > 1235°C$) the point defects given by irradiation recombine between themselves even more easily and the terms linked to the exchange of vacancies between the grain surface and the bubbles predominate and have to balance out. The system tends to $C_v = C_v^{eq}(j) = C_v^{eq}(P_{cav} - \frac{2\gamma}{R_{cav}})$, that is to say, the bubbles tend to the equilibrium.

In connection with Chapter 2 and Turnbull's approach to measure the re-solution frequency, we can finally see how a temperature of $1200°C$ is very close to the estimated point where irradiation vacancies and thermal vacancies have the same value. Therefore, no clear statement regarding the equilibrium of bubble at that temperature can be drawn.
In connection with Chapter 5, this appendix justifies that for rods in base irradiation,

where the temperature remains below 1200°C, thermal vacancies do not prevail.

D. OLANDER model implies a flat re-solution profile

If we consider a bubble of radius R_b surrounded by a solid of radius R_{ext}, and if we suppose that the re-solution profile around the bubble is flat, then the re-solution may be modeled as a constant source term $\beta_r = bC_{Xeb}$, where b is the re-solution frequency (s^{-1}) and C_{Xeb} is the gas content of the bubble divided by the volume of the solid [mol/m^3]. If many identical bubbles are in a solid, we can relate their density (in [bubbles / m^3 of solid]) with R_{ext} and R_b by the equation:

$$C_b = \frac{1}{\frac{4}{3}\pi\left(R_{ext}^3 - R_b^3\right)} \tag{D.1}$$

We solve the diffusion equation in the solid around the bubble with the limit condition $C_{Xe}(R_b) = 0$ and $\left.\frac{dC_{Xe}}{dr}\right|_{r=R_{ext}} = 0$ (for symmetry reason):

$$D_{Xe}\nabla^2 C_{Xe} + \beta_r = 0 \tag{D.2}$$

The solution is:

$$C_{Xe}(r) = \frac{\beta_r}{6D_{Xe}}\left(R_b^2 - r^2 + \frac{2R_{ext}^3}{R_b} - \frac{2R_{ext}^3}{r}\right) \tag{D.3}$$

The mean of $C_{Xe}(r)$ is equal to:

$$\begin{aligned} C_{XeM} &= \frac{\int_{R_b}^{R_{ext}} C_{Xe}(r) 4\pi r^2 dr}{\frac{4\pi}{3}(R_{ext}^3 - R_b^3)} \\ &= \frac{\beta_r}{6D_{Xe}}\left[\frac{R_b^3 + 2R_{ext}^3}{R_b} - \frac{3}{5}\frac{R_{ext}^5 - R_b^5}{R_{ext}^3 - R_b^3} - \frac{3}{2}\frac{R_{ext}^3(R_{ext}^2 - R_b^2)}{R_{ext}^3 - R_b^3}\right] \end{aligned} \tag{D.4}$$

When $R_{ext} \gg R_b$, we have:

$$\begin{aligned} C_{XeM} &\approx \frac{\beta_r R_{ext}^3}{3D_{Xe}R_b} \\ C_{Xe}^{far} &= C_{Xe}(R_{ext}) \approx \frac{\beta_r R_{ext}^3}{3D_{Xe}R_b} \end{aligned} \tag{D.5}$$

Where the second equality comes from eq. D.3.

D. OLANDER model implies a flat re-solution profile –

Using eq. D.1, we find:

$$4\pi R_b D_{Xe} C_b C_{XeM} \approx 4\pi R_b D_{Xe} C_b C_{Xe}^{far} \approx \beta_r = b C_{Xeb} \tag{D.6}$$

So, we find what we have named the "Olander" model of trapping and re-solution $4\pi R_b D_{Xe} C_b C_{XeM}$ / $b C_{Xeb}$.
Hence, this model is consistent with a flat re-solution profile in the volume around the bubble.

E. Expression of the re-solution frequency as a function of the radius of the cavities

If we want to calculate the rate of re-solution of Xenon atoms from intra-granular bubbles, we need an expression of the re-solution frequency, b[1].

Different expressions of b as a function of the radius of the bubble have been proposed in literature [Setyawan et al. 2018; Losonen 2017; Veshchunov and Tarasov 2013; J. A. Turnbull 1980].

For small bubbles, the most trustful expression present in literature seems Setyawan's one [Setyawan et al. 2018], which is derived using Molecular Dynamics (see figure 2.1). However, this expression cannot be used with confidence for large bubbles, since it is obtained by fitting the results of MD calculations using bubbles with a radius between 0.6 and 3 [nm].

In Losonen's paper [Losonen 2017], we find the following expression for b:

$$b = \frac{3(R_b + R_f)^2 \lambda M N_{res}}{2\rho R_b^3 N_A} \times \dot{F} \tag{E.1}$$

which goes as $\approx \frac{A}{R_b}$ for big bubbles (where A is equal to $\frac{3\lambda M N_{res}}{2\rho N_A}$). In the expression above, R_f is the radius of a fission spike $[m]$, M is the molar mass of Xenon $[g/mol]$, λ is the fission fragment range $[m]$, N_{res} is the average number of gas atoms removed from a bubble in one encounter with a fission fragment, ρ is the gas density in the bubble $[g/m^3]$, N_A is the Avogadro's constant and $\dot{F}$ is the fission rate.

In Veshchunov's paper [Veshchunov and Tarasov 2013], we can find two main expressions for b: one that considers backward diffusion and the spatial distribution of the re-soluted gas, and one that does not. Following what we have written in the previous Sections, we can consider the first expression as referring to b^{mod}, while the second to b. The expression in which we are interested here is the latter (eq. 19 of the article [ibid.]):

1. In the sense of b^{MD}, following what we have written in Chapter 2

E. Expression of the re-solution frequency as a function of the radius of the cavities –

$$b = b_0 \left(\frac{4}{3}\pi R_b^3 - \frac{4}{3}\pi (R_b - d)^3 \right) \left(\frac{4}{3}\pi R_b^3 \right)^{-1} \approx b_0 \frac{3d}{3d + R_b} \tag{E.2}$$

In fact, using the model that we have developed in Section 2.3.2 (PHI-R5-NML-V), we know how to link b to the modified re-solution frequency, b^{mod}, that we need to use inside fission gas release codes such as MARGARET.
Equation E.2[2] is derived supposing that only atoms situated in a thin layer close to the surface can be re-dissolved.
In the above expression, in the article [Veshchunov and Tarasov 2013], $d \approx 1 - 1.5\ nm$ is the critical distance from the bubble surface where gas atoms may be re-dissolved by an encounter with a fission spike and $b_0 \approx (2-3) \times 10^{-23}\ [m^3]$ is a parameter.
This expression has been developed considering the homogeneous re-solution as the main phenomenon causing re-solution of gas atoms in the bubbles. However, we can apply it also if the main cause of re-solution are fission spikes. In fact, the work of Setyawan and coworkers [Setyawan et al. 2018] showed how fission spikes are not able to re-dissolved entirely small bubbles of the order of few nanometers. Therefore, it is plausable to assume that, for bigger bubbles, the atoms far from the surface could not be re-dissolved by a fission spike. Moreover, since the radius of the fission spike is ≈ 4 nm [ibid.], for big bubbles the fission spikes would always interact with only a portion of the bubble, keeping the overall reasoning intact.

We can note how both Losonen and Veshchunov's expression goes as $\approx C/R_b$ for big bubbles, where C is a constant that changes between the two expressions. In case of Losonen's expression, C depends on the density of the gas in the bubbles. However, in Setyawan's article [ibid.] it seems that b is independent of the density of the bubbles: *"the results suggest that the re-solution probability does not depend on gas density"*.
Therefore, for big bubbles, we choose to use Veshchunov's expression (eq. E.2), using b_0 as a parameter of MARGARET.

Now, we need to construct a continuous expression that can be used for all the values that R_b can assume.
For small bubbles, until $R_b = 15\ nm$, we can use Setyawan's expression. For bubbles with R_b bigger than 20 nm we use Veshchunov's expression (eq. E.2). For bubbles in between, we decided to use a linear interpolation between Setyawan's expression at $R_b = 15\ nm$ and Veshchunov's expression at $R_b = 20\ nm$. The boundary between the two expressions is somewhat arbitrary and can be changed, if needed.

Finally, we can determine the new value of the b_0 parameter with the intent of obtaining a "smooth" transition in the range $15\,nm < R_b < 20\,nm$ between Setyawan's expression and Veshchunov's expression. If, for example, we multiply $b_0 = 2 \times 10^{-23}$

2. The expression would give: $b = b_0 \frac{3d}{R_b}\left(1 - \frac{d}{R_b} + \frac{d^2}{3Rb^2}\right)$. If, for big bubbles, we neglect $\frac{d^2}{3Rb^2} << 1$, we obtain $b = \frac{b_0 3d}{R_b + d} \approx \frac{b03d}{Rb}$. Since, instead, for $R_b < d$, b have be be equal to b_0, Veshchunov has introduced the 3 that multiplies d at the denominator.

$[m^3]$ by 2.2, we obtain a quite "smooth" transition between Setyawan's expression with $\zeta = 0.85$ and Veshchunov's expression, as it can be seen in figure E.1.

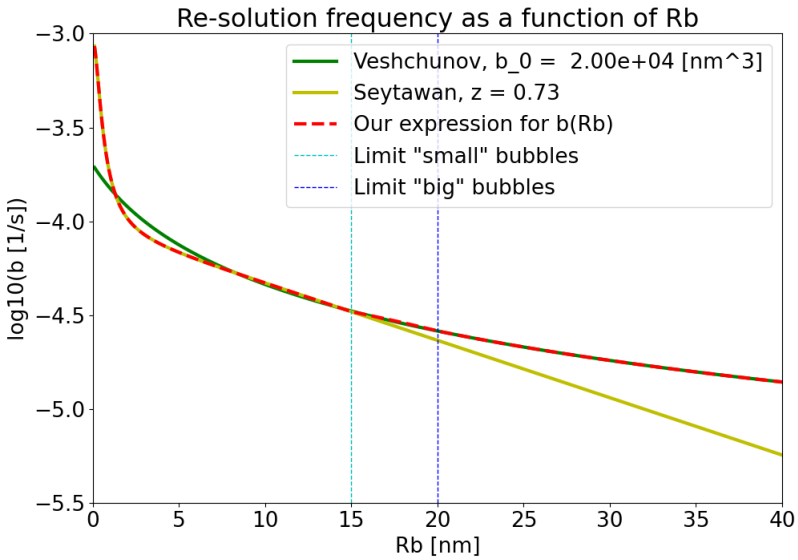

Figure E.1. – Example of the re-solution function to be included in MARGARET.

Regarding the possibility of total destruction of bubbles by fission spikes, phenomenon invoked by some authors [J. A. Turnbull 1980], Setyawan and colleagues [Setyawan et al. 2018], in their work, did not find any evidence of such an occurrence. However, there are not enough evidence to discard entirely this phenomenon for very small bubbles. Therefore, we keep the description of the total destruction of bubbles by fission spikes presented in [L. Noirot 2011], which applies only to very small intra-granular bubbles.

Given the absence in literature of expressions of re-solution frequency derived specifically for bubbles on grain boundaries or on dislocations, the expression of b just described will be also used as a starting point to determine the re-solution frequency of inter-granular bubbles and precipitation bubbles (see Section 3.2.4).

F. Derivation of the defects equilibrium concentrations in the bulk near an inter-granular bubble by considering the GB as a surface without associated volume

We call s the number of normal sites in the lattice, v the number of Schottky defects in the lattice, x the number of gas atoms inside the bubble, p the number of Xenon atoms in a Schottky defect in the lattice, n the volume of the bubble divided by Ω (which represents the amount of Schottky defects that compose the bubble). We are not interested here in the concentration of interstitials.
A schematic representation of the problem can be seen in figure F.1.

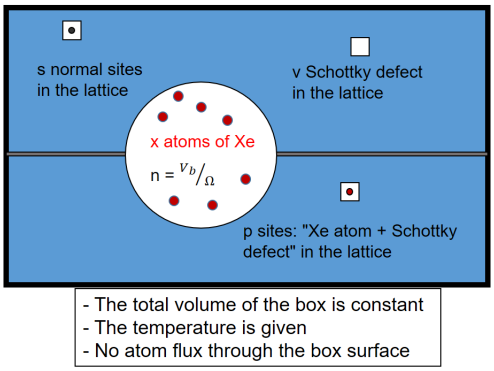

Figure F.1. – Schematic representation of the problem used to derive the equilibrium concentration of defects on the grain boundary near an inter-granular cavity, considering the GB as a surface without associated volume.

Using those definitions, we can write:

F. Derivation of the defects equilibrium concentrations in the bulk near an inter-granular bubble by considering the GB as a surface without associated volume –

$$\begin{aligned} s &= A\,[Total\ number\ of\ Uranium\ atoms] \\ p+x &= G\,[Number\ of\ gas\ atoms] \\ n+(v+s+p) &= \frac{L^3}{\Omega} \end{aligned} \tag{F.1}$$

Where A and G are constants, because A is equal to the number of Uranium atoms.

We have 5 unknowns and 3 equations. Therefore, we can choose 2 variables as the 'true' variables of the problem, for example v and p, and consider the other 3 variables as directly related to those.
From the equations F.1 we can write:

$$\begin{aligned} ds &= 0 \\ dp+dx &= 0 \\ dn+dv+dp &= 0 \end{aligned} \tag{F.2}$$

The total free energy of the system can be written as:

$$F = F_b + F_S + F_L + F_{SGB} \tag{F.3}$$

Where F_b is the free energy of the bubble (excluding the energy of the surface of the bubble), F_S is the free energy of the surface of the bubble, F_L is the free energy of the lattice, F_{SGB} is the free energy of the grain boundary surface (In Section 3.2.8, F_{SGB} was counted inside $F_{L'}$).

We can then write, using eq. 3.32 to relate R_{bj} and dn:

$$dF_b = -P_b\Omega dn - \mu dx \tag{F.4}$$

$$dF_S = \gamma \frac{B_\theta}{A_\theta}\frac{2\Omega}{R_{bj}}dn \tag{F.5}$$

$$F_{SGB} = (L^2 - \pi R_{bj}^2)\gamma_j \tag{F.6}$$

$$\begin{aligned} dF_{SGB} &= -2\pi R_{bj} dR_{bj} \times \gamma_j \\ &= \frac{-\Omega}{2A_\theta R_{bj}} dn \times \gamma_j \end{aligned} \tag{F.7}$$

Following the same reasoning as in Section 3.2.8, F_L can be written as:

F. Derivation of the defects equilibrium concentrations in the bulk near an inter-granular bubble by considering the GB as a surface without associated volume –

$$\begin{aligned} F_L = s\varepsilon_0 + v\varepsilon_v + p\varepsilon_p - kT\left((s+v+p)ln(s+v+p) - sln(s) - vln(v) - pln(p)\right) \\ - kT \times p \times ln(\mathcal{V}_{pp}) - kT \times s \times ln(\mathcal{V}) \end{aligned} \tag{F.8}$$

To find the equilibrium concentrations, we need to verify the following relations:

$$\begin{aligned} \frac{dF}{dp} &= 0 \\ \frac{dF}{dv} &= 0 \end{aligned} \tag{F.9}$$

The first relation gives the following:

$$\frac{dF}{dp} = P_b\Omega - \mu - \gamma\frac{B_\theta}{A_\theta}\frac{2\Omega}{R_{bj}} + \frac{\Omega}{2A_\theta R_{bj}} \times \gamma_j + \varepsilon_p + kTln\left(\frac{p}{s+p+v}\right) - kTln(\mathcal{V}_{pp}) = 0 \tag{F.10}$$

Using the fact that $\gamma_j = 2cos(\theta) \times \gamma$ and $\frac{2B_\theta - cos(\theta)}{A_\theta} = 2sin(\theta)$:

$$x_p^{eq} = exp\left[-\frac{1}{kT}\left[\varepsilon_p - \mu + \Omega\left(P_b - \gamma K_{bj}\right)\right]\right] \times \mathcal{V}_{pp} \tag{F.11}$$

Where $\left(K_{bj}\right)^{-1} = \frac{R_{bj}}{sin(\theta)}$ is the curvature radius of the bubble.

The second relation gives:

$$\begin{aligned} \frac{dF}{dv} = P_b\Omega - \gamma\frac{B_\theta}{A_\theta}\frac{2\Omega}{R_{bj}} + \frac{\Omega}{2A_\theta R_{bj}} \times \gamma_j + \varepsilon_v + kTln\left(\frac{v}{s+p+v}\right) = 0 \\ x_v^{eq} = exp\left[-\frac{1}{kT}\left[\varepsilon_v + \Omega\left(P_b - \gamma K_{bj}\right)\right]\right] \end{aligned} \tag{F.12}$$

Both the expressions for x_p^{eq} and x_v^{eq} are the same as the one derived in Section 3.2.8.

G. Detailed description of the subdomains in MARGARET

In the next sections, I present the variables used in the subdomain state, their associated ODE and the relations used to find the quantities present in those equations. Some of the terms present in the equations have not changed during the thesis. To avoid loosing the reader, these terms are only referenced, but not fully reported.

G.1. Equations of the evolution of the ODE variables in the subdomain state

G.1.1. Intra-subdomain

Initial conditions

When we switch from the "sound" to the subdomain state, the amount of gas dissolved is conserved and the intra-granular bubble population becomes the intra-subdomain population.

Intra-subdomain dissolved gas:

$\frac{dC_{XeM}}{dt} =$	Only one variable is considered, which has the meaning of the average concentration of dissolved gas in the subdomains.
β_c	Gas production. $\beta_c\,(mol/m^3/s)$ is the production rate of Xenon.
$-\frac{15D_{Xe}}{A_{sd}^2}(C_{XeM}-C_R)$	Diffusion of dissolved gas in the grain. See Section G.3.
Bubbles nucleation	Same expression as for the "sound" state. See [L. Noirot 2011]
$-geom_{cav}D_{Xe}$ $\times(C_{XeM}-C_{Xe}^{eq}(cav))$	Gas trapping in the intra-subdomain bubbles. For $C_{Xe}^{eq}(cav)$ see [L. Noirot 2014]
$+b(cav)\times C_{Xecav}$	Re-solution of gas from the cavities

A_{sd} is the radius of the subdomains, $D_{Xe}\,[m^2/s]$ is the diffusion coefficient of the gas

in the solid, C_R is boundary condition at the limit of the sphere that represents the subdomain, $geom_{cav}$ $[m^{-2}]$ is a geometric term calculated in function of R_{cav} (the radius of the cavities) and C_{cav} (the cavity density [cav / m^3 of fresh fuel]), $C_{Xe}^{eq}(cav)$ is the concentration of Xenon in equilibrium with an intra-subdomain bubbles ($C_{Xe}^{eq}(cav) \approx 0$ because Xenon is practically insoluble in the lattice), $b(cav)$ is the re-solution frequency of intra-subdomain bubbles.
$geom_{cav}$ is what we have called $GEOM2^{mod_Olander}$ in Chapter 2. $b(cav)$ comes from Chapter 2.

CONSIDERED CAVITIES :
We consider only one population of cavities in the subdomains.

CONDITIONS TO THE LIMIT OF THE SPHERE :
The sphere boundary condition C_R depends on the different inter-subdomain populations (inter-subdomain bubbles and pores), their fractional coverage of the subdomain (see Section G.2.1), and the frequencies of re-solution (re-dissolved gas from the inter-subdomain bubbles and pores and from the subdomain boundaries to the subdomain). See Section G.3 for the calculation of C_R in the subdomain state.

Intra-subdomain bubbles:

$\frac{dC_{cav}}{dt} =$	
Bubble nucleation	Same expression as for the "sound" state. See [L. Noirot 2011]
Geometric coalescence	Same expression as for the "sound" state. See [L. Noirot 2011]
Cavity destruction by fission spikes	Same expression as for the "sound" state. See [L. Noirot 2011]
$-H(cav)C_{cav}$	Loss of bubbles as they leave the subdomain. This term is active only at high temperature and depends on the radius of the subdomains, A_{SD}. See Chapter 6.

Gas contained in intra-subdomain bubbles :

$\frac{dC_{Xecav}}{dt} =$	
Contribution through the nucleation	Same expression as for the "sound" state. See [L. Noirot 2011]
$+geom_{cav}D_{Xe}(C_{XeM} - C_{Xe}^{eq}(cav))$	Trapping of dissolved gas in the cavities
$-b(cav)C_{Xecav}$	Re-solution of gas from the cavities (with or without cavity destruction)
$-H(cav)C_{Xecav}$	Gas loss when intra-subdomain bubbles leave the subdomain due to the movement of the bubbles at hight temperatures. It depends on A_{SD}. See Chapter 6.

In base irradiation, the trapping and re-solution terms quickly reach a balance, and the terms in H_{cav} is negligible because bubbles are almost immobile.

Volume of the intra-subdomain bubbles:

$\frac{dV_{cav}}{dt} =$	
$[Nucleation\,term$ $+geom_{cav}D_{Xe}(C_{XeM} - C_{Xe}^{eq}(cav))$ $-b_{Xe}(cav)C_{Xecav}] \times \zeta\Omega N_{Avogadro}$	Volume contribution accompanying the gas atoms themselves.
Decrease in volume accompanying Cavity destruction	Same expression as for the "sound" state. See [L. Noirot 2011].
$\frac{dV_{cav}}{dt}\Big\vert_{vac}$	Flux of volume due to thermal vacancies. See Chapter 5.
$-H(cav)V_{cav}$	Loss of volume when intra-subdomain bubbles leave the subdomain

Concerning the first term, see Section 5.1.5.

$b_{Xe}(cav)$ represents the gas re-solution frequency without cavity destruction and is equal to b^{MOD} defined in Chapter 2.

Volume of the solid (crystal):

The equation is unchanged compared to [L. Noirot 2011].
Note that the dissolved Xe atoms are always supposed to occupy a volume Ω.

G.1.2. Inter-subdomain

In the boundary between subdomains, we consider the dissolved gas, as well as two populations of cavities, namely the precipitation bubbles, $bprecjsd$, and the intra-granular pores, $porjsd$.

Initial conditions

When we switch from the "sound" to the subdomain state, the amount of gas in the subdomain boundaries is set equal to 0, a small part of the gas of the intra-granular bubbles is transferred to the precipitation bubbles, the intra-granular pores become inter-subdomain pores, while the precipitation bubbles are introduced with a size comparable to the intra-granular bubbles, and a fixed density [bubbles / m^3 of fresh fuel].

Gas dissolved at the subdomain boundary:

$\frac{\partial C_{Xejsd}(r)}{\partial t} =$	
$+D_{Xejsd}\nabla^2 C_{Xejsd}(r)$	Inter-subdomain boundary diffusion towards the grain boundary.
$+\frac{15D_{Xe}}{A_{sd}^2}\left(C_{XeM} - C^{loc}_{XeR\overline{jsd}}\right)F_{jsd} \times profile(r)$	Net contribution from gas dissolved in the subdomains that arrives to the subdomain boundary. $profile(r)$ is a normalized profile on the grain equivalent sphere. "Net" means that the re-solution from the subdomain boundary towards the subdomain is included in this term.
$-\sum_{cavjsd} geom_{cavjsd} \times D_{Xejsd} \times \left(C_{Xejsd}(r) - C^{eq}_{Xejsd}(cavjsd)\frac{3e_{pj}}{2A_{sd}}F'_{jsd}\right)$	Trapping into cavities that are on the subdomain boundaries. Here, $geom_{cavjsd}$ is calculated like in eq. 3.12.
$+\sum_{cavjsd} b_{jsd}(cavjsd) \times C_{Xecavjsd} \times profile(r)$	Re-solution of gas from inter-subdomain cavities towards subdomain boundaries. $profile(r)$ is a normalized profile on the grain equivalent sphere.

In the third term, F'_{jsd} is the fraction of the subdomain boundary surface that is a bare subdomain boundary. $\frac{3e_{pj}}{2A_{sd}}$ is equal to $S^{vol}_{jsd,tot}$, the surface of the subdomain boundary (covered or not by cavities) per m^3 of fuel (see eq. 3.13).

CONDITIONS TO THE LIMIT OF THE SPHERE :

The sphere boundary condition C_{XejsdR} depends on the different inter-granular populations (inter-granular bubbles and pores), their fractional coverage of the grain boundaries and the frequencies of re-solution (re-dissolved gas from the inter-granular bubbles and pores and from the grain boundaries to the subdomain boundary). See Section G.4.2 for the calculation of C_{XejsdR}.

The gradient is zero at the centre, for symmetry reasons.

Density of the inter-subdomain cavities (cavjsd = bprecjsd or porjsd) :

$\frac{dC_{cavjsd}}{dt} =$	
$-H(cavjsd) \times C_{cavjsd}$	Loss of cavities when they are swept out in the process of subdomain growth at high temperature. $H(cavjsd)$ is proportional to $\frac{dA_{sd}}{dt}$. See Chapter 6.

During base irradiation, the concentration of precipitation bubbles is considered as constant: see beginning of Section 4.2. Given the low mobility of intra-granular pores, we also model them as constant in the subdomain state.

Gas contained in the inter-subdomain cavities (cavjsd = bprecjsd or porjsd) :

$\frac{dC_{Xecavjsd}}{dt} =$	
$\frac{15D_{Xe}}{A_{sd}^2}\left(C_{XeM} - C^{loc}_{XeRcavjsd}\right)F_{cavjsd}$	Net contribution of gas from the subdomain arriving on the cavity-covered subdomain surface. "Net" means that the re-solution from the inter-subdomain cavity towards the subdomain is included in this term.
$+geom_{cavjsd} \times D_{Xejsd} \times \left(\overline{C_{Xejsd}} - C^{eq}_{Xejsd}(cavjsd)e_{pj}S^{vol}_{jsd,tot}F'_{jsd}\right)$	Trapping of dissolved inter-subdomain gas moving along the subdomain boundary. $\overline{C_{Xejsd}}$ is the average concentration of dissolved gas in the subdomain boundaries.
$-b_{jsd}(cavjsd)C_{Xecavjsd}$	Re-solution of gas from inter-subdomain cavities towards the subdomain boundaries
$+\left(F_{cavjsd} + F_{jsd}\frac{F_{cavjsd}}{\Sigma_{cavjsd}F_{cavjsd}}\right)H(b)C_{Xeb}$	Contribution from intra-subdomain bubbles leaving the subdomain. The term $F_{jsd}\frac{F_{cavjsd}}{\Sigma_{cavjsd}F_{cavjsd}}$ express the idea that a bubble remains a bubble. The gas of the bubbles that arrives to the sub-domain boundary is split between the populations of bubbles present here. The bigger the surface coverage of the bubbles population, the bigger the percentage of the gas allocated to them. See G.2.1 for the calculation of the term $\Sigma_{cavjsd}F_{cavjsd}$
$-H(cavjsd)C_{Xecavjsd}$	Loss of gas when inter-subdomain cavities are swept out in the process of subdomain growth at high temperature. See Chapter 6.

In the second term, $geom_{cavjsd}$ is calculated as presented in Section 3.2.2, eq. 3.12, for the inter-granular trapping term.

Total volume of the inter-subdomain cavities (cavjsd = bprecjsd or porjsd) :

$\frac{dV_{cavjsd}}{dt} =$	
$\left.\frac{dC_{Xecavjsd}}{dt}\right\|_{at} \times \zeta\Omega N_{Avogadro}$	Additional volume accompanying the gas atoms. $\left.\frac{dC_{Xecavjsd}}{dt}\right\|_{at}$ is the sum of first 3 terms of the ODE regarding $C_{Xecavjsd}$. These terms gather the exchanges of gas atoms with the crystal. Here again we use $\zeta = 1$.
$\left.\frac{dV_{cavjsd}}{dt}\right\|_{vac}$	Flux of volume due to thermal vacancies. See Chapter 5.
$+\left(F_{cavjsd} + F_{jsd}\frac{F_{cavjsd}}{\Sigma_{cavjsd}F_{cavjsd}}\right)H(b)V_b$	Contribution from intra-subdomain bubbles leaving the subdomain
$-H(cavjsd)V_{cavjsd}$	Loss of volume when inter-subdomain cavities are swept out in the process of subdomain growth at high temperature. See Chapter 6.

G.1.3. Inter-granular

There is almost no change (apart from the coupling between inter-granular and intra-granular variables, explained in the following Sections) in the description of the inter-granular behaviour of the fission gas between the "sound" and the subdomain state. An in-depth description of the inter-granular behaviour present in MARGARET before the modifications performed during this thesis can be found in [L. Noirot 2011], while the main differences between the reference [ibid.] and the current modelling are explained in the Chapters 3 and 5.
I report here only the current ODE used for C_{Xej}, which is valid for the subdomain state.

Gas dissolved at the grain boundary:

$\frac{dC_{Xej}(r)}{dt} =$	
$+D_{Xej}\nabla^2 C_{Xej}(r)$	Inter-granular diffusion at long distance
$+F_j \frac{3}{A_{gg}} D_{Xejsd} \frac{2}{\delta_{res}} \times$ $\left(C^{loc}_{XejsdR\bar{j}} - C^{eq}_{Xejsd}(\bar{j})\right) R_{VDA} \times profile(r)$	Contribution from the diffusion of gas along the suddomain boundaries.
$-b_{jsd}(j) C_{Xej}(r)$	Resolution from the grain boundary into subdomain boundary.
$-\sum_{cavj} geom_{cavj} \times D_{Xej} \times$ $\left(C_{Xej}(r) - C^{eq}_{Xej}(cavj) e_{pj} S^{vol}_{j,tot} F'_j\right)$	Trapping by inter-granular cavities. See Chapter 3, eq. 3.12.
$+\sum_{cavj} b_j(cavj) C_{Xecavj} \times profile(r)$	Re-solution of gas from inter-granular cavities towards grain boundaries $profile(r)$ is a normalized profile on the fragment equivalent sphere.
Disappearance due to Fracturing	See [L. Noirot 2011]

This is a space-time differential equation solved on the fragment equivalent sphere of radius A_{SE}.

δ_{res} is the re-solution distance: the maximum distance at which the gas dissolved on the grain boundaries can be re-soluted back into the grain by dynamic re-solution. In the code is taken equal to 2 [nm].
The calculation of the equilibrium concentrations is explained in Section 3.2.8.

BOUNDARY CONDITION:
The fuel fragment boundary condition is : $C_{Xej}(A_{SE}) = 0$.
The gradient is zero at the center, for symmetry reasons.

INITIAL CONDITIONS:
Everything is zero at the beginning of the calculation (which is the beginning of the irradiation).
When there is the switch between the "sound" to the subdomain state, the amount of Xenon on the GB is conserved.

G.2. Intra-subdomain / inter-subdomain coupling

G.2.1. Calculation of the fractional coverages for the subdomain surface

In the same way that only one representative grain was modeled in the "sound" state, we are going to use only one representative subdomain.

The following modelling choices are made:

— First, the subdomain is considered as totally embedded in the "non-HBS" zone, as explained at the beginning of section 4.2.

— Second, the subdomain is considered to be next to the subdomain boundary (jsd, bprecjsd, porjsd) but also, for a low fraction, next to the surface of the grain.

We use the following definitions :

S^{sd}_{jsd}	Surface of the subdomain covered by bare subdomain boundary (not covered by cavities) (m^2)
$S^{sd}_{bprecjsd}$	Surface of the subdomain covered by precipitation bubbles (m^2)
S^{sd}_{porjsd}	Surface of the subdomain covered by inter-subdomain pores (m^2)
S^{sd}_{g}	Surface of the subdomain that is also a surface of the grain (m^2)

Table G.1. – The different surfaces covering the subdomain

A_{sd} is the radius of the subdomain (m).
We have :
$4\pi A^2_{sd} = S^{sd}_{jsd} + S^{sd}_{bprecjsd} + S^{sd}_{porjsd} + S^{sd}_{g}$
and so :

$$1 = F_{jsd} + F_{bprecjsd} + F_{porjsd} + F_{gsd} \tag{G.1}$$

Where F_{jsd} is the fraction of the surface of the subdomain covered by bare subdomain boundary (not covered by cavities), $F_{bprecjsd}$ is the fraction of the surface of the subdomain covered by precipitation bubbles, F_{porjsd} is the fraction of the surface of the subdomain covered by inter-subdomain pores, F_{gsd} is the fraction of the surface of the subdomain that is also a surface of the grain.

The surface fractions are illustrated in figure G.1.

Calculation of F_{gsd}:
F_{gsd} can be calculated in this way :

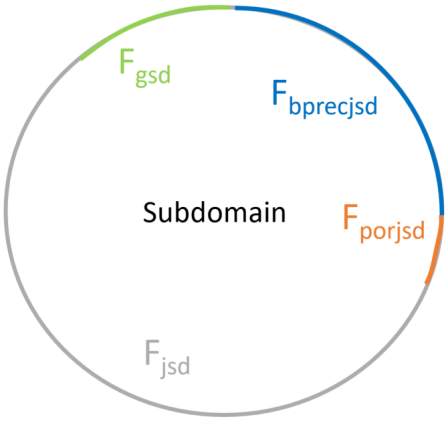

Figure G.1. – The different fractional coverage of the surface of the subdomain

If we call N_{sd} the number of subdomains in a grain, we can write:

$$N_{sd} \times \frac{4\pi}{3} A_{sd}^3 = \frac{4\pi}{3} A_{gg}^3 \tag{G.2}$$

Moreover :

$$F_{gsd} = \frac{4\pi A_{gg}^2}{N_{sd} 4\pi A_{sd}^2} \tag{G.3}$$

Where the numerator is the surface of the grain and the denominator is the sum of the surfaces of all the subdomains present in a grain.
Finally:

$$F_{gsd} = \frac{A_{sd}}{A_{gg}} \tag{G.4}$$

Calculation of $F_{bprecjsd}$:
We define $F_{bprecjsd}$ as $F_{bprecjsd}$ = Surface of the precipitation bubbles projected on the surface of the subdomains / Total surface of the subdomains.
We make the hypothesis that the precipitation bubbles are lenticular, and we call $R_{bprecjsd}$ the radius of the intersection of the bubble with the subdomain surface.
The surface of the precipitation bubbles projected on the surface of the subdomains / m^3 of fresh fuel is equal to $2\pi R_{bprecjsd}^2 C_{bprecjsd}$, because there are two projected discs per bubble.
The total surface of the subdomains / m^3 of fresh fuel is equal to:

$$\underbrace{4\pi A_{sd}^2}_{Surface\ of\ a\ subdomain} \times \underbrace{\frac{1}{\frac{4\pi}{3} A_{sd}^3}}_{Number\ of\ subdomains\ /m^3\ of\ fuel} = \frac{3}{A_{sd}} \tag{G.5}$$

We finally find: $F_{bprecjsd} = \frac{A_{sd}}{3} \times 2\pi R_{bprecjsd}^2 \times C_{bprecjsd}$

Calculation of F_{porjsd}:
Similarly to $F_{bprecjsd}$, we can find that :

$$F_{porjsd} = \frac{A_{sd}}{3} \times 2\pi R^2_{porjsd} \times C_{porjsd} \tag{G.6}$$

Calculation of F_{jsd}:
F_{jsd} can be find from the following relation :

$$F_{jsd} = 1 - F_{gsd} - F_{bprecjsd} - F_{porjsd} \tag{G.7}$$

G.3. Limit condition for the intra-subdomain diffusion problem at the vicinity of the subdomain boundary.

The aim is to derive an expression for C_R (limit condition for the diffusion of dissolved gas in the subdomains):

In the subdomains the diffusion process will be close to the permanent regime. This allows us to write the flux (in mol/s/m^3 of fresh fuel) of Xenon exiting the subdomain as:
$\frac{15 D_{Xe}}{A^2_{sd}} \times (C_{XeM} - C_R)$
This expression comes from solving the diffusion equation in steady state ($D_{Xe}\nabla^2 C_{Xe} = 0$) on a sphere of radius A_{sd} with boundary conditions: Gradient equal to 0 in the center for symmetry reasons and concentration of Xenon equal to C_R at $r = A_{sd}$. Once the concentration field is calculated, the total gas loss [moles/m^3] and the average concentration in the subdomain, C_{XeM}, can be related one to the other.
In our model, C_{XeM} is the only variable representing the dissolved gas in the subdomain and, physically, represent the average concentration of dissolved gas in the subdomain. D_{Xe} is the diffusion coefficient of the gas (m^2/s).

In order to find C_R, we can evaluate the local concentrations of gas in the limit re-solution layers facing each portion of the surface. The limit re-solution layers are parts of the volume of the subdomain, near the surface of the subdomain boundary, where re-solution of gas from the subdomain boundary (bare or covered with cavities) takes place. The depth of the layers is the re-solution distance δ_{rem} [1].
The relevant notations are defined in the table G.2.

To calculate these local concentrations, we can take $C^{loc}_{XeRporjsd}$ as an example. We perform a material balance in the limit re-solution layer neglecting the flux that arrives from the interior of the subdomain compared to the two other fluxes. We then make

1. Also called δ in Chapter 3

$C^{loc}_{XeR\overline{jsd}}$	Local concentration facing a bare subdomain boundary (mol/m^3)
$C^{loc}_{XeRbrecjsd}$	Local concentration facing the part of the subdomain boundary covered by precipitation bubbles (mol/m^3)
$C^{loc}_{XeRporjsd}$	Local concentration facing the part of the subdomain boundary covered by inter-subdomain pores (mol/m^3)
$C^{loc}_{XeRg\overline{sd}}$	Local concentration facing the surface of the grain (mol/m^3)

Table G.2. – Concentrations in the different limit shells of the subdomain

the hypothesis of permanent regime, which means that the sum of the fluxes entering the layer is null.
In figure G.2, it is showed the schematic representation of the problem.

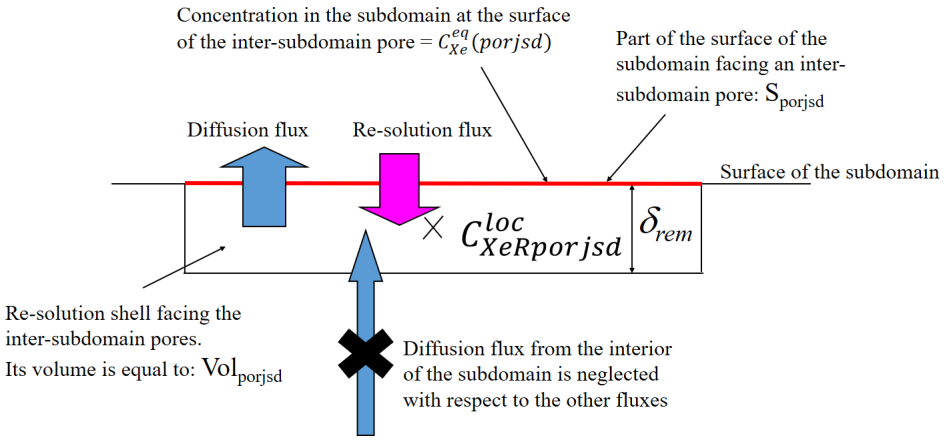

Figure G.2. – Schematic representation of the problem used to evaluate the local concentrations of gas in the limit re-solution shells facing each portion of the surface of a subdomain.

We perform the gas balance on the volume Vol_{porjsd}:

$$Vol_{porjsd}\frac{dC^{loc}_{XeRporjsd}}{dt} = -S_{porjsd}D_{Xe}\frac{C^{loc}_{XeRporjsd} - C^{eq}_{Xe}(porjsd)}{\frac{\delta_{rem}}{2}} + b(porjsd)\times C_{Xeporjsd}\frac{4}{3}\pi A^3_{sd} \tag{G.8}$$

$C^{eq}_{Xe}(porjsd)$ is the gas concentration in the lattice at thermodynamic equilibrium

with the near inter-subdomain pore. It is a local concentration, as $C^{loc}_{XeRporjsd}$. In practice, it is negligible for Xenon.

As the re-solution layer is very narrow, $\frac{dC^{loc}_{XeRporjsd}}{dt}$ is negligible compared to the 2 terms of the right hand side, and it is not considered. In this way, we can express $C^{loc}_{XeRporjsd}$ as a function of the other variables:

$$C^{loc}_{XeRporjsd} = C^{eq}_{Xe}(porjsd) + \frac{\delta_{rem}}{2}\frac{A_{sd}}{3F_{porjsd}}\frac{b(porjsd)}{D_{Xe}}C_{Xeporjsd} \tag{G.9}$$

With the same reasoning we can obtain equivalent formulas for the interfaces with jsd and bprecjsd:

$$\begin{aligned} C^{loc}_{XeR\overline{jsd}} &= C^{eq}_{Xe}(\overline{jsd}) + \frac{\delta_{rem}}{2}\frac{A_{sd}}{3F_{jsd}}\frac{b(jsd)}{D_{Xe}}\overline{C_{Xejsd}} \\ C^{loc}_{XeRbprecjsd} &= C^{eq}_{Xe}(bprecjsd) + \frac{\delta_{rem}}{2}\frac{A_{sd}}{3F_{bprecjsd}}\frac{b(bprecjsd)}{D_{Xe}}C_{Xebprecjsd} \\ C^{loc}_{XeRporjsd} &= C^{eq}_{Xe}(porjsd) + \frac{\delta_{rem}}{2}\frac{A_{sd}}{3F_{porjsd}}\frac{b(porjsd)}{D_{Xe}}C_{Xeporjsd} \end{aligned} \tag{G.10}$$

The notation $C^{loc}_{XeR\overline{jsd}}$ reminds that this quantity is calculated at the interface with the average dissolved inter-subdomain concentration of gas. The same works for $C^{eq}_{Xe}(\overline{jsd})$.

The same kind of reasoning could have been done splitting S^{sd}_g using the different fractional coverage of the surface of the grain by the inter-granular bubbles (bj), pores (proj), bare grain boundary (j) and free surface (ext). However, we faced the fact that, as the subdomain is nearly in the permanent state of diffusion, the limit condition greatly influences the inner concentration, C_{XeM}. Even if $F_{gsd} \times F_{ext}$ is low, considering a flux through this part of the surface artificially "empties the subdomains".
Therefore, a better approach is choosing to consider a null flux to the F_{gsd} fraction of the subdomain surface, or, in other words, $C^{loc}_{XeR\overline{g}} = C_{XeM}$.

We can write C_R as a weighting of the different local concentrations:

$$C_R = F_{jsd}C^{loc}_{XeR\overline{jsd}} + F_{bprecjsd}C^{loc}_{XeRbprecjsd} + F_{porjsd}C^{loc}_{XeRporjsd} + F_{gsd}\,C^{loc}_{XeR\overline{g}} \tag{G.11}$$

In the feasibility study mentioned in Section 4.2, L. Noirot demonstrated, by comparing this modelling solution with a similar one that uses a spherical volume divided in many shells, that the approach above is justified in the case of one re-solution layer.

In particular, the fact that it is possible to neglect the flux arriving from the grain in equation G.8 had been checked since it was not done in the reference problem finely meshed that served for comparison. Here, we have to use several re-solution layers because there are different populations at the surface.

This definition of C_R allows us to write the net quantity of gas leaving from the subdomain ($mol/m^3/s$):

$-\overline{D_{Xe}\Delta C_{Xe}} =$ $+\frac{15D_{Xe}}{A_{sd}^2} \times (C_{XeM} - C_R) =$	Dissolved gas leaving the subdomain, viewed from the subdomain.
$+F_{jsd}\frac{15D_{Xe}}{A_{sd}^2} \times \left(C_{XeM} - C^{loc}_{XeR\overline{jsd}}\right)$	Net gas entering the bare subdomain boundary. "Net" means that the re-solution of gas from the subdomain boundary towards the subdomains is already taken into account in this term.
$+F_{bprecjsd}\frac{15D_{Xe}}{A_{sd}^2} \times \left(C_{XeM} - C^{loc}_{XeRbprecjsd}\right)$	Net gas entering the precipitation bubbles
$+F_{porjsd}\frac{15D_{Xe}}{A_{sd}^2} \times \left(C_{XeM} - C^{loc}_{XeRporjsd}\right)$	Net gas entering the inter-subdomain pores
$+F_{gsd}\frac{15D_{Xe}}{A_{sd}^2} \times \left(C_{XeM} - C^{loc}_{XeR\bar{j}}\right)$	Net gas entering directly the grain boundary. This contribution is currently not considered: null flux.

G.4. Inter-subdomain / inter-granular coupling

G.4.1. Relation between local concentration and concentration /m^3 of fresh fuel for the inter-subdomain gas

We can pass from local concentrations on subdomain boundaries to homogeneous concentrations in the grain in the following way.

The volume of the subdomain boundaries per volume V_{tot} of the fuel can be written as:

$$e_{pj} \times N_{sd} \times \frac{4\pi A_{sd}^2}{2}$$

where
— A_{sd} is the radius of the subdomains
— N_{sd} is the number of subdomains in the volume V_{tot}
— e_{pj} is the depth of the grain boundary or subdomain boundary
— The division by 2 comes from the fact that the boundary is half of the ensemble of the surfaces of the subdomains taken separately.
The number of subdomains in the volume V_{tot} is: $N_{sd} = \frac{V_{tot}}{\frac{4}{3}\pi A_{sd}^3}$

Therefore, the volume of the subdomain boundaries / m^3 of fresh fuel is: $\frac{3e_{pj}}{2A_{sd}}$. We can call this ratio R_{VDA} for "Ratio between the volume where the diffusion is accelerated over the volume of fresh fuel."

Therefore, for example, to pass from a concentration C_{Xejsd}, expressed in atoms / m^3 of fresh fuel, to the local concentration C_{Xejsd}^{loc}, expressed in atoms / m^3 of subdomain boundary, we use the following relation:

$$C_{Xejsd} = C_{Xejsd}^{loc} \times R_{VDA} \times F_{jsd} \tag{G.12}$$

With

$$R_{VDA} = \frac{3e_{pj}}{2A_{sd}} \tag{G.13}$$

G.4.2. Calculation of the local inter-subdomain concentrations in the re-solution layers in front of the different portions of the grain boundary

This chapter focuses on what happens where the subdomain boundaries intersect the grain boundary. The subdomain boundary may arrive on an inter-granular bubble,

an inter-granular pore, the bare grain boundary or the free surface.

To explain the derivation, we use $C^{loc}_{XejsdRporj}$ (the local concentration of Xenon on the subdomain boundary in the proximity of an inter-granular pore) as an example. The schematic representation of the problem is showed in figure G.3.

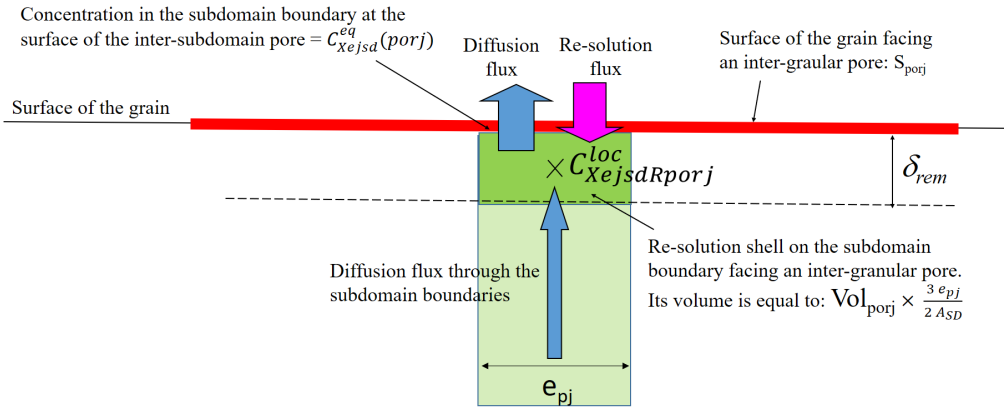

(a) Local view

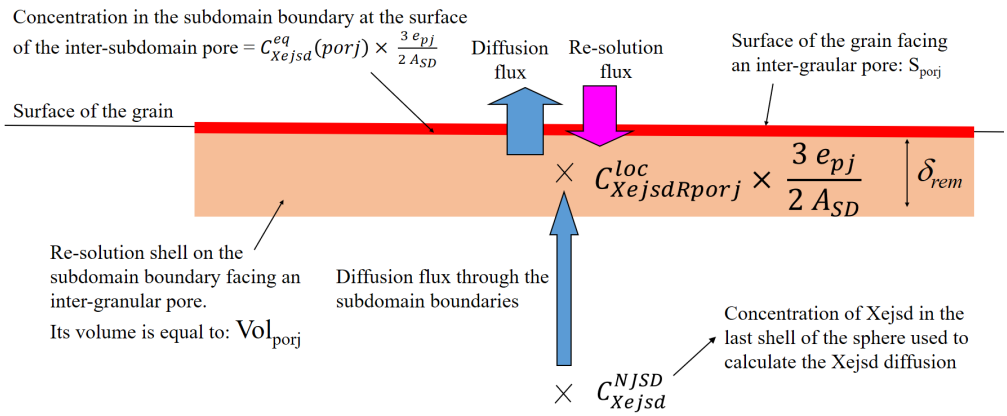

(b) Homogenized view

Figure G.3. – Interface between the subdomain boundary and the grain boundary.

As in the preceding Section, we write the gas balance on the re-solution layer of volume Vol_{porj}. This time the grain is meshed, while the re-solution layer is not meshed. The width of the re-solution layer is lower than the last layer of the meshing.

$$
\begin{aligned}
Vol_{porj}\frac{dC^{loc}_{XejsdRporj}R_{VDA}}{dt} &= S_{porj}D_{Xejsd}\frac{C^{NJSD}_{Xejsd}-C^{loc}_{XejsdRporj}R_{VDA}}{A_{gg}(1-rm_{NJSD})} \\
&\quad -S_{porj}D_{Xejsd}\frac{C^{loc}_{XejsdRporj}R_{VDA}-C^{eq}_{Xejsd}(porj)R_{VDA}}{\frac{\delta_{rem}}{2}} \\
&\quad +b_{jsd}(porj)C_{Xeporj}\times\frac{4}{3}\pi A^3_{gg}
\end{aligned}
\tag{G.14}
$$

Where:

— D_{Xejsd} is the diffusion coefficient of Xenon on the subdomain boundary, in the corresponding homogeneous medium. See Section 3.2.1.

— $NJSD$ labels the last shell used for the calculation of the inter-subdomain diffusion.

— C^{NJSD}_{Xejsd} is the concentration in mol/m^3 of fresh fuel, localized at mid-thickness of the last shell of the grain.

— rm_{NJSD} is the relative radius of the mid-thickness point of the last shell of the grain.

— $b_{jsd}(porj)$ is the re-solution frequency of the gas leaving the inter-granular pore and arriving in the subdomain boundaries.

We suppose that this limit layer attains rapidly (faster than the diffusion kinetic in the whole sphere) a permanent regime, which allows us to ignore the time derivative of $C_{XejsdRporj}$. We can then express $C^{loc}_{XejsdRporj}$ as a function of the other quantities.

$$
\begin{aligned}
C^{loc}_{XejsdRporj} &= \left[\begin{array}{ll} \frac{1}{R_{VDA}}C^{NJSD}_{Xejsd} & + \quad \frac{2A_{gg}(1-rm_{NJSD})}{\delta_{rem}}\times C^{eq}_{Xejsd}(porj) \\ & + \quad \frac{A^2_{gg}(1-rm_{NJSD})}{3F_{porj}D_{Xejsd}}\times\frac{1}{R_{VDA}}b_{jsd}(porj)C_{Xeporj}\end{array}\right] \\
&\quad \times\left[1+\frac{2A_{gg}(1-rm_{NJSD})}{\delta_{rem}}\right]^{-1}
\end{aligned}
\tag{G.15}
$$

Using the same derivation we obtain:

$$C^{loc}_{XejsdR\bar{j}} = \left[\begin{array}{lll} \frac{1}{R_{VDA}} C^{NJSD}_{Xejsd} & + & \frac{2A_{gg}(1-rm_{NJSD})}{\delta_{rem}} \times C^{eq}_{Xejsd}(\bar{j}) \\ & + & \frac{A^2_{gg}(1-rm_{NJSD})}{3F_j D_{Xejsd}} \times \frac{1}{R_{VDA}} b_{jsd}(j)\overline{C_{Xej}} \end{array}\right] \times \left[1 + \frac{2A_{gg}(1-rm_{NJSD})}{\delta_{rem}}\right]^{-1} \quad \text{(G.16)}$$

$$C^{loc}_{XejsdRbj} = \left[\begin{array}{lll} \frac{1}{R_{VDA}} C^{NJSD}_{Xejsd} & + & \frac{2A_{gg}(1-rm_{NJSD})}{\delta_{rem}} \times C^{eq}_{Xejsd}(bj) \\ & + & \frac{A^2_{gg}(1-rm_{NJSD})}{3F_{bj}(1-F_v) D_{Xejsd}} \times \frac{1}{R_{VDA}} b_{jsd}(bj) C_{Xebj} \end{array}\right] \times \left[1 + \frac{2A_{gg}(1-rm_{NJSD})}{\delta_{rem}}\right]^{-1} \quad \text{(G.17)}$$

$$C^{loc}_{XejsdRbjv} = \left[\begin{array}{lll} \frac{1}{R_{VDA}} C^{NJSD}_{Xejsd} & + & \frac{2A_{gg}(1-rm_{NJSD})}{\delta_{rem}} \times C^{eq}_{Xejsd}(bjv) \\ & + & \frac{A^2_{gg}(1-rm_{NJSD})}{3F_{bj}F_v D_{Xejsd}} \times \frac{1}{R_{VDA}} b_{jsd}(bjv) C_{Xebjv} \end{array}\right] \times \left[1 + \frac{2A_{gg}(1-rm_{NJSD})}{\delta_{rem}}\right]^{-1} \quad \text{(G.18)}$$

$$C^{loc}_{XejsdRext} = \left[\frac{1}{R_{VDA}} C^{NJSD}_{Xejsd} + \frac{2A_{gg}(1-rm_{NJSD})}{\delta_{rem}} \times C^{eq}_{Xejsd}(ext)\right] \times \left[1 + \frac{2A_{gg}(1-rm_{NJSD})}{\delta_{rem}}\right]^{-1} \quad \text{(G.19)}$$

The expression of $C^{loc}_{XejsdRext}$ is different from the others because there is no resolution of Xenon from the exterior.

G.4.3. Calculation of the limit condition for the inter-subdomain problem of diffusion : C_{XejsdR}

If we write the balance of gas leaving the grain by diffusion along the subdomain boundaries, we have:

$-D^{MAC}_{Xejsd} \times \frac{\partial C_{Xejsd}}{\partial r}\|_{r=1}(t) \times 4\pi A^2_{gg} =$ $+D_{Xejsd}\frac{C^{NJSD}_{Xejsd} - C^{loc}_{XejsdR\bar{j}} R_{VDA}}{A_{gg}(1-rm_{NSJD})} S_j$	Flux leaving towards the re-solution layer facing the bare grain boundary
$+D_{Xejsd}\frac{C^{NJSD}_{Xejsd} - C^{loc}_{XejsdRbj} R_{VDA}}{A_{gg}(1-rm_{NSJD})} S_{bj}$	Flux leaving towards the re-solution layer facing the inter-granular not connected bubbles.
$+D_{Xejsd}\frac{C^{NJSD}_{Xejsd} - C^{loc}_{XejsdRbjv} R_{VDA}}{A_{gg}(1-rm_{NSJD})} S_{bjv}$	Flux leaving towards the re-solution layer facing the inter-granular not connected bubbles.
$+D_{Xejsd}\frac{C^{NJSD}_{Xejsd} - C^{loc}_{XejsdRporj} R_{VDA}}{A_{gg}(1-rm_{NSJD})} S_{porj}$	Flux leaving towards the re-solution layer facing the inter-granular pores
$+D_{Xejsd}\frac{C^{NJSD}_{Xejsd} - C^{loc}_{XejsdRext} R_{VDA}}{A_{gg}(1-rm_{NSJD})} S_{ext}$	Flux leaving toward the exterior

We can use the fact that $D^{MAC}_{Xejsd} = D_{Xejsd}$ (see Section 3.2.1).
Dividing on both sides by $4\pi A^2_{gg}$, and using the definitions of the surface fractions in Section G.2.1 we obtain:

$$-D_{Xejsd} \times \frac{\partial C_{Xejsd}}{\partial dr}|_{r=1}(t) = D_{Xejsd}\frac{C^{NJSD}_{Xejsd} - C_{XejsdR}}{A_{gg}(1-rm_{NSJD})} \tag{G.20}$$

with

$$C_{XejsdR} = R_{VDA} \times \begin{pmatrix} F_j C^{loc}_{XejsdR\bar{j}} + F_{bj}(1-F_v) C^{loc}_{XejsdRbj} + F_{bj}F_v C^{loc}_{XejsdRbjv} \\ + F_{porj} C^{loc}_{XejsdRporj} + F_{ext} C^{loc}_{XejsdRext} \end{pmatrix} \tag{G.21}$$

G.4.4. Expression of the gradients and the fluxes of gas along the subdomains, feeding the different populations on the grain boundary and the exterior

The gradients between the limit re-solution shell and the surface of the grain, facing the bare grain boundary, the different inter-granular cavities populations and the

exterior, are defined by:

$$
\begin{aligned}
Grad_{Xejsd}(\bar{j}) = & \quad -\frac{2}{\delta_{rem}} R_{VDA}\left(C^{loc}_{XejsdR\bar{j}} - C^{eq}_{Xejsd}(\bar{j})\right) \\
Grad_{Xejsd}(bj) = & \quad -\frac{2}{\delta_{rem}} R_{VDA}\left(C^{loc}_{XejsdRbj} - C^{eq}_{Xejsd}(bj)\right) \\
Grad_{Xejsd}(bjv) = & \quad -\frac{2}{\delta_{rem}} R_{VDA}\left(C^{loc}_{XejsdRbjv} - C^{eq}_{Xejsd}(bjv)\right) \\
Grad_{Xejsd}(porj) = & \quad -\frac{2}{\delta_{rem}} R_{VDA}\left(C^{loc}_{XejsdRporj} - C^{eq}_{Xejsd}(porj)\right) \\
Grad_{Xejsd}(ext) = & \quad -\frac{2}{\delta_{rem}} R_{VDA}\left(C^{loc}_{XejsdRext} - C^{eq}_{Xejsd}(ext)\right)
\end{aligned}
\tag{G.22}
$$

This allows us to write the expression of the gas leaving the grain ($mol/m^3/s$) through the subdomain boundaries. We can use here the definition of C_{XejsdR}, the balance equation G.14 and the definition of the gradients. This relation is used to verify the global balance.

Each terms, from the second line of table G.3, are terms that appear in the evolution equation of C_{Xebj}, C_{Xebjv}, C_{Xeporj}, $C_{Xe,ext}$. $C_{Xe,ext}$ is the quantity of gas released from a particular point in the pellet mesh [mol/m^3].

$-\overline{D_{Xejsd}\nabla^2 C_{Xejsd}} =$ $+\frac{3}{A_{gg}} D_{Xejsd} \frac{C^{NJSD}_{Xejsd} - C_{XejsdR}}{A_{gg}(1-rm_{NSJD})} =$	Gas arriving to the grain boundary from the subdomain boundaries. The concentration profile in the grain takes into account the limit condition C_{XejsdR} (which, itself, considers the re-solution)
$-F_j \frac{3}{A_{gg}} D_{Xejsd} Grad_{Xejsd}(\overline{j})$	Gas arriving by diffusion from the appropriate limit re-solution shell to a bare grain boundary
$+b_{jsd}(j)\overline{C_{Xej}}$	Re-solution facing a bare grain boundary
$-(1-F_v)F_{bj} \frac{3}{A_{gg}} D_{Xejsd} Grad_{Xejsd}(bj)$	Gas arriving by diffusion from the appropriate limit re-solution shell to the inter-granular bubbles not-connected to the free volume
$+b_{jsd}(bj)C_{Xebj}$	Re-solution facing inter-granular bubbles not-connected to the free volume
$-F_v F_{bj} \frac{3}{A_{gg}} D_{Xejsd} Grad_{Xejsd}(bjv)$	Gas arriving by diffusion from the appropriate limit re-solution shell to the inter-granular bubbles connected to the free volume
$+b_{jsd}(bjv)C_{Xebjv}$	Re-solution facing inter-granular bubbles connected to the free volume
$-F_{porj} \frac{3}{A_{gg}} D_{Xejsd} Grad_{Xejsd}(porj)$	Gas arriving by diffusion from the appropriate limit re-solution shell to the inter-granular pores
$+b_{jsd}(porj)C_{Xeporj}$	Re-solution facing inter-granular pores
$-F_{ext} \frac{3}{A_{gg}} D_{Xejsd} Grad_{Xejsd}(ext)$	Gas arriving by diffusion from the appropriate limit re-solution shell to the free surface

Table G.3. – Expression of the gas leaving the grain ($mol/m^3/s$) through the subdomain boundaries

H. Derivation of the "generalized Speight model" for the behaviour of thermal vacancies in the subdomain and HBS states

H.1. Subdomain state

The derivation of the "generalized Speight model" in the subdomain state follows the derivation in the "sound" state. However, in the subdomain state, we have one more unknown, since we have to estimate the vacancy concentration in the subdomain boundaries.

Here, we make the hypothesis that the direct exchange of vacancies from the grain boundary to the subdomains is negligible and all the exchanges of vacancies between those two domains happen via the subdomain boundaries. This hypothesis is coherent with the choice of considering a null direct flux of dissolved Xenon from the subdomains to the grain boundary (see Section G.3).

In the subdomain state, equation 5.2 (which link v_{move} to $\beta_{v,j}$) remains valid, while the variation of the volume of the inter-granular cavities can be written as:

$$\left.\frac{dV_{cavj}}{dt}\right|_{vac} = v_{move}\frac{3}{2A_{gg}}F_{cavj} + \Phi_{v,j->cavj} \times \Omega + \Phi_{v,jsd->cavj} \times \Omega \tag{H.1}$$

Where $\Phi_{v,jsd->cavj}$ [Vacancies / m^3 of fresh fuel / s] is the vacancy flux from the subdomain boundaries to the inter-granular cavities.

The variation of the volume of the intra-granular cavities can be written as:

$$\left.\frac{dV_{cav}}{dt}\right|_{vac} = \Phi_{v,bulk->cav} \times \Omega \tag{H.2}$$

Which is the same expression as in the "sound" state.

The variation of the volume of the inter-subdomain cavities can be written as:

$$\left.\frac{dV_{cavjsd}}{dt}\right|_{vac} = \Phi_{v,bulk->cavjsd} \times \Omega + \Phi_{v,jsd->cavjsd} \times \Omega \tag{H.3}$$

Where $\Phi_{v,bulk>cavjsd}$ [Vacancies / m^3 of fresh fuel / s] is the vacancy flux from the bulk of the subdomain to the inter-subdomain cavities.

Following the reasoning detailed for the "sound" state, we use the hypothesis of quasi-steady state for the concentration of the vacancies in the bulk, on the subdomain boundaries and on the grain boundaries [1].
In this way, we obtain:

$$\sum_{cav} \Phi_{v,bulk->cav} + \sum_{cavjsd} \Phi_{v,bulk->cavjsd} + \Phi_{v,bulk->jsd} = 0 \tag{H.4}$$

$$\sum_{cavjsd} \Phi_{v,jsd->cavjsd} + \Phi_{v,jsd->j} + \sum_{cavj} \Phi_{v,jsd->cavj} + \Phi_{v,jsd->bulk} = 0 \tag{H.5}$$

$$\beta_{v,j} - \sum_{cavj} \Phi_{v,j->cavj} - \Phi_{v,j->ext} - \Phi_{v,j->jsd} = 0 \tag{H.6}$$

If we sum the above equations, we obtain:

$$\begin{aligned}\beta_{v,j} + \Phi_{v,ext->j} = \sum_{cavj} \Phi_{v,j->cavj} + \sum_{cav} \Phi_{v,bulk->cav} + \sum_{cavjsd} \Phi_{v,bulk->cavjsd} \\ + \sum_{cavjsd} \Phi_{v,jsd->cavjsd} + \sum_{cavj} \Phi_{v,jsd->cavj}\end{aligned} \tag{H.7}$$

Which states that the sum of the vacancies produced on the grain boundaries plus the flux of vacancies coming from the exterior is equal to the sum of the fluxes of vacancies going into the different cavities.

Remark

If we combine equations H.1, H.2, H.3, H.4, H.5 and H.6 we obtain:

1. In this case, differently from the "sound" state, we do consider in the model the presence of dislocations in the form of subdomain boundaries

$$\begin{aligned}\sum_{cavj}\frac{dV_{cavj}}{dt}\Big|_{vac}+\sum_{cavjsd}\frac{dV_{cavjsd}}{dt}\Big|_{vac}+\sum_{cav}\frac{dV_{cav}}{dt}\Big|_{vac}&=\\ =\upsilon_{move}\frac{3}{2A_{gg}}\sum_{cavj}F_{cavj}+\beta_{v,j}\times\Omega+\Phi_{v,ext->j}\times\Omega&\\ =\upsilon_{move}\frac{3}{2A_{gg}}\left(\sum_{cavj}F_{cavj}+F_j\right)+\Phi_{v,ext->j}\times\Omega&\\ =\frac{Swelling\ of\ the\ fragment}{Unit\ of\ time}\ [s]^{-1}&\end{aligned}\tag{H.8}$$

The above equation is the same as eq. 5.10. In fact, the only sources of vacancies in our model are the GB and the free surface, while we do not consider a production of vacancies on the subdomain boundaries.

Now, the last equation that we need is an energy balance. We state that the work performed by the external forces (with respect to the solid) must be equal to the energy gained by producing vacancies on the grain boundaries and by exchanging vacancies with the free surfaces and the different cavities:

$$\begin{aligned}-P_{Hydro}\times\frac{Swelling\ of\ the\ fragment}{Unit\ of\ time}\Big|_v&\\ +\sum_{cavj}\left(P_{int}(cavj)-\gamma K_{cavj}\right)\frac{dV_{cavj}}{dt}\Big|_{vac}&\\ +\sum_{cavjsd}\left(P_{int}(cavjsd)-\gamma K_{cavjsd}\right)\frac{dV_{cavjsd}}{dt}\Big|_{vac}&\\ +\sum_{cav}\left(P_{int}(cav)-\gamma K_{cav}\right)\frac{dV_{cav}}{dt}\Big|_{vac}&=\beta_{v,j}\times\mu_{v,j}\\ &+\Phi_{v,ext->j}\times\mu_{v,j/ext}\\ &-\sum_{cavj}\Phi_{v,j->cavj}\times\mu_{v,j/cavj}\\ &-\sum_{cavj}\Phi_{v,jsd->cavj}\times\mu_{v,jsd/cavj}\\ &-\sum_{cavjsd}\Phi_{v,jsd->cavjsd}\times\mu_{v,jsd/cavjsd}\\ &-\sum_{cavjsd}\Phi_{v,bulk->cavjsd}\times\mu_{v,bulk/cavjsd}\\ &-\sum_{cav}\Phi_{v,bulk->cav}\times\mu_{v,bulk/cav}\end{aligned}\tag{H.9}$$

Where the term on the left hand side is the work performed by the external forces, while the term on the right hand side is the energy gained because of the production of vacancies on the GB and the exchange with the free surface and the cavity.

If we use equations H.8, 5.2, H.1, H.3, and H.2, following a similar derivation as for the "sound" state, the energy balance can be written as:

$$\begin{aligned}\beta_{v,j}\frac{\Omega}{F_j}\Big[-P_{Hydro}\Big(\sum_{cavj}F_{cavj}+F_j\Big)+\sum_{cavj}P_{surf}(cavj)F_{cavj}\Big] = \\ = \beta_{v,j}\times\mu_{v,j}+\Phi_{v,ext->j}\times(\mu_{v,j/ext}+P_{Hydro}\times\Omega) \\ -\sum_{cavj}\Phi_{v,j->cavj}\times\big(\mu_{v,j/cavj}+P_{surf}(cavj)\times\Omega\big) \\ -\sum_{cavj}\Phi_{v,jsd->cavj}\times\big(\mu_{v,jsd/cavj}+P_{surf}(cavj)\times\Omega\big) \\ -\sum_{cavjsd}\Phi_{v,jsd->cavjsd}\times\big(\mu_{v,jsd/cavjsd}+P_{surf}(cavjsd)\times\Omega\big) \\ -\sum_{cavjsd}\Phi_{v,bulk->cavjsd}\times\big(\mu_{v,bulk/cavjsd}+P_{surf}(cavjsd)\times\Omega\big) \\ -\sum_{cav}\Phi_{v,bulk->cav}\times\big(\mu_{v,bulk/cav}+P_{surf}(cav)\times\Omega\big)\end{aligned} \tag{H.10}$$

Using the same hypothesis as for the "sound" state, we can write:

$$\mu_{v,medium_1\,/\,medium_2}\approx -P_{surf}(medium_2)\times\Omega \tag{H.11}$$

Therefore, we obtain once again equation 5.23 (the energy balance in the "sound" state).
At this point, we can express $x_{v,j}$ through equation 5.26 and $C^{loc}_{v,j}$ through equation 5.27.
We have found that, in our model, the expression for $C^{loc}_{v,j}$ does not change between the "sound" and the subdomain state.

Now that we have obtained $C^{loc}_{v,j}$, which is equal to the equilibrium concentration of vacancies on a grain boundary subjected to a stress equal to σ, we can calculate $C_{v,jsd}$, C_v and $\beta_{v,j}$.

We can write the flux of vacancies from the bulk of the subdomain to the intra-subdomain cavities ("cav") as:

$$\Phi_{v,bulk->cav} = geom_{cav}\times D_v\left(C_v - C_v^{eq}(cav)\right) \tag{H.12}$$

$\Phi_{v,bulk->cav}$ does not change with respect to the expression in the "sound" state.

The flux of vacancies from the bulk of the subdomain to the subdomain boundary can be written as:

$$\begin{aligned}\Phi_{v,bulk->jsd} &= \frac{15}{A_{sd}^2} \times D_v \left(C_v - C_v^{eq}(jsd)\right) \times F_{jsd} \\ \Phi_{v,bulk->jsd} &= \frac{15}{A_{sd}^2} \times D_v \left(C_v - exp\left(+\frac{E_{seg,v,jsd}}{kT}\right) C_{v,jsd}^{loc}\right) \times F_{jsd}\end{aligned} \tag{H.13}$$

Where A_{sd} is the radius of a subdomain, $C_v^{eq}(jsd)$ is the concentration of vacancies in the lattice in equilibrium with the concentration of vacancies on the subdomain boundary, F_{jsd} is the fraction of the subdomain boundary covered by bare subdomain boundary (see Section G.2.1). $E_{seg,v,jsd}$ is the segregation energy of a vacancy on the subdomain boundaries. The value $\frac{15}{A_{sd}^2}$ comes from the assumption of quasi-steady state of diffusion in the subdomains (see the beginning of Section G.3).

The flux of vacancies from the bulk of the subdomain to the inter-subdomain bubbles can be written as:

$$\Phi_{bulk->cavjsd} = \frac{15}{A_{sd}^2} \times D_v \left(C_v - C_v^{eq}(cavjsd)\right) \times F_{cavjsd} \tag{H.14}$$

Then, from the equation that express the permanent regime for the thermal vacancies in the bulk of the subdomains (eq. H.4), we can express C_v as an affine function of $C_{v,jsd}^{loc}$: $C_v = a_1 C_{v,jsd}^{loc} + b_1$, with:

$$a_1 = \frac{\frac{15F_{jsd}}{A_{sd}^2} exp\left(+\frac{E_{seg,v,jsd}}{kT}\right)}{denom_1} \; [adimensional] \tag{H.15}$$

and

$$b_1 = \frac{\sum_{cav} geom_{cav} C_v^{eq}(cav) + \frac{15}{A_{sd}^2} \sum_{cavjsd} F_{cavjsd} C_v^{eq}(cavjsd)}{denom_1} \; [vacancies/m^3] \tag{H.16}$$

Where

$$denom_1 = \sum_{cav} geom_{cav} + \frac{15}{A_{sd}^2} \left(F_{jsd} + \sum_{cavjsd} F_{cavjsd}\right) \tag{H.17}$$

We can now reformulate the expression of $\Phi_{bulk->jsd}$ (eq. H.13) as:

$$\Phi_{bulk->jsd} = \alpha_1 C_{v,jsd}^{loc} + \beta_1 \tag{H.18}$$

Where

$$\alpha_1 = \frac{15}{A_{sd}^2} \times D_v \times F_{jsd} \left(a_1 - exp\left(+ \frac{E_{seg,v,jsd}}{kT} \right) \right) \tag{H.19}$$

and

$$\beta_1 = \frac{15}{A_{sd}^2} \times D_v \times F_{jsd} \times b_1 \tag{H.20}$$

Now, the flux of vacancies from the subdomain boundary to the "cavjsd" cavities can be written as:

$$\Phi_{jsd->cavjsd} = geom_{cavjsd} \times D_{v,jsd} \times F'_{jsd} S^{vol}_{jsdtot} e_{pj} \left(C^{loc}_{v,jsd} - C^{eq}_{v}(cavjsd) \right) \tag{H.21}$$

Where $geom_{cavjsd}$ is the adaptation to the subdomain boundary of equation 3.12, $D_{v,jsd}$ is the vacancy diffusion coefficient on the subdomain boundaries, $F'_{jsd} = \frac{F_{jsd}}{1-F_{gsd}}$ (for the meaning of F_{gsd}, see Section G.2.1), $S^{vol}_{jsdtot} = \frac{3(1-F_{gsd})}{2A_{sd}}$.

The flux of vacancies from the subdomain boundary to the grain boundary can be written as:

$$\begin{aligned}
\Phi_{jsd->j} &= \frac{15}{A_{gg}^2} F_j \times D_{v,jsd} \times F'_{jsd} S^{vol}_{jsdtot} e_{pj} \left(C^{loc}_{v,jsd} - C^{eq}_{v,jsd}(j) \right) \\
\Phi_{jsd->j} &= \frac{15}{A_{gg}^2} F_j \times D_{v,jsd} \times F'_{jsd} S^{vol}_{jsdtot} e_{pj} \left(C^{loc}_{v,jsd} - exp\left(+ \frac{E_{seg,v,j} - E_{seg,v,jsd}}{kT} \right) C^{loc}_{v,j}(j) \right)
\end{aligned} \tag{H.22}$$

Where $E_{seg,v,j} - E_{seg,v,jsd}$ represents the difference between the segregation energy of a vacancy on the grain boundary and the segregation energy of vacancy on the subdomain boundary.

The flux of vacancies from the subdomain boundary to the inter-granular bubbles can be written as:

$$\Phi_{jsd->cavj} = \frac{15}{A_{gg}^2} F_{cavj} \times D_{v,jsd} \times F'_{jsd} S^{vol}_{jsdtot} e_{pj} \left(C^{loc}_{v,jsd} - C^{eq}_{v,jsd}(j) \right) \tag{H.23}$$

The permanent regime for the thermal vacancies on the subdomain boundaries (eq. H.5) allows us to express a linear relation between $C^{loc}_{v,jsd}$ and $C^{loc}_{v,j}$: $C^{loc}_{v,jsd} = a_2 C^{loc}_{v,j} + b_2$, with:

$$a_2 = \frac{\frac{15}{A_{gg}^2} F_j \times D_{v,jsd} \times F'_{jsd} S^{vol}_{jsdtot} e_{pj} \times exp\left(+\frac{E_{seg,v,j} - E_{seg,v,jsd}}{kT}\right)}{denom_2} \; [adimensional] \tag{H.24}$$

$$b_2 = D_{v,jsd} \times F'_{jsd} S^{vol}_{jsdtot} e_{pj} \times \times \frac{\left[\sum_{cavjsd} geom_{cavjsd} C^{eq}_{v,jsd}(cavjsd) + \sum_{cavj} \frac{15}{A_{gg}^2} F_{cavj} C^{eq}_{v,jsd}(cavj)\right]}{denom_2} + \frac{\beta_1}{denom_2} \quad [vac/m^3] \tag{H.25}$$

Where $denom_2$ is:

$$denom_2 = D_{v,jsd} \times F'_{jsd} S^{vol}_{jsdtot} e_{pj} \times \times \left(\sum_{cavjsd} geom_{cavjsd} + \sum_{cavj} \frac{15}{A_{gg}^2} F_{cavj} + \frac{15}{A_{gg}^2} F_j\right) - \alpha_1 \; [s^{-1}] \tag{H.26}$$

We can now re-write the expression of $\Phi_{jsd->j}$, from eq. H.22, as:

$$\Phi_{jsd->j} = \alpha_2 C^{loc}_{v,j} + \beta_2 \tag{H.27}$$

With

$$\alpha_2 = \frac{15}{A_{gg}^2} F_j \times D_{v,jsd} \times F'_{jsd} S^{vol}_{jsdtot} e_{pj} \times \left(a_2 - exp\left(+\frac{E_{seg,v,j} - E_{seg,v,jsd}}{kT}\right)\right) \; [s^{-1}] \tag{H.28}$$

$$\beta_2 = \frac{15}{A_{gg}^2} F_j \times D_{v,jsd} \times F'_{jsd} S^{vol}_{jsdtot} e_{pj} \times b_2 \; [vac/m^3/s] \tag{H.29}$$

The flux of vacancies from the grain boundary to the "cavj" cavities can be written as:

$$\Phi_{j->cavj} = geom_{cavj} \times D_{v,j} \times F'_j S^{vol}_{jtot} e_{pj} \left(C^{loc}_{v,j} - C^{eq}_{v,j}(cavj)\right) \tag{H.30}$$

Where $geom_{cavj}$ is described by equation 3.12.
The expression does not change with respect to the "sound" state.

The flux of vacancies from the grain boundary to the exterior can be written as:

$$\Phi_{j->ext} = \frac{15}{A_{se}^2} \times D_{v,j} \times F_j^{'} S_{jtot}^{vol} e_{pj} \left(C_{v,j}^{loc} - C_{v,j}^{eq}(ext) \right) \tag{H.31}$$

Also this expression does not change with respect to the "sound" state.

The permanent regime for the thermal vacancies on the GB (eq. H.6) allows us to express a linear relation between $\beta_{v,j}$ and $C_{v,j}^{loc}$:

$$\beta_{v,j} = \alpha_3 C_{v,j}^{loc} + \beta_3 \tag{H.32}$$

Where

$$\alpha_3 = -\alpha_2 + D_{v,j} \times F_j^{'} S_{jtot}^{vol} e_{pj} \left(\sum_{cavj} geom_{cavj} + \frac{15}{A_{se}^2} \right) \; [s^{-1}] \tag{H.33}$$

$$\beta_3 = -\beta_2 - D_{v,j} \times F_j^{'} S_{jtot}^{vol} e_{pj} \left(\sum_{cavj} geom_{cavj} C_{v,j}^{eq}(cavj) + \frac{15}{A_{se}^2} C_{v,j}^{eq}(ext) \right) \; [vac/m^3/s] \tag{H.34}$$

At this point, we have everything that we need.

In the code, the calculations are performed in a similar order as for the "sound" state, starting from the calculation of $C_{v,j}^{loc}$ from eq. 5.27 (which stays the same for both the "sound" and the subdomain state, as I have already pointed out).

As for the "sound" state, our global model for the thermal vacancy contribution to the volume of the cavities will be consistent if the contribution to the intra-granular nano-bubbles will be negligible in base irradiation.
At the same time, we expect a not negligible flux of thermal vacancies from the grain boundaries to the precipitation bubbles. This flux is driven by a new diffusion coefficient, $D_{v,jsd}$, which is the diffusion coefficient of vacancies on the subdomain boundaries.
As for eq. H.35, we can express the link between $D_{v,jsd}$ and $D_{Ujsd,th}$, the thermal part of the Uranium auto-diffusion coefficient on the subdomain boundaries, as:

$$D_{Uj,th} = D_{v,j} \times x_{v,jsd}^{eq}(P_{surf} \approx 0) \tag{H.35}$$

See Section 7.1.6 for an estimation of $D_{Ujsd,th}$.

H.2. Restructured (HBS) state

If vacancies are created on the grain boundaries of HBS grains, those grains will move away one from the other with a velocity v_{move}.
We can describe the same phenomenon stating that each grain grows with a velocity $v_{move}/2$ at the surfaces facing a bare grain boundary.

In this case, the cavities are subjected to an homothety of the lengths equal to $\frac{A_{pg}+\frac{v_{move}\Delta t}{2}}{A_{pg}} = \frac{1+\frac{v_{move}\Delta t}{2A_{pg}}}{1}$, which translates to an increase in their volume (see figure I.1) of :

$$\left(1+\frac{v_{move}\Delta t}{2A_{pg}}\right)^3 \approx 1+\frac{3v_{move}\Delta t}{2A_{pg}} \tag{H.36}$$

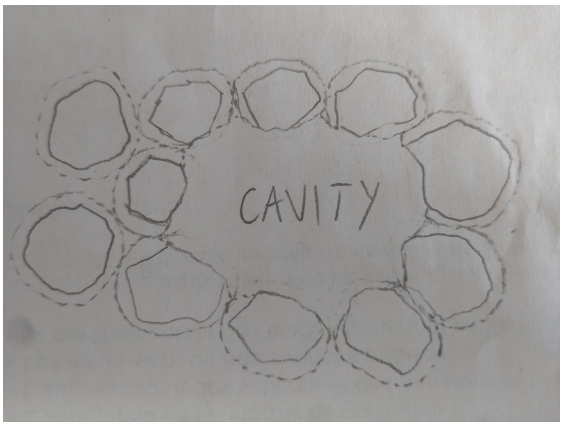

Figure H.1. – Growth of the HBS cavities due to the growth of the HBS grains.

If we call $\beta_{v,jrim}$ the rate at which the vacancies are created on the bare grain boundary over m^3 of not swelled restructured fuel (which is the volume of restructured fuel before irradiation, named $V_{0,rim}$), in [vacancies / s / m^3 of fresh fuel], we can state that:

$$\begin{aligned}\beta_{v,jrim} &= \frac{Surface\ of\ restructured\ bare\ GB}{V_{0,rim}} \times \frac{vacancies\ created\ /\ s}{Surface\ of\ restructured\ bare\ GB} \\ &= \frac{3F_{jrim}}{2A_{pg}} \times \frac{Produced\ Volume\ /\ s}{Surface\ of\ restructured\ bare\ GB} \times \Omega^{-1} \\ &= \frac{3F_{jrim}}{2A_{pg}} \times v_{move} \times \Omega^{-1}\end{aligned} \tag{H.37}$$

And therefore:

$$v_{move} = \beta_{v,jrim} \times \frac{2A_{pg}}{3F_{jrim}} \times \Omega \tag{H.38}$$

Which is similar to eq. 5.2.

Using eq. H.36, we can now write the increase of volume of the cavities over $V_{0,rim}$, V^{HBS}_{cavrim}, during dt, due to the moving away of the HBS grains as:

$$\frac{dV^{HBS}_{cavrim}}{dt}\Big|_{move\ away} = \frac{3v_{move}}{2A_{pg}} \times V^{HBS}_{cavrim} = \frac{\beta_{v,jrim}\Omega}{F_{jrim}} \times V^{HBS}_{cavrim} \tag{H.39}$$

The first equality is the expression of the homothety, and the second equality uses H.38.

The change in the volume of the fragment over $V_{0,rim}$ during dt, due to the growth of the grains (that induces the homothety on the cavities) is equal to:

$$\frac{1}{V_{0,rim}}\frac{dV_{fragment}}{dt}\Big|_{move\ away} = \frac{3F_{jrim}}{2A_{pg}} \times v_{move} + \sum_{cavrim} V^{HBS}_{cavrim} \times \frac{3v_{move}}{2A_{pg}} \tag{H.40}$$

Then, using eq. H.38 :

$$\frac{1}{V_{0,rim}}\frac{dV_{fragment}}{dt}\Big|_{move\ away} = \beta_{v,jrim} \times \Omega + \frac{\beta_{v,jrim}\Omega}{F_{jrim}} \sum_{cavrim} V^{HBS}_{cavrim} \tag{H.41}$$

At this point, we have to add the effect of the fluxes of vacancies from the grain boundaries of the restructured grains to the exterior and the cavities.
The total change in the volume of the fragment / $V_{0,rim}$ during dt is equal to:

$$\frac{1}{V_{0,rim}}\frac{dV_{fragment}}{dt} = \beta_{v,jrim} \times \Omega \times \left(1 + \frac{1}{F_{jrim}} \sum_{cavrim} V^{HBS}_{cavrim}\right) + \Phi_{ext->jrim} \times \Omega \tag{H.42}$$

If, once again, we make the hypothesis of quasi-steady state for the thermal vacancies on the grain boundary, we can write:

$$\beta_{v,jrim} + \sum_{cavrim} \Phi_{cavrim->jrim} + \Phi_{ext->jrim} = 0 \tag{H.43}$$

The rate of change of V^{HBS}_{cavrim} due to the flux of vacancies can then be written as:

$$\frac{dV^{HBS}_{cavrim}}{dt}\Big|_{flux\ vacancies} = \Phi_{jrim->cavrim} \times \Omega \tag{H.44}$$

And so:

$$\left.\frac{dV_{cavrim}^{HBS}}{dt}\right|_v = \Phi_{jrim->cavrim}\times\Omega + \frac{3v_{move}}{2A_{pg}}\times V_{cavrim}^{HBS} = \Phi_{jrim->cavrim}\times\Omega + \frac{\beta_{v,jrim}\Omega}{F_{jrim}}\times V_{cavrim}^{HBS} \tag{H.45}$$

Where $\left.\frac{dV_{cavrim}^{HBS}}{dt}\right|_v$ is the change of the volume of one population of HBS cavities (bubbles or pores) due to both the moving away of the HBS grains and the flux of thermal vacancies.

Using eq. H.43 and H.45, we can write the total swelling of the cavities considering both the moving away of the HBS grains and the flux of vacancies from the grain boundary to the cavities as:

$$\sum_{cavrim}\left.\frac{dV_{cavrim}^{HBS}}{dt}\right|_v = \beta_{v,jrim}\times\Omega + \frac{\beta_{v,jrim}\Omega}{F_{jrim}}\times\sum_{cavrim}V_{cavrim}^{HBS} + \Phi_{ext->jrim}\times\Omega \tag{H.46}$$

Which is equal to the swelling of the HBS fragment due to the thermal vacancies (see eq. H.42). Like in Sections 5.2.1 and H.1, we have verified that thermal vacancies only accumulate in the cavities.

We can now write the energy balance on the fragment:

$$\begin{aligned} -P_{Hydro}\times\frac{Swelling\ of\ the\ fragment}{Unit\ of\ time} & \\ +\sum_{cavrim}P_{surf}(cavrim)\times\frac{dV_{cavrim}^{HBS}}{dt} &= \beta_{v,jrim}\times\mu_{v,jrim} \\ &\quad -\Phi_{jrim->ext}\times\mu_{v,jrim/ext} \\ &\quad -\sum_{cavrim}\Phi_{jrim->cavrim}\times\mu_{v,jrim/cavrim} \end{aligned} \tag{H.47}$$

Which, using eq. H.42 and H.46, becomes:

$$
\begin{aligned}
-P_{Hydro} \times \left(1 + \frac{\sum_{cavrim} V_{cavrim}^{HBS}}{F_{jrim}}\right) \beta_{v,jrim} \times \Omega + \Phi_{jrim->ext} \times \Omega \times P_{Hydro} \\
+ \sum_{cavrim} P_{surf}(cavrim) \times \left(\frac{\beta_{v,jrim}\Omega}{F_{jrim}} \times \sum_{cavrim} V_{cavrim}^{HBS} + \Phi_{jrim->cavrim} \times \Omega\right) = \\
= \beta_{v,jrim}\mu_{v,jrim} - \Phi_{jrim->ext} \times \mu_{v,jrim/ext} \\
- \sum_{cavrim} \Phi_{jrim->cavrim} \times \mu_{v,jrim/cavjrim}
\end{aligned}
\tag{H.48}
$$

We can then find:

$$
\begin{aligned}
0 = \beta_{v,jrim} \times \left[\mu_{v,jrim} + \Omega \times \left[P_{Hydro} + \frac{\sum_{cavrim} \left(P_{Hydro} - P_{surf}(cavrim)\right) V_{cavrim}^{HBS}}{F_{jrim}}\right]\right] \\
- \Phi_{jrim->ext} \times \left(\mu_{v,jrim/ext} + P_{Hydro}\Omega\right) \\
- \sum_{cavrim} \Phi_{jrim->cavrim} \times \left(\mu_{v,jrim/cavjrim} + P_{surf}(cavjrim)\Omega\right)
\end{aligned}
\tag{H.49}
$$

As for the "sound" state, the last two terms are null.

Therefore, we obtain:

$$
\mu_{v,jrim} = -\frac{\Omega}{F_{jrim}} \times \left[P_{Hydro} \times F_{jrim} + \sum_{cavrim} \left(P_{Hydro} - P_{surf}(cavrim)\right) V_{cavrim}^{HBS}\right]
\tag{H.50}
$$

and, from eq. 5.16 and defining $\varepsilon_{v,jrim}$ as the formation energy of a vacancy on the HBS grain boundary, we get:

$$
x_{v,jrim} = exp\left(\frac{-\varepsilon_{v,jrim}}{kT}\right) exp\left[-\frac{\Omega}{kTF_{jrim}}\left[F_{jrim}P_{Hydro} - \sum_{cavrim} \left(P_{Hydro} - P_{surf}(cavrim)\right) V_{cavrim}^{HBS}\right]\right.
\tag{H.51}
$$

Knowing $x_{v,jrim}$ and $C_{v,jrim}^{loc} = x_{v,jrim}$ / Ω, we can calculate the fluxes of vacancies (in [mol / m^3 of not swelled HBS volume]):

$$\begin{aligned}
\Phi_{jrim->cavrim} =& 4\pi R_{cavrim} D_{v,jrim} \frac{3F_{jrim}}{2A_{pg}} e_{pj} \left(C^{loc}_{v,jrim} - C^{eq}_{v,jrim}(cavrim) \right) \\
& \times C^{HBS}_{cavrim} \times \Omega \\
\Phi_{jrim->cavrim} =& 4\pi R_{cavrim} \times \left(D_{v,jrim} \times \Omega \times c^{eq}_{v,jrim}(0,0) \right) \times \frac{3F_{jrim}}{2A_{pg}} e_{pj} \\
& \times \left(\frac{C^{loc}_{v,jrim}}{C^{eq}_{v,jrim}(0,0)} - exp\left(-\frac{P_{surf}(cavrim)\Omega}{kT} \right) \right) \times C^{HBS}_{cavrim} \\
\Phi_{jrim->cavrim} =& 4\pi R_{cavrim} \times D_{U,jrim} \times \frac{3F_{jrim}}{2A_{pg}} e_{pj} \\
& \times \left(\frac{C^{loc}_{v,jrim}}{C^{eq}_{v,jrim}(0,0)} - exp\left(-\frac{P_{surf}(cavrim)\Omega}{kT} \right) \right) \times C^{HBS}_{cavrim}
\end{aligned} \tag{H.52}$$

Where $C^{eq}_{v,jrim}(0,0)$ is the concentration of vacancies on the grain boundary in equilibrium at a pressure equal to zero and without influence of the curvature and C^{HBS}_{cavrim} is the density of bubbles in the restructured zone [bubbles / m^3 of not-swelled HBS volume].

Using eq. H.45, and $V_{cavrim} = V^{HBS}_{cavrim} \times fr$, $C_{cavrim} = C^{HBS}_{cavrim} \times fr$ and $S^{vol}_{jrim,tot} = \frac{3}{2A_{pg}} \times fr$, the contribution to the volume of the HBS cavities due to the thermal vacancies (included in the general ODE system) is written as:

$$\begin{aligned}
\left.\frac{dV_{cavrim}}{dt}\right|_v =& \frac{3v_{move}}{2A_{pg}} \times V_{cavrim} + \Phi_{jrim->cavrim} \times \Omega \times fr \\
\left.\frac{dV_{cavrim}}{dt}\right|_v =& \frac{3v_{move}}{2A_{pg}} \times V_{cavrim} + \pi R_{cavrim} \times D_{U,jrim} \times \frac{S^{vol}_{jrim,tot}}{fr} e_{pj} \\
& \times \left(\frac{c^{loc}_{v,jrim}}{c^{eq}_{v,jrim}(0,0)} - exp\left(-\frac{P_{surf}(cavrim)\Omega}{kT} \right) \right) \times C_{cavrim}
\end{aligned} \tag{H.53}$$

The second term has exactly the same form as equation 3.14 for the trapping of the dissolved gas in the HBS grain boundaries by the HBS cavities.
As all the variables of the ODE system, V_{cavrim} is expressed in [volume of the "cavrim" cavities / m^3 of fresh fuel].

I. Creep term for HBS cavities

Since the temperatures experienced by the outer pellet during base irradiation are quite low (as a term of reference, in this region the auto-diffusion coefficient of Uranium in the bulk is determined by the athermal contribution), we expect the impact of the vacancy contribution calculated in Section H.2 to the swelling of HBS cavities to be quite modest.
However, the HBS part of the fuel is the one that experiences the highest swelling. Therefore, in order to better predict the swelling in this area, we added the contribution to the growth of the HBS cavities due to irradiation-induced creep.

A resume of the data on in-pile creep rate in UO_2 during irradiation can be found in [Neilson et al. 2024] (figure 1 of the article).

Experiments [Dienst 1977] suggest that irradiation-induced creep is almost temperature independent. Dienst [ibid.] proposed a correlation valid for ceramic fuels on the form:

$$\dot{\varepsilon}_{irr} = c \times \sigma \times \dot{F} \tag{I.1}$$

Where $\dot{\varepsilon}_{irr}$ is the deformation rate, c is a constant, σ is the stress and $\dot{F}$ is the fission rate.

From the data in the irradiation-induced creep domain presented in [Neilson et al. 2024] (figure 1 of the article), we can estimate c using the formula above. Doing so, we obtain: $c \approx 10^{-34}$ [m^3 / Pa].

Now, our objective is to derive a simple expression for the cavity growth due to irradiation-induced creep.
To do so, we can start by considering an isolated spherical void in a linearly viscous material, with an applied hydrostatic stress (see figure I.1 (a)). The corresponding growth (or shrinkage) rate is then the following [Riedel 1986]:

$$\dot{V} = \frac{9}{4} \times B \times \sigma_{hydro} \times V \tag{I.2}$$

Where B is the coefficient of the general Norton's creep law [Norton 1929]: $\dot{\varepsilon} = B \times \sigma^n$, where n is another parameter. From eq. I.1 we know that, in our case, $n = 1$ and $B = c \times \dot{F}$.
Therefore, we obtain:

$$\dot{V} = \frac{9}{4} \times c \times \dot{F} \times \sigma_{hydro} \times V \tag{I.3}$$

Since we want to consider also the pressure in the cavity, and as the volume change (due to creep) may be identified with the cavity volume change, we propose to use an equation of the form:

$$\frac{dV_{cavrim}}{dt} = coe_{creep} \times \dot{F} \times (P_{surf} - P_{hydro}) \times V_{cavrim} \tag{I.4}$$

Where coe_{creep} is a parameter that needs to be deduced during validation (from our derivation, it should be in the order of magnitude of $\approx 10^{-34}$ [m^3 / Pa]). The difference $P_{surf} - P_{hydro}$ allows to predict a growth of the cavity if $P_{surf} > P_{hydro}$, and a shrink of the cavity if the opposite is true.
Here, $P_{surf} = P_{int}(cavrim) - \frac{2\gamma}{R_{cavrim}}$ and P_{hydro} is the macroscopic hydrostatic pressure given by the thermo-mechanical calculation at the point of the pellet where MARGARET is used. In our case, P_{hydro} is calculated by ALCYONE, and it is an input parameter for MARGARET.

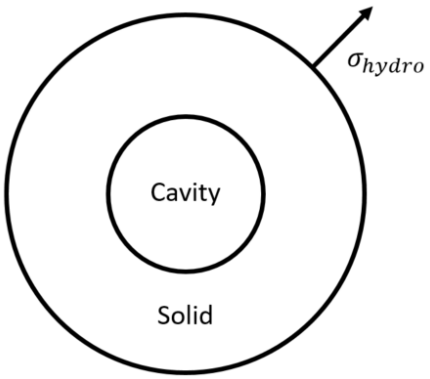

(a) Growth of an empty cavity due to creep, in the situation where an hydrostatic stress σ_{hydro} is present in the solid.

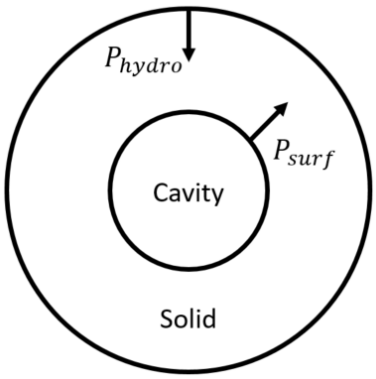

(b) Growth of a pressurized cavity due to creep, in the situation where an hydrostatic stress P_{hydro} is present in the solid.

Figure I.1. – Growth of the HBS cavities due to creep.

J. Derivation of the thermal vacancy contribution to the cavities in a limit scenario

If we exclude any exchange of vacancies between the grain boundary and the grain (D_U tends to 0 or A_{gg} tends to $+\infty$) and any exchange of vacancies between the grain boundary and the free surfaces (A_{se} tends to $+\infty$), we consider only one population of inter-granular cavities and no HBS formation, we would have:

$$F'_j = F_j \tag{J.1}$$

$$\Phi_{v,j->cavj} = geom_{cavj} \times D_{v,j} \times F_j S^{vol}_{jtot} e_{pj} \left(C^{loc}_{v,j} - C^{eq}_{v}(cavj) \right) \tag{J.2}$$

$$C^{loc}_{v,j} = exp\left(-\frac{\varepsilon_{v,j}}{kT}\right) exp\left(-\frac{\Omega}{kTF_j}\left[P_{Hydro} - P_{surf}(cavj)F_{cavj}\right]\right) \times \Omega^{-1} \tag{J.3}$$

$$C^{eq}_{v,j}(cavj) = exp\left(-\frac{\varepsilon_{v,j}}{kT}\right) exp\left(-\frac{P_{surf}(cavj)\Omega}{kT}\right) \times \Omega^{-1} \tag{J.4}$$

Where $exp\left(-\frac{\varepsilon_{v,j}}{kT}\right) = x^{eq}_v(P_{surf} = 0)$, which is the concentration of vacancies on the grain boundary in [vacancies / site] at equilibrium in the absence of an external pressure.

We then obtain:

$$\begin{aligned}\Phi_{v,j->cavj} =& geom_{cavj} \times D_{v,j} \times F_j S^{vol}_{jtot} e_{pj} \times \Omega^{-1} \times x^{eq,00}_v \times \\ & \times \left(exp\left(-\frac{\Omega}{kTF_j}\left[P_{Hydro} - P_{surf}(cavj)F_{cavj}\right]\right) - exp\left(-\frac{P_{surf}(cavj)\Omega}{kT}\right)\right)\end{aligned} \tag{J.5}$$

Using $exp(x) \approx 1 + x$ if $x << 1$, and with the hypothesis that both

$$\left| \frac{\Omega}{kTF_j}\left[P_{Hydro} - P_{surf}(cavj)F_{cavj}\right] \right| << 1 \tag{J.6}$$

and

$$\left|\frac{P_{surf}(cavj)\Omega}{kT}\right| << 1 \tag{J.7}$$

Then, since in this special case $F_{cavj} + F_j = 1$:

$$\begin{aligned}\Phi_{v,j->cavj} =& geom_{cavj} \times D_{v,j} \times F_j S^{vol}_{jtot} e_{pj} \times \Omega^{-1} \times x_v^{eq}(P_{surf} = 0) \times \\ &\times \left(\frac{-\left(P_{Hydro} - P_{surf}(cavj)\right)\Omega}{kTF_j}\right)\end{aligned} \tag{J.8}$$

Using the expression of $geom_{cavj}$ (eq. 3.12) and the relation between $D_{v,j}$ and $D_{U,j}$ (eqs. 5.48 and H.35), we obtain:

$$\Phi_{v,j->cavj} = \frac{8\pi \times (1 - F_{cavj}) \times D_{Uj} \times e_{pj}}{(3 - F_{cavj})(1 - F_{cavj}) + 2ln(F_{cavj})}\left(\frac{\left(P_{Hydro} - P_{surf}(cavj)\right)}{kT}\right)C_{cavj} \tag{J.9}$$

As we consider a permanent regime, $\Phi v, j- > cavj$ is also equal to β_{vj}, the production of vacancies on the grain boundary per m^3 of fuel and s.
Using the relation: $v_{move} = \frac{\beta_{v,j}\Omega}{F_j S_j^{tot}}$, the direct gain of volume by the bubble due to the fact that the grain centers move apart is:

$$F_{cavj} S^{vol}_{j,tot} v_{move} = \frac{F_{cavj}}{F_j}\beta_{v,j}\Omega \tag{J.10}$$

Finally, we find that:

$$\begin{aligned}\frac{V^{vac}_{cavj}}{dt} =& \Phi_{v,j->cavj} \times \Omega + \frac{F_{cavj}}{F_j}\beta_{v,j}\Omega \\ =& \Phi_{v,j->cavj}\left(1 + \frac{F_{cavj}}{F_j}\right)\Omega = \frac{-8\pi \times D_{Uj} \times e_{pj} \times \left(P_{surf}(cavj) - P_{Hydro}\right) \times \Omega}{\left[(3 - F_{cavj})(1 - F_{cavj}) + 2ln(F_{cavj})\right] \times kT} \times C_{cavj}\end{aligned} \tag{J.11}$$

Because $1 - F_{cavj} = F_j$.

This relation is the same as eq. 5.1 because $\sigma_{ext} = -P_{hydro}$ and $P_{surf}(cavj) = P_{int}(cavj) - \frac{2\gamma sin(\theta)}{R_{cavj}}$.